TESIS DE LA UNIVERSIDAD
DE ZARAGOZA

2024

59

José Manuel Pedrón Laserna

Intermediates in organic chemistry. A computational approach

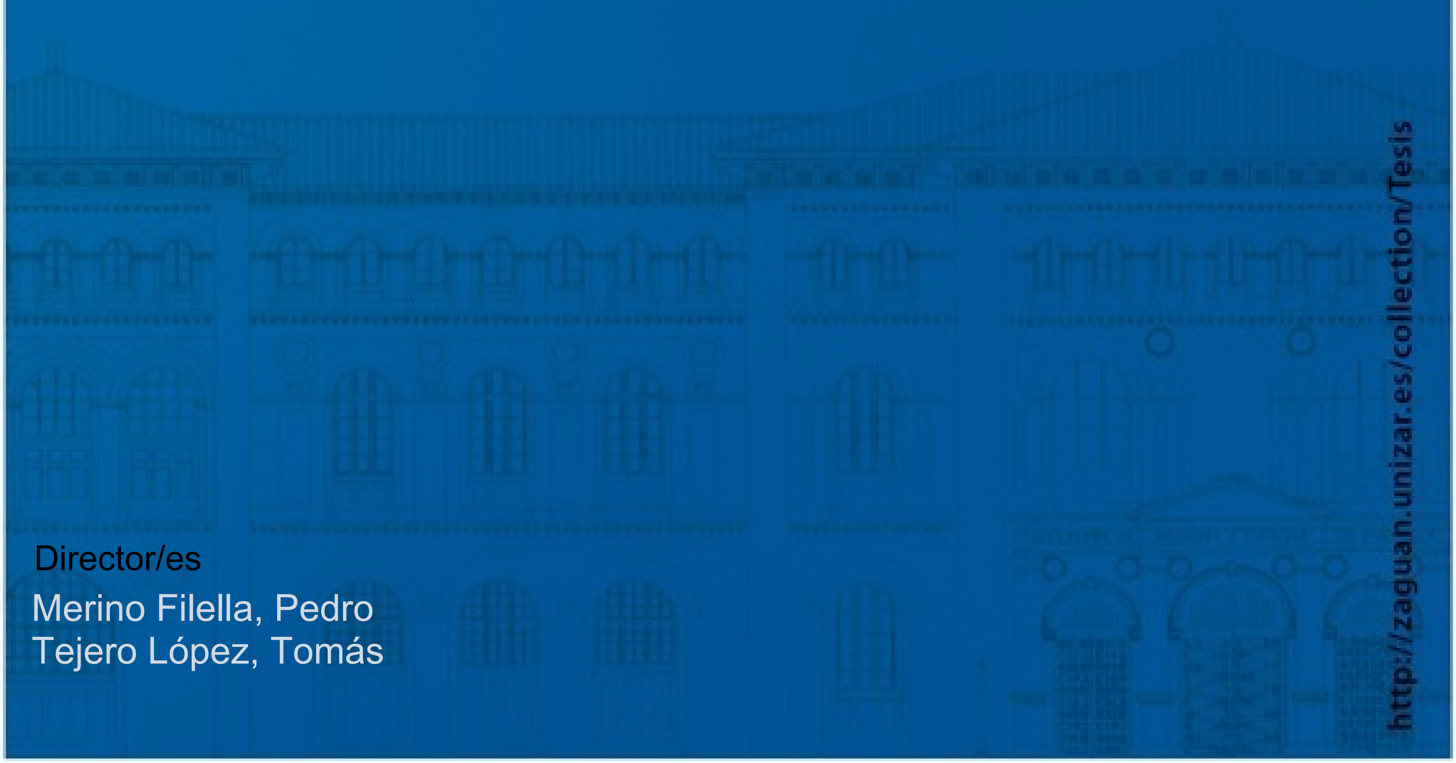

Director/es

Merino Filella, Pedro
Tejero López, Tomás

http://zaguan.unizar.es/collection/Tesis

ISSN 2254-7606

Prensas de la Universidad
Universidad Zaragoza

© Universidad de Zaragoza
Servicio de Publicaciones

ISSN 2254-7606

Tesis Doctoral

INTERMEDIATES IN ORGANIC CHEMISTRY. A COMPUTATIONAL APPROACH

Autor

José Manuel Pedrón Laserna

Director/es

Merino Filella, Pedro
Tejero López, Tomás

UNIVERSIDAD DE ZARAGOZA
Escuela de Doctorado

Programa de Doctorado en Química Orgánica

2023

Repositorio de la Universidad de Zaragoza – Zaguan   http://zaguan.unizar.es

Intermediates in organic reactions

A computational approach

Author

José Manuel Pedrón Laserna

Supervisors

Prof. Pedro Merino Filella

Prof. Tomás Tejero López

Universidad de Zaragoza

Programa de Doctorado en Química Orgánica

Zaragoza 2023

Universidad de Zaragoza

Departamento de Química Orgánica

Intermediates in organic reactions

A computational approach

Memoria presentada para acceder al título de Doctor por
José Manuel Pedrón Laserna

Zaragoza, 2023

Universidad
Zaragoza
1542

Pedro Merino Filella y ***Tomás Tejero López***, Catedráticos de Química Orgánica del Departamento de Química Orgánica de la Universidad de Zaragoza,

CERTIFICAN

Que D. Jose Manuel Pedrón Laserna ha realizado bajo su dirección, en el grupo de Química Biológica y Computacional del Departamento de Química Orgánica, el trabajo que se recoge en esta Memoria para optar al grado de Doctor en Química Orgánica, titulada:

Intermediates in organic reactions

A computational approach

Y autorizan la presentación de la misma ante la Universidad de Zaragoza para que se cumplan los trámites reglamentarios, de acuerdo con la legislación vigente.

Y para que así conste a los efectos oportunos, expedimos y firmamos el presente documento de autorización a fecha de:

25 de Agosto de 2023

Fdo. Prof. Dr. Pedro Merino Filella   Fdo. Prof. Dr. Tomás Tejero López

Science is constantly proved over time. If we take something like any fiction, and any holy book, and destroy it, in one thousand years' time, that wouldn't come back just as it was. Whereas if we took every science book and every fact and destroyed them all, in one thousand years they'd all be back because all the same tests would be the same result.

-Ricky Gervais-

TABLE OF CONTENTS

Abbreviations and acronyms 1

Resumen 4

CHAPTER I: GENERAL INTRODUCTION 14-45

1.1 Definition of reaction intermediates 16

1.2 Most common types of reactive intermediates 16

1.2.1 *Carbocations* 16

1.2.2 *Carbanions* 21

1.2.3 *Free Radicals* 23

1.2.4 *Carbenes* 25

1.3 Elusive and transient intermediates 28

1.4 Determination and characterization of reaction intermediates 30

1.4.1 *Spectroscopic techniques* 31

1.4.2 *Mass spectrometry* 32

1.4.3 *Trapping and isolation techniques* 33

1.5 Computational methods for the study of elusive intermediates 35

1.6 References 37

CHAPTER II: GENERAL OBJETIVES 48-52

2. Objectives 49

CHAPTER III: METHODOLOGIES 55-63

3.1 Experimental methods 57

3.2 Computational methods 57

3.3 References 60

CHAPTER IV: 5-MEMBERED-RING HETEROCYLCLES OXIDATION MEDIATED BY TRANSITION METAL OXIDES 65-100

4.1 Introduction 67

- 4.1.1 *The role of transition metal oxides in organic synthesis* 67
- 4.1.2 *Ruthenium tetroxide as a promising oxidation agent* 68
- 4.1.3 *Mechanistic discussion around RuO_4-mediated organic oxidations* 68

4.2 Results and discussion 71

- 4.2.1 *Searching carbocations in RuO_4 oxidation of saturated rings* 71
- 4.2.2 *Regioselectivity study on the RuO_4 oxidation of N-hydroxy pyrrolidines* 84

4.3 Conclusions 97

4.4 References 97

CHAPTER V: KINETIC AND COMPUTATIONAL STUDY ABOUT THE MIGRATION MECHANISM OF PROTECTIVE GROUPS IN CARBOHYDRATES 103-144

5.1 Introduction 105

5.1.1 *The role of acetyl groups beyond protecting agents* 105

5.1.2 *Migration of acetyl groups* 106

5.2 Results and discussion 110

5.2.1 *Experimental and kinetic studies of acetyl migration in monosaccharides* 110

5.2.2 *Kinetic insights derived from the mechanism of acetyl migration in monosaccharides* 114

5.2.3 *Evaluation of the protonation state and solvent model for the acetyl migration with glucopyranosides as study case* 117

5.2.4 *Modeling the pH dependence of acetyl migration: the definitive model* 122

5.2.5 *Acetyl migration in trisaccharides* 133

5.3 Conclusions 141

5.4 References 141

CHAPTER VI: COMPUTATIONAL EXPLORATION ON THE REACTION MECHANISMS AND THE ORIGIN OF THE SELECTIVITY IN ASYMETRIC ORGANOCATALYTIC PROCESSES 147-224

6.1 Introduction 149

6.1.1 *Evolution and advantages of organocatalysis* 149

6.1.2 *Enamine organocatalysis* 150

6.1.3 *Iminium-ion organocatalysis* 152

6.1.4 *Lewis base organocatalysis* 153

6.1.5 *Phase transfer catalysis* 155

6.1.6 *Hydrogen bond and Brønsted acid catalysis* 156

6.2 Results and discussion 159

6.2.1 *Enantioselectivity characterization of the transannular aminohalogenation of enesultams* 159

6.2.1.1 *Introduction* 159

6.2.1.2 *Results and discussion* 162

6.2.1.3 *Conclusions* 171

6.2.2 *Studying the concertedness of the BINOL-derived Mg(II)/ phosphate-catalyzed desymmetrizative ring expansion of 1-vinylcyclobutanos* 172

6.2.2.1 *Introduction* 172

6.2.2.2 *Results and discussion* 176

6.2.2.3 *Conclusions* 188

6.2.3 *Unraveling the mechanism of a switchable acid catalyzed cyclooctatetraene oxide contraction towards the enantioselective synthesis of homoallylic alcohols* 189

6.2.3.1 *Introduction* 189

6.2.3.2 *Results and discussion* 191

6.2.3.3 *Conclusions* 207

6.2.4 *Mechanistic study over an organocatalytic enantioselective Vinylcyclopropane-cyclopentene rearrangement* 207

6.2.4.1 *Introduction* 207

6.2.4.2 *Results and discussion* 211

6.2.4.3 *Conclusions* 217

6.3 Conclusions **218**

6.4 References **219**

CHAPTER VII: GENERAL CONCLUSIONS 227-229

7.1 General conclusions 229

ANNEX 231-235

Conclusiones generales 233

Scientific meetings 234

Publications based on the concept of the thesis 235

ABBREVIATIONS AND ACRONYMS

	δ	Chemical displacement
	°C	Degree Celsius
A	**Abs**	Absorbance
	Ac	Acetate
	ACN	Acetonitrile
	AIM	Atom in Molecules
	Anh.	Anhydrous
	Ar	Aryl
	Atm.	Atmosphere
	ATRP	Atom-transfer radical polymerization
B	**Bn**	Benzyl
	Boc	*Tert*-butoxycarbonyl
	Bu	Butyl
C	**Cat**	Catalyst
	COT	Ciclooctatetraene
	Cy	Cyclohexane
D	**DBU**	1,8-diazabicyclo(5.4.0)undec-7-ene
	DCE	1,2-dichloroethane
	DCM	Dichloromethane
	DIBAL	Diisobutylaluminium hydride
	DKR	Dynamic kinetic resolution
	DOSY	Diffusion-ordered NMR spectroscopy
	DYKAT	Dynamic kinetic asymmetric transformation
	d.r.	Diastereomeric ratio
E	**ee**	Enantiomeric excess
	ELF	Electron localization function
	EP	Encounter pair
	EPR	Electron paramagnetic resonance
	ESI	Electrospray ionization
	ESR	Electron spin resonance
	Et	Ethyl
	EWG	Electron withdrawing group
	Exp	Experimental
G	**Gal**	Galactose
	Glc	Glucose

	Glu	Glucoside
H	**Hex**	Hexane
	HOMO	Highest occupied molecular orbital
	HPLC	High-performance liquid chromatography
	HRMS	High-resolution mass spectroscopy
I	**^{i}Pr**	*Iso*-propyl
	IRC	Intrinsic reaction coordinate
	IUPAC	International union of pure and applied chemistry
K	**KIE**	Kinetic isotopic effect
L	**LA**	Lewis acid
	LB	Lewis base
	LG	Leaving Group
	LUMO	Lowest unoccupied molecular orbital
M	**MALDI**	Matrix-assisted laser desorption/ionization
	Man	Mannose
	MD	Molecular dynamics
	Me	Methyl
	MM	Molecular mechanics
	MO	Molecular orbital
N	**NBS**	N-Bromosuccinimide
	NCD	Norcaradiene
	NCI	Non-covalent interactions
	NMR	Nuclear magnetic resonance
	Nu	Nucleophile
P	**PES**	Potential energy surface
	Ph	Phenyl
	Pin	Pinacol
	Piv	Pivaloyl
	ppm	Parts per million
	PR	Product
	PT	Phase transfer
	PTC	Phase transfer catalysis
	p-TsOH	p-Toluenesulfonic acid
Q	**QM**	Quantum mechanics
R	**RDS**	Rate determining state
	Ref	Reference
	RT	Room temperature
S	**SEP**	Single electron transfer
	SI	Supporting information

T	**^{t}Bu**	*Tert*-butyl
	TBDMS	*Tert*-butyldimethylsilyl
	TEMPO	(2,2,6,6-Tetramethylpiperidin-1-yl)oxyl
	TMS	Trimethylsilyl
	Tf	Trifluoromethanesulfonate
	THF	Tetrahydrofuran
	THT	Tetrahydrothiophene
	TLC	Thin layer chromatography
	Ts	p-Toluenesulfonic
	TS	Transition state
X	**Xyl**	Xylose

RESUMEN

CAPÍTULO I: Introducción

El estudio del mecanismo de reacciones orgánicas es hoy una materia transversal dentro del campo de la Química, y como tal debe considerarse desde un punto de vista multidisciplinar que aborde diversos puntos de vista tanto teóricos como experimentales. El proyecto de investigación, en el que se enmarca el desarrollo de esta Tesis Doctoral, se centra principalmente en el uso de técnicas computacionales para el estudio mecanístico de reacciones orgánicas.

Concretamente, las reacciones que van a servir de objeto de estudio presentan, en su mayoría, intermedios inestables o transientes que difícilmente pueden ser detectados por técnicas experimentales, y necesitan pues, de técnicas computacionales para su estudio.

CAPÍTULO II: Objetivos

El objetivo principal de este proyecto de investigación es el estudio mecanístico de reacciones orgánicas y la justificación por medio de técnicas computacionales de los resultados obtenidos experimentalmente.

Como ejemplos de reacciones orgánicas se han escogido tres tipos:

1) Reacciones de oxidación de heterociclos
2) Migración de grupos protectores en carbohidratos
3) Procesos organocatalíticos

CAPÍTULO III: Metodología

Los estudios mecanísticos se han desarrollado principalmente de manera computacional, siendo la optimización mediante cálculos DFT la principal herramienta para el estudio de los diversos sistemas. Sin embargo, para la caracterización de los puntos de inflexión (reactivos, productos, intermedios y estados de transición), se ha hecho uso de las más modernas técnicas computacionales como son el estudio de la función de localización electrónica (ELF), el análisis de las interacciones no covalentes (NCI) ó cálculos de dinámica molecular (MD).

Por otro lado, en caso de ausencia de resultados experimentales con los que contrastar los datos teóricos, dichos resultados se han obtenido de manera experimental, principalmente haciendo uso de técnicas espectroscópicas (RMN) para estudiar el desarrollo de la reacción.

CAPÍTULO IV: Oxidación de heterociclos de 5 miembros con óxidos de metales de transición

En este capítulo se estudia le sincronicidad de las oxidaciones de diversos heterociclos al ser oxidados con tetróxido de rutenio. El mecanismo de esta reacción ha sido objeto de debate durante años, y este proyecto arroja algo de luz al asunto demostrando que heterociclos donde el heteroátomo es capaz de estabilizar por resonancia el intermedio de reacción, se oxidan siguiendo un mecanismo por pasos, mientras que aquellos en los que el heteroátomo este ausente, o sea incapaz de estabilizar la carga se verán oxidados siguiendo una vía concertada (**Esquema 1**).

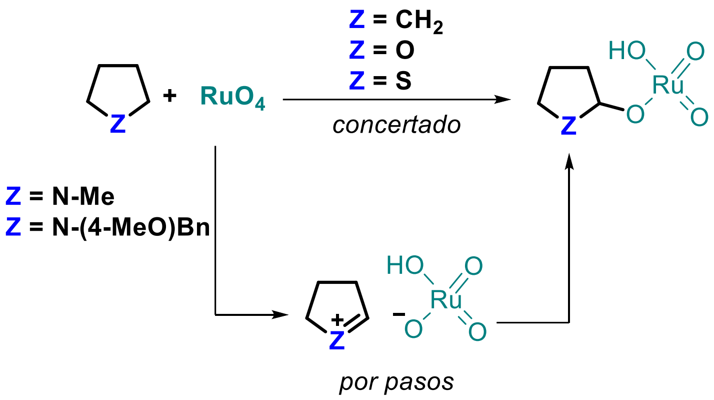

***Esquema 1**: Mecanismos de reacción para la oxidación de heterociclos con teróxido de rutenio.*

En el segundo apartado del capítulo, se estudia la misma oxidación, pero usando como sustrato una hidroxilamina cíclica. Aparte de la determinación del mecanismo de reacción, se estudia la regioselectividad de la reacción cuando se lleva a cabo la oxidación de hidroxilaminas cíclicas de 5 miembros sustituidas en la posición 3’.

A diferencia de las pirrolidinas del primer apartado, las hidroxilaminas se oxidan siguiendo una ruta concertada, en la que el estado de transición coincide con la abstracción del hidrógeno del grupo hidroxilo. Este hecho hace que la influencia del sustituyente en la posición 3’ del anillo se vea reducida en la mayoría de los casos a efectos estéricos, y no electrónicos como se teorizaba en un principio, reduciendo en gran medida la regioselectividad de la reacción. Esto es debido a que sólo la abstracción de uno de los 4 hidrógenos por los que puede transcurrir la reacción (Ha en el **Esquema 2**) se puede ver dificultada por el impedimento estérico entre el sustituyente y el oxidante.

Dada la ausencia de resultados experimentales en la oxidación de hidroxilaminas con RuO_4, se han sintetizado y hecho reaccionar varias hidroxilaminas con este oxidante observando, de acuerdo con los resultados computacionales bajas regioselectividades en todos los casos.

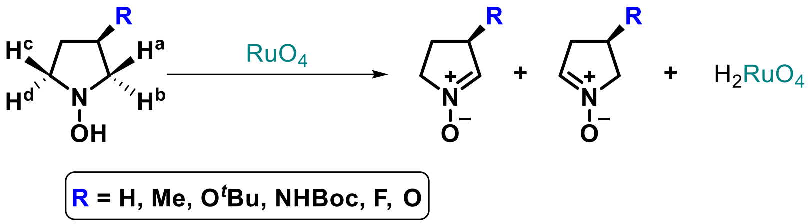

***Esquema 2:** Reacción general entre hidroxilaminas cíclicas de 5 miembros sustituidas sobre la posición 3' y tetróxido de rutenio.*

CAPÍTULO V: Estudio cinético y computacional del mecanismo de migración de grupos protectores en carbohidratos

La migración de grupos protectores en carbohidratos en un fenómeno conocido que dificulta el aislamiento y la purificación de muchos de estos compuestos. En este capítulo, se propone un modelo teórico sobre la migración de estos grupos protectores, usando como ejemplo la migración de acetilos en diversos mono- y trisacáridos. Los resultados teóricos serán contrastados con medidas cinéticas experimentales que auguran diferencias de energía muy pequeñas entre los múltiples isómeros de cada carbohidrato. Este hecho, unido a la gran variabilidad conformacional de los azúcares, y a que la reacción se lleva a cabo en medio acuoso, hacen necesario un análisis conformacional en profundidad y el establecimiento de un modelo de solvatación adecuado para reducir al mínimo posible los errores derivados de contrastar constantes cinéticas experimentales con barreras de energía obtenidas mediante cálculos computacionales.

Para modelizar correctamente la influencia del disolvente, diversos modelos de solvatación, tanto intrínsecos como extrínsecos fueron puestos a prueba.

Dada la influencia del pH en la velocidad de reacción, el modelo teórico tiene que ser capaz de explicar también dicha dependencia, por lo que es necesario realizar un estudio de la acidez de los diferentes carbohidratos y justificar su influencia sobre la migración.

El modelo finalmente propuesto hace uso del equilibrio ácido-base entre la forma protonada y desprotonada del azúcar, done la velocidad de migración se ve incrementada de manera exponencial cuando el carbohidrato presenta el hidroxilo vecinal al grupo protector desprotonado, dado el mayor carácter nucleófilo del anión. Sin embargo, dado que el pH del medio es cercano a neutro, la forma protonada actúa como *resting state*, haciendo así que la concentración de la especie desprotonada sea baja, reduciendo en consecuencia la velocidad de migración. Este modelo permite explicar también por qué la velocidad de reacción se incrementa de manera exponencial con el pH del medio, pues de la misma manera que se incrementa el pH, aumenta en consecuencia la concentración del azúcar desprotonado (**Esquema 3**).

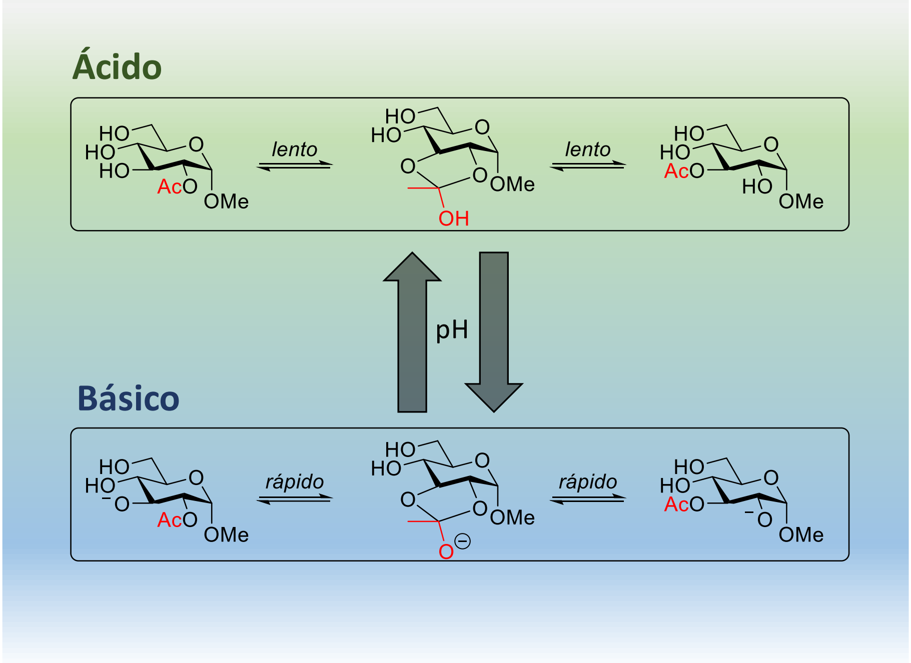

Esquema 3: *Mecanismo general, teniendo en cuenta el pH del medio para la migración de acetilos en un derivado de glucosa.*

Finalmente, el modelo fue puesto a prueba con trisacáridos, donde la migración puede darse también entre las distintas unidades de monosacáridos. El modelo, resultó ser adecuado para este nuevo sistema, aunque la mayor variabilidad conformacional de los trisacáridos en comparación con los monosacáridos incrementó la desviación del modelo teórico de los resultados experimentales.

CAPÍTULO VI: Exploración computacional de mecanismos de reacción y selectividad en procesos organocatalíticos asimétricos

El último capítulo se centra en el estudio computacional del mecanismo de reacción y el origen de la selectividad en una serie de procesos organocatalíticos enantioselectivos que presentan como factor común el uso de materiales de partida aquirales o en forma racémica. En la mayoría de los casos, la reacción transcurre a través de intermedios transientes o de baja estabilidad que dificultan su detección experimental. En total se han estudiado 4 sistemas, ilustrados en el **Esquema 4**.

El primero se trata de una aminohalogenación transanular de enesultamas. Esta reacción se inicia por la inserción del bromo en el doble enlace del anillo, seguido por el ataque intramolecular del nitrógeno a la posición homobencílica. El estudio se centra en dar explicación a la aparente inversión de la regioselectividad a través del análisis del mecanismo de reacción, pues en este tipo de sistemas, lo habitual es que la inserción del bromo se produzca en la posición contigua al anillo aromático, formando un intermedio carbocatiónico bencílico, mucho más estable.

Un análisis conformacional inicial reveló que la tensión del anillo impide la conjugación entre el doble enlace endocíclico y el anillo aromático, impidiendo en todas las conformaciones la estabilización del intermedio catiónico. A pesar de la falta de estabilización por parte del anillo aromático, este intermedio esta estabilizado por una interacción de carácter dador con el nitrógeno endocíclico, que es la responsable de la aparente inversión de la regioselectividad. En última instancia, esta interacción se intensifica y lleva al ataque nucleófilo de este mismo nitrógeno sobre la posición homobencílica, a través de un segundo estado de transición casi plano, finalizando la reacción.

A pesar de que el reactivo de partida es aquiral, la barrera de interconversión entre sus imágenes especulares es relativamente alta, lo que genera una situación similar a una DKR. La enantioselectividad del proceso es consecuencia de la formación de un *π-stacking* entre uno de los anillos aromáticos el organocatalizador con el anillo aromático de la enesultama en uno de los enantiómeros del reactivo de partida.

Cap. 6.3.1: Enantioselective transannular aminohalogenation of enesultams

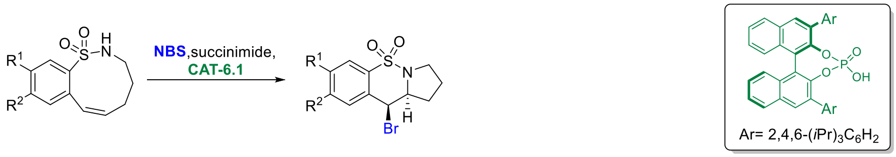
R1
R2
O
O
S
H
N
NBS,succinimide,
CAT-6.1
R1
R2
O
O
S
N
H
Br
Ar
O
O
P
O
OH
Ar
Ar= 2,4,6-(iPr)3C6H2

Cap. 6.3.2: Mg(II)/Phosphate-catalyzed desymmetrizative ring expansion of 1-vinylcyclobutanols

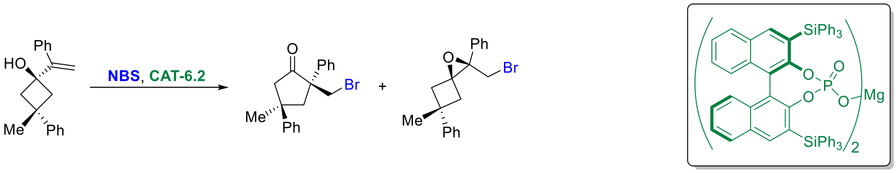
Ph
HO
Me
Ph
NBS, CAT-6.2
O
Ph
Br
Me
Ph
+
Ph
O
Br
Me
Ph
SiPh3
O
O
P
O
O
Mg
SiPh3
2

Cap. 6.3.3: Switchable acid catalyzed cyclooctatetraene oxide contraction

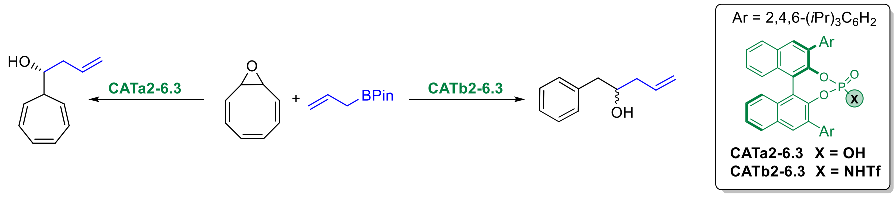
HO
CATa2-6.3
O
+
BPin
CATb2-6.3
OH
Ar = 2,4,6-(iPr)3C6H2
Ar
O
O
P
O
X
Ar
CATa2-6.3 X = OH
CATb2-6.3 X = NHTf

Cap. 6.3.4: Organocatalytic enantioselective vinylcyclopropane-cyclopentene rearrangement

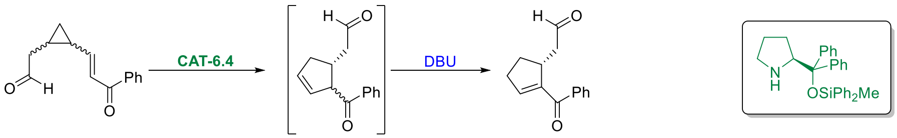
O
H
Ph
O
CAT-6.4
H
O
Ph
O
DBU
H
O
Ph
O
N
H
Ph
Ph
OSiPh2Me

Esquema 4: *Sistemas organocatalíticos enantioselectivos estudiados.*

El segundo apartado se centra en el estudio de la selectividad de la expansión de anillo iniciada mediante la bromación del grupo vinilo de diferentes vinilciclobutanoles, para dar ciclopentenonas. En esta reacción que recuerda, en parte, a una transposición semipinacolínica, se podía obtener también un epóxido por el ataque intramolecular del alcohol. El mecanismo para la formación de ambos productos resulta ser concertado pero altamente asíncrono, con un intermedio transiente cuya vida media excede los 200 fs. La mayor proporción del producto carbonílico se debe a las tensiones intramoleculares del estado de transición para la formación del epóxido, que debido a la disposición del catalizador, obliga a los orbitales no enlazantes del alcohol a apuntar en la dirección contraria al grupo vinilo, teniendo que producirse su inversión piramidal, y aumentando así su energía. Sin embargo grupos electro-dadores sobre el anillo aromático del grupo vinilo estabilizan en mayor medida al estado de transición que conduce al epóxido, aumentando así la proporción de este último en el producto final.

El tercer apartado estudia la reacción de contracción de anillo del óxido de ciclooctatetraeno mediada por ácidos fosfónicos y aminofosfónicos quirales, seguida por una posterior alilación enantioselectiva. Los estudios cinéticos demuestran la capacidad de los ácidos aminofosfóricos de catalizar una doble contracción de anillo, que da como resultado la formación de aldehídos aromáticos. El factor clave que controla la contracción de anillo es la acidez del organocatalizador. En el caso de los organocatalizadores más ácidos, como los ácidos aminofosfóricos, la etapa limitante es la apertura del epóxido en el óxido de ciclooctatetraeno, por lo que una vez se abre el epóxido, la reacción continúa hacia la doble contracción con barreras siempre más bajas que la inicial. Por otro lado, en el caso de los ácidos fosfóricos, más suaves, la etapa limitante es la segunda contracción de anillo, por lo que a temperaturas moderadas se puede obtener mayoritariamente el producto correspondiente a una única contracción.

Finalmente, en el último apartado se estudia la expansión de anillo de vinilciclopropanos catalizada vía iminio. Esta reacción transcurre de manera concertada, formando un intermedio transiente en el que toda la información configuracional ha sido transformada en conformacional y viceversa. Esto produce que independientemente del isómero de partida, el intermedio sea común, y evolucione siempre a través del estado de transición de menor energía hacia la misma distribución de productos, pudiendo catalogar al proceso como una DIKAT de tipo II.

CHAPTER I

GENERAL INTRODUCTION

1.1 Definition of reaction intermediates

The IUPAC Gold Book defines intermediate as "*a molecular entity with a lifetime significantly longer than a molecular vibration (corresponding to a local potential energy minimum of depth greater than RT) that is formed (either directly or indirectly) from the reactants and further reacts to produce (either directly or indirectly) the products of a chemical reaction*". [1]

Note that while the second part of the definition simply establishes that the intermediate exists between reactants and products, the first part refers to the intermediate's lifetime being "appreciably longer than a molecular vibration," which is open to interpretation.

Commonly, it is said that a reactive intermediate is a short-lived, high-energy, and highly reactive molecule that forms during a chemical reaction and rapidly evolves into a more stable molecule. [2]

Characterizing these intermediates plays a major role in the study of reaction mechanisms, which has gained significant importance in recent years. This is not only because it can explain experimental results but also because it can predict and estimate other properties of the different substrates, such as atom distances, conformational minima, or various types of spectra. In organic chemistry, reactive intermediates typically fall into one of these categories: carbocations, carbanions, free radicals and carbenes.

1.2 Most common types of reactive intermediates

1.2.1 Carbocations

A carbocation is defined as an ionic species with a positive charge on a carbon atom. They were first postulated more than 100 years ago when Hans Meerwein, Sir Christopher Ingold, and Frank Whitmore observed certain experimental phenomena related to substituent effects and orientation in electrophilic additions and substitutions. [3]

However, it was not until the 1960s that the modern era of carbocation chemistry began with George Olah's discovery. He found that carbocations, such as Me_3C^+ could be observable at low temperatures using superacids like SbF_5/SO_2. [4] These superacids are strong enough to protonate double bonds and generate a sufficient concentration of carbocations that could be measured using the NMR spectrometers available at that time (they can be up to 10^{18} times stronger than concentrated sulfuric acid). Using this system, Olah and his team were able to measure the ^{1}H-NMR and ^{13}C-NMR spectra, which revealed chemical shifts of 13.0 ppm and 320.6 ppm for the hydrogen and carbon atoms of the isopropyl cation, respectively. These chemical shifts could only be explained by the presence of a pure carbocation. Since then, numerous studies have been published on this topic. [5]

During that time, around the 1960s, these cations were initially referred to as "carbonium ions," a term adopted due to their similarity to other positively charged molecules such as ammonium, phosphonium, or sulphonium. [6] However, in later years, with the discovery of electron-deficient bonds, George Olah reserved the term "carbenium" to describe classical trivalent carbocations, while "carbonium" was used for the newer two-electron, three-center bond carbocations that exhibited penta- or hexacoordinate geometries. [7]

Carbenium ions are the classical carbocations with which we are all familiar. They have a planar geometry, are sp^2 hybridized, and exhibit electron deficiency. As shown in **Figure 1.1**, carbenium ions possess an empty p-orbital perpendicular to the plane of C-H bonds, which corresponds to the lowest unoccupied molecular orbital (LUMO). In reactions involving this type of carbocations, their natural reactivity is attributed to the interaction between this LUMO and the highest occupied molecular orbital (HOMO) of another species.

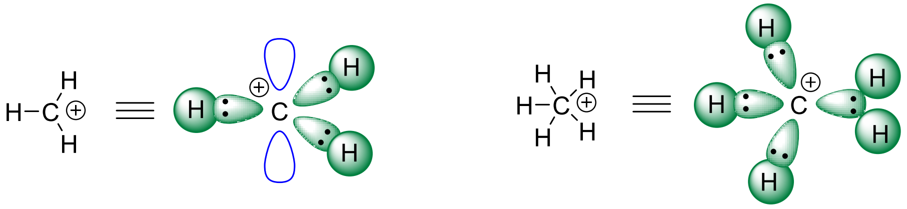

$^+CH_3$ = ***Carbenium ion***

$^+CH_5$ = ***Carbonium ion***

Figure 1.1: *Structure representation of carbenium and carbonium ions, following Olah's nomenclature.*

On the other hand, there is a limited list of examples of sp-type carbocations, in which the geometry around the cation is nearly linear. **Scheme 1.1** demonstrates that resonance within an alkynyl carbenium results in a linear carbocation.

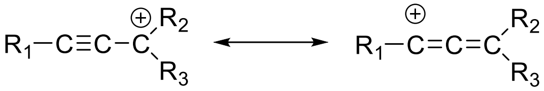

Scheme 1.1: *Alkynyl carbenium, example of a sp carbocation.*

Their stability increases with increasing substitution. The ΔH for heterolytic dissociation of alkanes into the corresponding carbocation and a hydride, in the gas phase follows the trend: methyl > ethyl > isopropyl > tert-butyl. This generalization suggests that more substituted carbocations are more stable. The explanation for this phenomenon is based on two factors: induction and hyperconjugation.

Firstly, the stabilization through induction occurs because a sp^3-hybridized carbon atom has a lower electronegativity by 0.25 units compared to a sp^2-hybridized carbon atom of the same type. As a result, an electron polarization occurs through σ bonds.

However, induction alone cannot fully explain their relative stability, and this is where hyperconjugation comes into play. As shown in **Figure 1.2**, hyperconjugation is based on the interaction between the σ C-H bonds adjacent to the empty p orbital of the carbocation, whereby they donate electron density to the carbocation, thereby increasing its stability.

Moreover, as the number of methyl groups increases, there are more C-H bonds available to stabilize the positive charge, resulting in a more stable carbocation. [8] Additionally, other factors such as resonance or solvent effects also contribute to the stabilization of the carbocation.

Nonclassical carbocations, or carbonium ions following Olah's nomenclature, cannot be accurately represented by a single Lewis structure due to the presence of a hypervalent carbon atom that contains at least one two-electron, three-center bond. Unlike classical carbocations, these structures have their valence shell completed and therefore do not exhibit any empty p orbital that would render them electron deficient. [9]

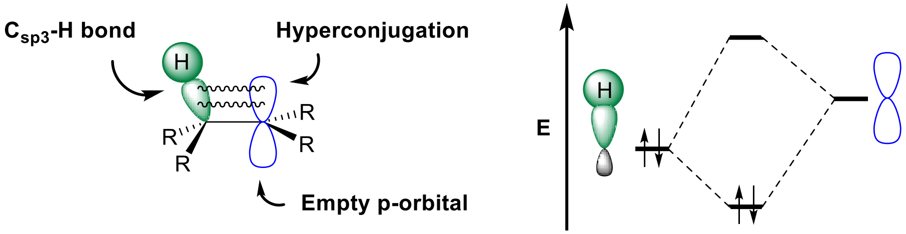

Figure 1.2: ***(Left)*** *Representation of hyperconjugation in a model scheme.* ***(Right)*** *Effect of the hyperconjugation through a MO diagram.*

The most known example of a hypervalent carbocation is the 2-norbornyl cation. [10] As mentioned earlier, this carbocation cannot be accurately described by a single Lewis structure, and as depicted in **Scheme 1.2**, 6 structures are required. While the existence of the non-classical 2-norbornyl cation was a subject of debate in the past century, it has now been unequivocally confirmed through both experimental and computational studies. [11]ww

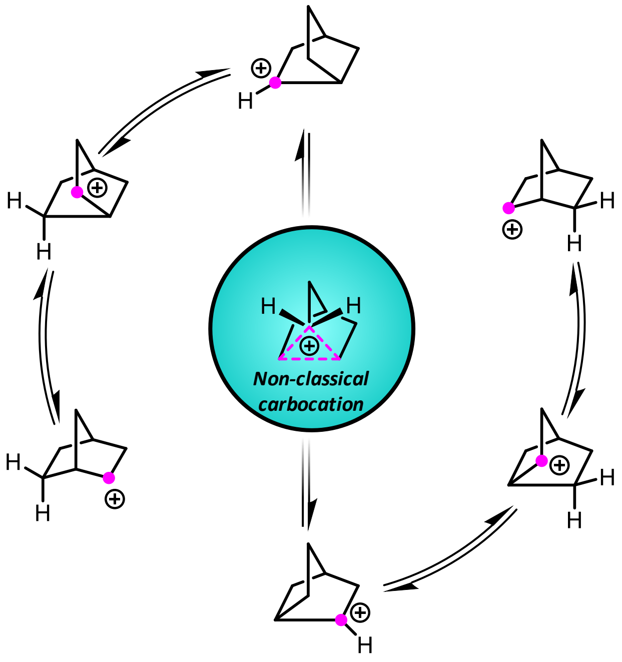

Scheme 1.2: *Comparison between classical and non-classical 2-norbornyl cations structures.*

Since then, many non-classical carbocation structures have been described. [12] Some of representative examples are depicted in **Scheme 1.3**. The cyclopropyl-carbinyl cation **1-1** was one of the first non-classical carbocations proposed, and higher concentrations of the bicyclobutonium ion have been demonstrated in superacid solutions. [13] On the other hand, structure **2-1**, corresponding to the 2-butyl cation, has been under study for many years. The structure was thought to exhibit a rapid equilibrium between two forms: one with a three-center, two-electron hydrogen bond, and another where the hydrogen atom is substituted by a methyl group. [14] More recent computational calculations have shown an almost 50:50 ratio between both isomers, [15] as well as the potential of these non-classical structures to act as C-H hydrogen bond donors with ammonia, which could be involved in enzyme-catalyzed terpenoid synthesis. [16]

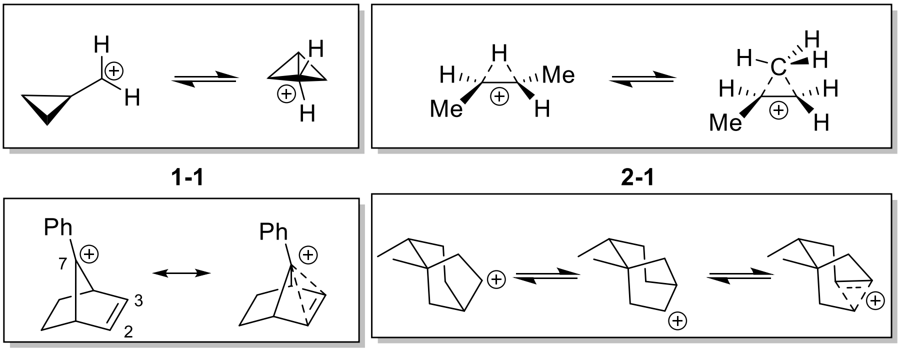

1-1 **2-1**

3-1 **4-1**

Scheme 1.3: *Examples of non-classical carbocations (carbonium ions).*

The 7-phenyl-7-norbornenyl cation **3-1** serves as an example of a homoallylic cation. It adopts a pyramid-like form, where the empty p orbital at C7 overlaps with the double bond MOs. The crystalline structure of a C2-C3 di-methylated analogue reveals an elongated double bond of 1.41Å and a distance between C2, C3, and C7 of only 1.87 Å. [17] These findings support the nonclassical nature of the non-methylated analogue.

Furthermore, **4-1** exhibits similarities to the 2-norbornyl cation and acts as a model for key intermediates in the biosynthesis of diterpenes. It undergoes an unexpected "triple shift reaction" that proceeds in a concerted manner. Ab initio molecular dynamic simulations of this system result in a highly complex mixture of structures interconnected by a remarkably flat potential energy surface. [18] This example serves as evidence that even after a century, the study of carbocations remains a challenge. While the existence of non-classical carbocations and their role as reactive intermediates have been well-established, there is still a significant amount of ongoing research in the field. [19]

1.2.2 Carbanions

Carbanion chemistry, like its positive counterparts, has a history that dates back more than 100 years. Although carbanions were postulated as intermediates in organic reactions, it was not until the middle of the nineteenth century when the first carbanion metal salt was synthesized. [20] This discovery involved the synthesis of an organomagnesium compound, with Grignard being responsible for popularizing these compounds. [21]

Carbanions have found extensive applications in organic synthesis, playing a crucial role in the construction of complex molecular structures. They are commonly utilized in nucleophilic addition reactions, allowing for the introduction of various functional groups to carbon skeletons. By serving as nucleophiles, carbanions facilitate the formation of new carbon-carbon bonds and contribute to the synthesis of diverse organic compounds.

Carbanions are the counterpart concept to carbocations: they consist of a negatively charged carbon atom with a completely filled valence shell, and they tend to act as nucleophiles or bases depending on the reaction conditions. Carbanions can be generated through various methods, with the most common one being the deprotonation of carbon-based compounds. [22] This methodology serves as the initial step in many well-known organic processes, such as the Michael, Darzen, or Knoevenagel reactions. Other methods of generating carbanions include decarboxylation, [23] addition of nucleophiles to alkenes, [24] or the formation of organometallic compounds. [25]

Since carbanions have a tetrahedral geometry due to their complete valence shell, it is possible to generate chiral carbanions with varying degrees of stability depending on their substituents. [26] Interestingly, a carbanion can undergo a pyramidal inversion, in a similar way to other groups containing lone pairs, the energy of which depends on its substituents (**Figure 1.3**). For example, a methyl carbanion exhibits a 19.2 kcal/mol energy barrier for pyramidal inversion, while this barrier increases to 53.3 kcal/mol with difluoromethyl anion, [27] making its configuration remarkably stable. These inversion barriers play a significant role in chiral carbanions, as the inversion process leads to racemization.

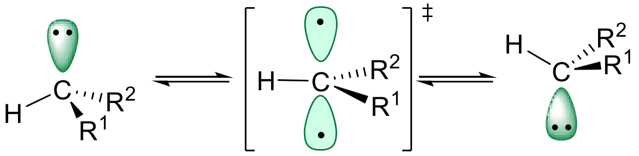

$R^1 = R^2 = H$	**[19.2]**
$R^1 = H; R^2 = F$	**[32.6]**
$R^1 = R^2 = F$	**[53.3]**

Figure 1.3: *Carbanionic inversion mechanism along with the relative energies in kcal/mol of different substituted methyl carbocations.*

The stability of these species relies on the same factors as carbocations but with the opposite effect. Carbanions are better stabilized with electronegative substituents at their α position or groups with empty orbitals such as metals or boranes. The inductive effect produces destabilization rather than stabilization compared to carbocations, owing to their intrinsic electron abundance. Thus, carbanions prefer a lower degree of alkyl substitution.

Carbanions serve as intermediates in many organic reactions, such as aldol condensations, Claisen condensations, or Michael additions, making their study a valuable tool for understanding organic processes.

Carbanions represent a fascinating class of reactive intermediates with immense synthetic potential. Their nucleophilic nature and reactivity make them valuable tools in organic synthesis, enabling chemists to construct complex molecules and functionalize carbon skeletons. Understanding the formation, properties, and reactivity of carbanions opens avenues for developing novel synthetic methodologies and advancing our understanding of chemical transformations. Continued research in this field promises to uncover new applications and expand the frontiers of organic synthesis.

1.2.3 Free radicals

In contrast to cations or anions, organic radicals are characterized by the presence of unpaired electrons, which gives these species their characteristic high reactivity and transient nature. [28] These properties have attracted significant attention in many fields, including organic chemistry.

Organic radicals can be formed primarily through two ways: homolytic cleavage of covalent bonds and single electron transfer processes. These processes can be facilitated through various methods, such as radical initiators, metal catalysis, or thermal or photochemical processes.

Their unpaired electrons allow radicals to act as both electron donors and electron acceptors, depending on their electronic nature and substituents. Radical stability is influenced by factors similar to other intermediates, such as resonance effects, hyperconjugation, and steric hindrance. However, due to their highly reactive and transient nature, directly detecting and characterizing them can be challenging. Therefore, several techniques have been developed for their study, such as electron spin resonance (ESR) or radical trapping.

Organic radicals play a crucial role in various strategies for organic synthesis. [29] They are involved in radical chain reactions, including radical polymerizations and free radical reactions. Additionally, radicals are employed in functional group transformations such as radical additions, substitutions, and cyclizations, enabling the synthesis of complex organic molecules. Radicals also find applications in natural product synthesis, medicinal chemistry, and materials science, contributing to the development of new drugs, polymers, and materials. [30]

The fundamental understanding of radical processes emerged after the first useful reaction involving radicals, [31] with the discovery of the trityl radical by Gombert. [32] From that point the emergence of radical processes began, with notable examples such as Meerwein’s arylation [33] or Birch reduction. [34] Noteworthy discoveries were made years later by Barton and Breslow, demonstrating the immense power of radical translocation. [35] Other studies, such as Mn(III)-mediated oxidative addition to olefins, [36] radical-based cross-coupling chemistry, [37] or the Minisci heterocycle C-H alkylation, [38] served as starting points for the further development of radical chemistry. From this point, many other processes involving radicals have been developed. For example, the development of atom-transfer radical polymerization (ATRP) has led to countless applications in material science. [39]

Summarizing, organic radicals offer a rich playground for exploring new chemical transformations and synthetic methodologies. Their participation in radical reactions and their ability to form new bonds make them valuable intermediates in organic synthesis. Understanding the formation, properties, and reactivity of organic radicals enables chemists to develop innovative strategies for constructing complex organic molecules. Continued research in this field will unravel new synthetic opportunities and expand our knowledge of radical chemistry, opening doors to exciting advancements in organic synthesis and materials science.

1.2.4 Carbenes

Once the loss and gain of electron pairs to form cations and anions, respectively, has been explored, as well as semi-occupied orbitals, we can now turn our attention to a specific type of intermediate that possesses both a lone electron pair and an empty p orbital. When this electronic disposition is located on a carbon atom, it is referred to as a carbene, whereas if it is on a nitrogen atom, it is called a nitrene. These species are renowned for their unique electronic structures and reactivity patterns, which have opened up new avenues for the development of efficient and diverse synthetic methodologies. Both carbenes and nitrenes can be classified into two types: singlet and triplet species, and their reactivity strongly depends on this electronic state. Singlet species are generally more stable and exhibit greater reactivity due to the pairing of their electrons (**Figure 1.4**). [40]

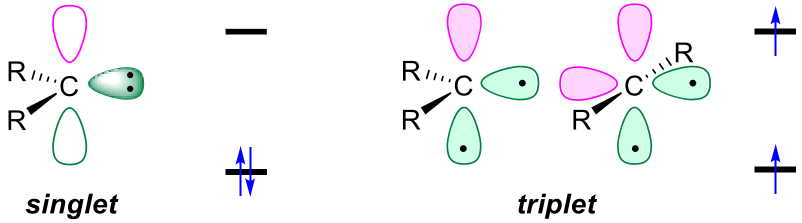

Figure 1.4: *Geometries and electronic dispositions of both singlet and triplet carbenes.*

Singlet carbenes are characterized by the absence of unpaired electrons, having a total spin of zero, a sp^2 hybrid structure, and being diamagnetic. Due to the presence of both lone pair electrons and an empty orbital, these species can act as both nucleophiles and electrophiles in an attempt to complete their valence shell. A wide range of reactions, including insertions, additions, cycloadditions, or even C-H insertions, can be performed, enabling the functionalization of inactivated C-H bonds. [41]

On the other hand, triplet carbenes present two unpaired electrons, enabling both sp^2 and sp hybrid structures. In most cases, the linear structure is not found, although it can be dominant with less electronegative substituents. [42] Due to their unpaired electrons, these compounds are paramagnetic, and thus, they can be observed through ESR. [43] Additionally, triplet carbenes have a longer lifetime compared to singlet carbenes, making them easier to detect using triplet trapping. [44] Since they can be defined as diradicals, [45] their reactivity differs from singlet carbenes and is closer to radical chemistry. For example, like other radicals, triplet carbenes are able to abstract hydrogen atoms from organic solvents. [46] Another difference between singlet and triplet carbenes is their selectivity in C-C double bond insertions, where singlet carbenes react through a concerted pathway with retention of the substrate's configuration, while triplets, due to their electronic configuration, tend to react via a stepwise mechanism, losing stereospecificity (**Scheme 1.4**). [47]

Carbenes are often generated as short-lived reaction intermediates through various methods, including the thermal or photochemical decomposition of different precursors such as diazo-compounds [48] or 3H-diazirines [49] for carbenes or azides for nitrenes. [50] Other alternatives include metal-catalyzed or metal mediated reactions. [51] These species are generated as singlet unless a photosensitizer is used since the precursors are also in the singlet state. [52]

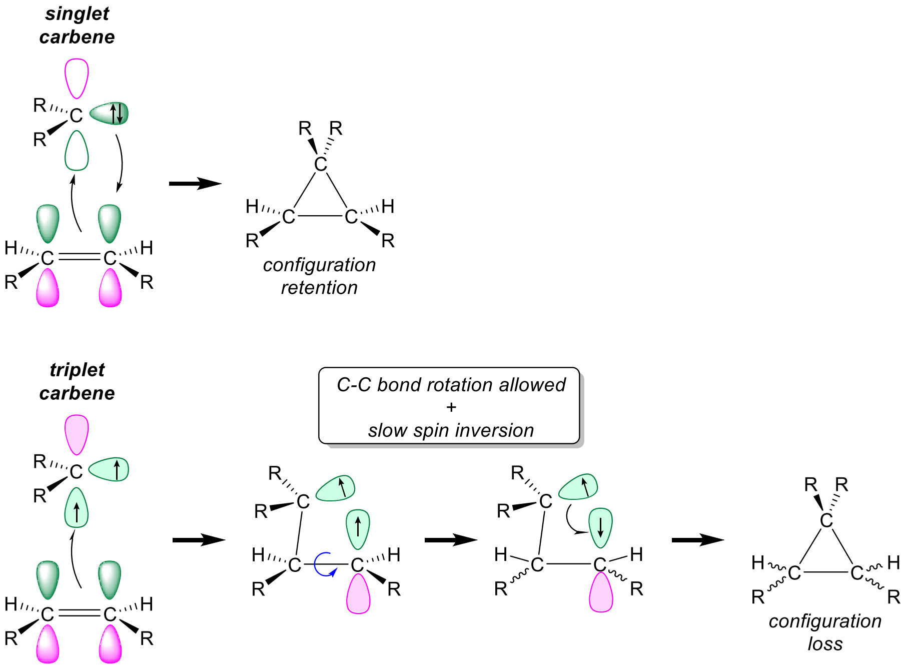
singlet carbene
configuration retention
triplet carbene
C-C bond rotation allowed
+
slow spin inversion
configuration loss

***Scheme 1.4**: Synchronicity comparison between singlet (top) and triplet (bottom) carbenes in C-C double bond insertions.*

Carbenes have found extensive applications in the synthesis of natural products, pharmaceuticals, and fine chemicals. [53] Transition metal-catalyzed carbene reactions, such as olefin metathesis and cyclopropanation, have revolutionized the field of organic synthesis by enabling the construction of complex molecular architectures with high efficiency and selectivity. [54] Additionally, carbenes have been employed in the synthesis of heterocycles, such as pyrroles and indoles, through intramolecular cycloaddition reactions. [55]

On the other hand, nitrenes have also found many applications in the synthesis of pharmaceuticals, agrochemicals, and materials. [56] The ability of nitrenes to selectively insert into C-H bonds has been harnessed for the late-stage functionalization of complex molecules, facilitating the rapid diversification of drug candidates. [57] Nitrene-based cycloadditions have been employed in the synthesis of nitrogen-containing heterocycles, which are prevalent in pharmaceuticals and bioactive compounds. [58]

1.3 Elusive and transient intermediates

In recent years, the importance of characterizing intermediates in the identification and isolation process has grown significantly, playing a fundamental role in understanding reaction mechanisms. Nowadays, there are multiple experimental and theoretical methods available to approach the characterization of intermediates.

Due to the inherently transient nature of intermediates, research in this field has often been limited. This was particularly evident in the last century, where mechanisms and intermediates were primarily inferred through the direct analysis of reactants and products. [59] During this time, the situation resembled that of transition states, with the distinction that it is possible to detect or even isolate intermediates depending on their relative stability. This stability is determined by the PES that surrounds them. Intermediates with low barriers on the PES exhibit high kinetic constant values, resulting in lower concentrations throughout the reaction. Consequently, the characterization of such intermediates becomes more challenging. **Figure 1.5** depicts a comparison between two extreme situations. In the central diagrams, where the kinetic constants share values (k_1=k_2), he concentration of the intermediate remains significant throughout the reaction. However, in the lower situation, where k_1 = 1/8 k_2, the abundance of the intermediate is nearly zero at all times, significantly reducing the chances of locating the intermediate.

On the other hand, it is well-known that reactions in which no intermediate is formed throughout the entire course of the reaction are called concerted reactions. While the terms "concerted" and "stepwise" have been familiar for decades, there are scenarios in which classification can be challenging. [60] **Figure 1.6** illustrates a borderline scenario in which it is questionable whether a second TS exists, thus making it uncertain whether the reaction is concerted or stepwise. Although such situations were uncommon in the 90s, there are now several examples in the literature, such as the addition of vinylidene to acetylidene, resulting in methylenecyclopropene, [61] or the addition of hydrogen fluoride to ethylene. [62]

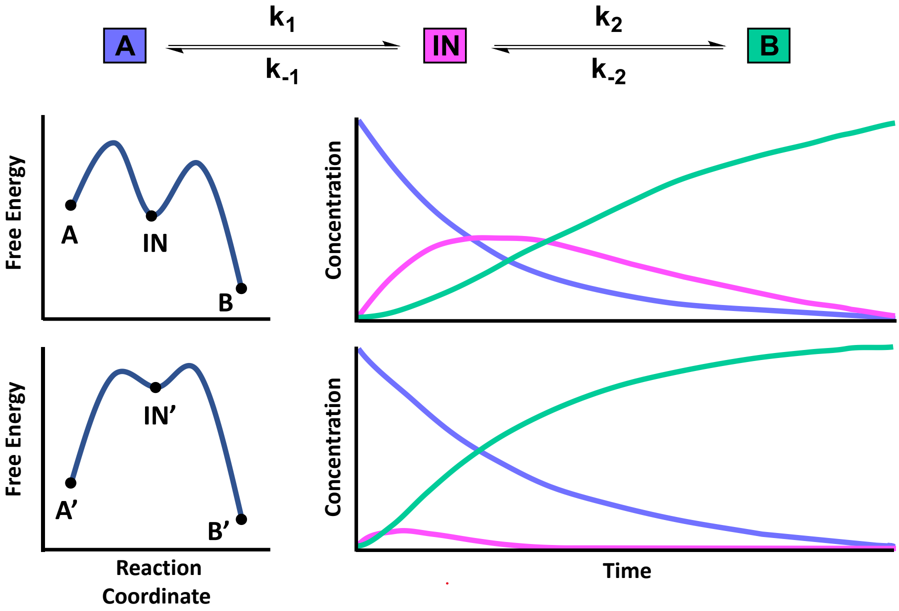

***Figure 1.5**: **(Up)** Kinetic scheme for a two-step reaction. **(Center)** Energy diagram and simulation of the evolution of species concentration over time for k_1=k_2. **(Bottom)** Energy diagram and simulation of the evolution of species concentration over time for k_1= 1/8 k_2.*

These transient species, which exist only momentarily during the course of a reaction, can play a crucial role in determining the outcome, efficiency, and selectivity of chemical transformations. Previous studies have demonstrated that transient intermediates have a lifespan during which they can react with other species, even they are not a minimum energy state, similar to real intermediates. [63] In other cases, the formation of a transient carbocationic intermediate allows for the utilization of racemic starting materials, creating a DYKAT system. [64] Further examples of these cases will be explored in the discussion of this thesis.

Transient intermediates can be anticipated by a shoulder shape, [65] or a flat surface on the IRC. [66] However, the characterization of these intermediates requires more advanced techniques, such as ELF or dynamic calculations. [67]

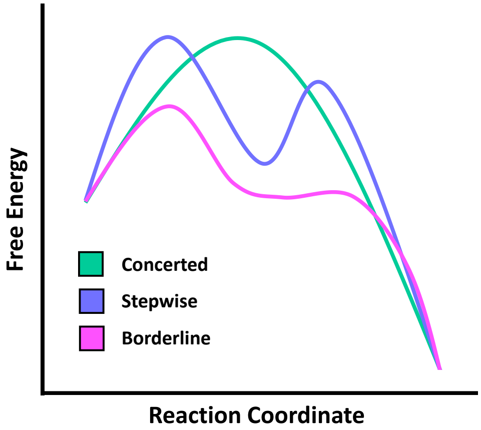

Figure 1.6: *Representation of reaction synchronicity for a concerted reaction (orange), stepwise reaction (blue) and a borderline scenario (green).*

Given the wide range of intermediate types and their varying stability, as well as the influence of factors such as solvent and temperature, it is evident that there is a need for a broader range of characterization techniques for intermediates.

1.4 Determination and characterization of reaction intermediates

Historically, experimental characterization methods were the first to be developed to identify reaction intermediates. The choice of the most suitable technique for studying a particular intermediate depends on several factors, including the reaction temperature, solvent, and, most importantly, the stability of the species. A higher stability corresponds to a higher concentration of the intermediate, making it easier to study.

Nowadays, computational techniques have advanced to a point where they are considered reliable sources of molecular information. One major advantage they have over experimental methods is that they are not affected by issues such as low concentration or solvent limitations. In practice, a combination of experimental and computational data provides a synergistic approach for mechanistic studies. [68] Therefore, in this context, we will present some of the most useful techniques for identifying and studying reaction intermediates.

1.4.1 Spectroscopic techniques

Spectroscopic methods provide valuable information about the structure and properties of reaction intermediates. Over the years, numerous methodologies have been developed in this field. Among all spectroscopic techniques, NMR stands out as the most powerful and widely utilized technique for determining molecular structure. Given that various nuclei can be measured using NMR, and multiple experiments can be performed, the versatility of this technique is one of its key strengths. [69]

However, NMR need a relatively high concentration of the desired intermediate to be detected, and its half-life time must fall within the measurement window. In addition, the measure of paramagnetic species with NMR proves to be challenging, and alternative techniques must be employed. The typical spectroscopic technique for studying paramagnetic species is electron spin resonance (ESR), also referred to as electron paramagnetic resonance (EPR). This technique, similar to NMR, involves subjecting the sample to an oscillating magnetic field, typically in the microwave range (GHz). However, in ESR, the magnetic field excites the spins of electrons instead of nuclei, and the transitions between different electron spin levels provide information about local symmetry, valence state, or local internal fields. This information is summarized by the g-value. ESR has played a crucial role in the discovery of many paramagnetic reaction intermediates, and its compatibility with other methods such as radical trapping has further expanded its applications. [70]

Other classical techniques, such as infrared (IR) spectroscopy or ultraviolet-visible (UV-Vis) spectroscopy, are also employed in the characterization of reaction intermediates. While these techniques may provide less structural information compared to others, they are not hindered by the presence of unpaired electrons. Both IR and UV-Vis spectroscopy offer time-resolved versions that enable the study of short-lived intermediates within the timescale of the reaction, offering valuable insights into their lifetime and reactivity (**Figure 1.7**). [71]

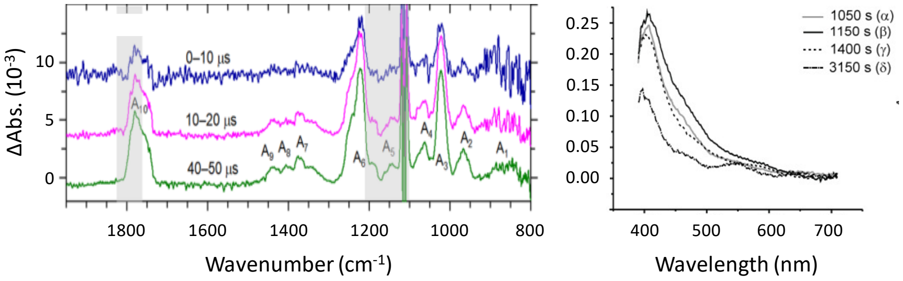

***Figure 1.7:** Time evolution of the IR spectra (**left**) and the UV-Vis spectra (**right**) of two different reactions. Source: ref. 71a (**left**), ref. 71d (**right**).*

1.4.2 Mass spectrometry

Mass spectrometry is a powerful technique for the identification of reaction intermediates. It provides information about the mass-to-charge ratio (m/z) of ions, allowing for the determination of their molecular weight and fragmentation patterns. By analyzing the mass spectra of reaction mixtures, is possible to detect and characterize intermediate species based on their unique mass signatures. Techniques such as Electrospray Ionization (ESI) and Matrix-Assisted Laser Desorption/Ionization (MALDI) are commonly used for the ionization and analysis of reaction intermediates. [72]

These techniques offer multiple advantages, including their high sensitivity, which enables the detection of intermediates even at very low concentrations. [73] Furthermore, once the molecule is transferred to the gas phase, the possibility of intermolecular reactions is nearly nonexistent. Additionally, similar to the previous examples, this technique can also be time-monitored, which can aid in the detection of short-lived species at low concentrations. [74]

However, techniques such as ESI may introduce interference in the reaction results by generating undesired products that are not present in the original reaction solution. [75] To distinguish genuine reaction intermediates from other species formed during the ESI experiment, isotopically labeled reagents can be employed, [76] providing further insights into the chemical rearrangements occurring in the reaction. Moreover, in certain situations, isotopic labeling can be utilized to predict the enantioselectivity of a given reaction. [77]

Modern techniques such as infrared multiphoton dissociation (IRMPD) spectroscopy allow for a more precise determination of atom connectivity, especially in complex molecules such as organometallic species or high-energy reaction intermediates. [73c, 77a] In this technique, ions are trapped in the ion cyclotron resonance cell of the mass spectrometer and exposed to infrared laser beams, enabling the measurement of vibrational spectra of the trapped species, including reaction intermediates. [78]

All these factors make mass spectrometry a powerful tool in the determination and characterization of intermediates. The wide range of ionization methods and technical modifications available for mass spectrometry increases its versatility in mechanistic studies.

1.4.3 Trapping and isolation techniques

Chemical trapping of reaction intermediates allows to capture and study elusive and short-lived species that play a crucial role in chemical reactions. Trapping methods involve the introduction of specific trapping agents or reagents that selectively react with the transient species, forming stable adducts. These adducts can be isolated, purified, and subjected to various spectroscopic or analytical techniques to elucidate their structure and properties.

In the last century, chemical trapping was the only method available for studying many chemical reaction mechanisms, [79] and as a result, numerous methodologies were developed during that time. [80] It was initially used in classical organic chemistry, [81] and its application was later extended to the study of mechanisms in homogeneous catalysis [82] and eventually in heterogeneous catalysis. [83]

The most widely used methods of chemical trapping involve nucleophilic or electrophilic additions to trap intermediates. The progress of the reaction can be monitored using various spectroscopic and spectrometric techniques, or the trapped adducts can be isolated. Nucleophiles, such as amines, alcohols, or thiols, can be employed to trap electrophilic intermediates. [84] Conversely, electrophiles like diazo or carbonyl compounds can be used to trap nucleophilic intermediates, such as carbanions. [85] These trapping strategies can be further enhanced by using specific trapping agents that selectively react with a particular functional group. [86] Additionally, radical intermediates can also be trapped using radical-trapping agents such as phenols, diarylamines, or other hindered amines like TEMPO. These agents are capable of forming stable radicals that can interact with the radical intermediates. [87]

Labelled compounds can also be utilized. It is possible to introduce a labelled amount of the postulated intermediate and study its incorporation into the desired product (

Scheme 1.5, **1**). [88] If the labelled intermediate is not commercially available, another option is to generate it *in situ* (

Scheme 1.5, **2***)*. [89] Alternatively, the reaction can be conducted directly from the presumed intermediate, and the obtained results can be compared to those obtained using the original reactants (

Scheme 1.5, **3**). [90]

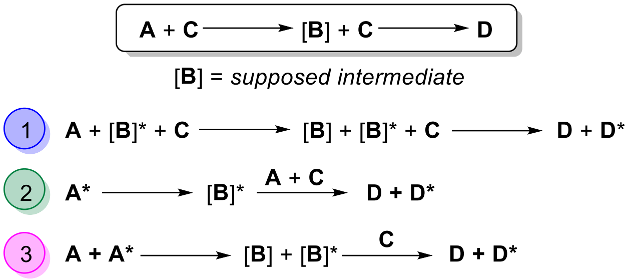

Scheme 1.5: *Typical procedures of the use of labelled compounds in the determination of the reaction intermediates. X* refers to the labelled version of compound X (X = A-F).*

All this different trapping strategies, coupled with various spectroscopic techniques for characterization, has maintained chemical trapping into an indispensable tool in modern organic chemistry research, providing insights into reaction mechanisms and facilitating the development of new synthetic strategies.

1.5 Computational methods for the study of elusive intermediates

The traditional experimental techniques often struggle to directly observe and characterize elusive reaction intermediates due to their transient nature. To solve this problem, computational techniques have evolved to provide valuable insights into reaction mechanisms and aid in the identification of reaction intermediates.

Computational approaches allow for the establishment of the relative energies of starting materials, intermediates and other stationary points on the potential energy surface, allowing for the determination of many chemical properties such as preferred pathways for a given reaction, estimation of kinetic constants, diastereo- and enantioselectivities determinations, or the study of relatives stabilities among different structures. [60a] IRC calculations offers further insights in the characterization of a given TS by connecting reactant(s) and product(s).

Different computational approaches can be applied in the study of a given system, being the most commonly used:

(1) Classical study of stationary points located on the PES, including minima and saddle-points corresponding to TS, through their optimization and analysis of their frequencies. This approach provides information about the energetics of the reaction and offers insights into the mechanism. Intrinsic Reaction Coordinate (IRC) calculations must be performed to fully characterize a given TS. [91]

(2) Quantum dynamics calculations, a useful computational technique that predicts the time-evolution of a given system. During the MD simulation the molecule will spend more time in the most stable conformations, and so, this technique becomes very useful in conformational analysis. Since this is usually performed in big systems like proteins, MM theory is applied to reduce the computational costs. However, with smaller systems, QM theory could be also applied, and then, bonds can be created or destroyed during the course of the dynamic. These QM-Molecular dynamics also allows us to predict the reaction's speed, or the intermediate stability in time. [92]

(3) Topological approaches such as the study of the electron localization function (ELF), which contains information about the electronic distribution in a given system and can distinguish the exact moment when a bond is formed or broken, or other types of electronic redistributions. The success of this technique relies in the concept of basins which are the domains in which the probability of finding an electron pair is maximal. [67a, 67b, 93] The basins are classified as core and valence basins. The latter are characterised by the synaptic order, i.e. the number of atomic valence shells in which they participate. [94] Thus, there are monosynaptic, disynaptic, basins and so on. Monosynaptic basins, labelled V(A), correspond to lone pairs or non-bonding regions, while disynaptic basins, labelled V(A,B), connect the core of two nuclei A and B and, thus, correspond to a bonding region between A and B. This description recovers the Lewis bonding model, and the representation of the evolution of electron population of basins along the reaction coordinate (IRC) provides a very intuitive graphical representation of how the

molecular system and their electron density evolves during the reaction. During these representations, basins could merge, disappear or appear again. As these basins truly represent a maxima in electron density, the disappearance of a disynaptic basin between two atoms corresponds to a bond breaking process, and a bond formation for the basin appearance. This make possible to stablish the exact moment when a particular bond is created or destroyed during an IRC.

Other alternatives include the study of the non-covalent-interactions (NCI), [95] that provides a complete representation of the van der Waals interactions, hydrogen bonds, and steric repulsions. The type of interaction is defined by the sign of the second Hessian eigenvalue, and its strength can be derived from the density on the noncovalent interaction surface. Different interactions are defined by different colours, providing a rapid identification and a rich representation of this interactions. Together with the electronic information obtained by ELF calculations, allows for a full characterization of a given system.

On the other hand, the Atom in Molecules (AIM) theory forms a parallel conceptual framework, that is used to analyse the distribution of electron density within a molecule. AIM provides insights into the nature of chemical bonding and the topology of the electron density in a molecular system by the partition of the molecular system into individual atoms and study the electron density near each nucleus. This technique is able to identify different types of interactions such as covalent bonds, hydrogen bonds, van der Waals interactions, and more. [96]

By employing a mixture of these techniques, it is possible to explore potential energy surfaces, evaluate reaction energetics, and predict the stability and reactivity of intermediates. These methods enable the exploration of reaction pathways that may not be easily accessible experimentally and provide a deeper understanding of complex chemical transformations. [64, 97]

Therefore, the study of the mechanism of organic reactions is now a cross-cutting subject within the field of chemistry, and it is common to approach it from a multidisciplinary perspective that considers various theoretical and experimental viewpoints. [98]

1.6 References

[1] P. Muller, *Pure Appl. Chem.* **1994**, *66*, 1077-1184.

[2] F. A. Carey, R. J. Sundberg, *Advanced Organic Chemistry Part A: Structure and Mechanisms*, **2007**.

[3] R. A. Moss, M. S. Platz, J. Maitland Jones, *Reactive Intermediate Chemistry*, John Wiley & Sons, Hoboken, New Jersey., **2004**.

[4] G. A. Olah, W. S. Tolgyesi, *J. Am. Chem. Soc.* **1961**, *83*, 5031-5032.

[5] a) P. Ahlberg, M. Ek, *ChemComm.* **1979**, 624-625; b) M. Saunders, D. Cox, J. R. Lloyd, *J. Am. Chem. Soc.* **1979**, *101*, 6656-6658; c) M. Winkler, W. Sander, *Angew. Chem.. Int. Edit.* **2000**, *39*, 2014-+.

[6] D. Bethell, V. Gold, *Carbonium Ions, An Introduction*, Academic Press, New York, N. Y., **1967**.

[7] G. A. Olah, *J. Am. Chem. Soc.* **1972**, *94*, 808-820.

[8] J. E. McMurry, *Fundamentals of Organic Chemistry*, Cengage Learning, **2010**.

[9] H. C. Brown, *Bull. Hist. Chem.* **2000**, *25*, 123-131.

[10] a) H. C. Brown, *Acc. Chem. Res.* **1983**, *16*, 432-440; b) G. A. Olah, G. K. S. Prakash, M. Saunders, *Acc. Chem. Res.* **1983**, *16*, 440-448; c) C. Walling, *Acc. Chem. Res.* **1983**, *16*, 448-454.

[11] a) P. von Ragué Schleyer, S. Sieber, *Angew. Chem., Int. Ed. Engl.* **1993**, *32*, 1606-1608; b) R. A. Moss, *J. Phys. Org. Chem.* **2014**, *27*, 374-379; c) X. M. Tang, W. Chen, X. F. Yi, Z. Q. Liu, Y. Xiao, Z. F. Chen, A. M. Zheng, *Angew. Chem.. Int. Edit.* **2021**, *60*, 4581-4587; d) C. S. Yannoni, V. Macho, P. C. Myhre, *J. Am. Chem. Soc.* **1982**, *104*, 7380-7381.

[12] a) M. Saunders, H. A. Jimenez-Vazquez, *Chem. Rev.* **1991**, *91*, 375-397; b) G. K. S. Prakash, P. von R. Schleyer, *Stable Carbocation Chemistry*, Wiley, **1996**.

[13] a) M. Saunders, H. U. Siehl, *J. Am. Chem. Soc.* **1980**, *102*, 6868-6869; b) W. J. Brittain, M. E. Squillacote, J. D. Roberts, *J. Am. Chem. Soc.* **1984**, *106*, 7280-7282.

[14] a) M. Saunders, E. L. Hagen, J. Rosenfeld, *J. Am. Chem. Soc.* **1968**, *90*, 6882-6884; b) M. Saunders, M. R. Kates, *J. Am. Chem. Soc.* **1978**, *100*, 7082-7083; c) G. A. Olah, D. J. Donovan, *J. Am. Chem. Soc.* **1977**, *99*, 5026-5039.

[15] G. Rasul, G. K. S. Prakash, G. A. Olah, *J. Phys. Chem. A* **2015**, *119*, 5762-5769.

[16] M. D. Bojin, D. J. Tantillo, *J. Phys. Chem. A* **2006**, *110*, 4810-4816.

[17] T. Laube, G. A. Olah, R. Bau, *J. Am. Chem. Soc.* **1997**, *119*, 3087-3092.

[18] M. Castiñeira Reis, C. S. López, O. Nieto Faza, D. J. Tantillo, *Chem. Sci.* **2019**, *10*, 2159-2170.

[19] a) M. Kreuzahler, G. Haberhauer, *Angew. Chem.. Int. Edit.* **2020**, *59*, 17739-17749; b) K. Sakamoto, H. Sato, M. Uchiyama, *J. Org. Chem.* **2022**, *87*, 6432-6437; c) Z. W. Qu, H. Zhu, S. Grimme, *Eur. J. Org. Chem.* **2022**, *2022*, 4.

[20] a) W. Hallwachs, F. Schafarik, *Annals* **1859**, *109*, 206; b) A. Cahours, *Annals* **1859**, *114*, 227.

[21] V. Grignard, *Ann. Chim. Phys.* **1901**, *24*, 433-490.

[22] a) Y. Zhang, W. Wang, *Catal. Sci. Technol.* **2012**, *2*, 42-53; b) D. S. Khachatryan, K. R. Matevosyan, *Russ. Chem. Bull.* **2016**, *65*, 14-28; c) Y.-R. Yang, W.-D. Z. Li, *J. Org. Chem.* **2005**, *70*, 8224-8227.

[23] a) F. Y. Yeoh, R. R. Cuasito, C. C. Capule, F. M. Wong, W. Wu, *Bioorg. Chem.* **2007**, *35*, 338-343; b) R. Kluger, G. Ikeda, Q. Hu, P. Cao, J. Drewry, *J. Am. Chem. Soc.* **2006**, *128*, 15856-15864.

[24] a) A. R. Burns, G. D. McAllister, S. E. Shanahan, R. J. K. Taylor, *Angew. Chem. Int. Ed.* **2010**, *49*, 5574-5577; b) Y. Tian, M. Tang, C. Lian, R. Song, D. Yang, J. Lv, *Org. Chem. Front.* **2023**, *10*, 3039-3044.

[25] R. H. Crabtree, *Chem. Rev.* **1985**, *85*, 245-269.

[26] a) W. C. Still, C. Sreekumar, *J. Am. Chem. Soc.* **1980**, *102*, 1201-1202; b) M. Sasaki, K. Takeda, *Synlett.* **2012**, *23*, 2153-2164; c) F. Gerhards, N. Griebel, J. Runsink, G. Raabe, H.-J. Gais, *Chem. Eur. J.* **2015**, *21*, 17904-17920.

[27] H. M. Niemeyer, *Tetrahedron* **1977**, *33*, 2267-2270.

[28] a) C. Walling, *Tetrahedron* **1985**, *41*, 3887-3900; b) K. U. Ingold, *Pure Appl. Chem.* **1997**, *69*, 241-244.

[29] M. Yan, J. C. Lo, J. T. Edwards, P. S. Baran, *J. Am. Chem. Soc.* **2016**, *138*, 12692-12714.

[30] a) C. P. Jasperse, D. P. Curran, T. L. Fevig, *Chem. Rev.* **1991**, *91*, 1237-1286; b) R. A. Jackson, **1974**; c) D. P. Curran, *Synth.* **1988**, *1988*, 417-439; d) D. P. Curran, *Synth.* **1988**, *1988*, 489-513.

[31] a) A. Borodine, *Liebigs Ann.* **1861**, *119*, 121-123; b) A. Hofmann, *Ber. Dtsch. Chem. Ges.* **1879**, *12*, 984-990; c) R. Fittig, *Liebigs Ann.* **1859**, *110*, 17-23.

[32] M. Gomberg, *J. Am. Chem. Soc.* **1900**, *22*, 757-771.

[33] H. Meerwein, E. Büchner, K. van Emster,J. Prakt. Chem. **1939**, *152*, 237-266.

[34] a) A. J. Birch, *J. Chem. Soc. (Resumed)* **1944**, 430-436; b) A. J. Birch, *J. Chem. Soc. (Resumed)* **1945**, 809-813; c) A. J. Birch, *J. Chem. Soc. (Resumed)* **1946**, 593-597; d) A. J. Birch, *J. Chem. Soc. (Resumed)* **1947**, 102-105; e) A. J. Birch, *J. Chem. Soc. (Resumed)* **1947**, 1642-1648; f) A. Birch, S. Mukherji, *J. Chem. Soc. (Resumed)* **1949**, 2531-2536.

[35] a) D. Barton, J. Beaton, L. Geller, M. Pechet, *J. Am. Chem. Soc.* **1960**, *82*, 2640-2641; b) R. Breslow, S. W. Baldwin, *J. Am. Chem. Soc.* **1970**, *92*, 732-734; c) R. Breslow, P. C. Scholl, *J. Am. Chem. Soc.* **1971**, *93*, 2331-2333.

[36] a) J. B. Bush Jr, H. Finkbeiner, *J. Am. Chem. Soc.* **1968**, *90*, 5903-5905; b) E. Heiba, R. Dessau, W. Koehl Jr, *J. Am. Chem. Soc.* **1968**, *90*, 5905-5906.

[37] J. K. Kochi, *Acc. Chem. Res.* **1974**, *7*, 351-360.

[38] F. Minisci, R. Bernardi, F. Bertini, R. Galli, M. Perchinummo, *Tetrahedron* **1971**, *27*, 3575-3579.

[39] a) M. Kato, M. Kamigaito, M. Sawamoto, T. Higashimura, *Macromolecules* **1995**, *28*, 1721-1723; b) J.-S. Wang, K. Matyjaszewski, *J. Am. Chem. Soc.* **1995**, *117*, 5614-5615; c) K. Matyjaszewski, *Macromolecules* **2012**, *45*, 4015-4039.

[40] a) E. Vessally, *Heteroat. Chem.* **2008**, *19*, 245-251; b) A. P. Scott, M. S. Platz, L. Radom, *J. Am. Chem. Soc.* **2001**, *123*, 6069-6076.

[41] a) U. H. Brinker, *Advances in Carbene Chemistry, Vol. 1*, Elsevier, Greenwich, CT, **1994**; b) U. H. Brinker, *Advances in Carbene Chemistry, Vol. 2*, Elsevier, Stamford, CT, **1998**; c) U. H. Brinker, *Advances in Carbene Chemistry, Vol. 3*, Elsevier, Amsterdam, **2001**.

[42] a) W. W. Schoeller, *J. Chem. Soc., ChemComm.* **1980**, 124-125; b) D. A. Dixon, K. D. Dobbs, A. J. Arduengo, III, G. Bertrand, *J. Am. Chem. Soc.* **1991**, *113*, 8782-8785; c) M. Z. Kassaee, M. Koohi, R. Mohammadi, M. Ghavami, *J. Phys. Org. Chem.* **2013**, *26*, 908-916.

[43] a) N. J. Turro, *Modern molecular photochemistry*, University science books, **1991**; b) C. Wentrup, *Reactive Molecules*, Wiley, New York, **1984**.

[44] a) A. R. Forrester, J. S. Sadd, *J. Chem. Soc., ChemComm.* **1976**, 631-632; b) A. R. Forrester, J. S. Sadd, *J. Chem. Soc., Perkin Transactions 2* **1982**, 1273-1278.

[45] R. Moss, N. Turro, *by MS Platz, Plenum Press, New York* **1990**, 213-238.

[46] G. Wu, M. Jones, R. Walton, P. M. Lahti, *J. Org. Chem.* **1998**, *63*, 5368-5371.

[47] a) R. C. Woodworth, P. S. Skell, *J. Am. Chem. Soc.* **1959**, *81*, 3383-3386; b) P. S. Skell, *Tetrahedron (Oxford. Print)* **1985**, *41*, 1427-1428; c) M.-D. Su, *J. Phys. Chem.* **1996**, *100*, 4339-4349.

[48] a) E. Schmitz, D. Habisch, A. Stark, *Angew. Chem., Int. Ed. Engl.* **1963**, *2*, 548-548; b) J. Scheffer, J. Yang, W. Horspool, P. Sean, *Horspool, WM, Song, PS, Eds* **1995**, 204-221; c) S. Patai, *The chemistry of diazonium and diazo groups, Part 1-2, Vol. 23*, Wiley, **1978**.

[49] a) R. A. Moss, *Acc. Chem. Res.* **2006**, *39*, 267-272; b) M. T. H. Liu, *Chem. Soc. Rev.* **1982**, *11*, 127-140.

[50] R. K. Smalley, Suschitz.H, *Chem. Ind.* **1970**, 1338-&.

[51] O. M. Nefedov, M. P. Egorov, A. I. Ioffe, L. G. Menchikov, P. S. Zuev, V. I. Minkin, B. Y. Simkin, M. N. Glukhovstev, *Pure Appl. Chem.* **1992**, *64*, 265-314.

[52] E. Wigner, E. E. Witmer, *Z. Phys.* **1928**, *51*, 859 – 886.

[53] a) N. Satish, G. Sudhakar, *Synlett.* **2020**, *32*, 605-610; b) F. Dahcheh, D. Martin, D. W. Stephan, G. Bertrand, *Angew. Chem.. Int. Edit.* **2014**, *53*, 13159-13163; c) R. Jazzar, R. D. Dewhurst, J. B. Bourg, B. Donnadieu, Y. Canac, G. Bertrand, *Angew. Chem.. Int. Edit.* **2007**, *46*, 2899-2902.

[54] a) D. G. Gillingham, A. H. Hoveyda, *Angew. Chem.. Int. Edit.* **2007**, *46*, 3860-3864; b) C. V. Maftei, E. Fodor, P. G. Jones, M. Freytag, M. H. Franz, G. Kelter, H.-H. Fiebig, M. Tamm, I. Neda, *Eur. J. Med. Chem* **2015**, *101*, 431-441; c) P. de Fremont, N. Marion, S. P. Nolan, *Coord. Chem. Rev.* **2009**, *253*, 862-892.

[55] a) J. Xing, X.-R. Wang, C.-X. Yan, Y. Cheng, *J. Org. Chem.* **2011**, *76*, 4746-4752; b) V. N. G. Lindsay, H. M. F. Viart, R. Sarpong, *J. Am. Chem. Soc.* **2015**, *137*, 8368-8371.

[56] a) T. Q. Davies, M. J. Tilby, J. Ren, N. A. Parker, D. Skolc, A. Hall, F. Duarte, M. C. Willis, *J. Am. Chem. Soc.* **2020**, *142*, 15445-15453; b) K. M. van Vliet, L. H. Polak, M. A. Siegler, J. I. van der Vlugt, C. F. Guerra,

B. de Bruin, *J. Am. Chem. Soc.* **2019**, *141*, 15240-15249; c) T. Kametani, K. Ogasawara, T. Yamanaka, *J. Chem. Soc. C: Organic* **1968**, 1006-1007.

[57] a) M. J. B. Aguila, Y. M. Badiei, T. H. Warren, *J. Am. Chem. Soc.* **2013**, *135*, 9399-9406; b) G. Smolinsky, B. I. Feuer, *J. Am. Chem. Soc.* **1964**, *86*, 3085-3088; c) C. Pan, S.-Y. Yin, Q. Gu, S.-L. You, *Org. Biomol. Chem.* **2021**, *19*, 7264-7275.

[58] a) D. J. Varughese, M. S. Manhas, A. K. Bose, *Tetrahedron Lett.* **2006**, *47*, 6795-6797; b) E. Kozlowska-gramsz, G. Descotes, *Tetrahedron Lett.* **1981**, *22*, 563-566.

[59] a) M. J. Antal, W. S. L. Mok, G. N. Richards, *Carbohydr. Res.* **1990**, *199*, 91-109; b) R. Huisgen, *J. Org. Chem.* **1968**, *33*, 2291-&; c) C. J. Li, *Tetrahedron* **1996**, *52*, 5643-5668.

[60] a) E. Kraka, D. Cremer, *Acc. Chem. Res.* **2010**, *43*, 591-601; b) H. Joo, E. Kraka, W. Quapp, D. Cremer, *Mol. Phys.* **2007**, *105*, 2697-2717.

[61] W. Quapp, E. Kraka, D. Cremer, *J. Phys. Chem. A* **2007**, *111*, 11287-11293.

[62] D. Cremer, A. A. Wu, E. Kraka, *Phys. Chem. Chem. Phys.* **2001**, *3*, 674-687.

[63] a) M.-A. Chiacchio, L. Legnani, P. Caramella, T. Tejero, P. Merino, *Tetrahedron* **2018**, *74*, 5627-5634; b) P. Merino, M. A. Chiacchio, L. Legnani, T. Tejero, *Molecules* **2017**, *22*, 1371; c) A. Ortega, R. Manzano, U. Uria, L. Carrillo, E. Reyes, T. Tejero, P. Merino, J. L. Vicario, *Angew. Chem. Int. Ed.* **2018**, *57*, 8225-8229.

[64] A. Ortega, R. N. Manzano, U. Uria, L. Carrillo, E. Reyes, T. Tejero, P. Merino, J. L. Vicario, *Angew. Chem.. Int. Edit.* **2018**, *57*, 8225-8229.

[65] Q. N. N. Nguyen, D. J. Tantillo, *Beilstein J. Org. Chem.* **2013**, *9*, 323-331.

[66] M. W. Lodewyk, P. Gutta, D. J. Tantillo, *J. Org. Chem.* **2008**, *73*, 6570-6579.

[67] a) B. Silvi, A. Savin, *Nature* **1994**, *371*, 683-686; b) A. Savin, A. D. Becke, J. Flad, R. Nesper, H. Preuss, H. G. von Schnering, *Angew. Chem., Int. Ed. Engl.* **1991**, *30*, 409-412; c) A. Savin, R. Nesper, S. Wengert, T. F. Fässler, *Angew. Chem., Int. Ed. Engl.* **1997**, *36*, 1808-1832.

[68] a) N. Labadie, S. C. Pellegrinet, *J. Org. Chem.* **2022**, *87*, 16776-16784; b) M. Y. Kawamura, J. V. Alegre-Requena, T. M. Barbosa, C. F.

Tormena, R. S. Paton, M. A. B. Ferreira, *Chem. Eur. J.***2022**, *28*; c) T. Ema, Y. Miyazaki, J. Shimonishi, C. Maeda, J. Y. Hasegawa, *J. Am. Chem. Soc.* **2014**, *136*, 15270-15279.

[69] a) M. T. Aronson, R. J. Gorte, W. E. Farneth, D. White, *J. Am. Chem. Soc.* **1989**, *111*, 840-846; b) S. O. Simonetti, T. S. Kaufman, R. M. Rasia, A. M. Sarotti, N. Grimblat, *Org. Biomol. Chem.* **2021**, *19*, 7374-7378; c) M. De Rosa, D. Arnold, *J. Org. Chem.* **2009**, *74*, 319-328; d) M. Karlsson, A. Ionescu, C. Andersson, *J. Mol. Catal. A Chem.* **2006**, *259*, 231-237.

[70] a) A. Bosnjakovic, M. K. Kadirov, S. Schlick, *Res. Chem. Intermed.* **2007**, *33*, 677-687; b) N. Levin, C. Casadevall, G. E. Cutsail, J. Lloret-Fillol, S. DeBeer, O. Rudiger, *ChemElectroChem* **2022**, *9*; c) M. A. Nesbit, P. H. Oyala, J. C. Peters, *J. Am. Chem. Soc.* **2019**, *141*, 8116-8127.

[71] a) B. Behera, K. Takahashi, Y.-P. Lee, *Phys. Chem. Chem. Phys.* **2022**, *24*, 18568-18581; b) T. Nomura, T. Kimura, Y. Kanematsu, D. Yamada, K. Yamashita, K. Hirata, G. Ueno, H. Murakami, T. Hisano, R. Yamagiwa, H. Takeda, C. Gopalasingam, R. Kousaka, S. Yanagisawa, O. Shoji, T. Kumasaka, M. Yamamoto, Y. Takano, H. Sugimoto, T. Tosha, M. Kubo, Y. Shiro, *P. Natl. Acad. Sci .USA* **2021**, *118*; c) J. F. Perez-Benito, J. Nicolas-Rivases, *Int. J. Chem. Kinet.* **2018**, *50*, 591-603; d) K. Hemelsoet, Q. Qian, T. De Meyer, K. De Wispelaere, B. De Sterck , B. M. Weckhuysen, M. Waroquier, V. Van Speybroeck, *Chem. Eur. J.* **2013**, *19*, 16595-16606.

[72] a) P. Chen, *Angew. Chem.* **2003**, *115*, 2938-2954; b) P. Chen, *Angew. Chem. Int. Ed.* **2003**, *42*, 2832-2847.

[73] a) E. Alhajji, A. Boulghobra, M. Bonose, F. Berthias, F. Moussa, P. Maître, *Anal. Chem.* **2022**, *94*, 12578-12585; b) Y. Zheng, B. Miao, L. Zhang, *Chin. J. Chem.* **2020**, *38*, 106-107; c) J. Roithová, *Chem. Soc. Rev.* **2012**, *41*, 547-559.

[74] C. Iacobucci, S. Reale, F. De Angelis, *Angew. Chem. Int. Ed.* **2016**, *55*, 2980-2993.

[75] L. P. E. Yunker, R. L. Stoddard, J. S. McIndoe, *J. Mass Spectrom.* **2014**, *49*, 1-8.

[76] a) J. Schulz, L. Jašíková, A. Škríba, J. Roithová, *J. Am. Chem. Soc.* **2014**, *136*, 11513-11523; b) J. Roithová, Š. Janková, L. Jašíková, J. Váňa, S. Hybelbauerová, *Angew. Chem. Int. Ed.* **2012**, *51*, 8378-8382; c) J.

Roithová, Š. Janková, L. Jašíková, J. Váňa, S. Hybelbauerová, *Angew. Chem.* **2012**, *124*, 8503-8507.

[77] a) C. Markert, A. Pfaltz, *Angew. Chem. Int. Ed.* **2004**, *43*, 2498-2500; b) C. A. Müller, C. Markert, A. M. Teichert, A. Pfaltz, *ChemComm.* **2009**, 1607-1618.

[78] a) N. N. Mikawy, H. A. Roy, E. Israel, L. A. Hamlow, Y. Zhu, G. Berden, J. Oomens, C. E. Frieler, M. T. Rodgers, *J. Am. Soc. Mass Spectrom.* **2022**; b) C. P. Harrilal, A. F. DeBlase, S. A. McLuckey, T. S. Zwier, *J. Phys. Chem. A* **2021**, *125*, 9394-9404; c) O. W. Wheeler, R. A. Coates, V. J. F. Lapoutre, J. M. Bakker, P. B. Armentrout, *Int. J. Mass Spectrom.* **2019**, *442*, 83-94.

[79] A. Deluzarche, J.-P. Hindermann, A. Kiennemann, R. Kieffer,J. Mol. Catal. **1985**, *31*, 225-250.

[80] a) V. Bolcato, *Science* **1950**, *112*, 252-254; b) J. B. Wolfe, D. Ivler, S. C. Rittenberg, *J. Biol. Chem.* **1954**, *209*, 875-883; c) J. Macleod, J. Donnelly, *Ann. Appl. Biol.* **1956**, *44*, 80-104; d) J. Kumamoto, H. E. De La Mare, F. F. Rust, *J. Am. Chem. Soc.* **1960**, *82*, 1935-1939; e) M. Flavin, C. Slaughter, *Biochem.* **1964**, *3*, 885-&.

[81] E. S. Gould, *Mechanism and Structure in Organic Chemistry*, Holt, Rinehart and Winston, **1963**.

[82] a) E. A. Kelly, P. M. Bailey, P. M. Maitlis, *J. Chem. Soc., ChemComm.* **1977**, 289-291; b) M. E. Vol'Pin, I. S. Kolomnikov, in *Coordination Chemistry–XIV* (Ed.: A. B. P. Lever), Butterworth-Heinemann, **1973**, pp. 567-581.

[83] a) H. Matsumoto, C. O. Bennett, *J. Catal.* **1978**, *53*, 331-344; b) J. A. Rabo, A. P. Risch, M. L. Poutsma, *J. Catal.* **1978**, *53*, 295-311.

[84] a) H. Nüske, M. Noltemeyer, A. de Meijere, *Angew. Chem. Int. Ed.* **2001**, *40*, 3411-3413; b) Q. Liu, A. P. Marchington, N. Boden, C. M. Rayner, *J. Chem. Soc., Perkin trans. 1* **1997**, 511-526; c) F.-D. Boyer, P.-H. Ducrot, *Tetrahedron Lett.* **2005**, *46*, 5177-5180.

[85] a) J. Che, A. Gopi Krishna Reddy, L. Niu, D. Xing, W. Hu, *Org. Lett.* **2019**, *21*, 4571-4574; b) J. H. Kim, Y. S. Chun, H. Shin, S.-g. Lee, *Synth.* **2012**, *44*, 1809-1817; c) M. Novak, K. J. Kayser, M. E. Brooks, *J. Org. Chem.* **1998**, *63*, 5489-5496.

[86] a) C. E. Marjo, R. Bishop, D. C. Craig, A. O'Brien, M. L. Scudder, *J. Chem. Soc., ChemComm.* **1994**, 2513-2514; b) S. L. Ioffe, I. y. M. Lyapkalo, A.

A. Tishkov, V. M. Danilenko, Y. A. Strelenko, V. A. Tartakovsky, *Tetrahedron* **1997**, *53*, 13085-13098.

[87] a) K. U. Ingold, D. A. Pratt, *Chem. Rev.* **2014**, *114*, 9022-9046; b) M. C. Foti, R. Amorati, *J. Pharm. Pharmacol.* **2009**, *61*, 1435-1448.

[88] a) J. T. Kummer, W. T. De, P. H. Emmett, *J. Am. Chem. Soc.* **1948**, *70*, 3632-3643; b) W. K. Hall, R. J. Kokes, P. H. Emmett, *J. Am. Chem. Soc.* **1957**, *79*, 2983-2989; c) H. Wang, J. Liu, J. Fu, H. Wan, K. Tsai, *Catal. Letters* **1992**, *12*, 87-96.

[89] R. C. Brady III, R. Pettit, *J. Am. Chem. Soc.* **1980**, *102*, 6181-6182.

[90] N. N. Bezinger, G. D. Galpern, Karichev.Vn, Y. B. Kryukov, *Ind. Lab.* **1969**, *35*, 1096-1101.

[91] K. Fukui, *Acc. Chem. Res.* **1981**, *14*, 363-368.

[92] P. J. Ollitrault, A. Miessen, I. Tavernelli, *Acc. Chem. Res.* **2021**, *54*, 4229-4238.

[93] a) A. Savin, R. Nesper, S. Wengert, T. F. Fässler, *Angew. Chem., Int. Ed. Engl.* **1997**, *36*, 1808-1832; b) B. Silvi, I. Fourré, M. E. Alikhani, *Monatsh. Chem.* **2005**, *136*, 855-879.

[94] A. Savin, *J. Chem. Sci.* **2005**, *117*, 473-475.

[95] a) E. R. Johnson, S. Keinan, P. Mori-Sanchez, J. Contreras-Garcia, A. J. Cohen, W. Yang, *J. Am. Chem. Soc.* **2010**, *132*, 6498-6506; b) J. R. Lane, J. Contreras-Garcia, J.-P. Piquemal, B. J. Miller, H. G. Kjaergaard, *J. Chem. Theory. Comput.* **2013**, *9*, 3263-3266.

[96] a) R. F. W. Bader, *Acc. Chem. Res.* **1985**, *18*, 9-15; b) P. Politzer, J. S. Murray, *Theor. Chem. Acc.* **2002**, *108*, 134-142; c) J. Poater, M. Duran, M. Sola, B. Silvi, *Chem. Rev.* **2005**, *105*, 3911-3947.

[97] a) J.-L. Zhu, Y. Zhang, C. Liu, A.-M. Zheng, W. Wang, *J. Org. Chem.* **2012**, *77*, 9813-9825; b) H. Gao, D. H. Ess, M. Yousufuddin, L. Kürti, *J. Am. Chem. Soc.* **2013**, *135*, 7086-7089; c) D. Roca-López, A. Darù, T. Tejero, P. Merino, *RSC Adv.* **2016**, *6*, 22161-22173; d) D. Roca-López, T. Tejero, P. Merino, *J. Org. Chem.* **2014**, *79*, 8358-8365.

[98] a) D. Sádaba, I. Delso, T. Tejero, P. Merino, *Tetrahedron Lett.* **2011**, *52*, 5976-5979; b) P. Brandt, C. Hedberg, P. G. Andersson, *Chem. Eur. J.* **2003**, *9*, 339-347; c) V. M. Fernandez-Alvarez, M. Nappi, P. Melchiorre, F. Maseras, *Org. Lett.* **2015**, *17*, 2676-2679.

CHAPTER II

GENERAL OBJECTIVES

2. Objectives

The main aim of this work is to use of these last computational methods to study the reaction pathways and determine the synchronicity of different types of organic reactions, from redox processes to organocatalytic reactions. For this purpose, the following general objectives are defined:

1. To use quantum mechanical calculations, (mainly DFT methods) for determining molecular structures, calculate energy profiles, and predict reaction barriers providing additional insights into the electronic properties, bonding, and charge distributions of intermediates.

2. To apply modern topological techniques such as the study of the electron localization function (ELF) and non-covalent interaction (NCI).

3. To study the processes in a dynamic way by using restricted QM/MD calculations.

4. By using additional experimental data including kinetic studies to complement or extract new fundamental information for the characterization of the mechanism.

To achieve these objectives a series of specific objectives based on the mechanistic study of a series of representative processes are defined to study:

1) Redox reactions:

The oxidation with RuO_4 of various 5-membered ring heterocycles will be explored, paying special attention on the influence of the heteroatom in the synchronicity of the reaction. Once the mechanism is clarified, the heterocycle will be substituted by 5-membered ring hydroxylamines. With these new substrates, apart from the synchronicity, it will be also studied the influence of the ring substituents on the regioselectivity of the reaction (**Scheme 2.1**).

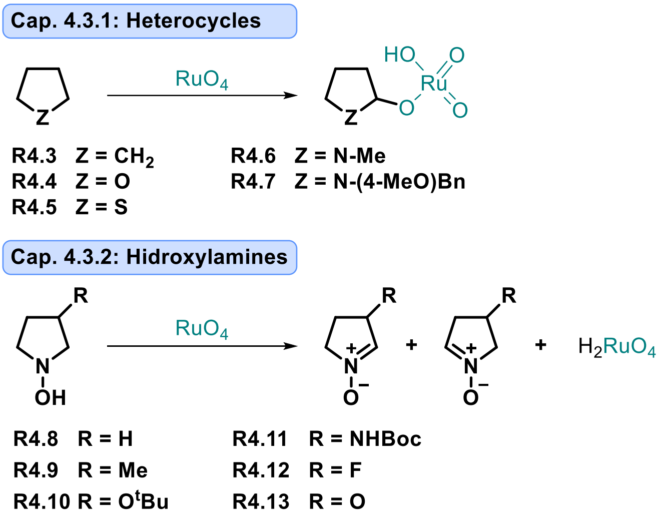
Cap. 4.3.1: Heterocycles
RuO4
Z
HO
O
Ru
O
O
R4.3 Z = CH2
R4.4 Z = O
R4.5 Z = S
R4.6 Z = N-Me
R4.7 Z = N-(4-MeO)Bn
Cap. 4.3.2: Hidroxylamines
R
N
OH
RuO4
+
H2RuO4
R4.8 R = H
R4.9 R = Me
R4.10 R = OtBu
R4.11 R = NHBoc
R4.12 R = F
R4.13 R = O

Scheme 2.1*: Main substrates for the study of oxidation mechanism of heterocycles.*

2) Acetyl migrations:

The second chapter consist of the study of the acetyl migration mechanism in mono- and tri-saccharides (**Scheme 2.2**). The obtained mechanism and barriers will be compared with kinetic experiments. Since the interconversion of kinetic constants and energy barriers involves an exponential relationship, very exact calculations must be performed to reduce errors. For this purpose, all the possible equilibria must be considered. Since the reaction presents a pH-dependence acid-base equilibriums must be also taken into account, which are not easy to recreate computationally.

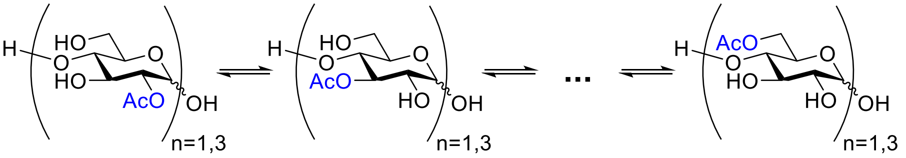
H
HO
O
O
HO
AcO
OH
n=1,3
H
HO
O
O
AcO
HO
OH
n=1,3
...
H
AcO
O
O
HO
HO
OH
n=1,3

Scheme 2.2: *General reaction pathway for the acetyl migration in mono- (n=1) and trisaccharides (n=3).*

3) Organocatalytic processes:

Finally, the last chapter involves the mechanism study of a series of organocatalytic reactions. Most of these reactions involves achiral or racemic starting materials that are converted into enantio-enriched products via unstable or transient intermediates that cannot be detected experimentally in most of the cases. The study will be focused on the use of the newest computational techniques to investigate the structure and stability of these intermediates as well as giving explanation about the observed selectivities in each study case. All systems investigated are displayed in **Scheme 2.3**.

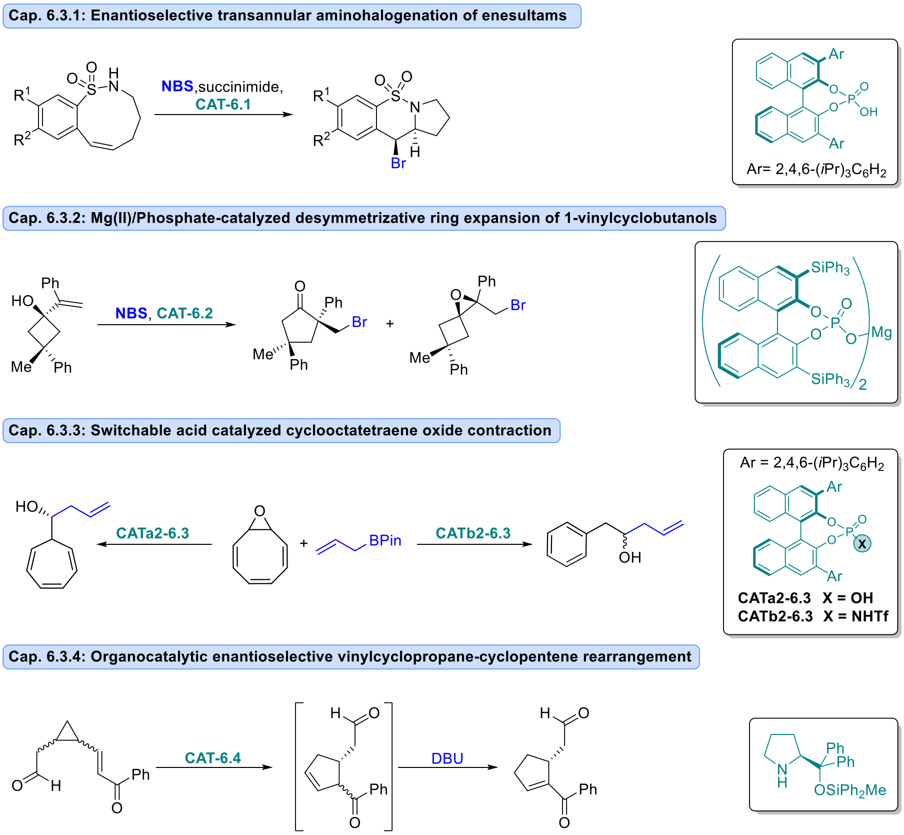
Cap. 6.3.1: Enantioselective transannular aminohalogenation of enesultams
NBS, succinimide, CAT-6.1
R1
R2
Br
H
Ar
OH
Ar= 2,4,6-(iPr)3C6H2
Cap. 6.3.2: Mg(II)/Phosphate-catalyzed desymmetrizative ring expansion of 1-vinylcyclobutanols
NBS, CAT-6.2
HO
Ph
Me
Br
+
SiPh3
Mg
SiPh3/2
Cap. 6.3.3: Switchable acid catalyzed cyclooctatetraene oxide contraction
CATa2-6.3
CATb2-6.3
BPin
OH
Ar = 2,4,6-(iPr)3C6H2
X
CATa2-6.3 X = OH
CATb2-6.3 X = NHTf
Cap. 6.3.4: Organocatalytic enantioselective vinylcyclopropane-cyclopentene rearrangement
CAT-6.4
DBU
H
O
Ph
N
H
Ph
Ph
OSiPh2Me

Scheme 2.3: General reaction pathway of the studied organocatalytic reactions.

In many cases, the experimental data crucial to this project has been acquired through collaborative efforts involving multiple investigation groups. By pooling together the expertise and resources of multiple teams, it was possible to amass more comprehensive and diverse results yielding deeper insights and more robust conclusions. This collaborative effort showcases once again the power of experimental and computational chemist cooperation in advancing chemical knowledge.

CHAPTER III

METHODOLOGIES

3.1 Experimental methods

Miscellaneous: Analytical grade solvents and commercially available reagents were used without further purification. Anhydrous solvents were purified and dried with activated molecular sieves prior to use. For reactions carried out under inert conditions, the argon was previously dried through a column of P_2O_5 and a column of KOH and $CaCl_2$. All the glassware was dried for at least 12 hours prior to use in an oven at 140ºC, and allowed to cool under a dehumidified atmosphere. Reactions were monitored using analytical thin layer chromatography (TLC), in pre-coated silica-backed plates (Merk Kieselgel 60 F254). These were visualized by ultraviolet irradiation, permanganate potassium or *p*-anisaldehyde dips. For chromatography 60, 0.06-0.2 mm (70-230 mesh ASTM) silica gel was used. For the removal of solvents under reduced pressure Büchi R-210 rotary evaporators were used.

NMR: ^{1}H NMR, ^{13}C NMR, ^{19}F NMR were acquired at 25ºC on Bruker AC-300 spectrometer 300 MHz, Bruker Avance 400 MHz or AVANCE II 300 MHz instruments in the stated solvent. Chemical shifts (δ) are reported in ppm relative to residual solvent signals and coupling constants (*J*) in hertz (Hz). The following abbreviations are used to indicate the multiplicity in NMR spectra: s, singlet; d, doublet; t, triplet; q, quartet; p, pentuplet; app, apparent; m, multiplet; bs, broad signal. NMR assignments were performed using standard 2D experiments.

HRMS: High-resolution mass spectra (HRMS) were recorded on a QToF Spectrometer equipped with an ESI (electrospray ionization) source (microToF-Q, Bruker Daltonik) using sodium formate as external reference.

Optical Rotatory Power: Optical rotatory powers were measured in a polarimeter Jasco DIP-370 at stated temperature, in 1dm cells, with different diameters, and using HPLC-quality solvents and milli-Q water.

3.2 Computational methods

General methods: All the calculations were performed using the Gaussian09 program. [1] A benchmark of different levels of theory was done in most of the cases. M06-2X, [2] ωB97X-D, [3] TPPSh, [4] and B3LYP [5] were used as hybrid functionals. When working with TPPSh and B3LYP functionals, gd3bj

Grimme's correction was applied. [6] In conjunction with them, another list of basis set was employed, being def2-bases [7] the most used. Pople's [8] and Dunning's [9] basis sets were also utilized in other cases. Geometry full optimizations were performed with the 2-ζ version of these basis sets. To obtain the energy values, 3-ζ single point calculations were performed over the optimized 2-ζ geometries. In bigger systems, ONIOM [10] calculations were done using the same QM methods as before for the high layer and PM6 (MM method) [11] for the low one.

Solvent effects were considered using SMD, [12] PCM, [13] and CPCM, [14] this last one for the most polar solvents like water. The level-of-theory selection for each calculation was made by results comparison with experimental data (if available), synergy between functionals, basis sets and solvents models; and depending on the key interactions the system presents. If needed, diffuse functions were added to simulate long-range interactions between molecular species, like hydrogen bonds. Polarization functions were added as well in other cases to model more accurately the orbital's shape of light and hypervalent elements, and so improve the results of equilibrium geometries and normal-mode vibrational frequencies. [15]

The nature of stationary points was defined on the basis of calculations of normal vibrational frequencies (force constant Hessian matrix). The optimizations were carried out using the Berny analytical gradient optimization method. [16] Minimum energy pathways for the reactions studied were found by gradient descent of transition states in the forward and backward direction of the transition vector (IRC analysis). [17] Analytical second derivatives of the energy were calculated to classify the nature of every stationary point, to determine the harmonic vibrational frequencies, and to provide zero-point vibrational energy corrections. The thermal and entropic contributions to the free energies were also obtained from the vibrational frequency calculations, using the unscaled frequencies. Structural representations were generated using CYLView. [18]

Molecular dynamics: MD simulations were carried out with AMBER20 suite of programs. [19] Parameters were generated with the antechamber module using the general Amber force field (GAFF2), [20] with partial charges calculated using AM1-BCC method and GLYCAM06 force field for mono- and trisaccharides. If the reaction took place in water, a 12 Å buffer TIP3P water molecules box was used to simulate solvent effects. [21] Other solvents were parametrised, and GAFF2 was used as force field.

A two-stage geometry optimization approach was carried out: (i) minimization of only the positions of solvent molecules executed by 500 cycles of steepest descent minimization followed by 500 cycles of conjugate gradient minimization, and (ii) unrestrained minimization of all the atoms in the simulation cell executed by 2500 cycles of steepest descent minimization followed by 2500 cycles of conjugate gradient minimization. After system optimization, running of MD simulations was started on the systems by gradually heating each system in the NVT ensemble from 0 to 300 K for 100 ps using a Langevin thermostat with a coupling coefficient of 1.0/ps. Harmonic restraints of 10 kcal/mol were applied to the solute, and the Langevin temperature coupling scheme [22] was used to control and equalize the temperature. The time step was kept at 2 fs during the heating stages, allowing potential inhomogeneities to self-adjust.

Water molecules are treated with the SHAKE algorithm such that the angle between the hydrogen atoms is kept fixed. Long-range electrostatic effects are modelled using the particle-mesh-Ewald method. [23] Then 5 ns of density equilibration with a force constant of 2.0 kcal/mol·Å was performed by releasing all the restraints. Finally, production trajectories were then run for 100 ns under the same simulation conditions with an integration time step of 2 fs, recording geometry every 0.05 ps and with snapshots written each 2 ps, producing 50,000 frames per simulation. All MD simulations were replicated three times to ensure feasibility. The conformation analysis was carried out using cpptraj module with average linkage as the clustering algorithm.

Macromodel conformational searches: The software Macromodel as implemented in Schrödinger package [24] was also used as a tool for analysing molecular conformations. This technique creates different conformers by rotating all bonds separately by a given angle. The smaller is the angle, the higher the number of conformations becomes. Then, the software estimates the energy difference between these geometries and discard every geometry whose energy is above the limit you state. Is important to know that all these geometries do not necessary correspond to an exact energy minima, and they have to be further optimised with other software to obtain the real minimal energy geometries and estimate more exactly the energy difference and between them.

The conformational searches were carried out using the Monte Carlo algorithm with OPLS-2005 force field, [25] GB/SA solvation model for water, intermediate torsion sampling with 50 000 Monte Carlo steps and an RMSD cut-off set to 2.0 Å. A Molecular Mechanics energy minimization was performed at each Monte Carlo step, as implemented in Macromodel. Each conformation was energy minimized using Polak-Ribière type conjugate gradient (PRCG) with a maximum of 5000 steps. All conformations within 5 kcal/mol from the global minimum were saved. All ensembles generated by the conformational searches were combined and elimination of redundant conformations was performed by comparison of heavy atom coordinates applying an RMSD cutoff set to 2.0 Å to give the final set of conformations.

NCI: NCIs were computed using the methodology previously described. [26] Data were obtained with the NCIPLOT program. [27] A density cutoff of $\rho=0.1$ a.u. was applied and the pictures were created for an isosurface value of $s=0.35$ and colored in the [-0.03,0.03] a.u. $\mathrm{sign}(\lambda_2)\rho$ range using VMD software. [28]

ELF: The ELF studies has been performed with the TopMod program [29] using the corresponding monodeterminantal wavefunctions of all the structures of the IRC. Structural representations were generated using CYLView. [18]

3.3 References

[1] M. J. Frisch, G. W. Trucks, H. B. Schlegel, G. E. Scuseria, M. A. Robb, J. R. Cheeseman, G. Scalmani, V. Barone, G. A. Petersson, H. Nakatsuji, X. Li, M. Caricato, A. V. Marenich, J. Bloino, B. G. Janesko, R. Gomperts, B. Mennucci, H. P. Hratchian, J. V. Ortiz, A. F. Izmaylov, J. L. Sonnenberg, Williams, F. Ding, F. Lipparini, F. Egidi, J. Goings, B. Peng, A. Petrone, T. Henderson, D. Ranasinghe, V. G. Zakrzewski, J. Gao, N. Rega, G. Zheng, W. Liang, M. Hada, M. Ehara, K. Toyota, R. Fukuda, J. Hasegawa, M. Ishida, T. Nakajima, Y. Honda, O. Kitao, H.

Nakai, T. Vreven, K. Throssell, J. A. Montgomery Jr., J. E. Peralta, F. Ogliaro, M. J. Bearpark, J. J. Heyd, E. N. Brothers, K. N. Kudin, V. N. Staroverov, T. A. Keith, R. Kobayashi, J. Normand, K. Raghavachari, A. P. Rendell, J. C. Burant, S. S. Iyengar, J. Tomasi, M. Cossi, J. M. Millam, M. Klene, C. Adamo, R. Cammi, J. W. Ochterski, R. L. Martin, K. Morokuma, O. Farkas, J. B. Foresman, D. J. Fox, Wallingford, CT, **2016**.

[2] Y. Zhao, D. G. Truhlar, *Acc. Chem. Res.* **2008**, *41*, 157-167.

[3] J. D. Chai, M. Head-Gordon, *Phys. Chem. Chem. Phys.* **2008**, *10*, 6615-6620.

[4] a) V. N. Staroverov, G. E. Scuseria, J. Tao, J. P. Perdew, *J. Chem. Phys.* **2003**, *119*, 12129-12137; b) J. Tao, J. P. Perdew, V. N. Staroverov, G. E. Scuseria, *Phys. Rev. Lett.* **2003**, *91*, 146401.

[5] B. Miehlich, A. Savin, H. Stoll, H. Preuss, **1989**, *157*, 200-205.

[6] S. Grimme, S. Ehrlich, L. Goerigk, *J. Comput. Chem.* **2011**, *32*, 1456-1465.

[7] a) F. Weigend, *Phys. Chem. Chem. Phys.* **2006**, *8*, 227-236; b) F. Weigend, R. Ahlrichs, *Phys. Chem. Chem. Phys.* **2005**, *7*, 3297-3305.

[8] a) R. Ditchfield, W. J. Hehre, J. A. Pople, *J. Chem. Phys.* **1971**, *54*, 724-728; b) W. J. Hehre, R. Ditchfield, J. A. Pople, *J. Chem. Phys.* **1972**, *56*, 2257-2261.

[9] a) T. H. Dunning Jr., *J. Chem. Phys.* **1989**, *90*, 1007-1023; b) R. A. Kendall, T. H. Dunning Jr., R. J. Harris, *J. Chem. Phys.* **1992**, *96*, 6796-6806.

[10] a) F. Maseras, K. Morokuma, *J. Comput. Chem.* **1995**, *16*, 1170-1179; b) S. Humbel, S. Sieber, K. Morokuma, *J. Chem. Phys.* **1996**, *105*, 1959-1967; c) L. W. Chung, W. M. C. Sameera, R. Ramozzi, A. J. Page, M. Hatanaka, G. P. Petrova, T. V. Harris, X. Li, Z. Ke, F. Liu, H.-B. Li, L. Ding, K. Morokuma, *Chem. Rev.* **2015**, *115*, 5678-5796.

[11] J. J. P. Stewart, *J. Mol. Model.* **2013**, *19*, 1-32.

[12] A. V. Marenich, C. J. Cramer, D. G. Truhlar, *J. Phys. Chem. B.* **2009**, *113*, 6378-6396.

[13] a) J. Tomasi, M. Persico, *Chem. Rev.* **1994**, *94*, 2027-2094; b) V. Barone, M. Cossi, J. Tomasi, *J. Comput. Chem.* **1998**, *19*, 404-417.

[14] a) V. Barone, M. Cossi, *J. Phys. Chem. A* **1998**, *102*, 1995-2001; b) M. Cossi, N. Rega, G. Scalmani, V. Barone, *J. Comput. Chem.* **2003**, *24*, 669-681.

[15] M. M. Francl, W. J. Pietro, W. J. Hehre, J. S. Binkley, M. S. Gordon, D. J. DeFrees, J. A. Pople, *J. Chem. Phys.* **1982**, *77*, 3654-3665.

[16] a) H. B. Schlegel, *J. Comput. Chem.* **1982**, *3*, 214218; b) H. B. Schlegel, in *Modern Electronic Structure Theory* (Ed.: D. R. Yarkony), World Scientific Publishing, Singapore, **1994**.

[17] a) K. Fukui, *Acc. Chem. Res.* **1981**, *14*, 363-368; b) K. Fukui, *J. Phys. Chem.* **1970**, *74*, 4161-4163.

[18] C. Y. Legault, *Université de Sherbrooke* **2009**, http://www.cylview.org (visited Mar 17th, 2023).

[19] D. A. Case, K. Belfon, I. Y. Ben-Shalom, S. R. Brozell, D. S. Cerutti, T. E. C. III, V. W. D. Cruzeiro, T. A. Darden, R. E. Duke, G. Giambasu, M. K. Gilson, H. Gohlke, R. H. A.W. Goetz, S. Izadi, S. A. Izmailov, K. Kasavajhala, A. Kovalenko, R. Krasny, T. Kurtzman, T. S. Lee, S. LeGrand, P. Li, C. Lin, J. Liu, T. Luchko, R. Luo, V. Man, K. M. Merz, Y. Miao, O. Mikhailovskii, G. Monard, H. Nguyen, A. Onufriev, F. Pan, S. Pantano, R. Qi, D. R. Roe, A. Roitberg, C. Sagui, S. Schott-Verdugo, J. Shen, C. L. Simmerling, N. R. Skrynnikov, J. Smith, J. Swails, R. C. Walker, J. Wang, L. Wilson, R. M. Wolf, X. Wu, Y. Xiong, Y. Xue, D. M. York, P. A. Kollman, *University of California, San Francisco* **2020**.

[20] J. Wang, W. Wang, P. A. Kollman, D. A. Case, *J. Mol. Graph. Mod.* **2006**, *25*.

[21] W. L. Jorgensen, J. Chandrasekhar, J. D. Madura, R. W. Impey, M. L. Klein, *J. Chem. Phys.* **1983**, *79*, 926.

[22] N. Matubayasi, M. Nakahara, *J. Chem. Phys.* **1999**, *110*, 3291-3301.

[23] T. Darden, D. York, L. Pedersen, *J. Chem. Phys.* **1993**, *98*, 10089-10092.

[24] a) F. Mohamadi, N. G. J. Richards, W. C. Guida, R. Liskamp, M. Lipton, C. Caufield, G. Chang, T. Hendrickson, W. C. Still, *J. Comput. Chem.* **1990**, *11*, 440-467; b) Schrödinger Release 2023-3: MacroModel, LLC, New York, NY, **2023**.

[25] a) W. L. Jorgensen, D. S. Maxwell, J. Tirado-Rives, *J. Am. Chem. Soc.* **1996**, *118*, 11225-11236; b) W. L. Jorgensen, J. Tirado-Rives, *J. Am. Chem. Soc.* **1988**, *110*, 1657-1666.

[26] a) E. R. Johnson, S. Keinan, P. Mori-Sanchez, J. Contreras-Garcia, A. J. Cohen, W. Yang, *J. Am. Chem. Soc.* **2010**, *132*, 6498-6506; b) J. R. Lane, J. Contreras-Garcia, J.-P. Piquemal, B. J. Miller, H. G. Kjaergaard, *J. Chem. Theory. Comput.* **2013**, *9*, 3263-3266.

[27] J. Contreras-Garcia, E. R. Johnson, S. Keinan, R. Chaudret, J.-P. Piquemal, D. N. Beratan, W. Yang, *J. Chem. Theory. Comput.* **2011**, *7*, 625-632.

[28] W. Humphrey, A. Dalke, K. Schulten, *J. Mol. Graph.* **1996**, *14*, 33-38.

[29] S. Noury, X. Krokidis, F. Fuster, B. Silvi, *Comput. Chem.* **1999**, *23*, 597-604.

CHAPTER IV

5-MEMBERED-RING HETEROCYLCLES OXIDATION MEDIATED BY TRANSITION METAL OXIDES

4.1 Introduction

4.1.1 The role of transition metal oxides in organic synthesis

Transition metal oxides are an important class of inorganic compounds. They have diverse applications in various fields such as materials science, [1] catalysis, [2] and organic synthesis. In the last century, transition metal oxides have emerged as efficient oxidants for the synthesis of various organic compounds. Some of these oxides possess unique electronic and structural properties, which make them ideal for selective oxidation reactions. Due to their high redox potentials, transition metal oxides act as powerful oxidants, promoting the transformation of various organic compounds into valuable intermediates or final products. Therefore, there is a growing interest in using transition metal oxides like TiO_2, ZnO, CrO_3 or V_2O_5 in synthetic chemistry. [3]

However, the same properties that make metal oxides a nice oxidant choice also make them difficult to study theoretically. Most metal oxides are not molecular species but instead form a three-dimensional network of oxygen and metal atoms. [4] In addition, the presence of multiple oxidation states can lead to situations where the oxidation occurs via single-electron transfers (SETs), involving radical intermediates. In such cases, open-shell calculations must be performed. Furthermore, defects in the crystalline structure can, in some cases, be responsible of their electronic properties. [5] Given the large size and complexity of this systems, the high number of electrons on second and third-period transition metals, and the possibility of radical intermediates, computational studies involving metal oxides often rely on small basis sets or model simplifications. [6]

4.1.2 Ruthenium tetroxide as a promising oxidation agent

In modern times, other metal oxides have been explored for their oxidizing or catalytic properties, and among them, ruthenium tetroxide has occupied a privileged position due to their versatility in functionalizing a wide range of functional groups. [7] RuO_4 is not just capable of functionalizing alkanes, which remains a challenging task to date, [8] but also leads to the formation of esters [9] or amides, [10] if oxygen or nitrogen atoms are present, respectively. Typically, the reaction is performed by oxidizing catalytic lower oxidation state ruthenium species such as $RuCl_3$ or RuO_2 with oxidants like $NaIO_4$ or NaOCl in a biphasic system. However, slow and incomplete reactions may occur due to the formation of low-valent ruthenium carboxylate complexes. This problem can be solved by adding acetonitrile to the reaction mixture. [9a]

Another advantage of RuO_4 is its molecular structure, which makes computational studies far easier than in the previous cases, allowing for more accurate calculations without oversimplifying the system or sacrificing calculation levels. [11] However, despite this advantage, DFT studies on organic oxidations are uncommon, and there are some discrepancies regarding the particular oxidation mechanism, which will be discussed in the next point. Nonetheless, RuO_4 remains a promising candidate for use as a model in the search for intermediates in organic oxidations.

4.1.3 Mechanistic discussion around RuO_4-mediated organic oxidations

The first mechanistic studies on alkanes were performed by Bakke et al. in 1986. After discarding radical intermediates, they suggested the formation of intermediate ionic species before the rate-limiting state, based on kinetic isotopic effects (KIEs) and substituent and solvent effects (see **Scheme 4.1**). [12] The ionic specie was then supposed to evolve to intermediate **4.1** from which the final product was obtained after hydrolysis. The major oxidation on tertiary carbons over the secondary ones pointed to the formation of organic carbocations as intermediates, and the higher stability of tertiary carbocations was the cause of the observed regioselectivity. However, three years later, Waegell et al. proposed a (2 + 2) concerted mechanism, [13] which better explained the retention of configuration over the reactive positions. Despite this, an extensive kinetic study by Bakke et al. obtained higher KIEs than expected for a concerted process. Thus, the new proposal relied on ion pairs as intermediates (still carbocations, but with the capability of retaining the configuration) or the presence of two competitive pathways, his and Waegell's. [14] At this time, Waegell proposed a new mechanism that avoided the possibility of β-elimination in intermediate **4.1** if some of the substituents were substituted by a hydrogen atom. This favourable scenario would drive directly to the ketone without any alcohol intermediate, contradicting experimental data. As a result, a new (3 + 2) mechanism was proposed, leading to intermediate **4.2**. [15]

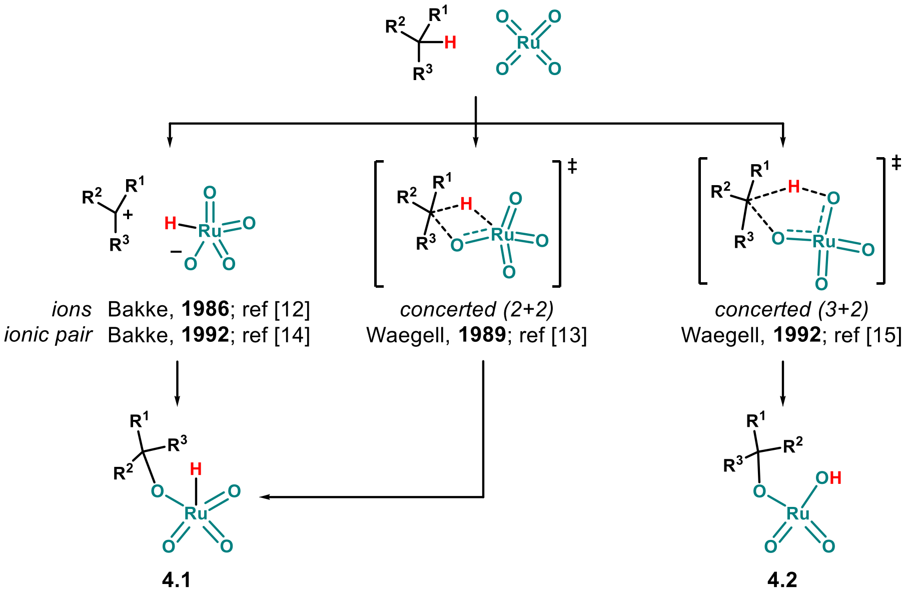
ions Bakke, **1986**; ref [12]
ionic pair Bakke, **1992**; ref [14]
concerted (2+2)
Waegell, **1989**; ref [13]
concerted (3+2)
Waegell, **1992**; ref [15]
4.1
4.2

Scheme 4.1: *Discussed mechanisms for RuO_4 oxidation of alkanes.*

This new mechanism was further supported by Bakke et al. when they observed no rearrangements (or significantly fewer than expected) in the oxidation of polycyclic hydrocarbons and no significant dependence on solvent polarity. [16] However, they also noted that more stabilized carbocations could still be formed depending on the substituents. The complete mechanism is depicted in **Figure 4.1**, which shows the oxidation of alkanes with RuO_4 in a biphasic system.

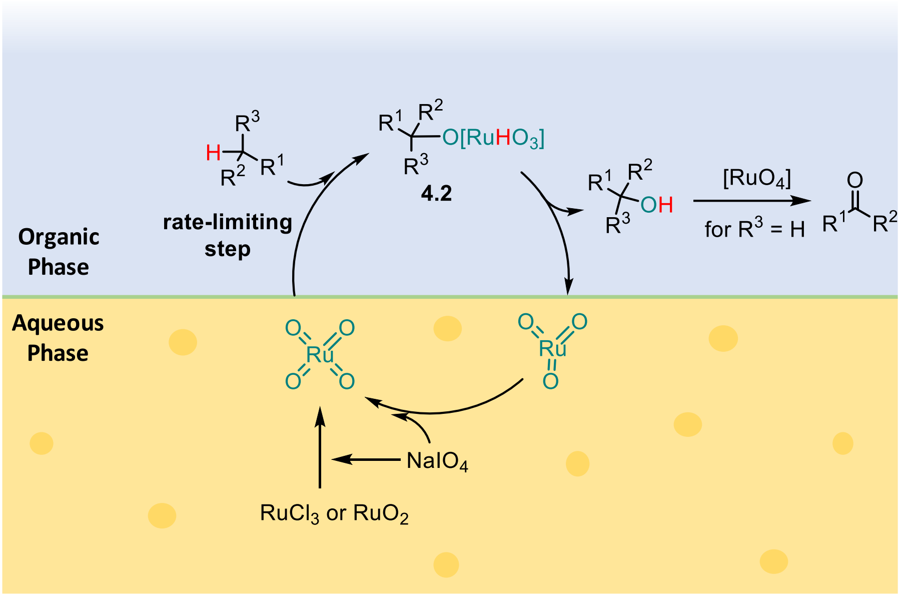

Figure 4.1: Oxidation of alkanes with RuO_4 in a biphasic system.

Years later, DFT studies carried out by Strassner et al. confirmed Waegell's (3 + 2) mechanism and the formation of intermediate **4.2** during the reaction.[17] However, contrary to Waegell's proposal and following Bakke's predictions, iminium cations were found as intermediates by Petride et al. in the RuO_4-mediated oxidation of tertiary amines by trapping them with cyanide anion. [18] This fact makes the study of cationic intermediates in RuO_4-mediated oxidations of organic compounds an interesting research field, and suggests the formation of transient carbocations in some situations.

The objective of this chapter is to study the RuO_4-mediated oxidation of different 5-membered-ring saturated heterocycles, as well as cyclopentane, as models for diverse functionalized alkanes. With this information, it will be easier to rationalize *a priori* which of the two mechanisms will operate for oxidations with RuO_4.

For that purpose, IRC-based ELF studies will be performed on this system for the first time to estimate the relative stability of the different intermediates.

Once the situation is clarified, the study will move from heterocycles to a more complex system, where saturated 5-membered-ring hydroxylamines will act as reductors. For this new system, the regio- and enantioselectivity will also be studied, as there have been previous issues in controlling the regioselectivity in the oxidation of 3’-substituted 5-membered-ring hydroxylamines. Since there is no experimental data on RuO_4-mediated oxidation of hydroxylamines, different 3’-subtituted 5-membered-ring hydroxylamines will be synthetised, and experimental and computational oxidation results will be contrasted.

4.2 Results and discussion

4.2.1 Searching carbocations in RuO_4 oxidation of saturated rings

The saturated 5-membered-ring compounds studied in this chapter are cyclopentane, tetrahydrofuran (THF), tetrahydrothiophene (THT), and *N*-methyl- and *N*-(*p*-methoxybenzyl)pyrrolidine (**Scheme 4.2**). The RuO_4-mediated oxidation of cyclopentane [19] and tetrahydrofuran [20] has been experimentally reported before, as well as the oxidation of *N*-acylpyrrolidines leading to the corresponding lactams. [21] However, the oxidation of tetrahydrothiophene with RuO_4 has not been studied before. Since the (3+2) mechanism has been computationally confirmed by Strassner et al., the study will be restricted to this approach. [17] Only the rate-determining stage (RDS) will be studied, since the hydrolysis of intermediate **4.2** and the next reaction stages are not relevant for the objective of this chapter. For the purpose of comparison, optimizations will be carried out at both the gas phase and with consideration of solvent effects (using both acetonitrile and water). However, since the experimental conditions for the oxidation reactions usually involve a polar medium containing water, all discussions will be based on data obtained with consideration of solvent effects (for the results using other levels of theory see the Supporting Information).

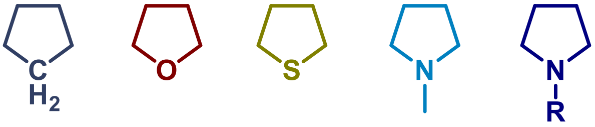

R4.3 **R4.4** **R4.5** **R4.6** **R4.7**

Scheme 4.2: *Studied models of saturated rings. R substituent for pyrrolidine* ***R4.7*** *corresponds with 4-methoxybenzyl substituent.*

The first 5-membered rings studied in this chapter were cyclopentane (**R4.3**), tetrahydrofuran (**R4.4**) and tetrahydrothiophene (**R4.5**). From their optimized structures, transition states **TS4.3**, **TS4.4**, and **TS4.5** were located respectively. All attempts to locate ionic pair intermediates **IN4.3**, **IN4.4**, and **IN4.5** failed, and the optimization of such structures resulted in hydroxides **P4.3 - 4.5**, indicating that these ionic pair structures collapse to form a real O-C bond. The obtained barriers and the general mechanism for these three cycles are depicted in **Figure 4.2**. The slower energy barriers in water are in agreement with a highly polar reaction. The calculations also predict an easier oxidation for the heterocyclic compounds compared to cyclopropane.

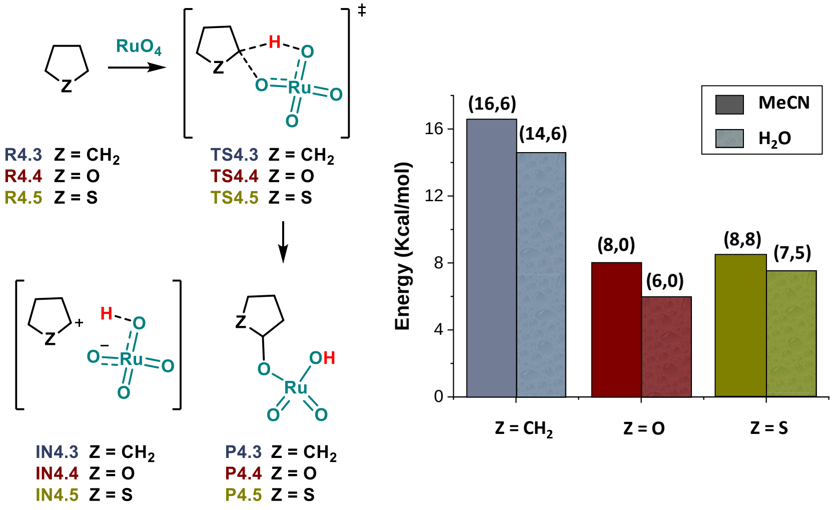

Figure 4.2: (Right) *Energy barriers (B3LYP-gj3bj/def2TZVP/CPCM//B3LYP-gd3bj/def2SVP/CPCM) for the oxidation with* RuO_4 *for cyclopentane (blue), THF (red) and THT (dark yellow) in PCM=acetonitrile (darker colour) and CPCM= water (lighter colour). Relative to reactants (*RuO_4 *+ R4.x).* ***(Left)*** *Mechanism and nomenclature of different oxidation stages with* RuO_4*.*

A comparison between the three transition structures in Figure 4.3 showed three asynchronous concerted processes, resulting in different C-O distances due to the stronger ability of the α-heteroatom in heterocycles to stabilize, the incipient positive charge generated during the hydrogen abstraction via mesomeric effect. The C-O distances were 2.65 Å for cyclopentane, 3.00 Å for THF and 3.15 Å for THT. These variations, compared to the small changes in the C-H-O bonds, indicated a more synchronous process for cyclopentane and a more asynchronous one for THT.

This effect is even more evident comparing the corresponding IRCs for the three transition structures. All three IRCs confirmed a concerted reaction connecting their corresponding encounter pairs **EP4.3**, **EP4.4** and **EP4.5**, (formed by adding RuO_4 to the reagents **R4.3-5**) with **P4.3**, **P4.4** and **P4.5**. A closer examination of the shape of these IRCs revealed a characteristic shoulder typical of transient carbocations, [22] which pronunciation follows the sequence cyclopentane < THF < THT. The evolution of C-O and C-H-O distances during the IRC confirmed the initial guess about the synchronicity of the three systems, following the same sequence as the shoulder pronunciation.

Although the IRC analysis clearly shows a typical one-step-two-stage process, [23] only a topological analysis of the ELF can provide accurate information about the formation and stability of the supposed transient carbocation.

As a model for the three reactions, the ELF for cyclopentane oxidation will be described first. The electron density evolution, as well as the descriptor basins for this reaction, are depicted in **Figure 4.4**. During the first steps of the ELF, the electron density remains approximately constant until point 77, corresponding to the **TS4.3** (29% of IRC). Once the reaction coordinate reaches the TS, the C1-H bond is broken, and a monosynaptic basin appears over C1. With this event, the transient carbocation is formed. The hydrogen atom previously bonded to C1 immediately forms a new bond with O3 creating the O3-H basin at point 81. The transient carbocation lasts until another oxygen atom (O6) attacks it, forming the new C1-O6 basin at point 128 and closing the carbocationic window (48% of IRC).

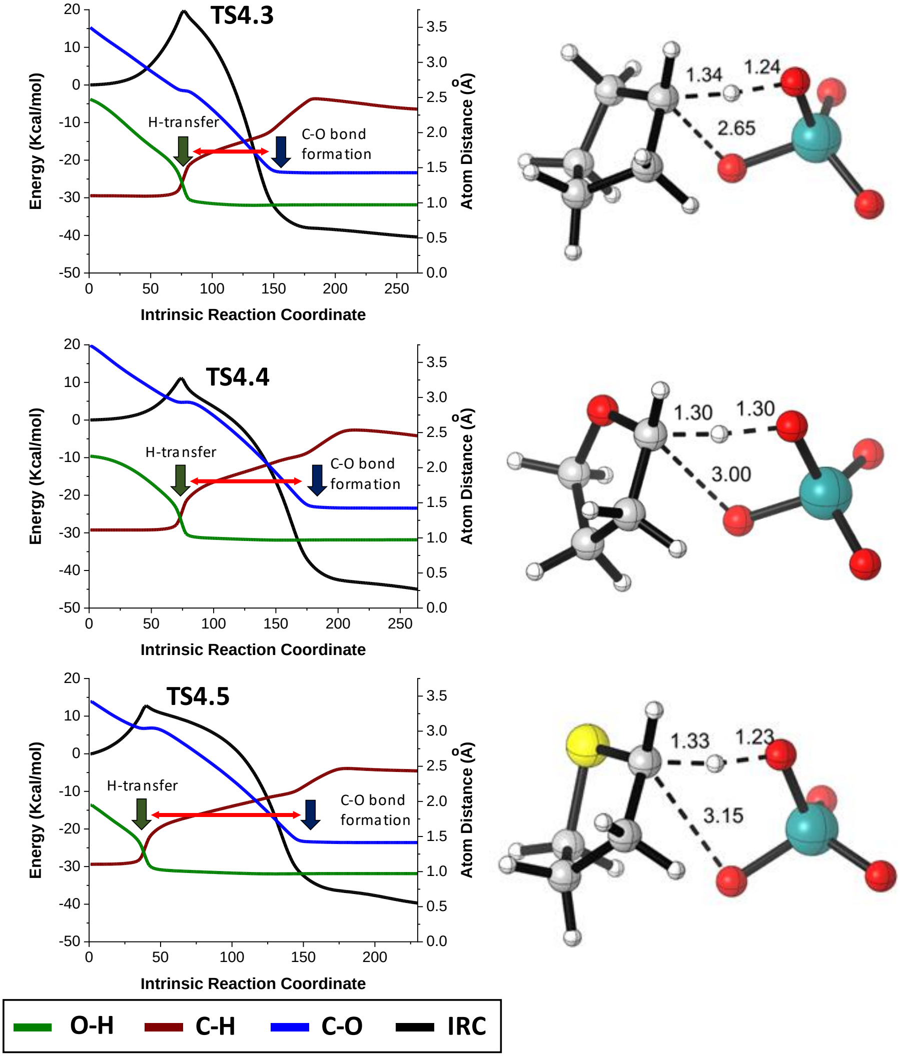

Figure 4.3: (Right) Optimized (B3LYP-d3bj/Def2SVP/cpcm=H_2O) geometries of transition structures corresponding to the oxidation of cyclopentane (**TS4.3**), tetrahydrofuran (**TS4.4**) and tetrahydrothiophene (**TS4.5**). **(Left)** The IRC (black trace) and O-H (green trace), C-H (brown trace), and C-O (blue trace*) distances evolution. The double red arrow indicates the delay between H-transfer and C-O bond formation. Energies are relative to* ***EP4.x****.*

Throughout this window, the carbocation is slightly stabilised by the electron density of the surrounding bonds (C1-C2 and C1-C8). This accumulation can be observed over the entire carbocationic window in the C1-C2 and C1-C8 basins, respectively (both overlapped due to the symmetry of the system). This inductive stabilization can be increased by the introduction of heteroatoms which, thanks to the presence of lone pair electrons, can transform this inductive effect into a mesomeric one (**Scheme 4.3**).

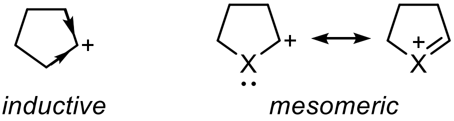

Scheme 4.3: *Comparison between inductive and mesomeric effects.*

Comparing the ELF from cyclopentane with that of THF (**Figure 4.5**) the same one-step-two-stages situation can be seen, but with a wider carbocationic window. Thanks to the stabilization provided by the endocyclic oxygen atom, the gap between the H transfer and the formation of the C1-O6 bond has increased from 17% of IRC for cyclopentane to 30% for THF. The H transfer begins three points after the TS (on point 77), opening the carbocationic window. During this time, as shown for cyclopentane, the adjacent bonds of the carbocation stabilize the positive charge. However, in this case, the presence of the heteroatom allows for mesomeric stabilization. This can be seen by the relocation of the oxygen's lone pair electron density to C1-O10 bond during the transient carbocation's lifetime. Then, at point 157, the C1-O6 bond is formed, and once again, the carbocationic window closes with this event.

The same situation can be observed for THT in **Figure 4.6**, but with a greater effect due to the higher capacity of the sulfur atom to stabilize the incipient positive charge over C1.

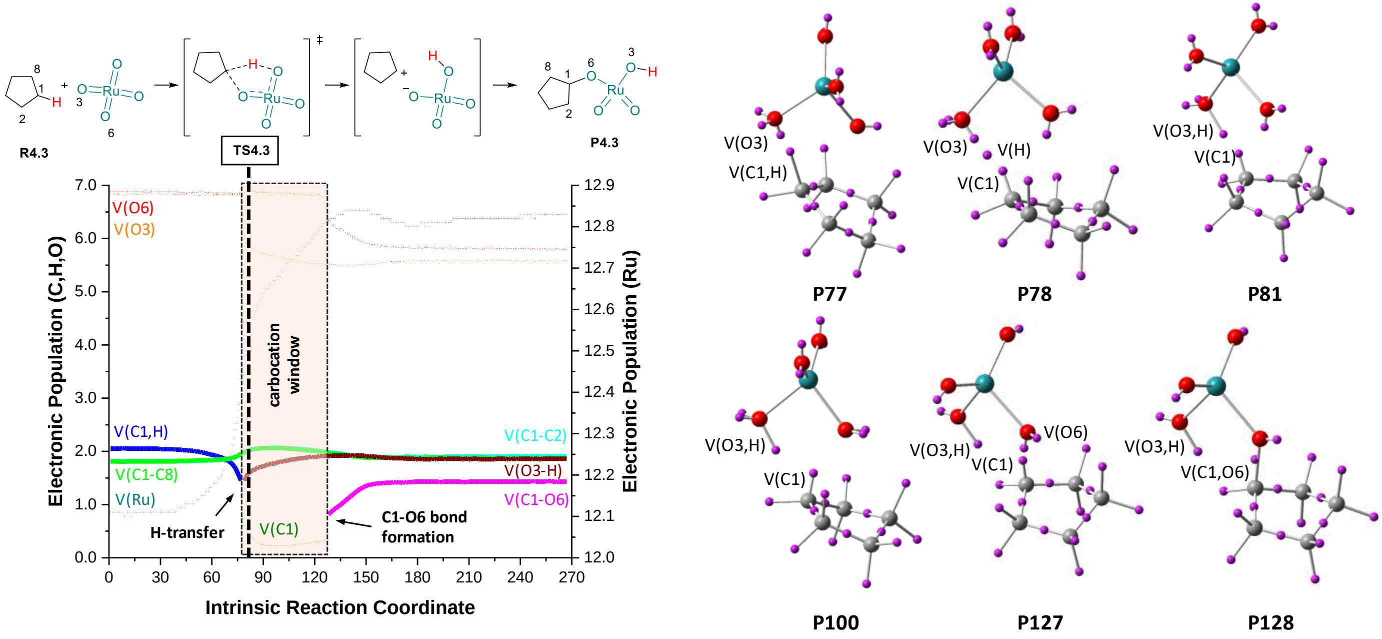

Figure 4.4: *ELF analysis for the oxidation of cyclopentane (**R4.3**).* ***(Left)*** *Evolution of the electron population along the IRC.* Disynaptic (bonds) and monosynaptic (atoms) basins are represented as plain and dotted lines, respectively. ***(Right)*** *Descriptors of basins at* selected points of the IRC.

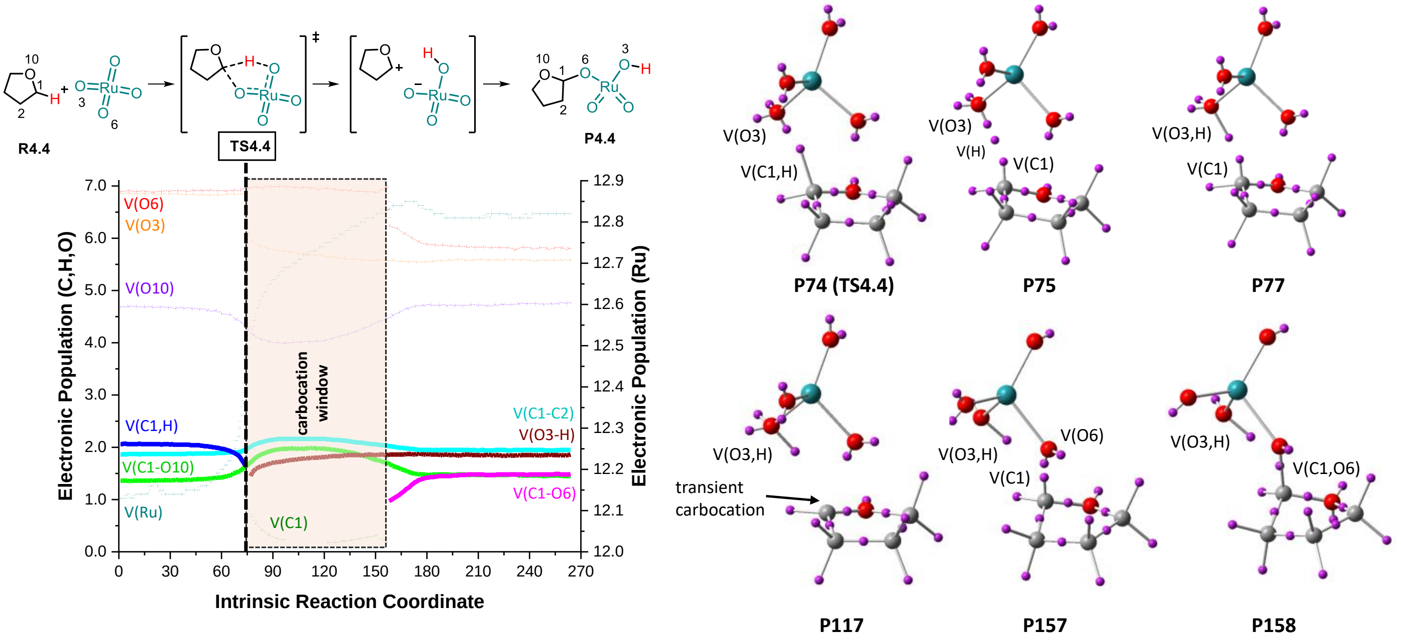

Figure 4.5: *ELF analysis for the oxidation of THF (**R4.4**).* ***(Left)*** *Evolution of the electron population along the IRC.* Disynaptic (bonds) and monosynaptic (atoms) basins are represented as plain and dotted lines, respectively. ***(Right)*** *Descriptors of basins at* selected points of the IRC.

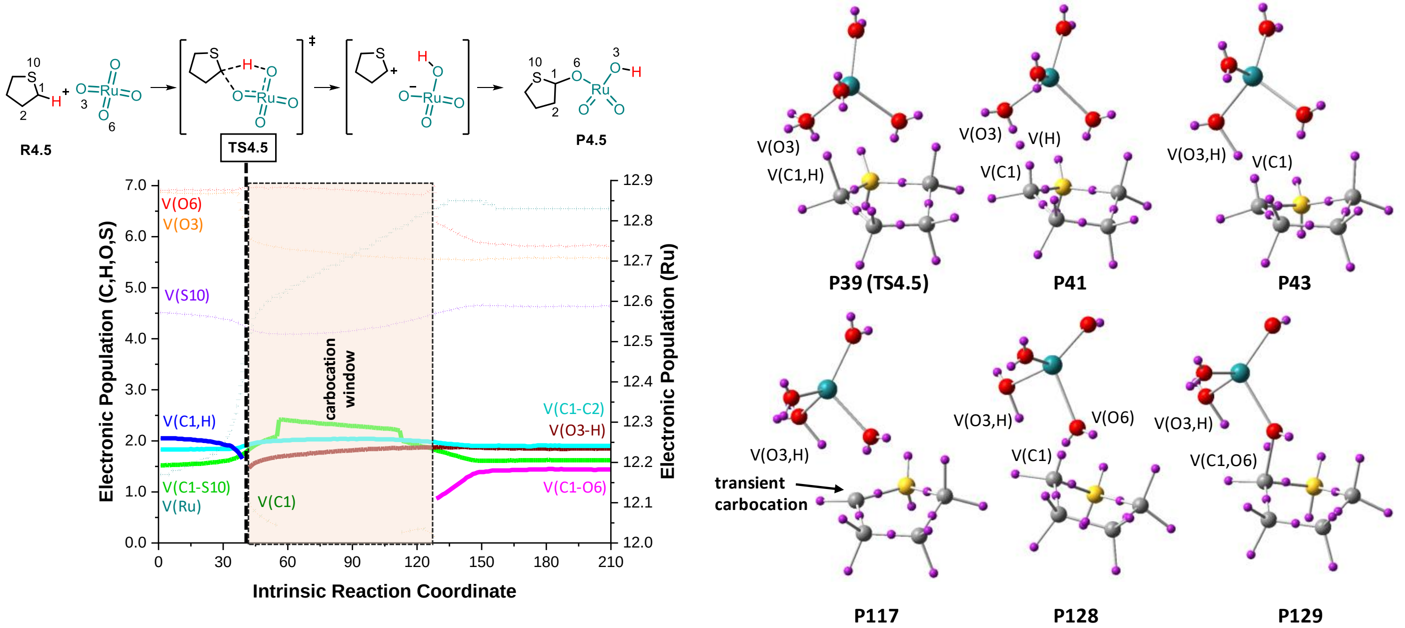

Figure 4.6: *ELF analysis for the oxidation of THT (**R4.5**).* ***(Left)*** *Evolution of the electron population along the IRC.* Disynaptic (bonds) and monosynaptic (atoms) basins are represented as plain and dotted lines, respectively. ***(Right)*** *Descriptors of basins at* selected points of the IRC.

The situation becomes completely different with the oxidation of *N*-methyl- and *N*-benzylpyrrolidine (**R4.6** and **R4.7** respectively). In this case, two regioisomeric oxidations can take place at the *endo* (cycle) and *exo* (*N*-chain) positions. The two transition structures were located for each pyrrolidine, with **TS4.6a** and **TS4.7a** being the TSs for the *endo* positions, and **TS4.6b** and **TS4.7b** for the *exo* series (**Scheme 4.4**).

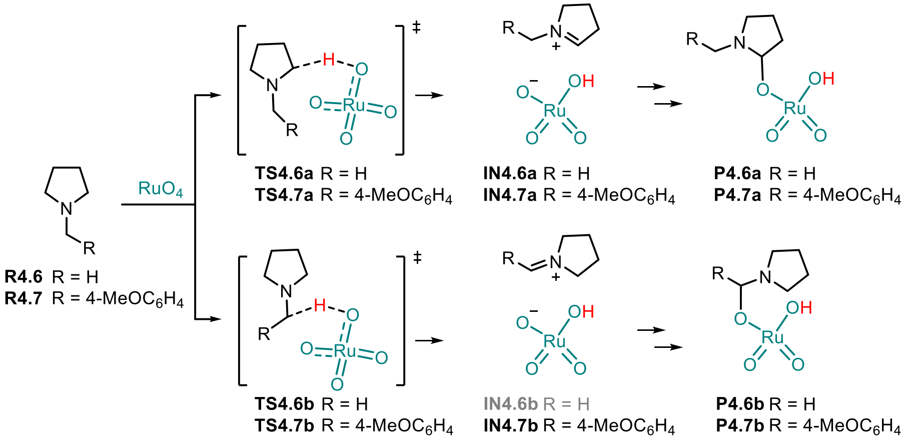

Scheme 4.4: *Selectivity-limiting step for the oxidation of N-methyl- and N-benzylpyrrolidines* ***R4.6*** *and* ***R4.7****, respectively.*

These transition structures were lower in energy than the reactants, demonstrating a favorable reaction and a stabilizing effect of the nitrogen. The energy diagram is depicted in **Figure 4.7**. In both cases, the *endo* oxidation was preferred over the *exo*. The difference was 1.3 kcal/mol for *N*-methylpyrrolidine and only 0.3 kcal/mol for *N*-benzylpyrrolidine, suggesting a directing effect of the *p*-methoxyphenyl group. Except for **TS4.6b**, the IRCs of the other transition structures ended in the corresponding ion pairs. The optimization of these structures led to **IN4.6a**, **IN4.7a** and **IN4.7b** as energy minima. Only the IRC of **TS4.6b** led straight to **P4.6b**, probably as a consequence of the formation of a less stabilized positive charge over the *N*-methyl group. The final evolution of the ion pair intermediates to the final products **P4.6a**, **P4.7a** and **P4.7b** was found to be almost barrierless. These intermediates could be defined as iminium ions, with **IN4.7b** being the most stable one due to the presence of a conjugated *p*-methoxyphenyl group that stabilizes the positive charge. These results are in agreement with the experimental demonstration of the existence of iminium ions as intermediates by Petride and co-workers. [18]

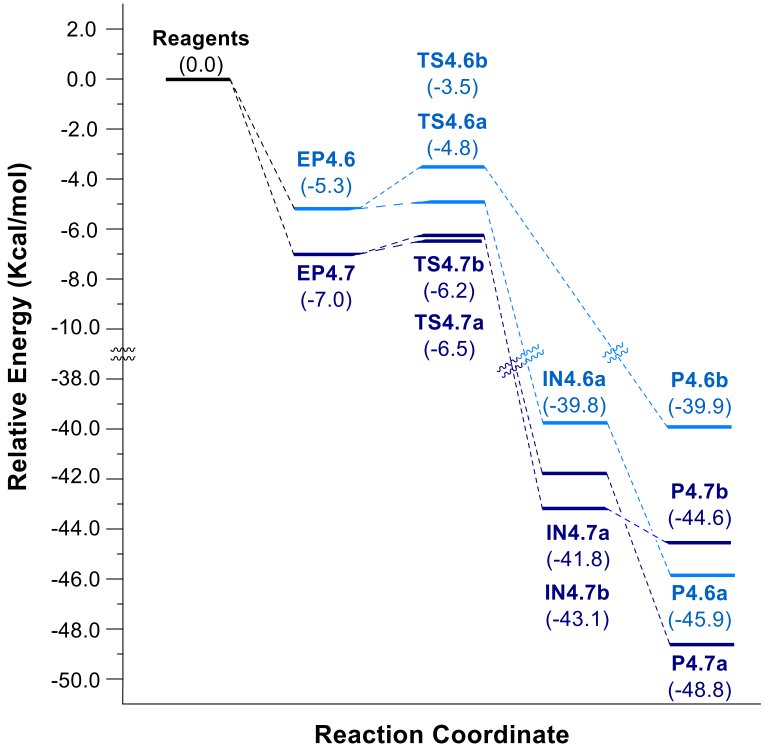

Figure 4.7: *Energy profile for the oxidation of* ***R4.6*** *(light blue) and* ***R4.7*** *(dark blue). Relative energies, calculated at B3LYP-gd3bj/def2TZVP/CPCM=water level of theory, are given in kcal/mol.*

Upon checking the geometry of the transition structures depicted in **Figure 4.8**, it can be observed that there are greater C-O distances in these four structures compared to those found in the other heterocycles from **Figure 4.3**. As these distances increase, the reactions become more asynchronous, and for the pyrrolidines, it turns into a two-step mechanism. In fact, **TS4.6b** presents the shorter C-O distance between the pyrrolidine's TSs, which is consistent with the fact that no intermediate could be located, and the final product **P4.6b** was found instead.

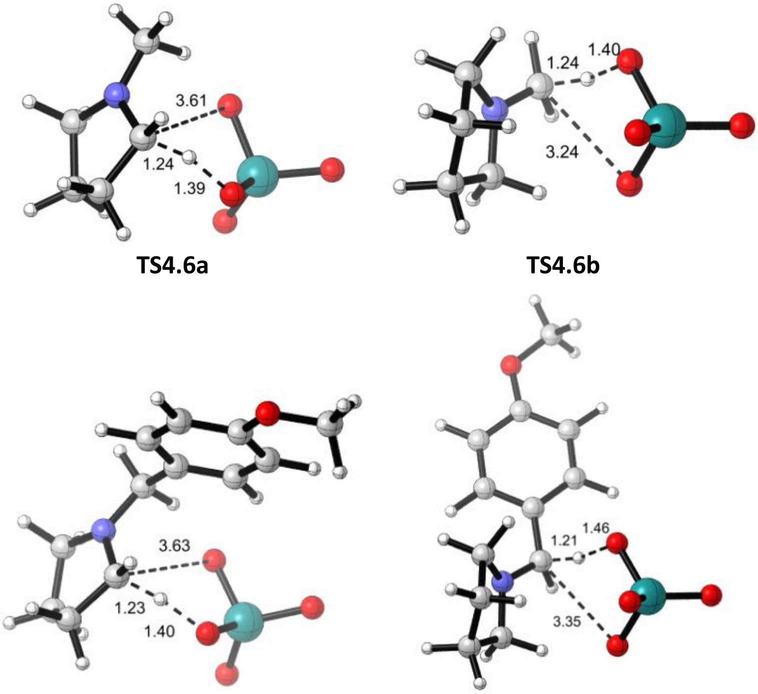

TS4.6a **TS4.6b**

TS4.7a **TS4.7b**

Figure 4.8: *Optimized (B3LYP-gd3bj/Def2SVP/CPCM=water) transition structures for the oxidation of **R4.6** and **R4.7**.*

Figure 4.9 shows the ELF and determinant basins for the oxidation of N-methylpyrrolidine **R4.6**, as it was done before with other heterocycles. Since the series *endo* exhibited lower energy barriers, only the ELF from **TS4.6a** is depicted. As has been demonstrated for other heterocycles, the breaking of C1-H bond defines the TS at point 43. The O3-H bond is formed almost instantaneously (point 45), and the incipient positive charge is stabilized by the heteroatom. In this particular case, once the hydrogen is transferred, the electron density from the nitrogen's lone pair begins to move towards the C1-N11 bond. This process culminates at point 69 with the complete formation of the iminium ion, which lasts until the end of the IRC at point 214.

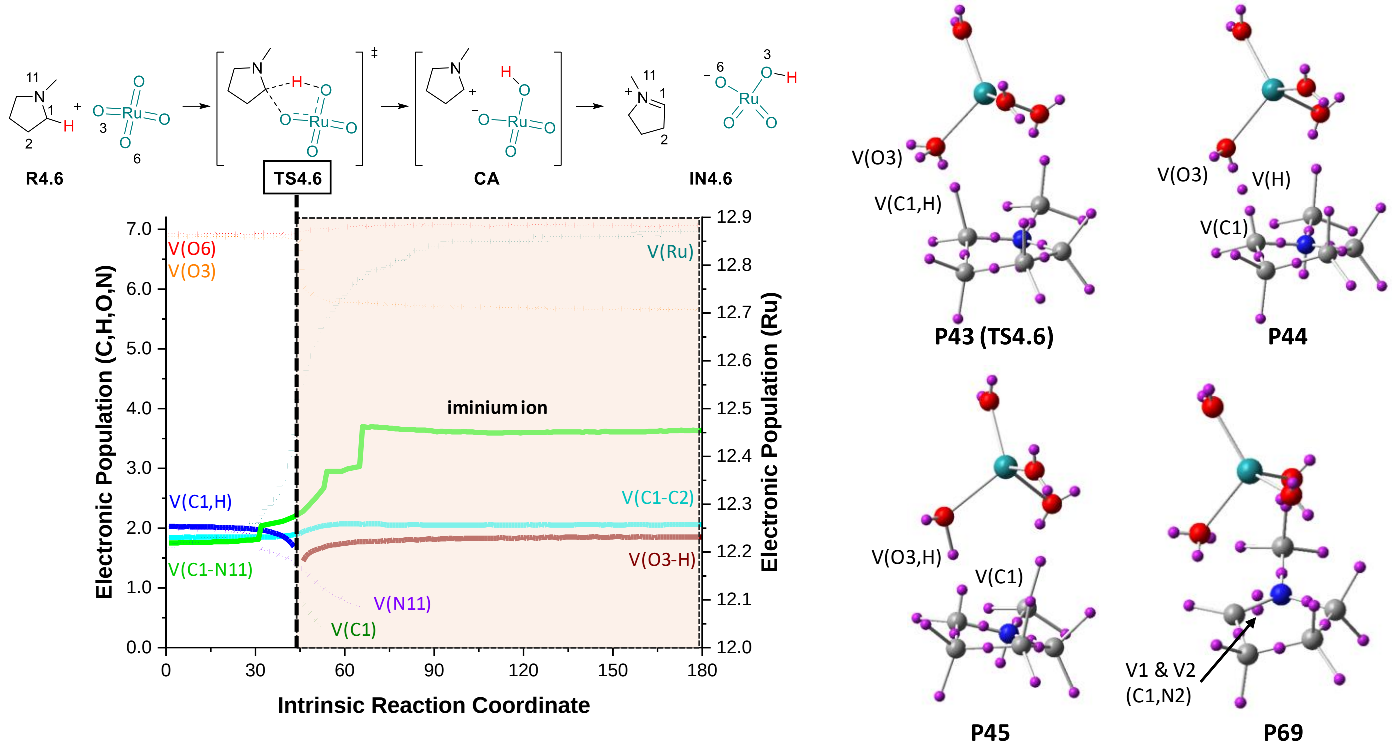

***Figure 4.9:** ELF analysis for the oxidation of N-methylpyrrolidine (**R4.6**). Only 180 from 214 IRC points are displayed for clarity.* ***(Left)** Evolution of the electron population along the IRC.* Disynaptic (bonds) and monosynaptic (atoms) basins are represented as plain and dotted lines, respectively. ***(Right)** Descriptors of basins at* selected points of the IRC.

Table 4.1 summarizes the differences observed in the cases studied. As shown, as the C-O distance at the TS increases, the reaction becomes more asynchronous. This can be measured by both the difference between hydrogen transfer and C-O bond formation and the percentage of carbocation during the IRC. The extreme case is **TS4.6**, which ultimately becomes a two-step process.

Table 4.1: *Summary of results*

	Barriers (ΔG) [a]	TS C1-O6 distance	% H Transfer [b]	% C-O Formation [b]	% carbo-cation [c]
R4.3	14.6	2.65	30	49	17
R4.4	6.0	3.00	29	60	30
R4.5	7.5	3.15	17	56	40
R4.6	-3.5[d]	3.61	20	-[e]	80

[a] Given in Kcal/mol relative to separate reagents. [b] Given in % with respect to the total number of points of the IRC. [c] Calculated on the number of points between the H transfer and the C-O bond formation with respect to the total number of points of the IRC. [d] The corresponding EP is 8.5 kcal/mol below the reagents. [e] Since the product of the reaction is the iminium ion no C-O bond is formed.

Even though the H transfer starts at approximately the same percentage of the IRC, the C-O bond formation requires more points as the heteroatom’s ability to stabilize the positive charge in their alpha position increases. This effect allows the carbocation to be more stabilized and, from being a brief transient intermediate for cyclopentane, it becomes a real intermediate in the case of pyrrolidine. These results are in agreement with both Bakke’s and Waegell’s mechanisms and predict that the two mechanisms could operate depending on the substituent’s ability to stabilize the intermediate.

4.2.2 Regioselectivity study on the RuO_4 oxidation of *N*-hydroxy pyrrolidines.

Hydroxylamines are organic compounds characterized by the presence of a *N*-hydroxyl group. Their corresponding oxidation gives rise to nitrones, [11c, 24] which could be used as precursors for synthesizing high-value products, such as isoxazolines and isoxazolidines, that exhibit biological activity; [25] or amidines, which are vital motifs in pharmaceuticals and natural products. [26] This high versatility is a consequence of the ease with which nitrones can participate in 1,3-dipolar cycloaddition reactions. [27] These reactions are so fast that they can even be used for biorthogonal chemistry. [28] On the other hand, thanks to their structural similarity with TEMPO, one of the most stable free radicals, [29] they could also reduce oxidative stress by serving as radical oxygen species scavengers. [30] Finally, the presence of a highly polarized C=N double bond makes them a privileged substrate for nucleophilic additions. [31] A summary of nitrone's reactivity is depicted in **Scheme 4.5**.

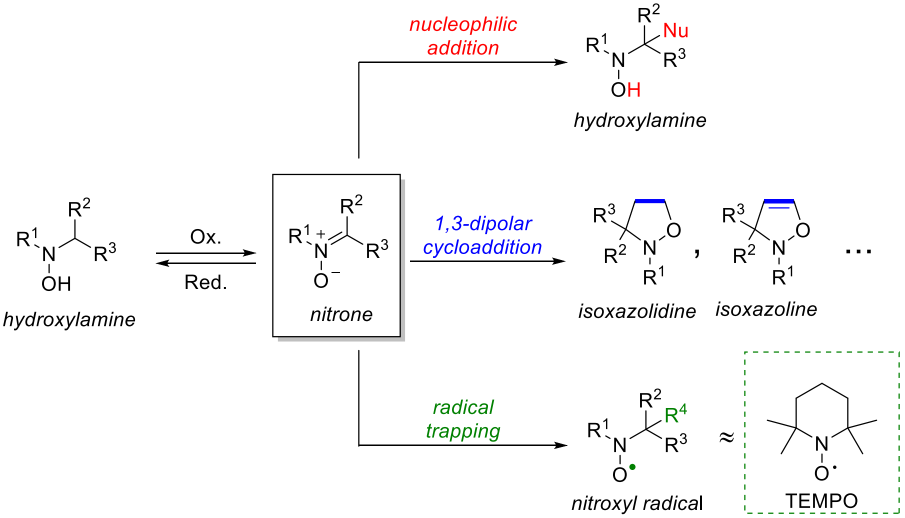
nucleophilic addition
R1
R2
Nu
R3
N
OH
hydroxylamine
R1
R2
R3
N
OH
hydroxylamine
Ox.
Red.
R1
R2
R3
N
O−
nitrone
1,3-dipolar cycloaddition
R3
R2
N
O
R1
isoxazolidine
R3
R2
N
O
R1
isoxazoline
...
radical trapping
R1
R2
R4
R3
N
O•
nitroxyl radical
≈
N
O•
TEMPO

Scheme 4.5: *Reactivity and synthesis of nitrones trough hydroxylamines.*

Within this vast field, 5-membered cyclic nitrones are particularly noteworthy due to their use as starting points for the synthesis of many heterocycles, such as polyhydroxylated pyrrolidines, which have gained significant interest since the discovery of their potential application as enzymatic inhibitors or as treatment of type-II diabetes. [32] These cyclic nitrones are synthetized by the oxidation of their corresponding cyclic hydroxylamines. In the case of any substitution on the ring, two possible regioisomers could be formed. This reaction has been extensively studied by Brandi and co-workers, and they have observed different regioselectivities by using several substrates and oxidants. [33]

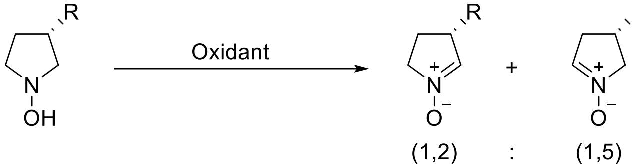

R = Me	HgO	1,8 : 1	Ref. 33a
R = Ph	HgO	2 : 1	Ref. 33a
R = NBn_2	HgO	4 : 1	Ref. 33b
R = OH	HgO	5 : 1	Ref. 33a
R = O^tBu	HgO	9 : 1	Ref. 33b
R = OTBDMS	HgO	12 : 1	Ref. 33b
R = O^tBu	NaOCl	5 : 1	Ref. 33c
R = O^tBu	MnO_2	7 : 1	Ref. 33d

Scheme 4.6: *Regioselectivity in the oxidation of 3'-susbtituted 5-membered ring hydroxylamines.*

Two mechanisms were proposed, with some similarities between them. Both propose a two-step mechanism with a rate-limiting step after the intermediate formation. This intermediate is formed by the hydrogen abstraction of the hydroxyl group; however, the discrepancies start here, with the nature of this first abstraction. Due to the stability of aminoxyl radicals such as TEMPO and the observation of some hydroxylamine radicals by EPR, [34] some authors proposed the formation of these aminoxyl radical intermediates. [35] Other authors proposed a cationic nitrosonium intermediate formed by an hydride abstraction from the hydroxylamine, followed by dehydrogenation, in the next step, forming the nitrone. [36] Both mechanism are illustrated on **Figure 4.10**, **left**. KIE experiments on the oxidation of cyclic hydroxylamines with HgO, performed by Brandi et al. supported this last mechanism and proposed a directing effect of the 3' substituent on the selection of the hydrogen to be abstracted in the RDS (**Figure 4.10**, **right**). [33a]

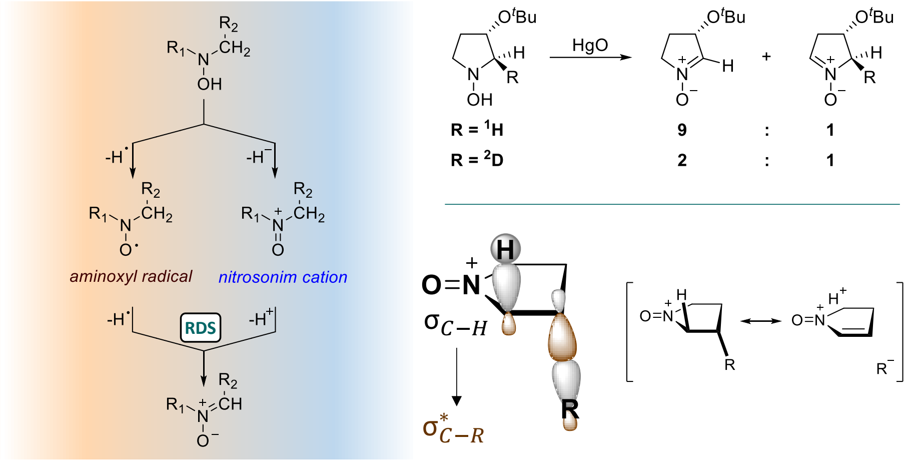

__Figure 4.10: (Left)__ Possible mechanisms for hydroxylamines oxidation to nitrones. __(Up right)__ Kinetic isotopic effects observed by Brandi's group (ref. 33a). __(Down right)__ MO interpretation of the 3' substituent's directing effect.

The KIE experiments revealed a kinetic preference for the hydrogen in the *anti*-position with respect to the 3' substituent at the rate-limiting step of the reaction. This preference was stipulated to be caused by a possible σ_{C-H}-σ^{*}_{C-R} interaction that specifically polarizes the *anti* C-H bond at the 2'-position. With strong electro-attractive groups on the 3'-position, the donation would be stronger, and the TS involving this C-H bond should be more stabilized. Since this last mechanism explains the regioselectivity observed for these systems more effectively, it is now commonly accepted as the mechanism for hydroxylamine oxidation. [24b] However, the radical approach is still applied in one-electron transfer oxidations. [37]

Despite the controversy surrounding the oxidation mechanism of these compounds, few computational studies have been done, in any case without considering regioselectivity. [38] Therefore, the main objective of this section is to study the oxidation of 3'-substitued 5-membered ring hydroxylamines with RuO_4, which, as previously mentioned, serve as an excellent model for high oxidation state transition metal oxides. The goal is to determine its mechanism and verify the regioselectivity.

As a starting point, cyclic hydroxylamine **R4.8** was chosen for standardizing the mechanism. Since no substituents are present, no regio- or enantioisomers should be considered. From this point, five transition structures were located: **TS4.8a**, **TS4.8b**, **TS4.8c**, **TS4.8d**, and **TS4.8e**.

TS4.8e was generated from the previous **TS4.6a** of the pyrrolidine, and like in that example, the oxidation starts from the *endo* C-H bond. This was the highest TS, with a difference of 4.4 kcal/mol compared to the next one. This result agrees with the experimental observations that the oxidation starts from the hydroxyl group and not from inside the cycle. Interestingly, the result of this IRC was highly dependent of the solvent. While in polar solvents like water or acetonitrile, the IRC ended in a structure similar to what was found for pyrrolidines in the previous section, in non-polar solvents such as dichloromethane, the result is the same as cyclopentane and THF, forming the C-O bond. **Figure 4.11** compares the geometry of some of the TS from the previous section with this new one. As it is depicted, the C-O distance of **TS4.8e** is slightly lower than **TS4.5**.

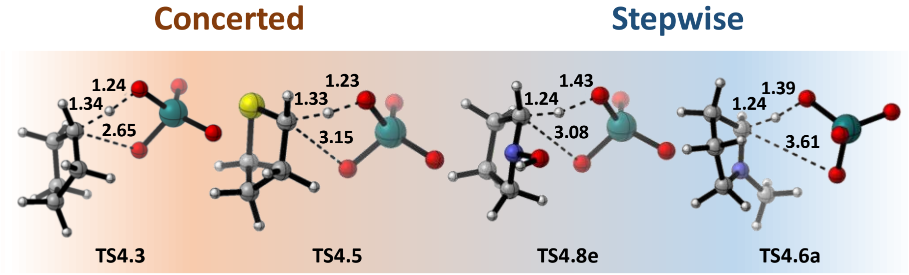

***Figure 4.11:** Optimized geometries for **TS4.8e** (ωb97XD/def2SVPP/CPCM=water) and TS from other heterocycles (B3LYP-gd3bj/Def2SVP/CPCM=water). Distances are measured in Angstroms.*

Once the oxidation through the C-H bond was discarded, the other two transition structures were located after performing a conformational analysis of the starting hydroxylamine. For that purpose, a conformational study was conducted on the isolated hydroxylamine **R4.8** through sequential scans. As the hydroxylamine possesses a symmetry plane, the same situation is transferred to the puckering, and only half of the cycle must be scanned.

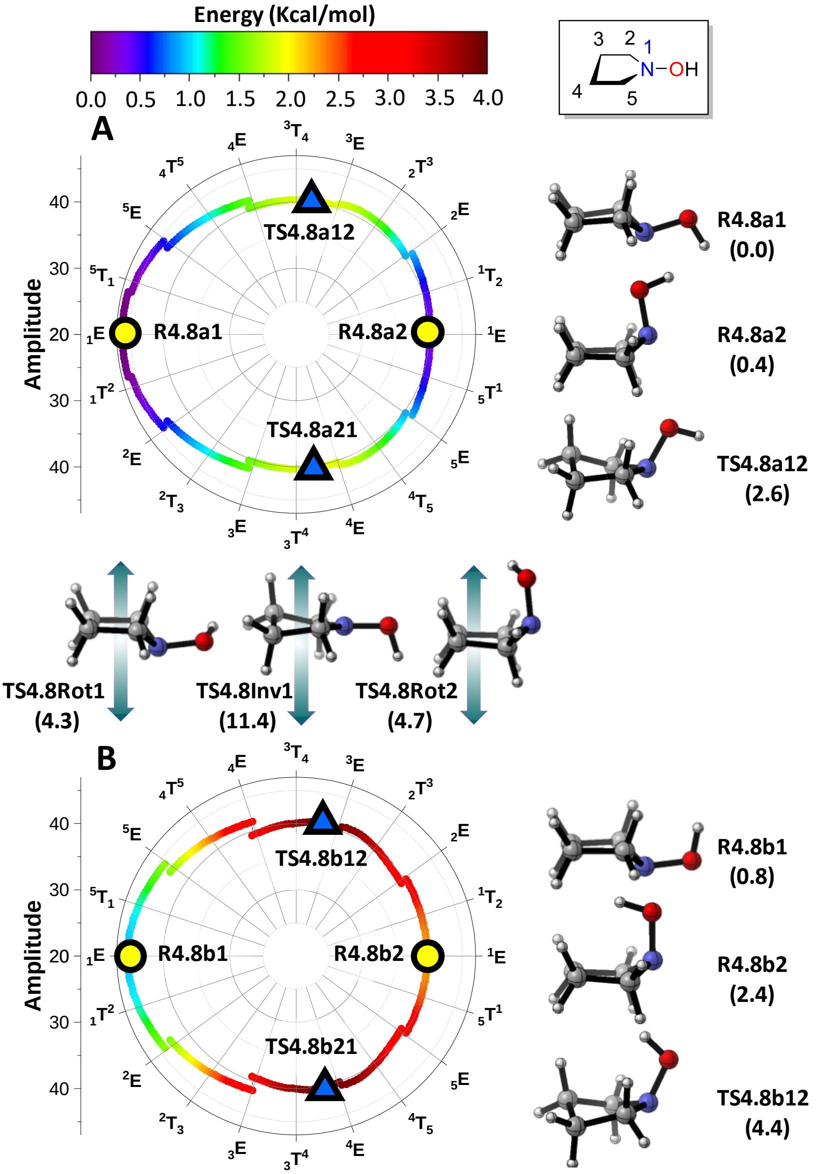

Figure 4.12: *Puckering of the hydroxylamine* ***R4.8****. Yellow-filled circles represent minimal conformations while blue triangles represent conformational TS. Optimized geometries (wb97XD/def2svpp/smd=DCM) are also depicted, and energy barriers (wb97XD/def2tzvpp/smd=DCM// wb97XD/def2svpp/smd=DCM) are given in brackets.*

Each conformational pathway presents 2 minima, corresponding to the ${}_{1}E$ and ${}^{1}E$ geometries: **R4.8a1** and **R4.8a2** for puckering A and **R4.8b1** and **R4.8b2** for puckering B. The two puckering rings (**Figure 4.12**, **A** and **B**) are a consequence of the two different positions the O-H bond can take. Because of this, the A and B pathways are connected at all points by the rotation of the O-H bond. This process is represented by the **TS4.8Rot1** and **TS4.8Rot2** structures, which connect both ${}_{1}E$ and ${}^{1}E$ geometries and have a relative energy of 5.0 and 5.8 kcal/mol, respectively.

Looking at just pathway **A**, **R4.8a1** and **R4.8a2** are separated by two conformational TS (**TS4.8a12** and **TS4.8b21**) with an average geometry of ${}^{3}T_{4}$ and ${}_{3}T^{4}$, which, due to the hydroxylamine's symmetry, are specular images and share the same activation energy. The same situation is repeated for pathway **B**.

In fact, both conformational itineraries are also connected by the pyramidal inversion of the nitrogen atom (**TS4.8Inv1**); however, the energy barrier for this process is 11.0 kcal/mol, higher than the rotation of the OH bond. As well as **TS4.8a12** and **TS4.8b12** this structure also presents a ${}^{3}T_{4}$ geometry and its mirror image, with a ${}_{3}T^{4}$ geometry, share the same energy.

As it was mentioned before, starting the oxidation for the α C-H bond with **TS4.8e**, creates the highest energy situation, and because of that, it was stated that the oxidation starts by the hydroxyl group. So, the incorporation of RuO_4 was done by keeping the hydrogen bond between the oxidant and the hydroxylamine. Doing so, and thanks to the RuO_4 tetrahedral symmetry, the last four minimal conformations evolve into only four encounter pairs: **EP4.8c1** and **EP4.8c2** from puckering **C** and **EP4.8d1** and **EP4.8d2** for **D** one. **Figure 4.13** shows the complete PES analysis for the system, as well as the energy barriers.

Same as the previous case, pathways **C** and **D** differ from each other in the orientation of the hydroxylamine's O-H bond. In pathway **C**, this orientation points in the same direction as the nitrogen's lone pair, which allows for an interaction between this nitrogen atom and the electron-deficient ruthenium. This interaction has two consequences: first, the stabilization of the starting EPs by at least 1.2 kcal/mol, making them the most stable EPs; and second, the elongation of the distance between the *endo*-hydrogen and the ruthenium tetroxide's oxygen. In contrast, in pathway **D**, since nitrogen's lone pair points in the opposite direction of the oxidant, no Ru-N interaction can be formed. This effect can be observed by checking the distances on both puckerings in **Figure 4.13**. Distances of 2.76 Å and 2.56 Å between the ruthenium and nitrogen atoms are observed in puckering **C** on **EP4.8c1** and **EP4.8c2**, respectively, which are longer than expected for a proper Ru-N bond. [39] This, together with the presence of an electronegative hydroxyl group on the nitrogen, and the saturation of the vacant coordination sites of the ruthenium, eliminates the possibility of a real Ru-N bond, but suggests a donor-acceptor interaction instead. For **EP4.8d1** and **EP4.8d2** distances of 4.49 Å and 5.23 Å (not depicted)**,** are observed, denoting an absence of any type of interaction. However, is possible to form a second hydrogen bond between one of the oxygens of the RuO_4 and one of the 2'-position hydrogens from this side; reducing the distance from 2.39 Å and 2.71 Å for **EP4.8c1** and **EP4.8c2** respectively, to 2.15 Å for **EP4.8d1**.

Like in **Figure 4.12**, four different conformational transition structures (**TS4.8c12**, **TS4.8c21, TS4.8d12** and **TS4.8d21**) separate these encounter pairs. The presence of the ruthenium tetroxide breaks the previous symmetry. Due to the formation of a double bond during the oxidation, the amplitude of the 5-membered ring is gradually reduced, and so, it can be monitored through these IRCs. As the minimal amplitude is reached when the nitrone is formed, its final amplitude could be used as a reference for the center of the cycle instead of zero. So, the IRCs of the oxidation should start from one of these EP and end on the center of the puckering PES.

As no more encounter pairs were located, the search for transition structures of the oxidation started with the exploration of the PES around these four structures. Another four oxidation transition structures were located: **TS4.8a**, **TS4.8b**, **TS4.8c** and **TS4.8d**. Notably, no TS connects neither **EP4.8c2** nor **EP4.8d2** with the nitrone.

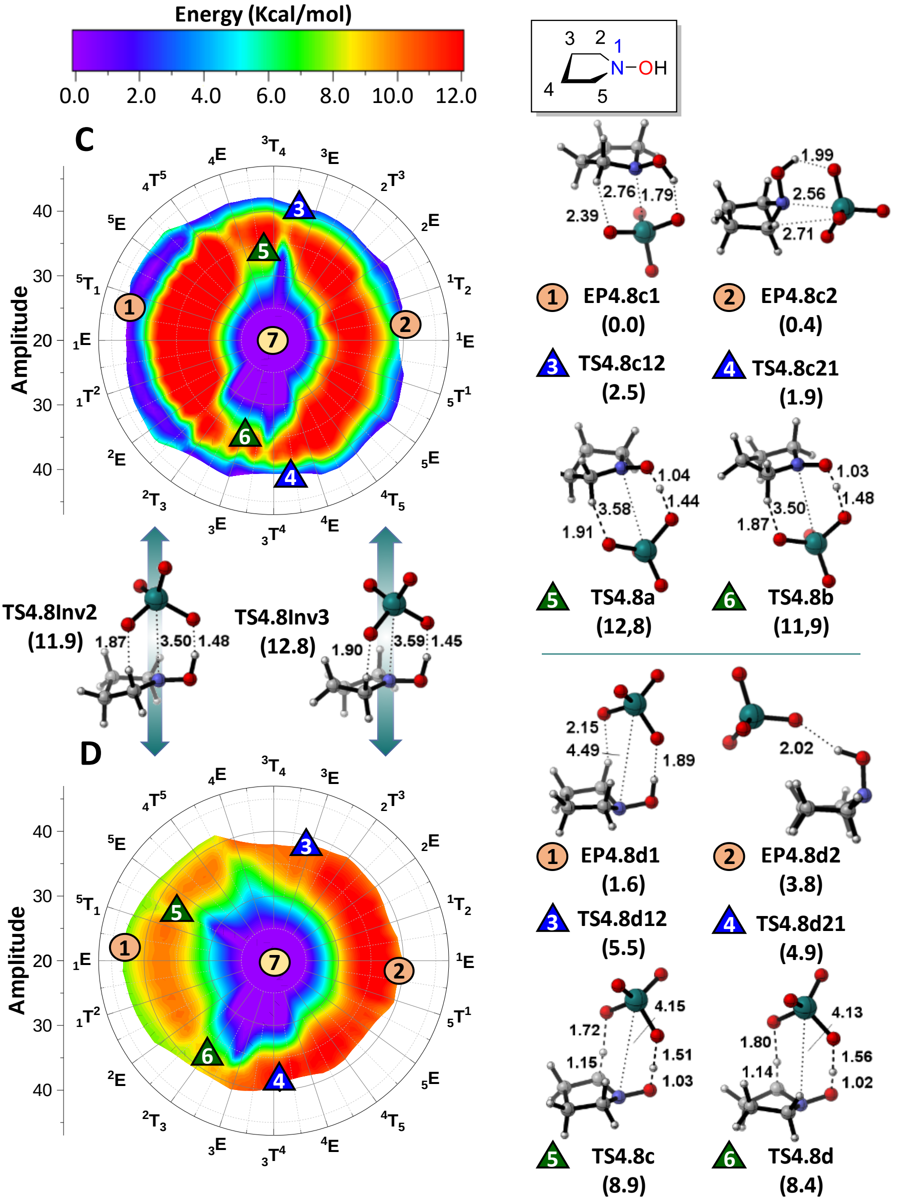

Figure 4.13: *Puckering of the complex RuO$_4$-hydroxylamine* ***EP4.8****. Circles represent minimal conformations while triangles represent TS. Optimized geometries (wb97XD/def2svpp/smd=DCM) are also depicted and energy barriers (wb97XD/def2tzvpp/smd=DCM//wb97XD/def2svpp/smd= DCM) are given in brackets. Geometries of TS connecting EPs (****3*** *and* ***4****) are omitted for clarity.*

As the Hammond's postulate states, these TSs retain some of the features found in their corresponding EPs. TSs originated from **EP4.8c1** exhibit shorter Ru-N distances and higher differences between the two O-H forming bonds compared to those originated from **EP4.8d1**. Due to this situation, the oxidation reactions trough **TS4.8c** and **TS4.8d** required fewer conformational changes than **TS4.8a** and **TS4.8b**. While the first two TSs need to adopt a $^{3}T_{4}$ and $_{3}E$ conformations respectively; **TS4.8c** and **TS4.8d** present dispositions that are more similar to **EP4.8d1** ($^{5}T_{1}$ and $^{2}T_{3}$, respectively). In **Figure 4.14**, those conformational changes make the IRC from **TS4.8a** and **TS4.8b** longer than the latter two. In the PES, the conformational changes can be seen by comparing the linear start of **TS4.8c** and **TS4.8d**, to the irregular one from the first two TSs. Once the Ru-N interaction has been broken, all IRCs run through the same valley, and all form first the O4-H9 bond.

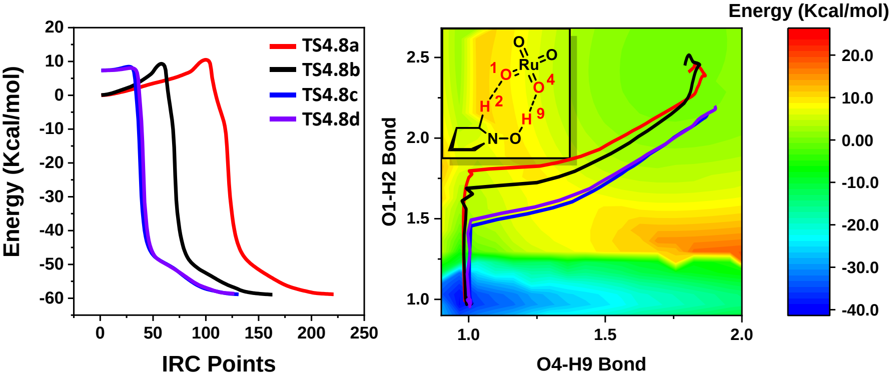

Figure 4.14: ***(Left)*** *IRC comparison from* ***TS4.8a*** *(red),* ***TS4.8b*** *(black),* ***TS4.8c*** *(blue) and* ***TS 4.8d*** *(purple) on wb97XD/def2svpp/smd= DCM level of theory.* ***(Right)*** *O4-H9 and O1-H2 bond distances evolution during the IRCs, represented over the PES defined over those two distances.*

The reason why the EPs from pathway **C** were more stable than those from puckering **D** was the Ru-N interaction. However, during the oxidation, this interaction appears to be broken due to the elongation of the distance for the TS, resulting in the loss of the energy advantage from pathway **C**. With this interaction broken, the starting hydrogen bond from **EP4.8d1**, which is maintained in **TS4.8c** and **TS4.8d**, is responsible for the greater stability of these two TSs.

To confirm or reject the radical nature of the oxidation, the optimization of the TSs was carried out using an unrestricted (open-shell) approach (uωb97XD). Values of S^2 close to zero were found in all cases, thus ruling out a single-electron transfer process and any type of radical formation during the reaction.

In contrast to Brandi’s mechanism, no real intermediate was found during RuO_4-mediated oxidation. ELF studies were performed on **TS4.8c** to establish the electron evolution of the system during the oxidation process. **Figure 4.15** shows the first 70 points of the IRC, revealing a highly concerted reaction. The TS corresponds to the breaking of the O2-H1 bond at point 28, followed by the formation of the O16-H1 bond at point 31. Subsequently, the breakage of the C3-H4 bond results in the development of a positive charge on C3, which is quickly compensated by the lone pair electrons of the nitrogen, forming a N-C3 double bond. The final bond formation between O15 and H4 ends with the electron rearrangement, and from this point, only the formation of a double hydrogen bond between reduced H_2RuO_4 and the recently formed nitrone continues the IRC progression. Since no relevant electronic changes were observed from this point, this part of the ELF was omitted for clarity. During the whole IRC, no significant changes were observed between the N-O2 bond, ruling out the possibility of any hidden nitrosonium intermediate. This fact, combined with the highly concerted nature of the reaction, revealed a new oxidation mechanism for hydroxylamines.

Due to the reaction’s concerted nature and the TS corresponding to the O-H bond rupture of the hydroxyl group, no significant electronic influence is expected from the 3’-substituent since it is far from the reactive positions. However, since the oxidation of hydroxylamines with RuO_4 has not been tested experimentally, three differently substituted hydroxylamines were synthetized: **R4.9**, **R4.10** and **R4.11** (**Table 4.2**), and they were oxidized with RuO_4 under two different conditions. First, the standard methodology was employed, using a catalytic amount of $RuCl_3$ that is continuously re-oxidized by an excess of $NaIO_4$, as is depicted in **Figure 4.1**. The oxidation of the hydroxylamine was carried out in a biphasic system where the $NaIO_4$ was dissolved in the aqueous phase, and the hydroxylamine remained in the organic phase, which was composed of a 1:1 mixture of acetonitrile and

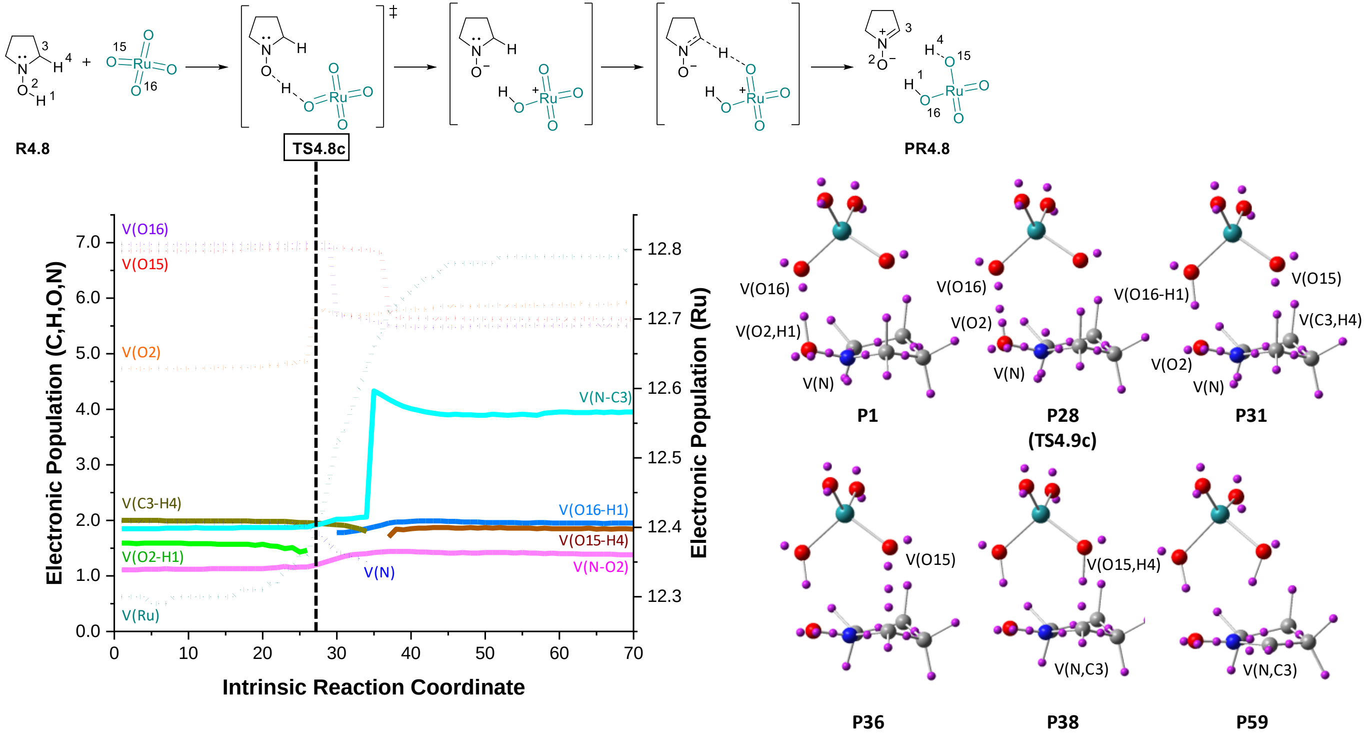

Figure 4.15: *ELF analysis for the oxidation of N-hydroxypirrolidine (**R4.8**). Only 70 from 131 IRC points are displayed for clarity. (**Left**) Evolution of the electron population along the IRC. Disynaptic (bonds) and monosynaptic (atoms) basins are represented as* plain and dotted lines, respectively. ***(Right)*** *Descriptors of basins at* selected points of the IRC.

carbon tetrachloride. The ruthenium species were able to phase transfer, and interact with both reactants. The second methodology consisted of using a 5:1 mixture of acetone and water as solvent. In this mixture, no phase transfer was necessary. For both systems, the oxidation was also carried out without $RuCl_3$ to confirm the influence of the RuO_4. In both cases, longer reaction times and decomposition of the starting hydroxylamine were observed. Once the reaction ended, the regioselectiviy was measured by NMR analysis.

In addition, computational calculations were performed on the hydroxylamines that were tested experimentally. Although the synthesis of **R4.12**, and **R4.13** failed for different reasons, they were computationally tested anyway, since they correspond to electron-withdrawing substituted hydroxylamines, and their results can contrast to the three firsts electron-enriched substituted hydroxylamines. In fact, hydroxylamine **R4.13** was an interesting study case due the presence of a carbonyl group that radically changes the relative acidity of the 2- and 5-position hydrogens.

To achieve this, the lowest barrier TSs **TS4.8c** and **TS4.8d** were used as starting points to create eight different transition structures for each system, two for each oxidizable hydrogen in the cycle: H^1 - H^4 (only four for **R4.13**, since the oxo-substituent relies on a sp^2 carbon, and so there is no difference between both faces of the hydroxylamine). Computational regioselectivity results, in both acetonitrile and water, are shown in **Table 4.2**, alongside the experimental regioselectivity for comparison. Other solvents like carbon tetrachloride or dichloromethane were also tested however, no significant differences were found (see SI).

Table 4.2: *Experimental (right) and computational (left) results of the regioselectivity on the oxidation of 3-substituted, 5-membered ring hydroxylamines.* [a] *Calculated via single-point on wb97xd/def2tzvpp/solvent//wb97xd/def2svpp/solvent.*

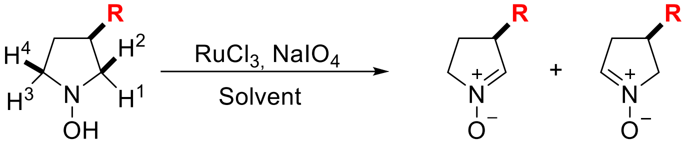

1,2 **1,5**

		Computational [a]				Experimental			
		SMD = ACN		CPCM = H_2O		CCl_4/ACN/H_2O (2:2:3)		Acetone/H_2O (5:1)	
Reference	**Substituent**	**1,2**	**1,5**	**1,2**	**1,5**	**1,2**	**1,5**	**1,2**	**1,5**
R4.9	**R = Me**	27.4	72.6	54.0	46.0	66.5	33.5	56.5	43.5
R4.10	**R = O^{t}Bu**	95.4	4.6	89.9	10.1	79.1	20.9	78.1	21.9
R4.11	**R = NHBoc**	80.2	19.8	53.3	46.7	71.1	28.9	78.9	21.1
R4.12	**R = F**	55.2	44.8	19.6	80.4	-	-	-	-
R4.13	**R = O**	37.9	62.1	73.0	27.0	-	-	-	-

Experimental and computationl results were in good agreement showing low regioselectivities. Since the electronic influence of the 3-substituent on the TS's barrier is almost non-existent, the regioselectivity mainly depends on steric hindrance between the 3-substituent and the RuO_4. Interestingly, even 2- and 5-position hydrogen's acidity from **R4.13** differs strongly, the scenario is not traduced to the oxidation barriers, and low regioselectivity values are also obtained. This result predicts a low regioselectivity in all cases using high oxidation state metal oxides that performs the oxidation in a concerted way, and with a two-electron-transfer processes.

4.3 Conclusions

A borderline mechanism in terms of concertedness has been observed for the oxidation of different heterocycles with RuO_4. With non-stabilizing groups present in the cycle, such as cyclopentane, the reactions evolve with the formation of no intermediate. On the other hand, stabilized ones such as pyrrolidine, pause in an intermediate stabilized by mesomeric effect. Cases between these two extremes like furan or thiophene give rise to situations where hidden intermediates can be found, and their existence period is determined by the ability of these groups to stabilize it.

The oxidation study of the simplest *N*-hydroxy pyrrolidine **R4.8**, showed a highly concerted reaction, with the TS corresponding to the breakage of the O-H bond from the hydroxyl group. This fact makes the influence of the 3'-substituent almost on-existent, and low regio- and enantioselectivities are obtained in all cases, both computational and experimentally.

4.4 References

[1] a) B. S. Kumar, R. Kumar, A. Pradeep, A. Amardeep, V. Srihari, H. K. Poswal, A. Chatterjee, A. Mukhopadhyay, *Chem. Mater.* **2022**, *34*, 10470-10483; b) N. Srivastava, S. K. Singh, D. Meghnani, R. Mishra, R. K. Tiwari, A. Patel, A. Tiwari, R. K. Singh, *ACS Appl. Energy Mater.* **2022**, *5*, 12183-12195.

[2] a) K. Rong, J. L. Wei, L. Huang, Y. X. Fang, S. J. Dong, *Nanoscale* **2020**, *12*, 20719-20725; b) I. Yamada, A. Takamatsu, K. Asai, H. Ohzuku, T. Shirakawa, T. Uchimura, S. Kawaguchi, H. Tsukasaki, S. Mori, K. Wada, H. Ikeno, S. Yagi, *ACS Appl. Energy Mater.* **2018**, *1*, 3711-3721.

[3] a) B. P. Benke, T. Kirschbaum, J. Graf, J. H. Gross, M. Mastalerz, *Nat. Chem.* **2023**, *15*, 413-423; b) Y.-Q. Dong, K. Wang, C.-X. Zhuo, *ACS Catal.* **2022**, *12*, 11428-11435.

[4] A. Thursfield, I. S. Melcalfe, A. Kruth, J. T. S. Irvine, in *Metal Oxides Chemistry and Applications* (Ed.: J. L. G. Fierro), CRC Taylor & Francis: Boca Raton, FL, USA, **2006**, pp. 55-85.

[5] J. C. Védrine, *Catalysts* **2017**, *7*, 341.

[6] a) R. Dwivedi, P. Sharma, A. Sisodiya, M. S. Batra, R. Prasad, *J. Catal.* **2017**, *345*, 245-257; b) H. Yao, Y. Chen, Z. Zhao, Y. Wei, Z. Liu, D. Zhai, B. Liu, C. Xu, *J. Catal.* **2013**, *305*, 67-75; c) Y. Dehmani, H. Lgaz, A. A.

Alrashdi, T. Lamhasni, S. Abouarnadasse, I.-M. Chung, *J. Mol. Liq.* **2021**, *324*, 114993.

[7] S.-I. Murahashi, N. Komiya, in *Modern Oxidation Methods* (Ed.: J.-E. Bäckvall), **2004**, pp. 165-191.

[8] A. J. L. Pombeiro, in *Alkane Functionalization* (Ed.: J. W. Sons), Chichester, United Kingdom, **2019**, pp. 1-15.

[9] a) P. H. J. Carlsen, T. Katsuki, V. S. Martin, K. B. Sharpless, *J. Org. Chem.* **1981**, *46*, 3936-3938; b) V. Dragojlović, S. Bajc, A. Amblès, D. Vitorović, *Org. Geochem.* **2005**, *36*, 1-12.

[10] a) S. Iqbal, N. N. Shaikh, K. M. Khan, S. Kiran, S. Naz, Z. Ul-Haq, S. Perveen, M. I. Choudhary, *Molecules* **2022**, *27*; b) M. Kaname, S. Yoshifuji, H. Sashida, *Tetrahedron Lett.* **2008**, *49*, 2786-2788.

[11] a) H. Rzepa, https://www.rzepa.net/blog/?p=15812 (visited Mar 16th, 2023); b) M. Drees, T. Strassner, *J. Org. Chem.* **2006**, *71*, 1755-1760; c) G. D'Adamio, C. Parmeggiani, A. Goti, F. Cardona, *Eur. J. Org. Chem.* **2015**, *2015*, 6541-6546.

[12] a) J. M. L. Bakke, Morten, *Act. Chem. Scand.* **1986**, *40b*, 430-433; b) J. M. B. Bakke, Jon Erik, *Act. Chem. Scand.* **1991**, *45*, 418-423.

[13] A. Tenaglia, E. Terranova, B. Waegell, *Tetrahedron Lett.* **1989**, *30*, 5271-5274.

[14] J. M. B. Bakke, Donald, *Act. Chem. Scand.* **1992**, *46*, 644-649.

[15] a) A. Tenaglia, E. Terranova, B. Waegell, *J. Org. Chem.* **1992**, *57*, 5523-5528; b) J. L. Coudret, B. Waegell, *Inorganica Chim. Acta* **1994**, *222*, 115-122.

[16] a) J. M. Bakke, A. E. Frøhaug, *J. Phys. Org. Chem.* **1996**, *9*, 507-513; b) J. M. Bakke, A. E. Frøhaug, *J. Phys. Org. Chem.* **1996**, *9*, 310-318.

[17] M. Drees, T. Strassner, *J. Org. Chem.* **2006**, *71*, 1755-1760.

[18] a) H. Petride, C. Drãghici, C. Florea, A. Petride, **2004**, *2*, 302-322; b) H. Petride, C. Drăghici, C. Florea, A. Petride, **2006**, *4*, 674-694.

[19] U. A. Spitzer, D. G. Lee, *J. Org. Chem.* **1975**, *40*, 2539-2540.

[20] D. G. Lee, M. V. D. Engh, *Can. J. Chem.* **1972**, *50*, 3129-3134.

[21] N. Tangari, V. Tortorella, *J. Chem. Soc., ChemComm.* **1975**, 71b-72.

[22] M.-A. Chiacchio, L. Legnani, P. Caramella, T. Tejero, P. Merino, *Tetrahedron* **2018**, *74*, 5627-5634.

[23] a) L. R. Domingo, M. Arnó, J. A. Sáez, *J. Org. Chem.* **2009**, *74*, 5934-5940; b) D. Roca-López, V. Polo, T. Tejero, P. Merino, *J. Org. Chem.* **2015**, *80*, 4076-4083; c) D. Roca-López, V. Polo, T. Tejero, P. Merino, *Eur. J. Org. Chem.* **2015**, *2015*, 4143-4152.

[24] a) S. Cicchi, A. Goti, A. Brandi, *J. Org. Chem.* **1995**, *60*, 4743-4748; b) C. Matassini, F. Cardona, *Chimia* **2017**, *71*, 558.

[25] a) A. Leggio, A. Liguori, A. Procopio, C. Siciliano, G. Sindona, *Tetrahedron Lett.* **1996**, *37*, 1277-1280; b) K. Kokosza, G. Andrei, D. Schols, R. Snoeck, D. G. Piotrowska, *Bioorg. Med. Chem.* **2015**, *23*, 3135-3146; c) M. M. Efremova, A. P. Molchanov, A. S. Novikov, G. L. Starova, A. A. Muryleva, A. V. Slita, V. V. Zarubaev, *Tetrahedron* **2020**, *76*, 131104.

[26] a) X. Shen, A. Shatskiy, Y. Chen, M. D. Kärkäs, X.-S. Wang, J.-Q. Liu, *J. Org. Chem.* **2020**, *85*, 3560-3567; b) M. R. Barbachyn, C. W. Ford, *Angew. Chem. Int. Ed.* **2003**, *42*, 2010-2023.

[27] a) K. Rück-Braun, T. H. E. Freysoldt, F. Wierschem, *Chem. Soc. Rev.* **2005**, *34*, 507-516; b) R. G. M. Silva, M. J. V. da Silva, A. P. Jacomini, S. Moura, D. F. Back, E. A. Basso, F. A. Rosa, *RSC Adv.* **2018**, *8*, 4773-4778; c) S. Thakur, A. Das, T. Das, *New J. Chem.* **2021**, *45*, 11420-11456.

[28] D. A. Bilodeau, K. D. Margison, M. Serhan, J. P. Pezacki, *Chem. Rev.* **2021**, *121*, 6699-6717.

[29] N. Naik, R. Braslau, *Tetrahedron* **1998**, *54*, 667-696.

[30] I. Varela-Nieto, S. Murillo-Cuesta, L. Rodríguez-de la Rosa, M. J. Oset-Gasque, J. Marco-Contelles, *Front. Cell. Neurosci.* **2021**, *15*.

[31] a) P. Merino, T. Tejero, in *Molecules, Vol. 4*, **1999**, pp. 169-179; b) P. Merino, *C. R. Chim.* **2005**, *8*, 775-788; c) E. Lieou Kui, A. Kanazawa, J.-F. Poisson, S. Py, *Tetrahedron Lett.* **2013**, *54*, 5103-5105.

[32] a) R. J. Nash, E. Arthur Bell, J. Michael Williams, *Phytochem.* **1985**, *24*, 1620-1622; b) Y.-X. Li, R. Iwaki, A. Kato, Y.-M. Jia, G. W. J. Fleet, X. Zhao, M. Xiao, C.-Y. Yu, *Eur. J. Org. Chem.* **2016**, *2016*, 1429-1438; c) V. Pingitore, M. Martínez-Bailén, A. T. Carmona, Z. Mészáros, N. Kulik, K. Slámová, V. Křen, P. Bojarová, I. Robina, A. J. Moreno-Vargas, *Bioorg. Chem.* **2022**, *120*, 105650; d) J.-Z. Wang, B. Cheng, A. Kato, M. Kise, Y. Shimadate, Y.-M. Jia, Y.-X. Li, G. W. J. Fleet, C.-Y. Yu, *Eur. J. Med. Chem* **2022**, *233*, 114230.

[33] a) S. Cicchi, A. Goti, A. Brandi, *J. Org. Chem.* **1995**, *60*, 4743-4748; b) A. Goti, S. Cicchi, V. Fedi, L. Nannelli, A. Brandi, *J. Org. Chem.* **1997**, *62*, 3119-3125; c) S. Cicchi, M. Corsi, A. Goti, *J. Org. Chem.* **1999**, *64*, 7243-7245; d) S. Cicchi, M. Marradi, A. Goti, A. Brandi, *Tetrahedron Lett.* **2001**, *42*, 6503-6505.

[34] C. J. W. Gutch, W. A. Waters, *J. Chem. Soc. (Resumed)* **1965**, 751-755.

[35] a) J. Lind, G. Merényi, *J. Phys. Chem. A* **2006**, *110*, 192-197; b) J. Duan, S.-y. Pang, Z. Wang, Y. Zhou, Y. Gao, J. Li, Q. Guo, J. Jiang, *Chemosphere* **2021**, *262*, 128390; c) K. B. G. Torssell, *Nitrile Oxides, Nitrones, and Nitronates in Organic Synthesis*, John Wiley and sons, New York, **1988**.

[36] S. A. Ali, M. I. M. Wazeer, *Tetrahedron Lett.* **1992**, *33*, 3219-3222.

[37] J. Duan, S. Y. Pang, Z. Wang, Y. Zhou, Y. Gao, J. Li, Q. Guo, J. Jiang, *Chemosphere* **2021**, *262*, 128390.

[38] a) D. Tang, L. Zhu, S. Qin, Z. Su, C. Hu, *J. Mol. Struct.* **2007**, *805*, 143-152; b) P. Chandra Mandal, M. Chakraborty, S. Das, C. Estarellas, D. Quiñonero, A. Frontera, S. Mukhopadhyay, *Dalton Trans.* **2011**, *40*, 9571-9579.

[39] a) J. A. Ibers, B. R. Davids, *Inorg. Chem.* **1970**, *9*, 2768-2774; b) J. F. Wishart, A. Bino, H. Taube, *Inorg. Chem.* **1986**, *25*, 3318-3321.

CHAPTER V

KINETIC AND COMPUTATIONAL STUDY ABOUT THE MIGRATION MECHANISM OF PROTECTIVE GROUPS IN CARBOHYDRATES

5.1 Introduction

5.1.1 The role of acetyl groups beyond protecting agents

Acyl groups are well-known protecting groups that are usually used for the protection of hydroxyl and amino groups. The most commonly used among them are acetyl (Ac), benzoyl (Bz), and pivaloyl (Piv). In general, these protective groups are stable under acidic and oxidative conditions, and they can be removed under basic or reductive conditions (**Scheme 5.1**).

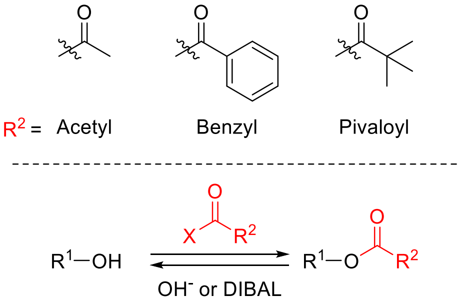

Scheme 5.1: *Most common acyl groups in synthetic chemistry.*

Acyl groups, particularly acetyl groups, are also commonly found in nature, where they can be found as backbones or side chains of many polysaccharides in plant cells, such as mannans, [1] arabinoxylans, [2] or xyloglucans. [3] The degree of acetylation can alter their properties, conformation, or hydrophobicity, depending on the location of these molecules inside the plant. [4] This acetylation process is controlled by the plant itself, indicating that these acetyl groups may play an important but less investigated biological function. [5] For example, the most common hemicellulose in spruce (*picea abies*), galactoglucomannan, [6] exists in both non-acetylated and partially acetylated forms, each displaying different biological applications. [7]

Furthermore, acetyl groups can participate in the activation and deactivation of other biologically active compounds [8] and are involved in many metabolic reactions, such as enzymatic acyl cleavage or acyl transfer processes. [9]

Finally, as mentioned before, the degree of acetylation can alter the properties of a given molecule. This can be applied to increase the lipid solubility of some drugs, thereby increasing their permeability across the blood-brain barrier, [10] such as the faster brain uptake of heroin compared to morphine.

5.1.2 Migration of acetyl groups

In spite of their utility as protecting groups, when the acyl groups are in close proximity to free hydroxyl, thiol, or amine groups, migration of these protective groups might occur. [11]

This well-known phenomenon not only affects the synthesis and purification of many organic molecules that contain multiple hydroxyl groups, such as carbohydrates, [12] but it could also be involved in various biological activation and deactivation processes, such as molecular recognition or other biosignaling processes occurring in many plants. [8]

Acyl group migration was first reported by Fischer in 1920 [13] and is now a well-known phenomenon that can cause difficulties during the synthesis, purification, and isolation of many organic compounds. As mentioned earlier, these problems are common in carbohydrate chemistry, where acyl groups are commonly used as protective agents for their multiple hydroxyl groups. In monosaccharides, unsuccessful attempts to migrate acetyl groups between two non-consecutive hydroxyls have demonstrated that acyl groups tend to migrate only to their neighboring hydroxyl groups (**Scheme 5.2**). [14]

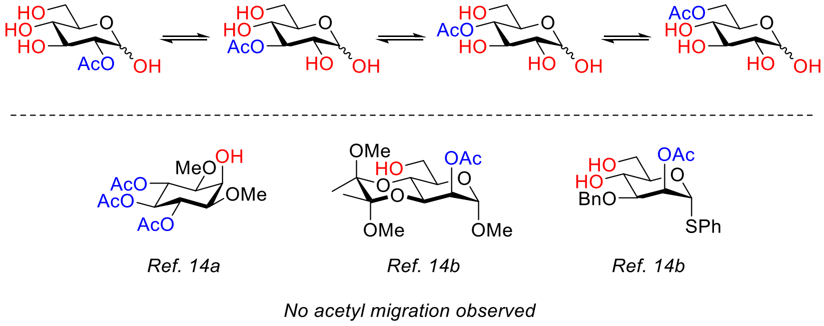

***Scheme 5.2:** (**Top**) Acetyl migration on carbohidrates. (**Bottom**) Examples where the acetyl migration is blocked due to the absence of hydroxyl groups near the acetyl.*

Based on all this experimental evidence, several mechanisms have been suggested, [15] with the most of them assuming the formation of an orthoester as the intermediate and the influence of the pH on acyl migration.

Thanks to the collective work, a widely accepted mechanism for acyl migration was established when Oesterling and Metzler consolidated all the pieces and proposed that the migration begins with the catalytic deprotonation of the hydroxyl group, followed by the formation of an orthoester as the intermediate (**Scheme 5.3**). [15a] This proposal was strongly supported by the isolation of the intermediate. [15c] The breakage of the orthoester from the original C-O bond releases the acetyl group to the new position, while the newly formed alkoxide is protonated, regenerating the base. Since the deprotonation of the neighboring hydroxyl groups of the acetyl serves as starting point, the pH of the medium significantly affects the rate. This can be observed in various experiments, where the migration rate exponentially increases with the pH of the buffer. [16]

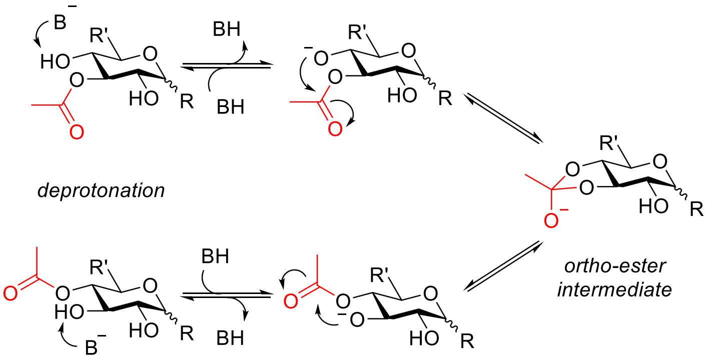

Scheme 5.3: *Base-catalysed mechanism for the acetyl migration in carbohydrates.*

Furthermore, the rate of migration in carbohydrates is influenced by factors beyond the pH, including the stereochemistry of the cycle and the electronic and steric properties of both the acyl and alkoxide groups. It has been demonstrated that acyl groups are more stable over primary hydroxyl groups, [17] mainly due to the steric hindrance reduction and their increased flexibility compared to secondary alcohols. As a result, the migration process typically proceeds in a clockwise direction from O2, the common starting point, to O6, as illustrated in **Scheme 5.2**. However, when the acyl group needs to reside on a secondary alcohol, equatorial positions are usually preferred, although this preference heavily depends on the conditions. [14a]

As mentioned earlier, the stereochemistry of the ring also affects the rate of migration. This effect becomes more evident when comparing *cis* and *trans* relationships. It has been demonstrated that, due to the lower ring strain in the five-membered TS, migration between secondary alcohols occurs faster when they share a *cis* relationship compared to a *trans* relationship. [17d, 18]

Finally, the substitution on the α-carbon of the acyl group also plays a significant role in the rate of migration. As the substitution on that carbon increases, steric hindrance prevents the approximation of both groups. This is consistent with the observation that bulkier protective groups, such as pivaloyl, exhibit a slower rate of migration. [17d]

The discussion thus far has primarily focused on pyranoses, as there have been limited studies on migration in furanoses [19] and oligo- and polysaccharides. A recent publication by Prof. R. Leino and co-workers has demonstrated, for the first time, that acyl groups can migrate not only between neighboring positions but also between different monosaccharide units in an oligosaccharide. [20] As is depicted in **Scheme 5.4**, the migration occurred between the O2' position of the second monosaccharide and the O6' position of the first one. KIE studies comparing the migration rate in deuterated and non-deuterated solvent suggest that the deprotonation of the first hydroxyl group is likely the rate-limiting-step of the reaction.

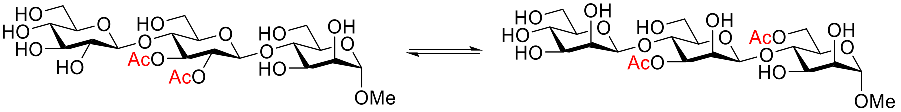

Scheme 5.4: *Acetyl migration in trisaccharides.*

Several computational studies were conducted on acyl migrations. In 1996, Nicholson and co-workers [21] performed computational studies on intramolecular acyl migration at semiempirical level, providing support for the existence of the orthoester intermediate, although no TSs were determined. In 2007, Gritsan and co-workers published another theoretical study on acetyl migration, [22] but in this case, the migration involved carbonyl groups rather than hydroxyl groups. Two years later, Stachulski and co-workers [23] considered a fully deprotonated anion as the starting point for their calculations and determined only the first TSs of the migration processes leading to the orthoester intermediate. However, using a naked anion as the starting point may be the cause of the lower barriers obtained compared to the experimental values. Furthermore, the absence of IRC studies on those TSs makes the connection between the acylated compound and the orthoester unclear. In a more recent publication, the same authors reported similar results for the intramolecular transacylation of acyl glucosides, once again calculating only the first TSs before the formation of the orthoester, assuming that it corresponds to the RDS for the reaction, in agreement with their kinetic experiments. [24]

Finally, Petkov and co-workers [25] provided further support for the stepwise mechanism and the formation of the orthoester as the intermediate. They also suggested the catalytic nature of the base, where once the alcohol is deprotonated, the migration occurs spontaneously. However, when calculating kinetic constants, it is important to note that while deprotonation is required for the reaction, considering a fully anionic mechanism is only valid if the species are fully deprotonated, which is not the case at the reaction pH. To obtain accurate estimations, the actual concentration of the anion needs to be considered, which is dependent on the pK_a of the corresponding hydroxyl group and the pH of the medium.

Regarding the migration in oligosaccharides illustrated in **Scheme 5.4**, Prof. Leino and co-workers [20] optimized only one of the multiple conformers of the O2’-O6’ acetyl migration TS, primarily due to the significant conformational variability present in trisaccharides. This particular TS demonstrated that the molecular flexibility of trisaccharides allows for the O6’ position of the first monosaccharide and the O2’ position of the second monosaccharide to approach closely enough for the acyl transfer to occur. However, this model once again employed the naked anion approximation and did not identify the orthoester as an intermediate.

Due to the lack of consistent conditions among early studies and the omission of certain stationary points in computational calculations, the reversibility of the process and other factors such as reaction conditions or solvent modeling have not been thoroughly explored. Therefore, a more comprehensive investigation of the acyl migration process in mono- and oligosaccharides is warranted.

The objective of this chapter is to conduct a comprehensive analysis of acyl migration in both mono- and trisaccharides. An extensive NMR kinetic study has been performed, and the results will be compared with computational findings obtained from the development of a kinetic model. The objective of the model is to accurately represent the multiple equilibria involved in acetyl migration in carbohydrates and provide the most precise kinetic constants. To conduct this study and obtain minimally accurate kinetic constants, it is necessary to address the significant conformational variability of the studied mono- and trisaccharides. Since the experimental determination of the corresponding constants usually involves more than one elemental step, a kinetic mathematical treatment of the reaction case must be done.

5.2 Results and discussion

5.2.1 Experimental kinetic studies of acetyl migration in monosaccharides

This work was carried out in collaboration with the group of Prof. R. Leino (Åbo Academy University, Finland). The finnish group conducted a kinetic migration analysis on several monosaccharides and acyl groups, namely Ac, Bz, Piv, (*R*)-, and (*S*)-2-Ph-propanoyl. The starting compounds for the acyl migration are illustrated in **Scheme 5.5**. The discussion and calculations will focus solely on the acetyl (Ac) migration of glucosides, (**R5.1** and **R5.6**, respectively), galactosides (**R5.11** and **R5.16**) and xylosides (**R5.26** and **R5.31**), attending their respective anomeric orientation. Full kinetic data, along the experimental procedures and NMR characterization is available in the original publication. [26]

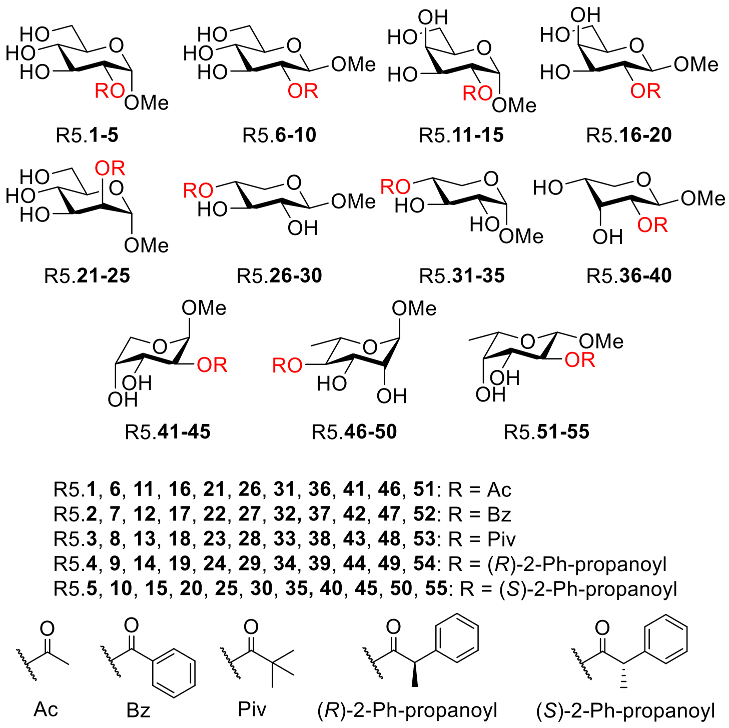
R5.**1-5**
R5.**6-10**
R5.**11-15**
R5.**16-20**
R5.**21-25**
R5.**26-30**
R5.**31-35**
R5.**36-40**
R5.**41-45**
R5.**46-50**
R5.**51-55**
Ac
Bz
Piv
(*R*)-2-Ph-propanoyl
(*S*)-2-Ph-propanoyl

R5.**1**, **6**, **11**, **16**, **21**, **26**, **31**, **36**, **41**, **46**, **51**: R = Ac
R5.**2**, **7**, **12**, **17**, **22**, **27**, **32**, **37**, **42**, **47**, **52**: R = Bz
R5.**3**, **8**, **13**, **18**, **23**, **28**, **33**, **38**, **43**, **48**, **53**: R = Piv
R5.**4**, **9**, **14**, **19**, **24**, **29**, **34**, **39**, **44**, **49**, **54**: R = (*R*)-2-Ph-propanoyl
R5.**5**, **10**, **15**, **20**, **25**, **30**, **35**, **40**, **45**, **50**, **55**: R = (*S*)-2-Ph-propanoyl

Scheme 5.5: *Starting compounds for the investigation of acyl group migration.*

In all the cases studied, the initial position of the acetyl group is determined based on the simplest method for protecting the carbohydrate starting material. For glucosides and galactosides, the initial position is O2’, while for xylosides is O4’. During the kinetic measurements, a certain degree of hydrolysis was detected and measured following **Scheme 5.6**. Procedure A was applied to glucosides and galactosides, while procedure B was used for xylosides.

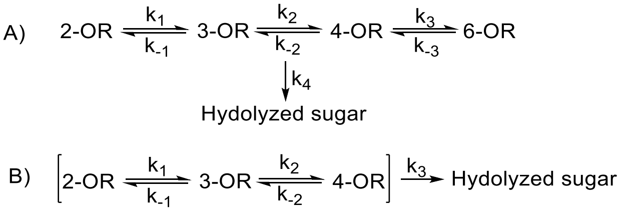
A)
2-OR
k1
k-1
3-OR
k2
k-2
4-OR
k3
k-3
6-OR
k4
Hydolyzed sugar
B)
2-OR
k1
k-1
3-OR
k2
k-2
4-OR
k3
Hydolyzed sugar

Scheme 5.6: *Reaction schemes used for calculating the kinetic constants.*

Experimental results on acyl migration over selected carbohydrates are presented in **Table 5.1**. A surprising finding from the data analysis is that the rate of migration for the axial anomeric OMe group is significantly slower (22-58%) compared to the equatorial position. This difference is displayed in **Figure 5.1**. However, the disparity is much smaller when the two groups share a *cis* relationship. This can be observed by comparing the difference in migration between α- and β-galactose for the first step (from O2' to O3') with the second step (from O3' to O4').

Table 5.1: *Rate constants for migration of the acetyl group in Me α- and β-D-glucopyranosides, Me α- and β-D-galactopyranosides according to path A displayed in* ***Scheme 5.6*** *and in Me α- and β-D-xylopyranosides according to path B from the same scheme.* [a]

R5.1 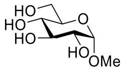 Me α-D-Glc	k_1 (s^{-1})	6.28E-05 ± 1.98E-06	**R5.6** 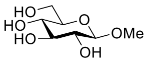 Me β-D-Glc	k_1 (s^{-1})	2.02E-04 ± 4.92E-06
	k_{-1} (s^{-1})	5.11E-05 ± 3.94E-06		k_{-1} (s^{-1})	1.11E-04 ± 6.28E-06
	k_2 (s^{-1})	5.06E-05 ± 3.42E-06		k_2 (s^{-1})	1.15E-04 ± 4.69E-06
	k_{-2} (s^{-1})	1.01E-04 ± 3.03E-05		k_{-2} (s^{-1})	1.28E-04 ± 3.22E-05
	k_3 (s^{-1})	1.21E-03 ± 6.11E-04		k_3 (s^{-1})	1.10E-03 ± 1.24E-04
	k_{-3} (s^{-1})	7.83E-05 ± 4.97E-05		k_{-3} (s^{-1})	4.56E-05 ± 9.72E-06
	k_4 (s^{-1})	8.81E-07 ± 7.50E-08		k_4 (s^{-1})	7.39E-07 ± 1.01E-07
R5.11 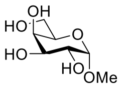 Me α-D-Gal	k_1 (s^{-1})	3.31E-05 ± 6.50E-07	**R5.16** 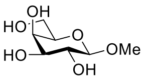 Me β -D-Gal	k_1 (s^{-1})	1.47E-04 ± 3.83E-06
	k_{-1} (s^{-1})	2.65E-05 ± 2.49E-06		k_{-1} (s^{-1})	6.08E-05 ± 4.56E-06
	k_2 (s^{-1})	2.43E-04 ± 2.77E-05		k_2 (s^{-1})	2.43E-04 ± 9.17E-06
	k_{-2} (s^{-1})	2.43E-04 ± 4.00E-05		k_{-2} (s^{-1})	1.72E-04 ± 1.13E-05
	k_3 (s^{-1})	2.83E-04 ± 2.83E-05		k_3 (s^{-1})	2.10E-04 ± 6.06E-06
	k_{-3} (s^{-1})	5.47E-05 ± 7.28E-06		k_{-3} (s^{-1})	5.72E-05 ± 2.60E-06
	k_4 (s^{-1})	2.06E-06 ± 1.26E-07		k_4 (s^{-1})	3.78E-06 ± 3.69E-07
R5.31 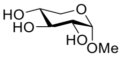 Me α-D-Xyl	k_1 (s^{-1})	5.86E-05 ± 6.94E-06	**R5.26** 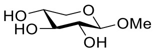 Me β -D-Xyl	k_1 (s^{-1})	1.65E-04 ± 8.78E-05
	k_{-1} (s^{-1})	4.25E-05 ± 4.00E-06		k_{-1} (s^{-1})	7.33E-05 ± 3.39E-05
	k_2 (s^{-1})	2.03E-05 ± 8.17E-07		k_2 (s^{-1})	9.11E-05 ± 8.61E-06
	k_{-2} (s^{-1})	2.34E-05 ± 3.75E-07		k_{-2} (s^{-1})	7.81E-05 ± 4.75E-06
	k_3 (s^{-1})	6.03E-07 ± 4.03E-08		k_3 (s^{-1})	1.63E-06 ± 2.94E-07

[a] *Conditions: 100 mM phosphate buffer with 10% D_2O, pH 8, 25 °C.*

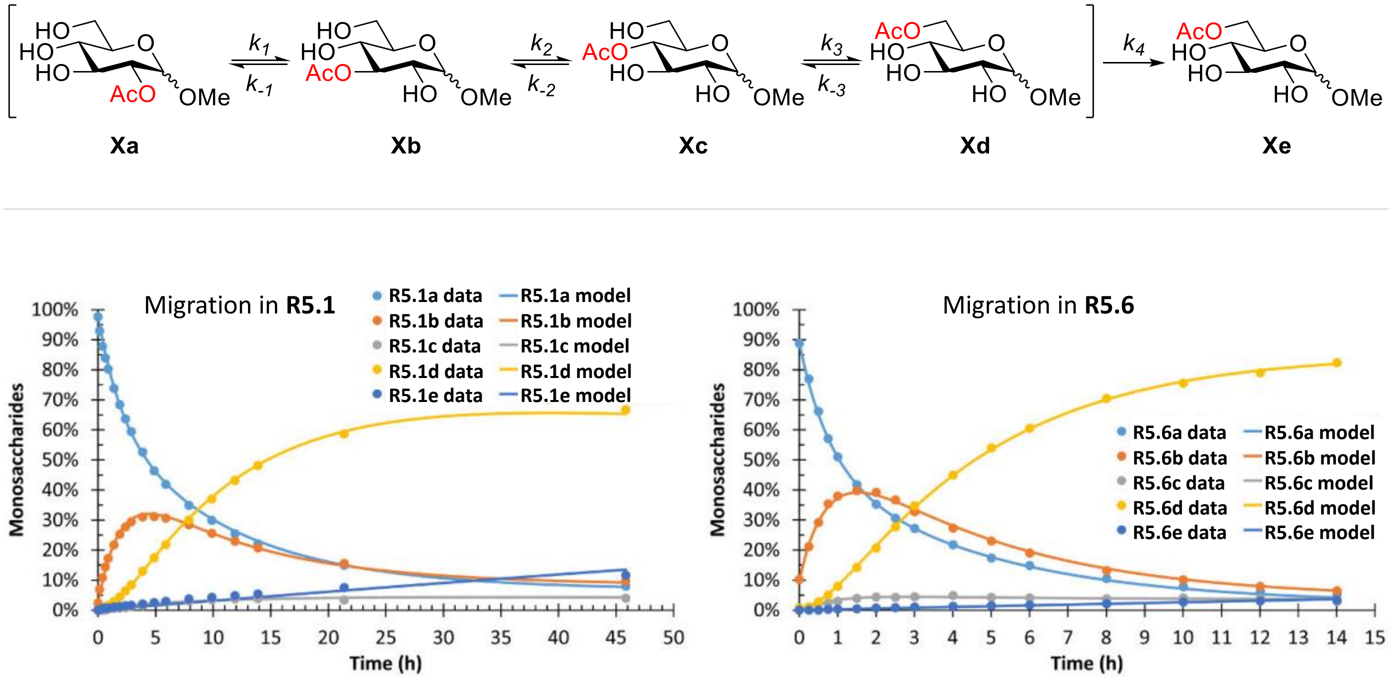

Figure 5.1: *Acetyl group migration in Me α- and β-D-glucopyranoside displaying the experimental data and the kinetic model made for comparison. Conditions: 100 mM phosphate buffer with 10%* D_2O*, pH 8, 25 °C.*

The reason for this could involve the anomeric effect. When O1 adopts an axial position, the bond between C1 and the ring oxygen becomes shorter, [27] introducing additional strain in the ring. This strain could increase the distance between the reacting groups, thus raising the energy barrier for the formation of the TS. However, this effect should be weaker when both groups share a *cis* disposition, as they are closer in space compared to the *trans* configuration, and the difference in strain between α- and β-isomers is not as noticeable.

It was also observed that similar types of migration exhibited similar rate constants. For example, when comparing the migration from O2' to O3' among the three carbohydrates with the same anomeric disposition, the rate constants showed similar values.

The easier migration between *cis*-disposed groups compared to *trans* can be noticed by comparing the migration from O3' to O4' in galactosides with the other two carbohydrates, which is likely due to the reduction of the strain in the TS.

5.2.2 Kinetic insights derived from the mechanism on the acetyl migration in monosaccharides

The first step in developing a kinetic model for a given reaction is to determine the actual mechanism and all the elementary steps involved in the process. To accomplish this, the O2'-O3' acetyl migration of Me α-D-glucopyranoside **R5.1** was used as a model, assuming that migrations to other positions and in other carbohydrates would proceed in a similar manner.

As mentioned earlier, computational studies involving carbohydrates are challenging due to the multitude of conformations that can be adopted within a narrow range of energy. Consequently, the study began with a conformational analysis of the given molecules to identify the true minimum energy configuration. This analysis was performed using the Macromodel software from the Schrödinger package. The results for the 2'-and 3'-acetyl are displayed in **Figure 5.2**.

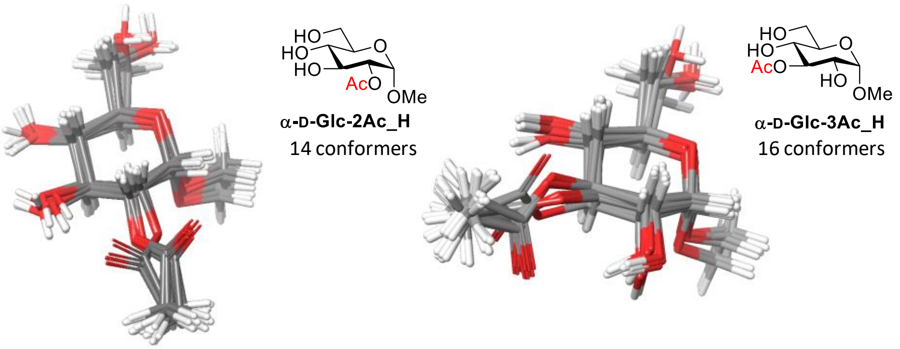

α-D-Glc-2Ac_H
14 conformers

α-D-Glc-3Ac_H
16 conformers

Figure 5.2: *Conformational search for the 2’- and 3’- acetylated derivatives of Me α-D-glucopyranosides.*

Once the minimal energy conformations for each isomer were obtained, transition structures were determined through relaxed scans starting from those structures. Two different TS, **α-D-Glc-TS1a_n_Si** and **α-D-Glc-TS1a_n_Re**, were obtained, corresponding to the attack from each face (Re/Si) of the acetyl group. IRC calculations from these TSs unequivocally connected the acetylated monosaccharides with the orthoester intermediates, confirming the findings of Petrov and co-workers. [25] Two additional transition structures, **α-D-Glc-TS1b_n_Si** and **α-D-Glc-TS1b_n_Re**, separated both intermediates from the 3’-acetyl glucoside (**Scheme 5.7**). The preferred pathway was selected based on the lower energy barriers for the overall process.

This procedure will be applied in further optimizations of both, energy minima and TSs.

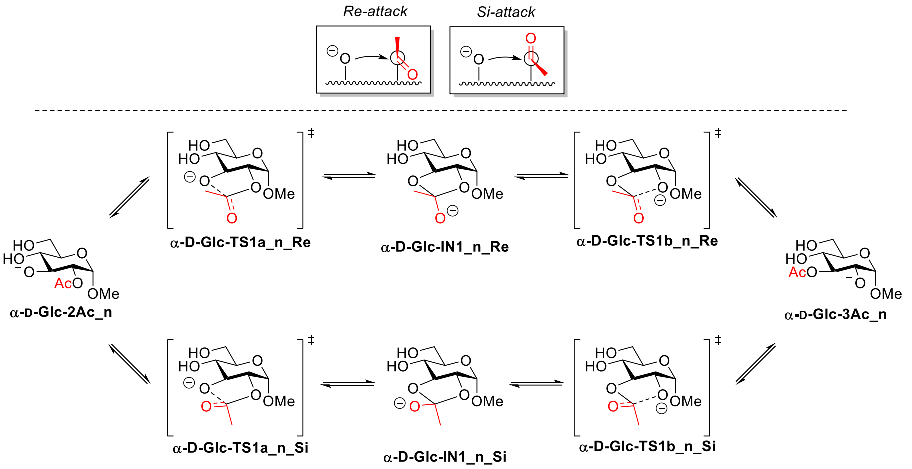
Re-attack
Si-attack
α-D-Glc-2Ac_n
α-D-Glc-TS1a_n_Re
α-D-Glc-IN1_n_Re
α-D-Glc-TS1b_n_Re
α-D-Glc-3Ac_n
α-D-Glc-TS1a_n_Si
α-D-Glc-IN1_n_Si
α-D-Glc-TS1b_n_Si

Scheme 5.7: *Mechanism of anionic acetyl migration through the nucleophilic attack to both faces of the acetyl group.*

Due to the presence of an orthoester intermediate between 2-acetyl and 3-acetyl glucoside (**Figure 5.3**), the calculation of the kinetic constants for the whole process must be calculated following **Eq. 1** and **Eq.2**.

$$k_j = \frac{k_i^a \cdot k_i^b}{k_i^{-a} + k_i^b} \qquad \text{(Eq. 1)}$$

$$k_{-j} = \frac{k_i^{-a} \cdot k_i^{-b}}{k_i^{-a} + k_i^b} \qquad \text{(Eq. 2)}$$

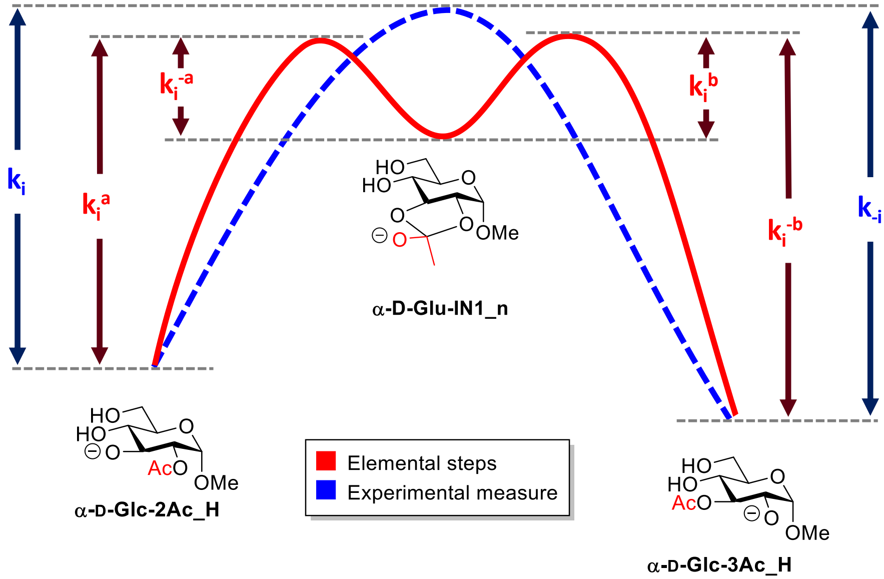
k_i
k_i^a
k_i^{-a}
k_i^b
k_i^{-b}
k_{-i}
α-D-Glu-IN1_n
α-D-Glc-2Ac_H
α-D-Glc-3Ac_H
Elemental steps
Experimental measure

Figure 5.3: *Energetic profile of the migration in Me α-D-glucopyranoside along with the definition of experimental and theoretical kinetic constants for the overall process. Examples are defined for i = 2, corresponding to the O2-O3 migration in Me α-D-glucopyranoside.*

5.2.3 Evaluation of the protonation state and solvent model for the acetyl migration with glucopyranosides as study case

In this section, experimental energy barriers will be compared using different solvation models to determine the optimal conditions for calculating migration rate constants. The conversion between energy barriers and kinetic constants can be achieved using the Eyring equation (**Eq.3**).

$$k_T = \frac{k_B T}{h\, c^0} e^{\frac{-\Delta G^0}{RT}} \qquad \text{(Eq. 3)}$$

By applying **Eq.3**, the experimental energy barriers for the first equilibrium of acetyl migration in Me α-D-glucopyranoside at pH 8 are determined to be 22.2 Kcal/mol for the direct process and 22.3 Kcal/mol for the inverse process. These values will serve as references for studying various solvation models.

Since most of the carbohydrate is in a neutral form at pH 8, the first model studied is the migration through a neutral mechanism. The direct transfer of the hydrogen from the hydroxyl to the carbonyl oxygen involves a highly strained 4-membered cycle TS. To alleviate this strain, extrinsic water molecules were introduced. In path A1 of **Scheme 5.8**, a water molecule bridge was constructed, forming hydrogen bonds between the hydroxyl and the carbonyl oxygen. By applying **Eq.3** to the energy barriers obtained and merging those two step constants into one using **Eq.1** and **Eq.2**, rate constants around 10^{-8} were obtained, which are 3 orders of magnitude lower than the experimental constants. Transforming those rate constants back into energy barriers using **Eq.3**, the corresponding barriers of 27.7 Kcal/mol and 28.3 Kcal/mol were obtained for the direct and reverse acetyl transfers from O2 to O3, respectively.

In an attempt to improve those results, another water molecule was introduced to the bridge, providing more flexibility to the system (path A2). However, the obtained barriers were similar (of 29.0 Kcal/mol for the O2-O3 migration, and 28.8 Kcal/mol for the reverse process). For this reason, path A2 was discarded, and path A1 was considered as the preferred acyl migration mechanism under neutral conditions.

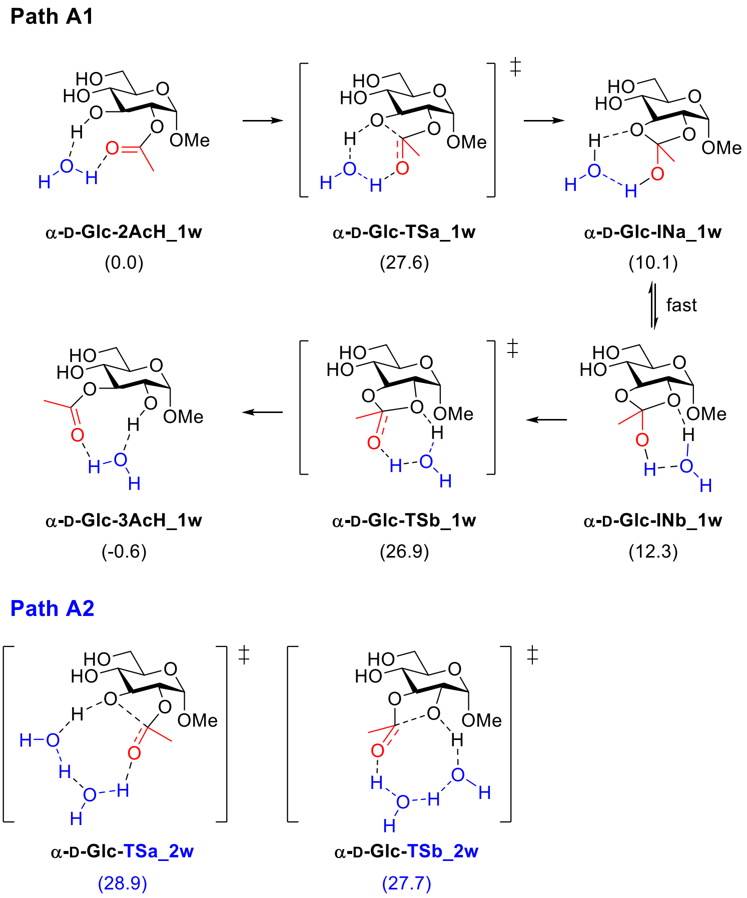
Path A1
α-D-Glc-2AcH_1w
(0.0)
α-D-Glc-TSa_1w
(27.6)
α-D-Glc-INa_1w
(10.1)
fast
α-D-Glc-3AcH_1w
(-0.6)
α-D-Glc-TSb_1w
(26.9)
α-D-Glc-INb_1w
(12.3)
Path A2
α-D-Glc-TSa_2w
(28.9)
α-D-Glc-TSb_2w
(27.7)
HO
OMe
‡

Scheme 5.8: *Neutral mechanisms through water-bridged transition structures for O2-O3 migration in Me α-D-glucopyranoside. Relative energies calculated at TPSSH/g3d3bj//def2tzvp(d)/cpcm= H_2O // TPSSH/g3d3bj/def2svp(d)/cpcm= H_2O are given in kcal/mol.*

Since the neutral barriers were too high in energy, the anionic mechanism was then explored. The possibility of an initial deprotonation as the starting point has been suggested many times. [15a, 23, 25] However, lower energy barriers than expected were obtained in all the cases involving a naked anion. Considering that the reaction takes place in water, it was recognized that a naked anion in a polar continuum medium might not precisely represent the real situation. To account for this, discrete water molecules surrounding the alkoxide anion were introduced. In fact, the importance of microsolvation in the accurate localization of TS has been recently demonstrated. [28]

For the purpose of comparison, a variable number of water molecules (from 0 to 6) was studied. To ensure an accurate analysis, the discussions will be based on the structures with the minimum energy. The general mechanism and energy values are illustrated on **Scheme 5.9**.

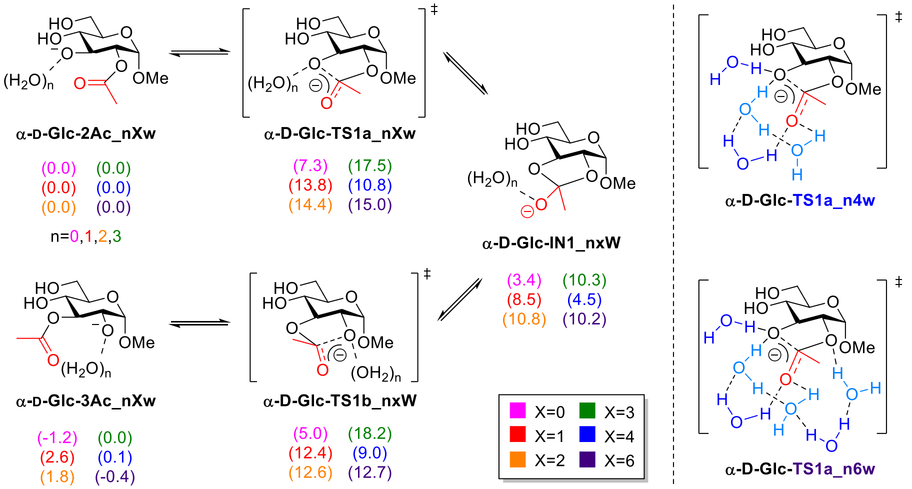
α-D-Glc-2Ac_nXw
(0.0) (0.0)
(0.0) (0.0)
(0.0) (0.0)
n=0,1,2,3
α-D-Glc-TS1a_nXw
(7.3) (17.5)
(13.8) (10.8)
(14.4) (15.0)
α-D-Glc-IN1_nxW
(3.4) (10.3)
(8.5) (4.5)
(10.8) (10.2)
α-D-Glc-3Ac_nXw
(-1.2) (0.0)
(2.6) (0.1)
(1.8) (-0.4)
α-D-Glc-TS1b_nxW
(5.0) (18.2)
(12.4) (9.0)
(12.6) (12.7)
🟪 X=0 🟩 X=3
🟥 X=1 🟦 X=4
🟧 X=2 🟪 X=6
α-D-Glc-TS1a_n4w
α-D-Glc-TS1a_n6w
HO
OMe
(H₂O)n
(OH₂)n
‡

***Scheme 5.9**: (**Left**) Anionic models incorporating from n= 0 - 3 explicit water molecules. Relative energies (wb97xd/6-311++G(d,p)/SMD=H_2O //wb97xd/6-31+G(d,p)/SMD=H_2O) in Kcal/mol are provided from X = 0 - 6 explicit water molecules. (**Right**) Models for TS1a incorporating 4 and 6 explicit water molecules.*

By utilizing **Eq.1** and **Eq.2** with the energy barriers depicted in **Scheme 5.9**, the overall barrier for the process can be determined. Trough the Eyring equation (**Eq. 3**), the theoretical kinetic constants can be calculated. The results are presented in **Table 5.2**.

***Table 5.2:** Comparison between calculated and experimental energy barriers and kinetic constants for the O2-O3 acetyl migration in Me α-D-glucopyranoside under the anionic mechanism with different number of explicit water molecules (X).*

	EXP.	X=0	X=1	X=2	X=3	X=4	X=6
ΔG_1 (Kcal/mol) [a]	22.2	7.3	13.8	14.4	18.3	10.9	15.0
ΔG_{-1} (Kcal/mol) [a]	22.3	8.5	11.2	12.6	18.5	10.8	15.4
k_1 (s^{-1})	6.28E-05	2.73E+07	4.50E+02	1.72E+02	2.18E-01	6.80E+04	6.59E+01
k_{-1} (s^{-1})	5.11E-05	3.39E+06	3.88E+04	3.48E+03	2.29E-01	8.11E+04	3.16E+01

[a] *Level of theory: wb97xd/6-311++G(d,p)/smd=H_2O//wb97xd/6-31+G(d,p)/smd= H_2O.*

As was mentioned previously, the naked anion model (X=0) is not suitable for describing the migration process, as evidenced by the lowest energy barriers and significant discrepancy of at least 11 orders of magnitude between experimental and theoretical kinetic constants. The inclusion of one and two water molecules in the system (X=1, 2) slightly improved the results by reducing the nucleophilicity of the alkoxide. Since the anion is better stabilized with two water molecules compared to one, the energy barrier increased further with the addition of the second water molecule.

The anionic model that best fitted the experimental results was the system with three water molecules (X=3). In this model, three water molecules were included, arranged in a tetrahedral orientation surrounding the alkoxide. A significant increase in the energy barrier is observed when comparing these results with the previous two models. The increase is not only due to the reduction in nucleophilicity of the anion but also because of the saturation of the alkoxide's lone pair electrons. In this case, since there are no available electrons for nucleophilic attack, one of the water molecules must be expelled, leading to the breaking of a hydrogen bond. This disruption of the hydrogen bond is responsible for the substantial increase in the energy barrier.

The inclusion of water molecules around the acetyl’s carbonyl did not significatively increase the barrier, and models with even more water molecules (X=4, 6) resulted in the inability to locate a transition state with three water molecules around the alkoxide. Instead, structures similar to those depicted in **Scheme 5.9** were obtained in all cases. Without the breaking of the hydrogen bond in the TS, lower barriers were once again observed.

The improvement in results with the inclusion of three water molecules was not entirely unexpected, as it has been reported that the optimization in the presence of three explicit water molecules is necessary for accurately calculating thiols’s pK_a. [29]

As shown in **Figure 5.4**, neither neutral or anionic mechanisms are close enough to the experimental barriers to be considered a suitable model. This is because both mechanisms are related through an acid-base equilibrium and take place simultaneously. The acid-base equilibrium must be considered not only to obtain accurate kinetic constants but also to model the well-known pH dependence of the migration.

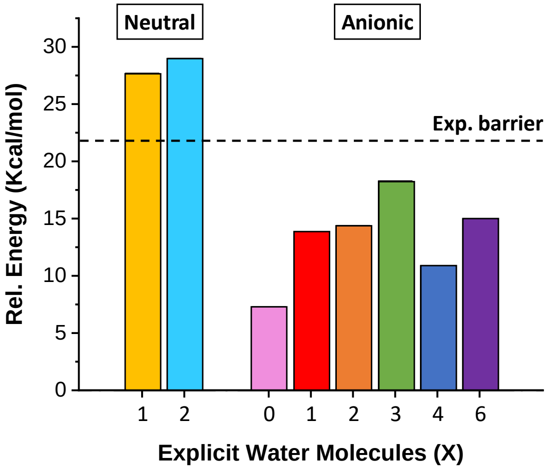

Figure 5.4: *Comparison between both neutral and anionic relative energies of the first acetyl migration (bars) compared to the experimentally obtained barrier (dotted line).*

5.2.4 Modeling the pH dependence of acetyl migration: the definitive model

The selection of both anionic and neutral mechanisms for the creation of the complete model was based on the better representation of each system in the aqueous environment. Therefore, path A1 from ***Scheme 5.8*** *(involving a one-water molecule bridge) and the X=3 model from* ***Scheme 5.9*** *(involving an anion surrounded by 3 water molecules) were merged in the complete model depicted in*

Scheme 5.10.

In this scheme, the first acetyl migration is depicted in detail, including the orthoester intermediate between both acetyl positions, while the other steps in further acetyl migrations are omitted for clarity. The blue constants k_n^{obs} and k_{-n}^{obs} (n=1-3) represent the experimental direct and reverse acetyl migration constants measured by NMR. Both mechanisms are related

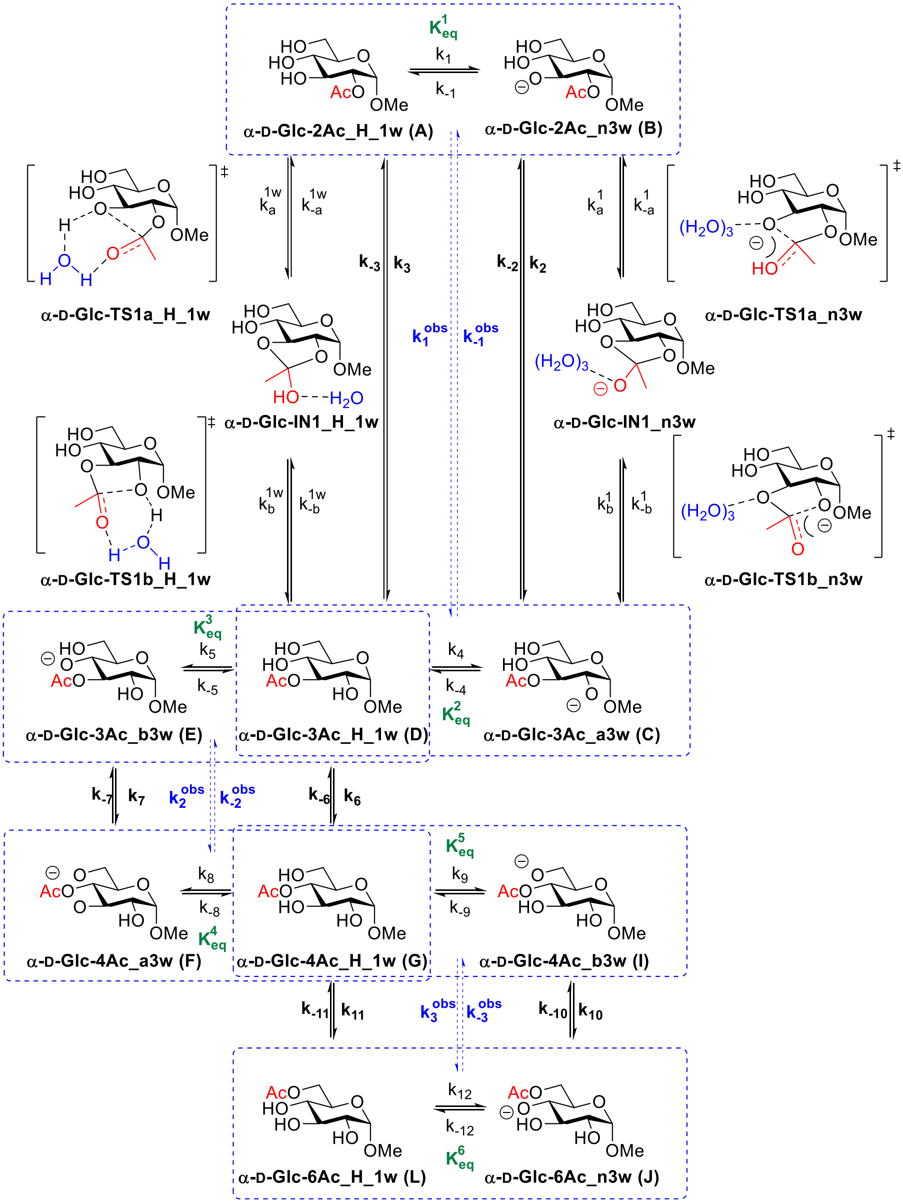
α-D-Glc-2Ac_H_1w (A)
α-D-Glc-2Ac_n3w (B)
α-D-Glc-TS1a_H_1w
α-D-Glc-IN1_H_1w
α-D-Glc-TS1b_H_1w
α-D-Glc-TS1a_n3w
α-D-Glc-IN1_n3w
α-D-Glc-TS1b_n3w
α-D-Glc-3Ac_b3w (E)
α-D-Glc-3Ac_H_1w (D)
α-D-Glc-3Ac_a3w (C)
α-D-Glc-4Ac_a3w (F)
α-D-Glc-4Ac_H_1w (G)
α-D-Glc-4Ac_b3w (I)
α-D-Glc-6Ac_H_1w (L)
α-D-Glc-6Ac_n3w (J)
K_{eq}^{1}
k_1
k_{-1}
k_a^{1w}
k_{-a}^{1w}
k_b^{1w}
k_{-b}^{1w}
k_a^{1}
k_{-a}^{1}
k_b^{1}
k_{-b}^{1}
k_{-3} k_3
k_{-2} k_2
k_1^{obs} k_{-1}^{obs}
K_{eq}^{3} k_5 k_{-5}
k_4 k_{-4} K_{eq}^{2}
k_{-7} k_7
k_2^{obs} k_{-2}^{obs}
k_{-6} k_6
K_{eq}^{5} k_9 k_{-9}
k_8 k_{-8} K_{eq}^{4}
k_{-11} k_{11}
k_3^{obs} k_{-3}^{obs}
k_{-10} k_{10}
k_{12} k_{-12} K_{eq}^{6}

Scheme 5.10: *Acetyl group migration in Me α-D-glucopyranosides. The first acetyl migration is fully depicted while the others are shortened for clarity.*

through k_n and k_{-n} (n = 1, 4, 5, 8, 9, 12), whose quotient gives rise to the acid-base constants K_{eq}^{n} (n=1-6) (**Eq. 4-9**). These constants, along with the available concentration of each protonation state of the carbohydrate, modulate the rate of migration. The concentration of each species, in turn, depends on the pH of the media and the pK_a values of the hydroxyl groups involved.

$$K_{eq}^{1} = \frac{\mathrm{k}_1}{\mathrm{k}_{-1}} = \frac{[\mathrm{B}]\cdot[\mathrm{H}^+]}{[\mathrm{A}]} \qquad \text{(Eq. 4)}$$

$$K_{eq}^{2} = \frac{k_4}{k_{-4}} = \frac{[C][H^+]}{[D]} \qquad \text{(Eq. 5)}$$

$$K_{eq}^{3} = \frac{k_5}{k_{-5}} = \frac{[E]\cdot[H^+]}{[D]} \qquad \text{(Eq. 6)}$$

$$K_{eq}^{4} = \frac{k_8}{k_{-8}} = \frac{[F][H^+]}{[G]} \qquad \text{(Eq. 7)}$$

$$K_{eq}^{5} = \frac{k_9}{k_{-9}} = \frac{[I]\cdot[H^+]}{[G]} \qquad \text{(Eq. 8)}$$

$$K_{eq}^{6} = \frac{k_{12}}{k_{-12}} = \frac{[J][H^+]}{[L]} \qquad \text{(Eq. 9)}$$

It should be noted that a more complex equilibrium involving other deprotonated forms exists, but these species are not productive for the migration process. Therefore, only the deprotonation of the hydroxyl group attacking the carbonyl group was considered in the model. Additionally, the hydrolysis side reaction was not taken into account, assuming that it affects all acylated compounds to a similar extent and can be neglected for calculations at pH > 7. ***Eq. 10-19*** *represent the rate equations for compounds* ***A-L****. As mentioned earlier, an orthoester intermediate exist between each acetyl position, as shown in the first migration depicted in*

Scheme 5.10. Therefore, those constants are calculated trough the other four via **Eq.1** and **Eq.2**.

$$\frac{d[A]}{dt} = -(k_1 + k_3)[A] + k_{-1}[B][H^+] + k_{-3}[D] \qquad \text{(Eq. 10)}$$

$$\frac{d[B]}{dt} = k_1[A] - k_{-1}[B][H^+] - k_2[B] + k_{-2}[C] \qquad \text{(Eq. 11)}$$

$$\frac{d[C]}{dt} = k_2[B] - k_{-2}[C] - k_{-4}[C][H^+] + k_4[D] \qquad \text{(Eq. 12)}$$

$$\frac{d[D]}{dt} = = k_3[A] + k_{-4}[C][H^+] + k_{-6}[G] + k_{-5}[E][H^+] -$$

$$-(k_4 + k_{-3} + k_5 + k_6)[D] \qquad \text{(Eq. 13)}$$

$$\frac{d[E]}{dt} = k_5[D] - k_{-5}[E][H^+] - k_7[E] + k_{-7}[F] \qquad \text{(Eq. 14)}$$

$$\frac{d[F]}{dt} = k_7[E] - k_{-7}[F] - k_{-8}[F][H^+] + k_8[G] \qquad \text{(Eq. 15)}$$

$$\frac{d[G]}{dt} = k_6[D] + k_{-8}[F][H^+] + k_{-11}[L] + k_{-9}[I][H^+] -$$

$$-(k_8 + k_{-6} + k_9 + k_{11})[G] \qquad \text{(Eq. 16)}$$

$$\frac{d[I]}{dt} = k_9[G] - k_{-9}[I][H^+] - k_{10}[I] + k_{-10}[J] \qquad \text{(Eq. 17)}$$

$$\frac{d[J]}{dt} = k_{10}[I] - k_{-10}[J] - k_{-12}[J][H^+] + k_{12}[L] \qquad \text{(Eq. 18)}$$

$$\frac{d[L]}{dt} = k_{11}[G] + k_{-12}[J][H^+] - (k_{12} + k_{-11})[L] \qquad \text{(Eq. 19)}$$

For the resolution of this system, stationery transition state theory was applied. This theory states that the concentration of a reactive intermediate (in this case, the anionic species) remains approximately constant during the reaction. Therefore, **Eq. 11**, **12**, **14**, **15**, **17** and **18** are set to zero. By combining these equations with the acid base equilibrium **Eq. 4-9** the observed kinetic constants K_{n}^{obs} (**Eq. 20-25**) can be defined.

$$k_1^{obs} = -k_3 + \frac{k_2 \cdot K_{eq}^1}{[H]^+} \qquad \text{(Eq.20)}$$

$$k_{-1}^{obs} = -k_{-3} + \frac{k_{-2} \cdot K_{eq}^2}{[H]^+} \qquad \text{(Eq.21)}$$

$$k_2^{obs} = -k_6 + \frac{k_7 \cdot K_{eq}^3}{[H]^+} \qquad \text{(Eq.22)}$$

$$k_{-2}^{obs} = -k_{-6} + \frac{k_{-7} \cdot K_{eq}^4}{[H]^+} \qquad \text{(Eq.23)}$$

$$k_3^{obs} = -k_{11} + \frac{k_{10} \cdot K_{eq}^5}{[H]^+} \qquad \text{(Eq.24)}$$

$$k_{-3}^{obs} = -k_{-11} + \frac{k_{-10} \cdot K_{eq}^6}{[H]^+} \qquad \text{(Eq.25)}$$

Those equations depend on two factors. The first factor is the constant of the neutral system that models the migration, and the second factor is a product of the anionic constant for the process, the pH-equilibrium constant, and the pH of the media, expressed as the proton concentration $[H^+]$. Since k_{n}^{obs} presents values around 10^{-5} s^{-1}, and neutral constants were three orders of magnitude lower than them, the contribution of the neutral constants can be considered negligible at pH>6. Thus, **Eq. 20-25** can be simplified to **Eq. 26-31**.

$$k_1^{obs} = \frac{k_2 \cdot K_{eq}^1}{[H]^+} \qquad \text{(Eq.26)}$$

$$k_{-1}^{obs} = \frac{k_{-2} \cdot K_{eq}^2}{[H]^+} \qquad \text{(Eq.27)}$$

$$k_2^{obs} = \frac{k_7 \cdot K_{eq}^3}{[H]^+} \qquad \text{(Eq.28)}$$

$$k_{-2}^{obs} = \frac{k_{-7} \cdot K_{eq}^4}{[H]^+} \qquad \text{(Eq.29)}$$

$$k_3^{obs} = \frac{k_{10} \cdot K_{eq}^5}{[H]^+} \qquad \text{(Eq.30)}$$

$$k_{-3}^{obs} = \frac{k_{-10} \cdot K_{eq}^6}{[H]^+} \qquad \text{(Eq.31)}$$

All the other variables are well-known, except for the pH-equilibrium constant. Calculating the pH-equilibrium constants can be done using the solution phase free energy of the deprotonation reaction (**Eq. 32**), which is derived from the Eyring equation (**Eq. 7**). However, the calculation of the energy barriers ΔG^{*}_{aq} is challenging. The reason is that even if both models have the same atom number (which is not always the case), the TSs of a water molecule or a hydroxide anion deprotonating an hydroxyl group from another molecule do not precisely represent the real situation where everything is solvated. This can lead to significant errors in the calculated pK_a values. [30] However, these results can be improved by adding several explicit water molecules. [31]

$$pK_a = \frac{\Delta G^{*}_{aq}}{2.303RT} \qquad \text{(Eq. 32)}$$

Therefore, instead of directly calculating the energy barrier ΔG^{*}_{aq} using transition states, a thermodynamic method developed by Schlegel and coworkers [31c] will be employed. In this method, the estimation of ΔG^{*}_{aq} is based on the summation of the TSs from each species involved in the acid-base equilibrium, considering the position of each species in the equation $\mathrm{AH} \rightleftarrows \mathrm{A}^{-} + \mathrm{H}^{+}$ (**Eq. 33**). To achieve higher accuracy, Schegel et al. incorporated three explicit water molecules to solvate the anion, as suggested in previous literature.

$$\Delta G^{*}_{aq} = G^{*}_{aq}\,(A^{-}) + G^{*}_{aq}\,(H^{+}) - G^{*}_{aq}\,(AH) + G^{1atm\rightarrow 1M} \qquad \text{(Eq. 33)}$$

$G^{*}_{aq}\,(A^{-})$ and $G^{*}_{aq}\,(AH)$ represent the respective free energies at 1M of the TSs for the migration from the anionic and the neutral models, $G^{*}_{aq}\,(H^{+})$ is the free energy of the proton in the aqueous phase, with a literatue value of -265.9 kcal/mol. [32] Finally, $G^{1atm\rightarrow 1M}$ corresponds to the free energy change when converting from the standard state of 1 atm to 1 M, and is 1.89 kcal/mol.

By applying this model to carbohydrates, pK_a values for the hydroxyl groups involved in the first migration were obtained. When combined with the $[H^{+}]$ at pH 8 and the TS free energy from the first migration, the resulting barriers fall within the range of 10^{-4} to 10^{-5}, which aligns closely with the experimental constants. Based on this success, the model was extended to the remaining hydroxyl groups involved in acetyl group migration. The corresponding pK_a values are presented in **Figure 5.5**.

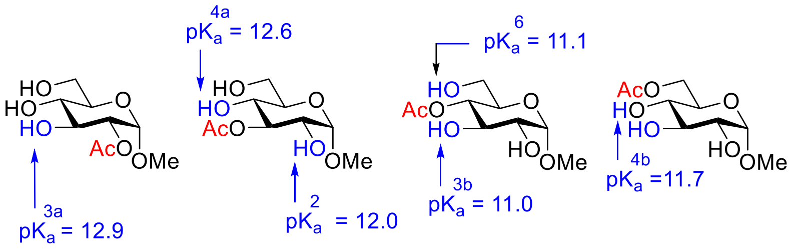

α-D-Glc-2Ac_H **α-D-Glc-3Ac_H** **α-D-Glc-4Ac_H** **α-D-Glc-6Ac_H**

Figure 5.5: *Calculated (m062x/cc-pvtz/SMD=water) pK_a values for α-D-Glc-2Ac_H, α-D-Glc-3Ac_H, α-D-Glc-4Ac_H and α-D-Glc-6Ac_H.*

The differences observed in pK_a values for similar hydroxyl groups can be attributed to small variations in energy, which can result in several units of difference in their calculation. It should be noted that a difference of 1 unit of pK_a corresponds to an error of 1.36 kcal/mol. [33] Even with accurate levels of theory, differences of 1-2 units could be expected. [34]

In terms of the results obtained for the first migration, the model was initially applied to the entire migration process for Me α-D-glucopyranoside, and then extended to other carbohydrates. **Table 5.3** presents a comparison between experimental and theoretical values, along with the relative errors for the migration kinetic constants. As mentioned earlier, these calculations required the evaluation of various conformations for both minima and TS for each carbohydrate in each model. To ensure reliable results, only structures with consistent water molecules interactions were selected. This approach avoids including unreliable results that may arise from additional interactions formed by some water molecules in certain conformations.

Table 5.3: *Calculated formal energy barriers [a] (kcal/mol) and rate constants [b] (s^{-1}) for the acetyl group migration in Me O-Ac-D-glycosides at pH= 8.*

		Experimental		Predicted		
		rate constant	ΔG	rate constant	ΔG	Error[c]
Me α-D-glc	k_{1}^{obs}	6.28E-05	23.2	3.35E-04	22.2	1.0
	k_{-1}^{obs}	5.11E-05	23.3	4.03E-05	23.5	0.2
	k_{2}^{obs}	5.06E-05	23.3	3.15E-06	25.0	1.6
	k_{-2}^{obs}	1.01E-04	22.9	4.50E-06	24.8	1.8
	k_{3}^{obs}	1.21E-03	21.4	6.32E-04	21.8	0.4
	k_{-3}^{obs}	7.83E-05	23.1	8.15E-05	23.1	0.0
Me α-D-gal	k_{1}^{obs}	3.31E-05	23.6	2.99E-04	22.3	1.3
	k_{-1}^{obs}	2.65E-05	23.7	1.56E-04	22.7	1.1
	k_{2}^{obs}	2.43E-04	22.4	6.75E-03	20.4	2.0
	k_{-2}^{obs}	2.43E-04	22.4	2.94E-05	23.7	1.3
	k_{3}^{obs}	2.83E-04	22.3	4.83E-04	22.0	0.3
	k_{-3}^{obs}	5.47E-05	23.3	2.34E-04	22.4	0.9
Me α-D-xyl	k_{1}^{obs}	5.86E-05	23.2	2.27E-04	22.4	0.8
	k_{-1}^{obs}	4.25E-05	23.4	9.44E-04	21.6	1.8
	k_{2}^{obs}	2.03E-05	23.9	1.47E-05	24.1	0.2
	k_{-2}^{obs}	2.34E-05	23.8	1.25E-04	22.8	1.0

		Experimental		Predicted		
		rate constant	ΔG	rate constant	ΔG	Error[c]
Me β-D-glc	k_{1}^{obs}	2.02E-04	22.5	2.72E-05	23.7	1.2
	k_{-1}^{obs}	1.11E-04	22.9	4.28E-04	22.1	0.8
	k_{2}^{obs}	1.15E-04	22.8	3.58E-04	22.2	0.7
	k_{-2}^{obs}	1.28E-04	22.8	4.71E-06	24.7	2.0
	k_{3}^{obs}	1.10E-03	21.5	5.48E-03	20.6	1.0
	k_{-3}^{obs}	4.56E-05	23.4	4.01E-04	22.1	1.3
Me β-D-gal	k_{1}^{obs}	1.47E-04	22.7	1.19E-04	22.8	0.1
	k_{-1}^{obs}	6.08E-05	23.2	3.94E-05	23.5	0.3
	k_{2}^{obs}	2.43E-04	22.4	1.88E-04	22.6	0.2
	k_{-2}^{obs}	1.72E-04	22.6	8.78E-06	24.4	1.8
	k_{3}^{obs}	2.10E-04	22.5	1.49E-03	21.3	1.2
	k_{-3}^{obs}	5.72E-05	23.3	5.54E-05	23.3	0.0
Me β-D-xyl	k_{1}^{obs}	1.65E-04	22.6	2.85E-05	23.7	1.0
	k_{-1}^{obs}	7.33E-05	23.1	3.52E-04	22.2	0.9
	k_{2}^{obs}	9.11E-05	23.0	3.27E-04	22.2	0.8
	k_{-2}^{obs}	7.81E-05	23.1	1.90E-03	21.2	1.9

[a] *Obtained from the individual barriers of the stepwise mechanism calculated at m062x/cc-pvtz/SMD=water//m062x/6-31+G(d,p)/SMD=water level of theory and then from the rate constants by using Eyring's equation* ***Eq.7****. [b] Obtained by applying equations* ***Eq. 24-29****. [c] Difference between experimental and calculated ΔG in kcal/mol.*

It should be noted that the expected deviations from DFT calculations, which are typically in the order of 1-2 kcal/mol [35], can result in deviations of 1-2 orders of magnitude in the kinetic constants due to their logarithmic dependence. Therefore, it can be considered that the predicted energy barriers are in good agreement with the experimental values.

For verifying that the acidity dependency is lineal beyond the pH interval 7-8, [16b] as the computational results predict trough **Eq. 26-31**, the migration of Me α-D-glucopyranoside **R5.1** was performed at pH=6, 7, 7.5, and 9. The rate constants calculated at pH 8 were used as reference to correlate the other rate constants.

Applying the water dissociation constant (**Eq.34**) to the definitive constants formula **Eq.26-31**, makes k_i^{obs} linear depend on [OH$^-$] (**Eq.35**).

$$K_w = [H^+] \cdot [OH^-] = 1{,}0 \ \cdot 10^{-14} \qquad \text{(Eq. 34)}$$

$$k_i^{obs} = [OH^-] \, \frac{k_j^{anionic} \cdot K_{eq}^m}{K_w} \qquad \text{(Eq. 35)}$$

Since $k_j^{anionic}$, K_{eq}^m and K_w are constants not dependent on the pH, the relationship between K_i^{obs} at different pHs will simply be the ratio between the reference and the specified [OH$^-$] concentrations (**Eq.36**).

$$\frac{k_{i,\ pH=x}^{obs}}{k_{i,\ pH=8}^{obs}} = \frac{[OH^-]_{pH=x}}{[OH^-]_{pH=8}} \qquad \text{(Eq. 36)}$$

Table 5.4 presents the correlation between the rate constants at pH 8 and other pH values. The experimental coefficients determined align well with the theoretical ones. The observed differences are likely attributed to measurements errors during the migration or in buffer preparation. The larger error at pH 9 may be caused by the faster migration at that pH, resulting in a lower signal accumulation in the NMR-spectra and increasing the deviation. These results confirm the requirement for deprotonation in the migration process and highlight the significant impact of the solution's ability to deprotonate the hydroxyl groups on the migration rate.

***Table 5.4:** theoretical and experimental values of the relationship of the migration rate of **R5.1** at different pHs with the migration at pH 8.*

pH	**Theoretical Coefficient**	**Experimental Coefficient**
9	10.0	7.1
8	1.0	1.0
7.5	0.32	0.35
7	0.1	0.085
6	0.01	0.0082

Given the multiple models, species, and equilibria involved in this method, as well as the minimal difference in barriers between each step, a conventional analysis based on the related structures is not sufficient to explain the observed differences between carbohydrates. Notably, no significant differences were found in the geometries of the TS corresponding to the same migration in α and β anomers. This suggests that the differences in the rate of migration rates are not primarily due to steric factors but rather to other well-known electronic features such as the anomeric effect.

Nevertheless, trends can still be analyzed. **Figure 5.6** provides a comparative energy diagram illustrating the complete migration process of the three studied monosaccharides, including both anomeric configurations and the theoretical values. This diagram highlights the close similarity between the experimental and theoretical results, as well as the overall trend of the system. Experimental kinetic results are also presented along the energy diagram. The kinetic experiments were conducted until equilibrium was reached, and the comparison between the trend of the energy diagram and the isomer proportions at the equilibrium reveals a matching pattern.

For glucosides and galactosides, a clear descending trend is observed in the energy diagram, with the 6-Ac being the most stable. This corresponds to the most abundant isomer observed at the equilibrium. On the other hand, in the case of xylosides, where primary alcohols are absent in the molecule, the stability of the different positions becomes more competitive. As a result, no clear descending trend or dominant isomer at equilibrium is observed.

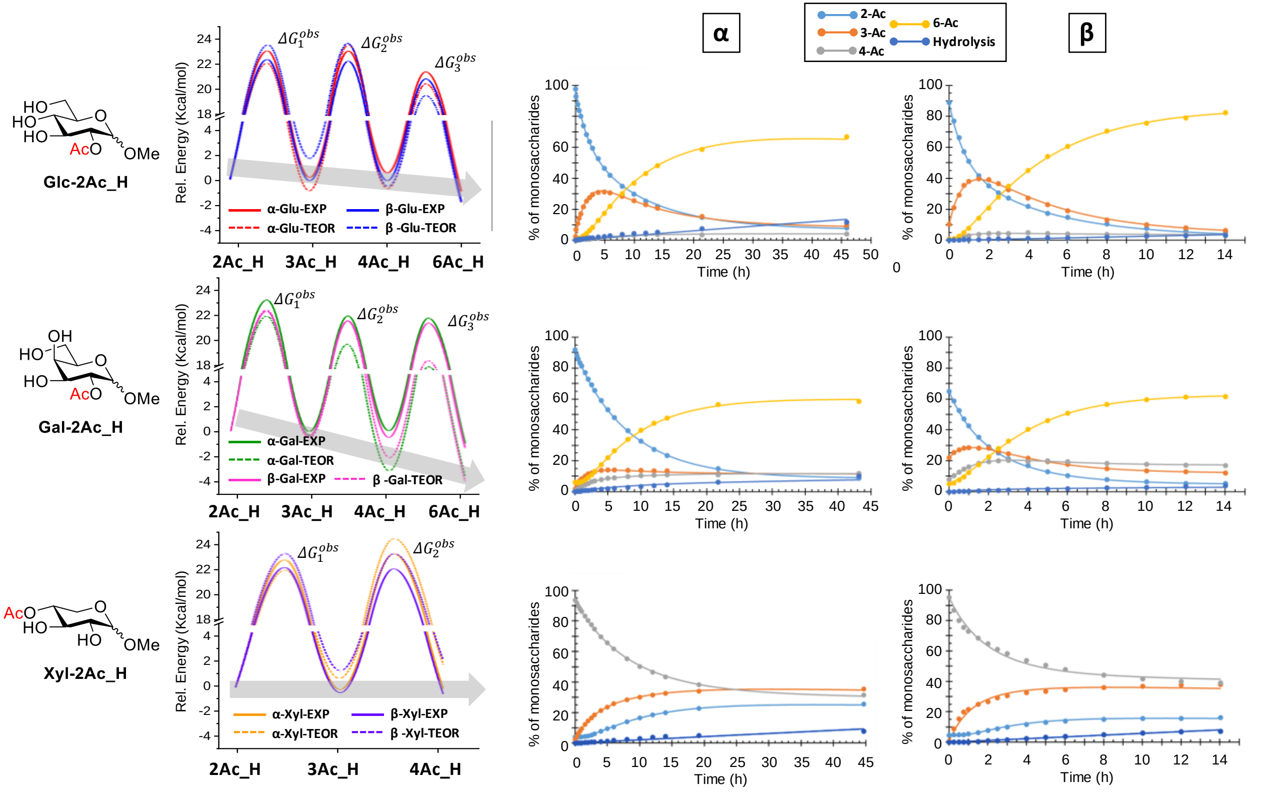

Figure 5.6: ***(Left)*** *Experimental and calculated (m062x/cc-pvtz/SMD=water//m062x/6-31+G(d,p)/SMD=water) energy profiles for the complete migration process in monosaccharides. The maxima correspond to formal barriers (ΔG_i^{obs}) calculated from the rate constants K_i^{obs}. The real barriers are those corresponding to two-step processes with an intermediate orthoester as discussed above.* ***(Right)*** *Kinetic results of acetyl migration in α/β gluco-, galacto- and xylopyranosides. Conditions: 100 mM phosphate buffer with 10% D_2O, pH 8, 25 °C.*

5.2.5 Acetyl migration in trisaccharides

Acyl group migration has traditionally been described as occurring within monosaccharides, where the acyl group moves from one hydroxyl group to a neighboring one. However, recent discoveries have revealed that this migration can also occur between different monosaccharide units in an oligosaccharide. [20, 36]

This newfound understanding of acyl group migration extends to other hemicelluloses such as mannans, glucans o xylans, which are molecules present in nearly all plant species. [37] The acetylation of these hemicelluloses plays a crucial role in determining their structure and function within the plant cell walls. [38] It has been demonstrated that the pH in plant cells undergoes changes during their life cycle, [39] and since the pH of the surrounding environment significantly affects the rate of acyl migrations, these acetyl migrations could be involved in various stages of plant development, [40] or even cellular signaling processes.

With this in mind, investigating the potential acetyl migration within and across the glycosidic linkages could provide valuable insights into the positioning of acetyl groups after biosynthesis and their evolution during cell growth.

To carry out this investigation, four β-(1 → 4)-linked glucan and xylan trisaccharides were synthetized (**Figure 5.7**) and subjected to similar migration conditions as those used for monosaccharides. The migration experiments for mannan trisaccharide were omitted since they had already been performed. [36] In cases where it was not possible to differentiate between different processes, such as hydrolysis from the secondary alcohols, or the different migrations occurring inside the monosaccharide units, were assumed to be the same. This approach is based on the assumption that similar types of reactions will have similar rate constants, thereby simplifying the kinetic model.

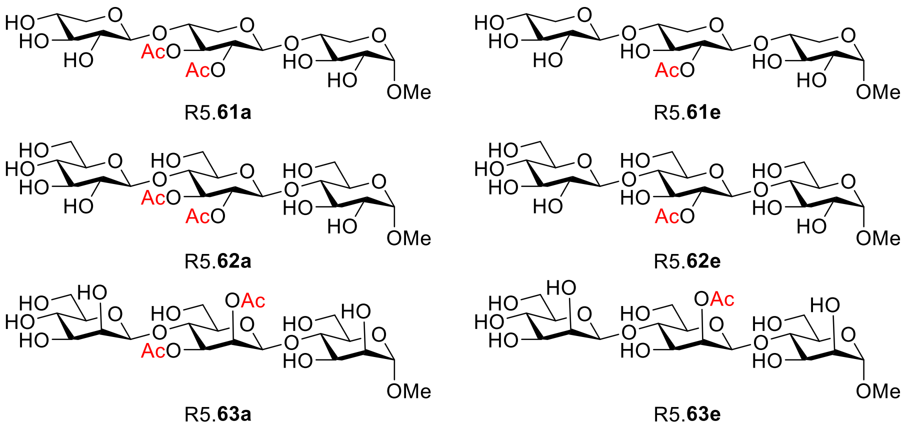

Figure 5.7: *Xylan (**R5.61a**, **R5.61e**), glucan (**R5.62a**, **R5.62e**), and mannan (**R5.63a**, **R5.63e**) model trisaccharides investigated in this section.*

Following the same procedure and conditions used for the kinetic studies in monosaccharides, it was demonstrated that migration between different saccharide units was only possible for the glucan model. However, for xylans **R5.61a** and **R5.61e**, the distance between an acetylated hydroxyl and other hydroxyl groups from neighboring monosaccharides prevented migration across the trisaccharide. As a result, the first step for **R5.61a** is the hydrolysis of one of its acetyl groups, followed by the establishment of an equilibrium between O2- and O3-acetylated trisaccharides. It was found that the hydrolysis of **R5.61a** is 40% slower than the hydrolysis of **R5.61e**, likely due to steric hindrance caused by the adjacent acetyl group. A general scheme of the migration and hydrolysis pathways is illustrated in

Scheme 5.11.

Table 5.5 presents the experimental kinetic results along with the corresponding computationally obtained values, which will be discussed later. Comparing O2 → O6 migration between monosaccharide units of the glucan and mannan models, a higher migration rate is observed in the glucan model. This can be attributed to the higher proximity of the O2 position to the O6 reducing end in the glucan. This finding could explain why acetyl groups are not typically found in the O2 position of glucose units in natural glucans.

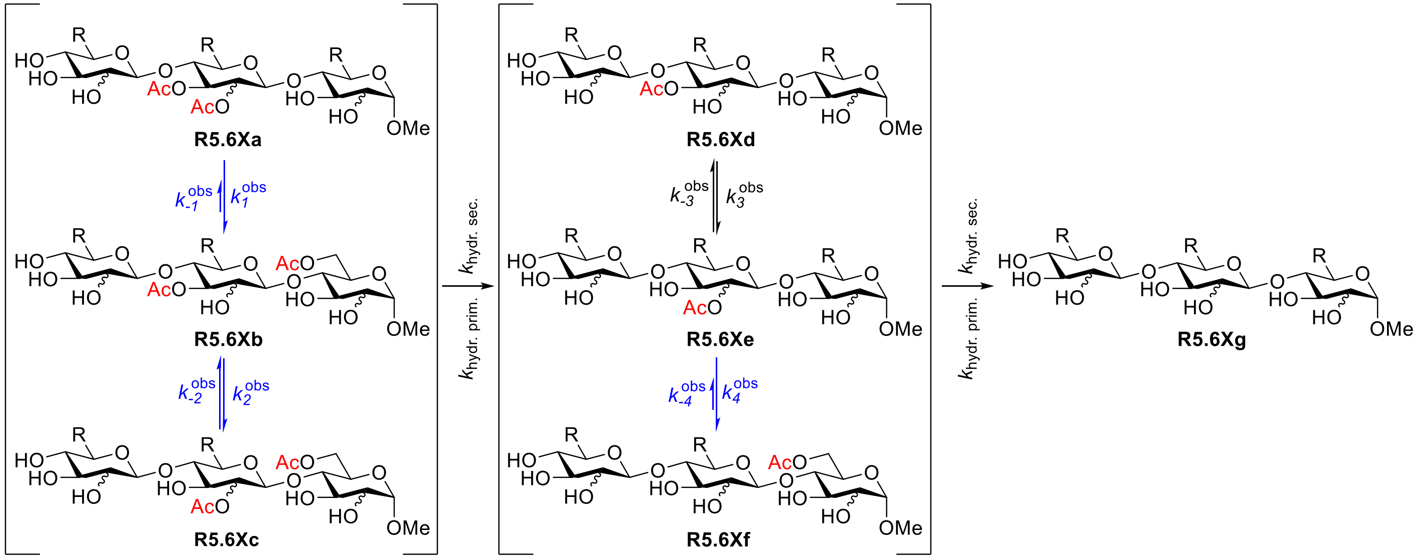
R5.6Xa
R5.6Xb
R5.6Xc
R5.6Xd
R5.6Xe
R5.6Xf
R5.6Xg
k_{-1}^{obs}
k_{1}^{obs}
k_{-2}^{obs}
k_{2}^{obs}
k_{-3}^{obs}
k_{3}^{obs}
k_{-4}^{obs}
k_{4}^{obs}
$k_{hydr.\ sec.}$
$k_{hydr.\ prim.}$
HO
AcO
OMe
R
O

Scheme 5.11: *General pathway for the migration and hydrolysis in xylan (R=H), glucan, and mannan (R=CH$_2$OH) trisaccharides. The blue arrows and constants represent steps that are forbidden in the xylan model. In the case of glucan and mannan trisaccharides, it was not possible to distinguish between the two reactions, so it was assumed that* $k_2^{obs} = k_3^{obs}$ *and* $k_{-2}^{obs} = k_{-3}^{obs}$.

The computational model described earlier was employed to estimate the kinetic constants. Due to the similarity between the xylan and glucan models, only the glucan model will be explored in detail. Migration in the mannan trisaccharide was also investigated for the purpose of comparison. The first step involved confirming the stepwise mechanism and the presence of the orthoester intermediate, similar to the case of monosaccharides. TS from O2 → O3 and O2 → O6 migrations were located, and its IRCs connected unequivocally with the orthoester intermediate. Consequently, **Eq.1** and **Eq.2** were used again for calculating the anionic kinetic constants. **Figure 5.8** provides examples of a TS for O2 → O6 migration and its corresponding 9-membered ring orthoester intermediate.

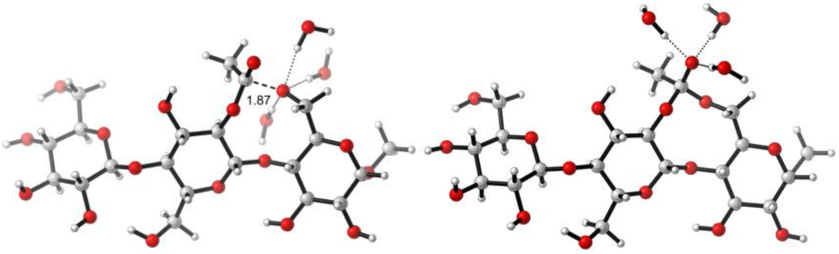

Figure 5.8: *Optimized structures at the wb97xd/6-31+G(d,p)/SMD=water level of theory for a TS of O2→O6 migration (left) and its associated orthoester intermediate (right). Distance is measured in Angstroms.*

Once the two-step mechanism has been confirmed, obtaining accurate results relies on carefully selecting the appropriate conformation for each species. The presence of a high number of conformations within a narrow energy range poses a challenge in accurately determining the trisaccharide geometry. Additionally, the multiple hydroxyl groups and explicit water molecules can form various hydrogen bonds between each other, leading to an increase in the energy range and potentially distorting the calculations. To mitigate this issue, a comprehensive conformational study of the trisaccharides was conducted.

Parallel MD calculations and Macromodel searches were conducted, and their results were almost coincident. All the structures within a range of 2 kcal/mol was further optimized at DFT level. A preliminary benchmark confirmed that wb97xd/6-311++G(d,p)/SMD=water//wb97xd/6-31+G(d,p)/SMD=water provided the closest approach to the experimental results. An example of this parallel conformational search is illustrated in **Figure 5.9**. By comparing the superposition of all the trisaccharide structures with the superposition of monosaccharides depicted in **Figure 5.2**, one can grasp the significant increase in the degrees of freedom exhibited by trisaccharides.

Transition structures were located by conducting relaxed scans over the selected structure for each acetylated trisaccharide. Locating the TSs for the anionic model required considerable effort, as it was challenging to maintain three water molecules surrounding the anion during its nucleophilic attack while having multiple hydroxyl groups ready for the formation of stable hydrogen bonds.

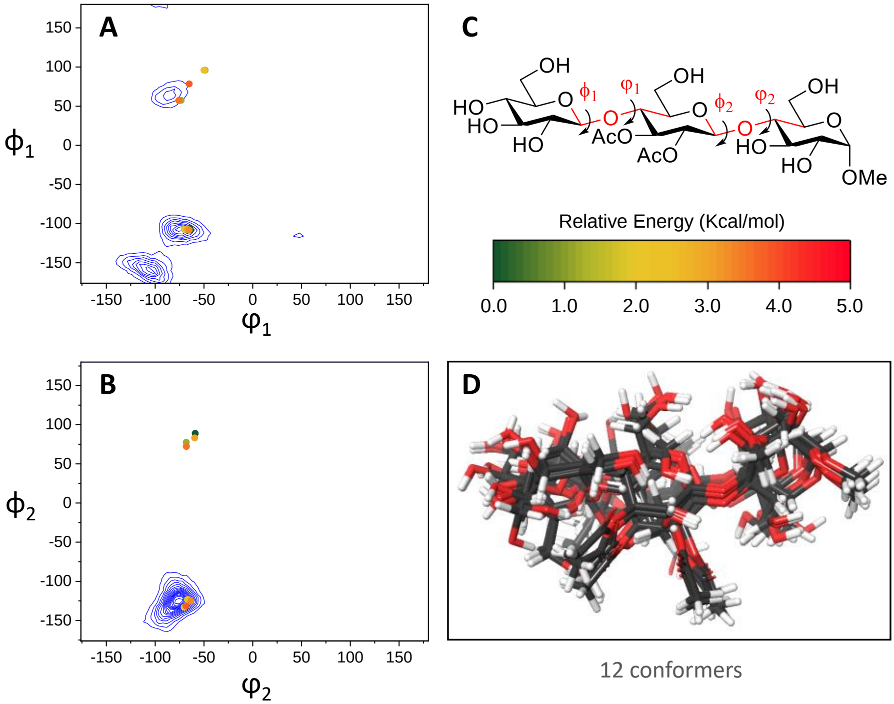

Figure 5.9: *(**A** and **B**) Conformational analysis of 8,9-di-Ac-Glucoside **R5.62a**. The MD population analysis was carried out with 50.000 snapshots, and there is a difference of 100 units of population between each level depicted as blue lines. Superposed colored dots represent the 12 conformers found with Macromodel. (**C**) Scheme highlighting the dihedral bonds studied in graphs **A** and **B**, along with the relative energy-color relationship for the Macromodel searches. (**D**) Superposition of the 12 conformers found by Macromodel.*

These explicit water molecules also posed challenges during the optimization of other structures, as they could form multiple hydrogen bonds that could result in energy deviations when a particular structure formed a different number of bonds compared to others. Since the solvation of each species in the real scenario is approximately the same, careful selection of the structures was necessary to discard those structures where the presence of a different number of hydrogen bonds would prevent a valid comparison of their relative energies. However, in some cases, maintaining the same number of interactions was not possible, leading to higher deviations in those values.

The kinetic model applied to trisaccharides was the same as that used for monosaccharides, consisting of the combination of the anionic model, where the anion was solvated with three explicit water molecules, with a slower neutral mechanism involving one explicit water molecule. The pH influence was also taken into account, requiring the estimation of the pK_a values for the relevant hydroxyls groups. The results for the estimation of pK_a values for the glucan and mannan models are illustrated in **Figure 5.10**. Higher deviations, resulting from the increased conformational variability, were observed compared to monosaccharides from **Figure 5.5**. Values that deviate significantly from the mean are caused by overstabilization resulting from the formation of extra hydrogen bonds in the deprotonated form (for the lower values) or the protonated form (for the higher values).

Following the approach used for monosaccharides, the contribution of the neutral model to the observed kinetic constants k_{n}^{obs}, was considered negligible due its low values. Thus, **Eq.1** was applied again with a pH value of 8. The calculated kinetic constants, along with the experimentally obtained ones, are listed in **Table 5.5**. It can be observed that greater deviations compared to monosaccharides are present, resulting again from the conformational variability and the formation of a varying number of hydrogen bonds in certain cases. However, despite these variations, the predicted values can still be considered to be reasonably consistent with the experimental results.

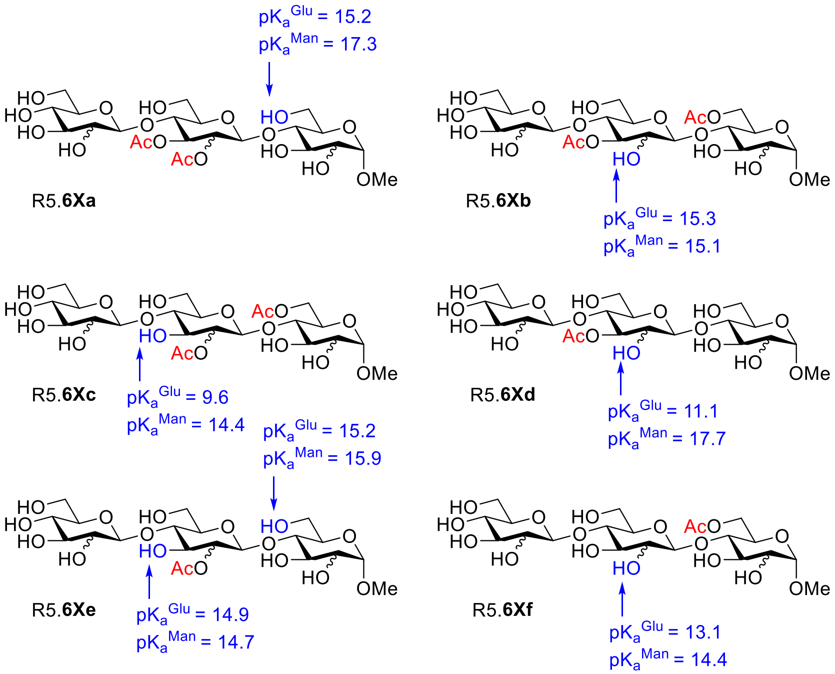
pKaGlu = 15.2
pKaMan = 17.3
R5.6Xa
R5.6Xb
pKaGlu = 15.3
pKaMan = 15.1
R5.6Xc
pKaGlu = 9.6
pKaMan = 14.4
R5.6Xd
pKaGlu = 11.1
pKaMan = 17.7
pKaGlu = 15.2
pKaMan = 15.9
R5.6Xe
pKaGlu = 14.9
pKaMan = 14.7
R5.6Xf
pKaGlu = 13.1
pKaMan = 14.4

Figure 5.10: *Calculated (wb97xd/def2tzvp/SMD=water) pK_a values for hydroxyl groups involved in the acetyl migration processes for glucan and mannan trisaccharides.*

Regarding the specific constants k_{-1}^{obs} and k_{-4}^{obs} for both trisaccharides, the model correctly predicts the highest barriers, which aligns with the experimental findings. This confirms that migration from a primary position to a secondary one is not favorable. Similarly, although with some deviation, the second highest barriers corresponding to k_{1}^{obs} and k_{4}^{obs} are also predicted to be higher than the rest. These barriers represent the migration between two different monosaccharide units, and the TSs involved in this process form a 9-membered ring. Compared to the 5-membered ring formed during the O2-O3 migration, higher values for these barriers are expected.

***Table 5.5:** Calculated formal energy barriers [a] (kcal/mol) and rate constants [b] (s^{-1}) for the acetyl group migration in trisaccharides at pH = 8.*

			Experimental		Predicted		
			rate constant	ΔG	rate constant	ΔG	Error[c]
Glucan Trisacch.	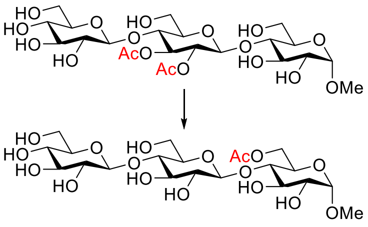	k_1^{obs}	9.25E-06	24.3	1.56E-07	26.7	2.4
		k_{-1}^{obs}[d]	<1.00E-14	>36.0	2.80E-12	33.2	-[e]
		k_2^{obs}	1.37E-04	22.7	2.01E-05	23.9	1.1
		k_{-2}^{obs}	1.34E-04	22.7	2.52E-05	23.7	1.0
		k_3^{obs}	1.37E-04	22.7	8.97E-05	23.0	0.2
		k_{-3}^{obs}	1.34E-04	22.7	6.79E-07	25.9	3.1
		k_4^{obs}	1.35E-06	25.5	8.25E-09	28.5	3.0
		k_{-4}^{obs}[d]	<1.00E-14	>36.0	6.73E-14	35.4	-[e]
Mannan Trisacch.	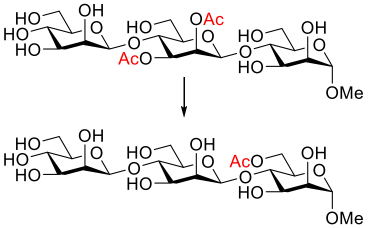	k_1^{obs}	5.72E-07	26.0	2.93E-08	27.7	1.8
		k_{-1}^{obs}[d]	<1.00E-14	>36.0	8.19E-13	33.9	-[e]
		k_2^{obs}	5.22E-04	21.9	1.95E-05	23.9	1.9
		k_{-2}^{obs}	2.81E-04	22.3	5.78E-05	23.2	0.9
		k_3^{obs}	5.22E-04	21.9	1.86E-03	21.2	0.8
		k_{-3}^{obs}	2.81E-04	22.3	1.16E-05	24.2	1.9
		k_4^{obs}	5.72E-07	26.0	2.57E-09	29.2	3.2
		k_{-4}^{obs}[d]	<1.00E-14	>36.0	1.97E-13	34.8	-[e]

[a] *Obtained from the individual barriers of the stepwise mechanism calculated at wb97xd/6-311++G(d,p)/SMD=water//wb97xd/6-31+G(d,p)/SMD=water level of theory and then from the rate constants by using Eyring's equation **Eq.7**. [b] Obtained by applying equation **Eq. 1**. [c] Difference between experimental and calculated ΔG in kcal/mol. [d] Since these constants has not been observed experimentally, it is considered very low and an arbitrary valor has been set. [e] Since the experimental value has not been measured, this error cannot be considered.*

These results confirm the suitability of the developed method for monosaccharides to be applied to more complex systems. Although the method did not originally consider migrations between monosaccharide units, it demonstrates an acceptable level of accuracy in reproducing the energy barriers associated with the 9-membered ring structures. The same mechanism and pH dependence has been found in all carbohydrate migrations.

The highest barriers observed in acetyl migrations from secondary to primary positions are not result of unstable TS, but rather arise from the high thermodynamic stability of the substrate when acetylated in the primary alcohol. Consequently, the observed acetyl migration towards the primary position is controlled by thermodynamics rather than kinetics.

5.3 Conclusions

It has been demonstrated that the configuration of the C1 atom has a significant impact on the rate of migration when the involved hydroxyl groups share a *trans* relationship.

A migration preference towards the primary alcohol has been observed. When no primary alcohols are present, as in the case of xylose-based models, a more distributed proportion of acetylated sugars is obtained.

In trisaccharides, a faster O2-O6 migration is observed in glucan models compared to mannan due to the higher proximity of the equatorial hydroxyl group to the O6 reducing end.

Computational calculations have confirmed the stepwise mechanism and the formation of the orthoester intermediate regardless the ring size.

The requirement of prior deprotonation of a neighboring hydroxyl group to initiate the migration has also been demonstrated.

A dependence on both the pK_a of the corresponding hydroxyl group and the pH of the media has been established. The model, which consist of an anionic system with three explicit water molecules surrounding the anion and a neutral model with one explicit water molecule for estimating the pK_a, successfully reproduces in good agreement the experimentally obtained barriers.

5.4 References

[1] a) R. Minjares-Fuentes, A. Femenia, F. Comas-Serra, V. M. Rodríguez-González, *J. AOAC Int.* **2018**, *101*, 1711-1719; b) X. Xing, S. W. Cui, S. Nie, G. O. Phillips, H. D. Goff, Q. Wang, *Bioact. Carbohydr. Diet.* **2014**, *4*, 74-83; c) X. Xing, S. W. Cui, S. Nie, G. O. Phillips, H. D. Goff, Q. Wang, *Carbohydr. Polym.* **2015**, *117*, 422-433; d) S. Willför, R. Sjöholm, C. Laine, M. Roslund, J. Hemming, B. Holmbom, *Carbohydr. Polym.* **2003**, *52*, 175-187; e) F. M. Nunes, M. R. Domingues, M. A. Coimbra, *Carbohydr. Res.* **2005**, *340*, 1689-1698.

[2] a) T. Ishii, *Phytochem.* **1991**, *30*, 2317-2320; b) M. A. Kabel, P. de Waard, H. A. Schols, A. G. Voragen, *Carbohydr. Res.* **2003**, *338*, 69-

77; c) A. Teleman, J. Lundqvist, F. Tjerneld, H. Stålbrand, O. Dahlman, *Carbohydr. Res.* **2000**, *329*, 807-815.

[3] a) L. L. Kiefer, W. S. York, A. G. Darvill, P. Albersheim, *Phytochem.* **1989**, *28*, 2105-2107; b) M. Hoffman, Z. Jia, M. J. Peña, M. Cash, A. Harper, A. R. Blackburn, 2nd, A. Darvill, W. S. York, *Carbohydr. Res.* **2005**, *340*, 1826-1840; c) Z. Jia, M. Cash, A. G. Darvill, W. S. York, *Carbohydr. Res.* **2005**, *340*, 1818-1825; d) D. M. Gibeaut, M. Pauly, A. Bacic, G. B. Fincher, *Planta* **2005**, *221*, 729-738.

[4] M. Pauly, K. Keegstra, *Curr. Opin. Plant. Biol.* **2010**, *13*, 305-312.

[5] a) F. Liners, T. Gaspar, P. Van Cutsem, *Planta* **1994**, *192*, 545-556; b) N. Obel, V. Erben, T. Schwarz, S. Kühnel, A. Fodor, M. Pauly, *Mol. Plant.* **2009**, *2*, 922-932; c) M. Pauly, S. Eberhard, P. Albersheim, A. Darvill, W. S. York, *Planta* **2001**, *214*, 67-74.

[6] a) S. Willför, K. Sundberg, M. Tenkanen, B. Holmbom, *Carbohydr. Polym.* **2008**, *72*, 197-210; b) S. Willför, A. Sundberg, A. Pranovich, B. Holmbom, *Wood Sci. Technol.* **2005**, *39*, 601-617.

[7] A. Ebringerova, Z. Hromadkova, V. Hríbalová, C. Xu, B. Holmbom, A. Sundberg, S. Willför, *Int. J. Biol. Macromol.* **2008**, *42*, 1-5.

[8] P. Portaleone, in *Encyclopedia of Endocrine Diseases, Vol. 1* (Ed.: L. Martini), New York, **2004**, p. 9−12.

[9] a) Z. Papackova, M. Cahova, in *Int. J. Mol. Sci.* **2015**, *16*, 3831-3855; b) C. P. S. Badenhorst, R. van der Sluis, E. Erasmus, A. A. van Dijk, *Expert Opin. Drug Metab. Toxicol.* **2013**, *9*, 1139-1153; c) C. P. S. Badenhorst, E. Erasmus, R. van der Sluis, C. Nortje, A. A. van Dijk, *Drug Metab. Rev.* **2014**, *46*, 343-361.

[10] L. Di, E. H. Kerns, *Drugs-Like Properties, Vol. 10 – Blood-brain Barrier*, Elsevier Inc., **2016**.

[11] a) A. P. Doerschuk, *J. Am. Chem. Soc.* **1952**, *74*, 4202-4203; b) R. B. Martin, R. I. Hedrick, *J. Am. Chem. Soc.* **1962**, *84*, 106-110.

[12] a) V. Dimakos, M. S. Taylor, *Chem. Rev.* **2018**, *118*, 11457-11517; b) F. S. Ekholm, R. Leino, in *Protecting Groups: Strategies and Applications in Carbohydrate Chemistry, Vol. 8* (Ed.: S. Vidal), Wiley-VCH Verlag GmbH & Co. KGaA, Wienheim, Germany, **2019**, pp. 227–241; c) A. A. Hettikankanamalage, R. Lassfolk, F. S. Ekholm, R. Leino, D. Crich, *Chem. Rev.* **2020**, *120*, 7104-7151.

[13] E. Fischer, in *Untersuchungen aus Verschiedenen Gebieten: Vorträge und Abhandlungen Allgemeinen Inhalts* (Eds.: E. Fischer, M. Bergmann), Springer Berlin Heidelberg, Berlin, Heidelberg, **1924**, pp. 643-655.

[14] a) S. J. Angyal, G. J. H. Melrose, *J. Chem. Soc. (Resumed)* **1965**, 6494-6500; b) F. S. Ekholm, A. Ardá, P. Eklund, S. André, H.-J. Gabius, J. Jiménez-Barbero, R. Leino, *Chem. Eur. J.* **2012**, *18*, 14392-14405.

[15] a) T. O. Oesterling, *Carbohydr. Res.* **1970**, *15*, 285-290; b) T. Horrobin, C. Hao Tran, D. Crout, *J. Chem. Soc., Perkin trans. 1* **1998**, 1069-1080; c) V. Petrović, S. Tomić, M. Matanović, *Carbohydr. Res.* **2002**, *337*, 863-867.

[16] a) H. Paul, A. Illing, I. D. Wilson, *Biochem. Pharmacol.* **1981**, *30*, 3381-3384; b) R. W. Mortensen, U. G. Sidelmann, J. Tjørnelund, S. H. Hansen, *Chirality* **2002**, *14*, 305-312; c) S. Khan, D. S. Teitz, M. Jemal, *Anal. Chem.* **1998**, *70*, 1622-1628.

[17] a) J. P. Kamerling, R. Schauer, A. K. Shukla, S. Stoll, H. Van Halbeek, J. F. Vliegenthart, *Eur. J. Biochem.* **1987**, *162*, 601-607; b) B. Reinhard, H. Faillard, *Liebigs Ann.* **1994**, *1994*, 193-203; c) K. Kefurt, Z. Kefurtová, J. Jarý, I. Horáková, M. Marek, *Carbohydr. Res.* **1992**, *223*, 137-145; d) M. U. Roslund, O. Aitio, J. Wärnå, H. Maaheimo, D. Y. Murzin, R. Leino, *J. Am. Chem. Soc.* **2008**, *130*, 8769-8772.

[18] M. Filice, T. Bavaro, R. Fernandez-Lafuente, M. Pregnolato, J. M. Guisan, J. M. Palomo, M. Terreni, *Cat. Today* **2009**, *140*, 11-18.

[19] O. P. Chevallier, M. E. Migaud, *Beilstein J. Org. Chem.* **2006**, *2*, 14.

[20] R. Lassfolk, J. Rahkila, M. P. Johansson, F. S. Ekholm, J. Wärnå, R. Leino, *J. Am. Chem. Soc.* **2019**, *141*, 1646-1654.

[21] A. W. Nicholls, K. Akira, J. C. Lindon, R. D. Farrant, I. D. Wilson, J. Harding, D. A. Killick, J. K. Nicholson, *Chem. Res. Toxicol.* **1996**, *9*, 1414-1424.

[22] E. A. Pritchina, N. P. Gritsan, G. T. Burdzinski, M. S. Platz, *J. Phys. Chem. A* **2007**, *111*, 10483-10489.

[23] N. G. Berry, L. Iddon, M. Iqbal, X. Meng, P. Jayapal, C. H. Johnson, J. K. Nicholson, J. C. Lindon, J. R. Harding, I. D. Wilson, A. V. Stachulski, *Org. Biomol. Chem.* **2009**, *7*, 2525-2533.

[24] P. R. Bradshaw, S. E. Richards, I. D. Wilson, A. V. Stachulski, J. C. Lindon, T. J. Athersuch, *Org. Biomol. Chem.* **2020**, *18*, 1389-1401.

[25] M. A. Rangelov, G. N. Vayssilov, D. D. Petkov, *Int. J. Quantum Chem.* **2006**, *106*, 1346-1356.

[26] R. Lassfolk, M. Pedrón, T. Tejero, P. Merino, J. Wärnå, R. Leino, *Chem. Eur. J.* **2022**, *28*, e202200499.

[27] C. Romers, C. Altona, H. R. Buys, E. Havinga, in *Topics in Stereochemistry*, **2007**, pp. 39-97.

[28] S. Kannath, P. Adamczyk, D. Ferro-Costas, A. Fernández-Ramos, D. T. Major, A. Dybala-Defratyka, *J. Chem. Theory Comput.* **2020**, *16*, 847-859.

[29] B. Thapa, H. B. Schlegel, *J. Phys. Chem. A* **2016**, *120*, 5726-5735.

[30] a) K. Alongi, G. Shields, *Annu. Rep. Comput. Chem.* **2010**, *6*, 113-138; b) J. Ho, M. Coote, *Wiley Interdiscip. Rev. Comput. Mol. Sci.* **2011**, *1*, 649-660; c) P. G. Seybold, G. C. Shields, *Wiley Interdiscip. Rev. Comput. Mol. Sci.* **2015**, *5*, 290-297.

[31] a) V. S. Bryantsev, M. S. Diallo, W. A. Goddard, 3rd, *J. Phys. Chem. B* **2008**, *112*, 9709-9719; b) F. Ding, J. M. Smith, H. Wang, *J. Org. Chem.* **2009**, *74*, 2679-2691; c) B. Thapa, H. B. Schlegel, *J. Phys. Chem. A* **2015**, *119*, 5134-5144.

[32] a) D. M. Camaioni, C. A. Schwerdtfeger, *J. Phys. Chem. A* **2005**, *109*, 10795-10797; b) A. A. Isse, A. Gennaro, *J. Phys. Chem. B* **2010**, *114*, 7894-7899; c) A. V. Marenich, J. Ho, M. L. Coote, C. J. Cramer, D. G. Truhlar, *Phys. Chem. Chem. Phys.* **2014**, *16*, 15068-15106.

[33] M. D. Liptak, G. C. Shields, *J. Am. Chem. Soc.* **2001**, *123*, 7314-7319.

[34] S. Feng, C. Bagia, G. Mpourmpakis, *J. Phys. Chem. A* **2013**, *117*, 5211-5219.

[35] A. N. Bootsma, S. E. Wheeler, *ChemRxiv. Cambridge: Cambridge Open Engage* **2019**.

[36] R. Lassfolk, S. Bertuzzi, A. Ardá, J. Wärnå, J. Jiménez-Barbero, R. Leino, *ChemBioChem* **2021**, *22*, 2986-2995.

[37] a) Z. A. Popper, *Curr. Opin. Plant Biol.* **2008**, *11*, 286-292; b) I. Moller, I. Sørensen, A. J. Bernal, C. Blaukopf, K. Lee, J. Øbro, F. Pettolino, A. Roberts, J. D. Mikkelsen, J. P. Knox, A. Bacic, W. G. T. Willats, *Plant J.* **2007**, *50*, 1118-1128; c) K. H. Caffall, D. Mohnen, *Carbohydr. Res.* **2009**, *344*, 1879-1900.

[38] Y. Yuan, Q. Teng, R. Zhong, Z.-H. Ye, *Plant Sci.* **2016**, *243*, 120-130.

[39] a) T. N. Bibikova, T. Jacob, I. Dahse, S. Gilroy, *Development* **1998**, *125*, 2925-2934; b) J. Guern, H. Felle, Y. Mathieu, A. Kurkdjian, in *International Review of Cytology, Vol. 127* (Eds.: K. W. Jeon, M. Friedlander), Academic Press, **1991**, pp. 111-173.

[40] a) S. Gille, M. Pauly, *Front. Plant Sci.* **2012**, *3*; b) M. Pauly, V. Ramírez, *Front. Plant Sci.* **2018**, *9*.

CHAPTER VI

COMPUTATIONAL EXPLORATION ON THE REACTION MECHANISMS AND THE ORIGIN OF THE SELECTIVITY IN ASYMETRIC ORGANOCATALYTIC PROCESSES

6.1 Introduction

6.1.1 Evolution and advantages of organocatalysis

Since the infamous thalidomide case more than 60 years ago, the industry of drug discovery has evolved from commercializing racemic mixtures to the synthesis of enantiopure compounds. In this context, the publication in 1992 of the document "Development of new stereoisomeric drugs" by the Food and Drug Administration served as a point of no return. This document stated that "unless it proves particularly difficult, the main pharmacological activities of the isomers should be compared in in vitro systems, in animals and/ or in humans". [1] These facts created a growing interest in the synthesis, separation, and identification of these chiral compounds.

Concerning the synthesis of enantiopure compounds, three main approaches can be used: [2] (i) resolution of racemic moistures, (ii) synthesis from the chiral pool, and (iii) synthesis from prochiral substrates. This last methodology is based on the use of chiral catalyst whose chiral information is transferred to a non-chiral substrate. These chiral catalysts can be enzymes (biocatalysis), metal complexes (metal catalysis) or small organic molecules (organocatalysis).

Nowadays, asymmetric organocatalysis has been earning attention because of their multiple advantages compared to metal and enzyme catalysis. While metal catalysis suffers from hazardous compounds or special reaction conditions such as inert atmospheres, and enzyme biocatalysis must deal with expensive costs, high substrate specificity and reduced reaction conditions, organocatalysts are generally cheap, stable, easy to handle, soluble in most organic solvents and effective under mild conditions.

While in metal catalysis the type and nature of the interactions between the catalyst and the substrate can vary significantly, in organocatalysis those interactions, and all the chemical reactions derived from them can be resumed in two generic activation modes: covalent and non-covalent organocatalysis (**Scheme 6.1**). [3]

Covalent organocatalysis is based on the reversible formation of a reactive intermediate through the creation of covalent interactions between the substrate and the catalyst. [4] While other examples of activation exists, such as activation via nitrogen heterocyclic compounds (NHC), [5] phosphines, [6] carbonyl compounds [7] or iodine derivatives, [8] the primary examples of covalent organocatalysis are aminocatalysis, which includes enamine and iminium-ion catalysis, and Lewis base catalysis.

On the other hand, in non-covalent organocatalysis, the interactions responsible for the reaction are weak interactions, [9] such as hydrogen bonding, [10] or ionic interactions, as seen in phase transfer catalysis. [11]

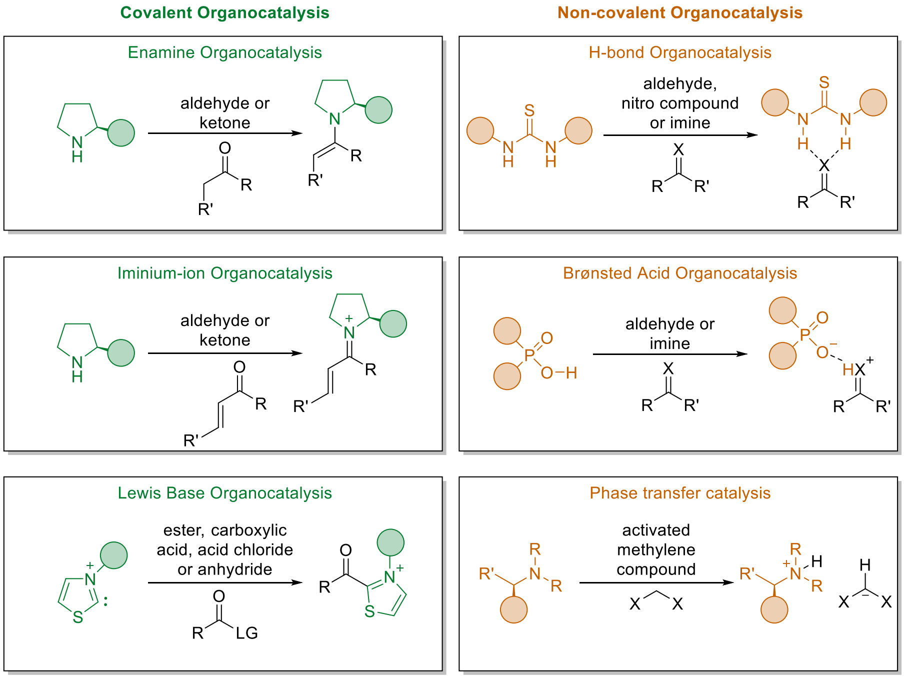
Covalent Organocatalysis
Non-covalent Organocatalysis
Enamine Organocatalysis
aldehyde or ketone
H-bond Organocatalysis
aldehyde, nitro compound or imine
Iminium-ion Organocatalysis
aldehyde or ketone
Brønsted Acid Organocatalysis
aldehyde or imine
Lewis Base Organocatalysis
ester, carboxylic acid, acid chloride or anhydride
Phase transfer catalysis
activated methylene compound

Scheme 6.1: *Examples of the main organocatalytic activation modes.*

6.1.2 Enamine organocatalysis

Enamine organocatalysis is based on the covalent activation of carbonyl compounds, typically aldehydes or ketones, by forming electron-enriched enamines through the interaction with secondary amines. These enamines can act as nucleophiles in a wide range of reactions, including Mannich reactions, Michael additions, and various α-functionalizations. [12] The catalytic cycle for the nucleophilic addition of a ketone (i.e. acetone) to an aldehyde is illustrated in **Scheme 6.2**.

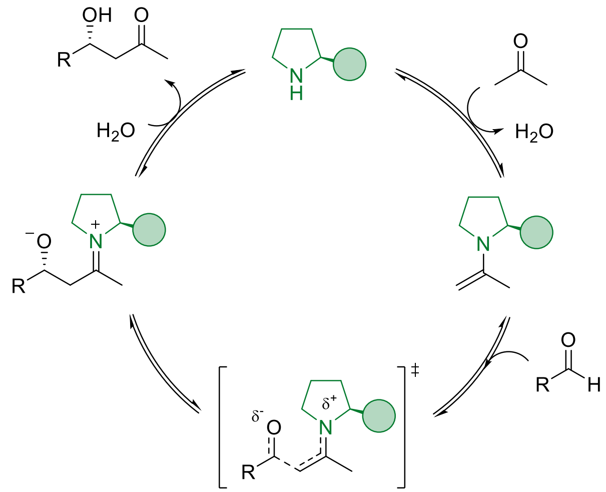

Scheme 6.2: *Simplified catalytic cycle for the intermolecular aldol reaction using acetone.*

The cycle starts with the condensation of the ketone with the proline catalyst, forming the corresponding enamine. This enamine acts as a nucleophile in the reaction with the aldehyde, resulting in the formation of a β-alkoxy-iminium. After hydrolysis and protonation, the final β-hydroxy-ketone is obtained. The interactions with the proline's substituent are the main cause of the enantioselectivity of the reaction. Consequently, various differently substituted pyrrolidines have been developed to establish different interactions with the substrate, thereby modulating the catalyst activity. **Figure 6.1** displays two of the most renowned enamine organocatalysts, L-proline and Jørgensen-Hayashi catalyst, along with their corresponding TSs in the reaction with acetone. It is worth noting that despite employing the same activation mode, different interactions between the catalyst and the substrate result in a distinct reactive face of the enamine in each case. When using L-proline, both enamine and H-bond organocatalysis operate simultaneously, leading to a predominant addition on the most hindered face. Such situations can introduce ambiguity when determining, a priori, the major product's enantiomer in a given reaction. As a result, computational calculations are typically necessary. [13]

All these facts: the high functionalization possibilities, the variability in catalyst selection and the high enantioselectivities that can be obtained, make enamine organocatalysis an important tool in the preparation of complex structures with high levels of enantioselectivities. Furthermore, enamine organocatalysis is compatible with other types of catalysis, such as NHC, [14] iminium, [15] or metal catalysis, [16] which increases even more the interest and applicability of this type of catalysis.

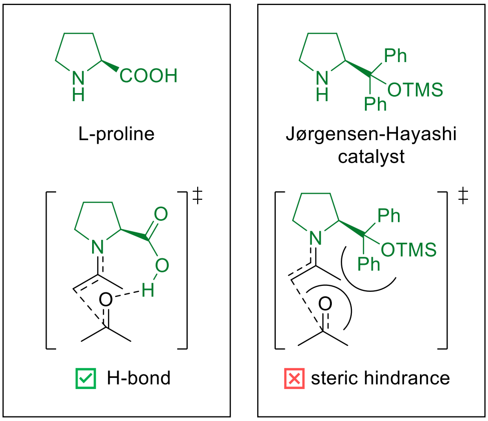

Figure 6.1: *Comparative between L-proline and Jørgensen-Hayashi catalyst interactions for the same face nucleophilic attack in the reaction with acetone.*

6.1.3 Iminium-ion organocatalysis

Iminium organocatalysis relies on similar principles and catalysts as enamine organocatalysis but with an α,β-unsaturated ketone or aldehyde. These unsaturated structures create an iminium intermediate whose LUMO is more stabilized than that of the uncondensed reactant, enhancing its reactivity as electrophiles, typically at the β position. The catalytic cycle that operates in this scenario is depicted in **Scheme 6.3**. Similar to enamine activation, multiple substrates and catalysts can be employed, usually achieving enantiomeric excesses above 90%.

Even the iminium ion generated can be used as a simple electrophile, reacting with a wide range of nucleophiles. [17] Among these reactions, cycloadditions and conjugate additions have garnered more attention.

Conjugate additions occur due to the formation of an enamine intermediate after the nucleophile inserts at the β position. Similar to the previous section, this enamine can interact with electrophiles at its α position, enabling double functionalization. The combination possibilities of these conjugate additions are one of the strongest advantages of these processes, encompassing a variety of aromatic and heteroaromatic compounds. [18] On the other hand, the range of cycloadditions that can be performed also include multiple processes, such as [4+2], [19] [3+2], [20] and [4+3]. [21]

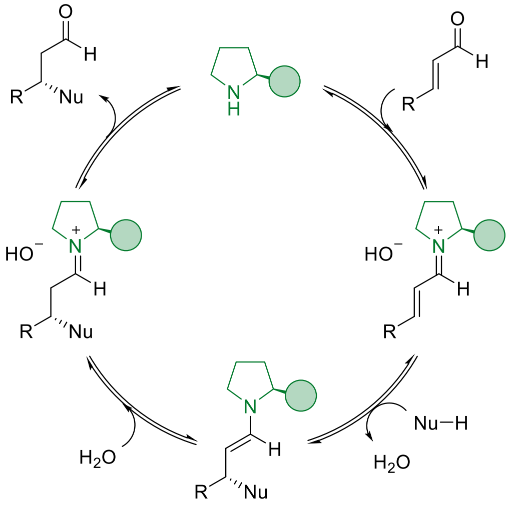

Scheme 6.3: *Simplified catalytic cycle for the iminium activation.*

In conclusion, iminium activation has emerged as a powerful strategy in modern synthetic chemistry, enabling the efficient and enantioselective synthesis of a wide range of complex molecules. Its advantages, including mild reaction conditions, cost-effectiveness, and environmental sustainability, make iminium activation hold great potential for the development of new synthetic methodologies and the production of valuable chemical compounds.

6.1.4 Lewis base organocatalysis

Lewis base organocatalysis is based on the formation of an acid-base adduct between the substrate and a Lewis base, which acts as the organocatalyst, thereby increasing the reaction rate. The binding of the Lewis base to the substrate typically results in an increased electron density on the starting material, enhancing its nucleophilic properties. However, the potential to enhance its electrophilic properties also exists, depending on the orbital interaction between the donor and the acceptor. [22]

The largest family of Lewis base catalyst is based on the interaction between the nonbonding electron pair of a Lewis base and a π* acceptor orbital from the substrate (n-π*). This interaction commonly involves unsaturated functional groups such as alkenes, alkynes or carbonyls. [23] A typical example of this catalysis using a carbonyl as the acceptor, is depicted in **Scheme 6.1**. In the case where the carbonyl is a ketone, the attack of the Lewis base leads to the formation of a zwitterionic, tetrahedral intermediate, enhancing the nucleophilicity of its oxygen atom. If the carbonyl compound contains a leaving group (LG), as shown in the example of **Scheme 6.1**, the tetrahedral intermediate collapses to form a new carbonyl compound with an enhanced electrophilic character at its sp^2 carbon atom. The fact that a Lewis base can promote both types of activations is a unique characteristic of this activation method.

However, other types of orbital interactions, such as n-σ* and n-n*, although less-well known, can be also found in the literature. These interactions require a Lewis acceptor capable of expanding its coordination sphere (**Scheme 6.4**). [24]

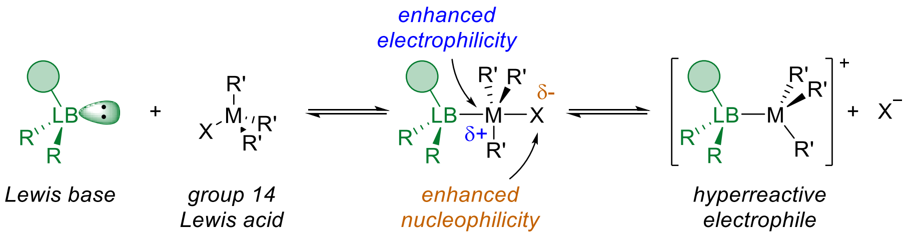

***Scheme 6.4**: Reactivity in n- σ* Lewis base catalysis.*

A wide range of examples of Lewis base organocatalyst can be employed, with the most common ones being tertiary amines, phosphines, ang NHC carbenes. [25]

6.1.5 Phase transfer catalysis

Phase transfer catalysis (PTC) consist of the use of small organic molecules that, via electrostatic interactions (non-covalent), transfer one of the substrates from one phase to another, thereby favoring the reaction. Although each system may have its particular mechanism, a general pathway is illustrated in **Scheme 6.5**. In that image, two different catalytic processes are observed. The first one is the primary objective of the PT catalyst, which is to facilitate the transfer of all reactants to the same phase. In this case, the hydroxide anion is transferred from the aqueous to the organic phase, where the deprotonation of the ketone occurs. The second process involves the interaction of the PT catalyst with the enolate through electrostatic interactions, promoting enantioselective electrophilic addition at the α position. This situation is not mandatory for PTC but is necessary if any enantiomeric induction is desired.

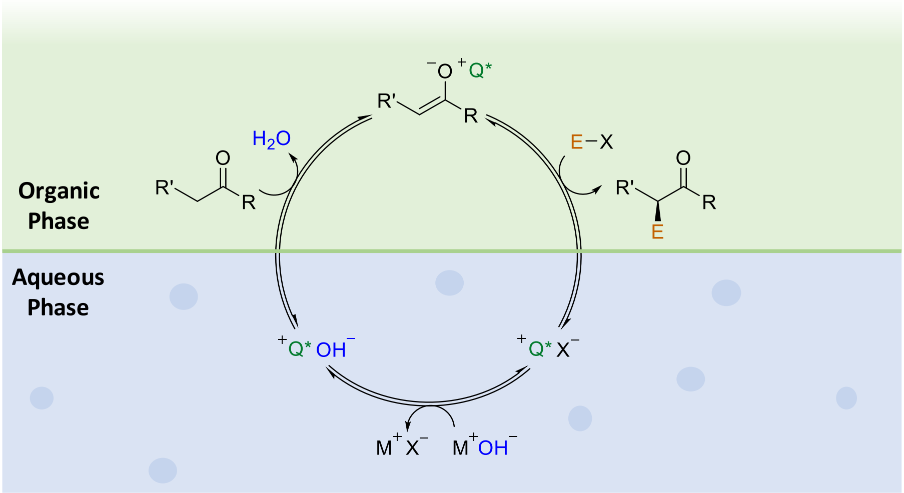

Scheme 6.5: *Example of phase transfer catalysis with enantiomeric induction*

Following the same principle, although using different schemes, numerous reactions have been developed. Various electrophiles have been tested, including Michael acceptors, aldehydes, imines, azoderivatives or haloalkenes, for alkylating the corresponding enolates. [11a, 26]

The catalysts employed for these reactions are generally based on quaternary amines or crown ethers. As depicted in **Figure 6.2**, the most commonly used PT catalyst are chiral, aiming to induce enantioselectivity in the reaction. Consequently, is common to see cinchona alkaloids, quaternary amines derived from BINOL, or crown ethers derived from carbohydrate as catalysts.

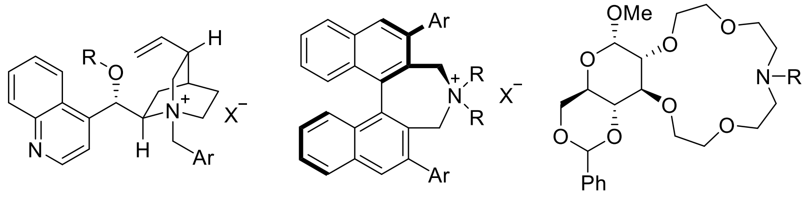

chincona alkaloid derived quaternary ammonium salt

BINOL derived quaternary ammonium salt

Sugar derived crown ether

Figure 6.2: *Common catalysts for PTC.*

6.1.6 Hydrogen bond and Brønsted acid catalysis

These activation modes are the most well-known in non-covalent organocatalysis. The catalytic activity can be attributed to the catalyst's ability to form hydrogen bond interactions with the substrate, thereby lowering their LUMO energy and activating them for nucleophilic additions.[27] **Figure 6.3** illustrates the changes in orbital energies and the electrostatic potential upon the addition of a hydrogen bond catalyst to formic acid. It is noteworthy that the addition of the organocatalyst not only lowers the LUMO energy of formic acid, but also increases the electrostatic potential for the carbon atom of formic acid, enhancing its electrophilicity. Depending on the substrate's basicity, either H-bond or Brønsted acid catalysis can operate. Asa a result, many times the distinction between the two is ambiguous.

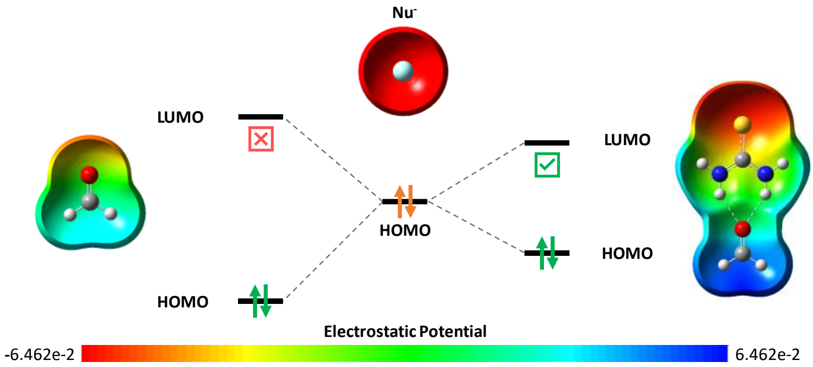

Figure 6.3: *Representation of the molecular orbitals implied on the nucleophilic addition of a nucleophile (Nu) to formaldehyde with and without thiourea. Electrostatic potential for both structures is displayed calculated at M062x/6-31G level of theory.*

Similar to PTC, bifunctional organocatalysis can be performed using chiral and bulky organocatalysts to achieve varying levels of enantioselectivity in the desired reaction. Thioureas, diols and phosphoric acids are the most extensively utilized organocatalysts in these fields. The extensive use of thioureas and diols in H-bond organocatalysis is primarily due to their ability to form double hydrogen bonds with the substrate. On the other hand, phosphoric acids, particularly BINOL-derided ones, are well-known in Brønsted acid catalysis due to their conformational rigidity, multiple substitution possibilities at their 3 and 3' positions, and the presence of an acid hydrogen adjacent to a Lewis basic site. **Figure 6.4** depicts the main activation mechanisms and provides some examples of catalysts.

While carbonyls are the most commonly activated group in this catalysis, other groups such as imines, nitroalkenes, epoxides, and other electron-deficient species can also be activated. Like other types of organocatalysis, a wide range of reactions can be performed on the activated substrates, including Friedel-Crafts, aldol, Michael or Mannich reactions, with the potential to render them enantioselective. [28]

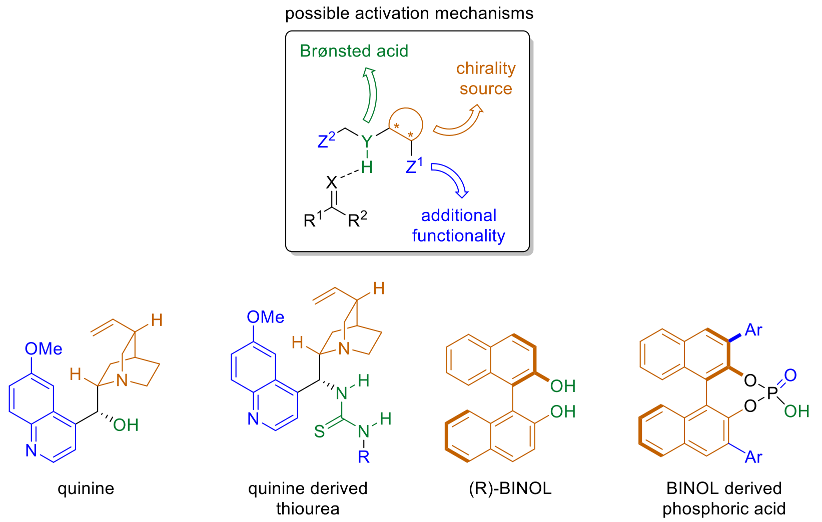

quinine

quinine derived thiourea

(R)-BINOL

BINOL derived phosphoric acid

Figure 6.4: (Up) *principal activation mechanism scheme for H-bond and Brønsted acid catalysis.* ***(Bottom)*** *Examples of the most used catalysts for H-bond and Brønsted acid catalysis.*

Unravelling the outcome of an organocatalytic process is a challenging task.[4] This difficulty arises due to the presence of multiple groups in both the substrates and the catalyst, as well as the small energy differences that may play a role in the step that determines selectivity. Therefore, it is crucial to conduct a comprehensive study of the mechanism of the specific reaction.

In this chapter, several enantioselective organocatalytic processes will be examined from a theoretical perspective, taking into account experimental results made in collaboration with the group of Prof. José Luis Vicario from the University of the Basque Country (Bilbao). The discussion will revolve around the selectivity of these reactions, which necessitates a precise characterization of all the involved mechanisms. Each stationary point will be analysed, with a particular emphasis on the concertedness of each reaction and the step that determines selectivity. The focus will primarily be on activation mechanisms such as H-bonding, Brøsted acid activation, and amine activation.

6.2 Results and discussion

6.2.1 Enantioselectivity characterization of the transannular aminohalogenation of enesultams

6.2.1.1 Introduction

Transannular reactions are intramolecular processes in which the two reacting points are part of a preceding cycle, resulting in the formation of two fused cycles from the previous one (**Scheme 6.6**). These reactions serve as a powerful approach for synthesizing relatively complex polycyclic structures. [29]

Due to the rigid geometry of the starting material, transannular reactions often exhibit high stereocontrol compared to both intermolecular and common intramolecular processes. As a result, there are numerous examples in the literature showcasing highly diastereoselective transannular reactions utilizing chiral starting materials [30] However, instances with achiral starting materials are relatively scarce. [31] Similarly, while there are several documented examples of transannular aminohalogenations in the literature, the majority of them rely on enantioenriched chiral starting materials. [32]

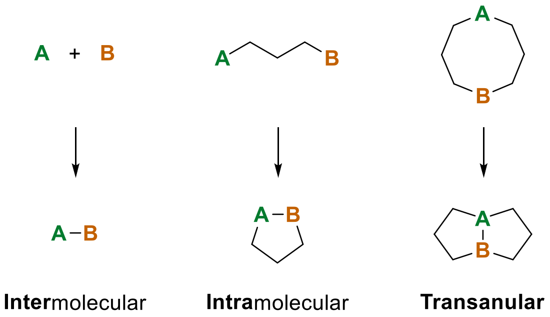

Scheme 6.6: *Comparison between intermolecular, intramolecular, and transannular reactions.*

In this section, an enantioselective transannular aminohalogenation is presented, utilizing achiral enesultams as starting materials. The reaction is catalyzed by a Brønsted acid, and different bromine sources are studied: a soluble halogenating reagent like NBS, as well as an insoluble electrophilic halogen source that requires the use of a phase transfer catalyst (**Scheme 6.7**).

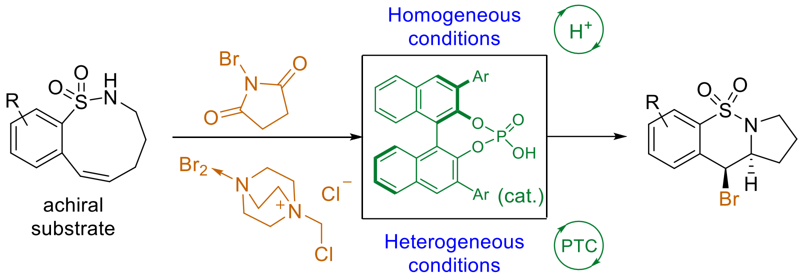

Scheme 6.7: *Stereocontrolled transannular aminohalogenation reactions.*

Both methodologies were optimized by the group of Prof. Vicario, and their scopes were evaluated, with the PTC approach proving to be the most robust option for conducting the reaction. A summary of these results is presented in **Table 6.1**. Interestingly, the reaction demonstrated effectiveness even in the absence of an acid catalyst, albeit with significantly longer reaction times (entries 1 and 2). It should be noted that this background reaction likely occurs without enantiocontrol in most cases, so longer reaction times in catalyzed reactions can lead to lower enantioselectivities in certain instances.

In the one-phase methodology, the inclusion of 5% succinimide led to an increase in enantioselectivity from 61% to 84% (entries 3 and 4), possibly due to the activation of the halogenating agent during the initial stages of the acid-catalyzed reaction. [33] Improved enantioselectivities were observed when electron-withdrawing groups were present in the *para-* position relative to the sulfonamide group in the starting material (entries 5-8). However, when the substituent was moved to the *meta-* position, this trend was reversed (entries 9 and 10). The size of the sulfonamide ring also played a crucial role in the reaction. An eight-member ring sulfonamide failed to yield the aminobrominating adduct, while a ten-member ring provided a better yield, albeit in the form of a racemic mixture (entries 11 and 12). For the biphasic methodology, the reaction was less influenced by the aromatic ring substitution (entries 16-18), and better yields and enantioselectivities results were obtained.

To provide a rational explanation for the reactivity observed, computational studies were conducted. These studies aimed to explore both the regio- and enantioselectivity and offer a comprehensive understanding of the reaction mechanism. As a starting point, Entry 1 from **Table 6.1** was chosen as a model for studying the reaction. Prior to analyzing the reaction mechanism, it is crucial to assess the molecular flexibility and identify the minimum energy conformations for each species involved in the reaction.

Table 6.1: *Best reaction condition screening and scope of the enantioselective transannular aminohalogenation of enesultams.*

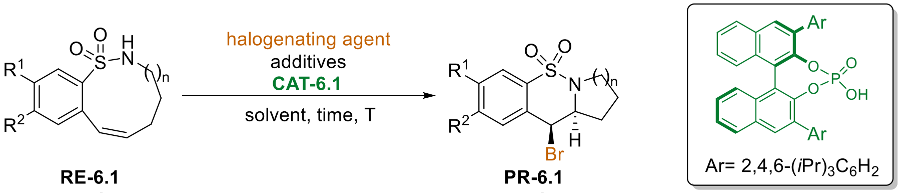

RE-6.1 a-i **PR-6.1 a-i**

		R^1	R^2	n	Additives	Solvent	T (°C)	Time	% Yield [b]	% ee [c]
NBS [a]	1	-H	-H	1	-	toluene	RT	15 min	89	65
	2 [d]	-H	-H	1	-	toluene	RT	3 h	70	-
	3	-H	-H	1	-	mesitylene	RT	15 min	92	74
	4	-H	-H	1	5% succinimide	mesitylene	RT	15 min	92	84
	5	-H	$-CF_3$	1	5% succinimide	mesitylene	RT	30 h	80	90
	6	-H	-F	1	5% succinimide	mesitylene	RT	1 h	85	64
	7	-H	-OMe	1	5% succinimide	mesitylene	RT	15 min	97	18
	8	-H	-Me	1	5% succinimide	mesitylene	RT	45 min	92	28
	9	-Me	-H	1	5% succinimide	mesitylene	RT	15 min	87	60
	10	$-CF_3$	-H	1	5% succinimide	mesitylene	RT	2 days	81	22
	11	-H	-H	0	5% succinimide	mesitylene	RT	30 h	< 5	n.d. [e]
	12	-H	-H	2	5% succinimide	mesitylene	RT	15 min	81	< 2
Br_2-PTC [f]	13	-H	-H	1	1 eq. Na_2CO_3	mesitylene	RT	3 h	92	79
	14	-H	-H	1	1 eq. Na_2CO_3	mesitylene	0	4.5 h	86	86
	15	-H	-H	1	1 eq. Na_2CO_3	mesitylene/hexane (1:1)	0	23 h	95	91
	16	-H	-OMe	1	1 eq. Na_2CO_3	mesitylene/hexane (1:1)	0	23 h	94	68
	17	-H	-Me	1	1 eq. Na_2CO_3	mesitylene/hexane (1:1)	0	23 h	97	76
	18	$-CF_3$	-H	1	1 eq. Na_2CO_3	mesitylene/hexane (1:1)	0	23 h	95	74

[a] *Reactions were performed with 0.072 mmol of enesultam, NBS (0.072 mmol) and catalyst* ***CAT-6.1*** *(5 mol%) in the selected solvent (0.5 M). [b] Isolated yield after flash column chromatography purification. [c] Calculated by HPLC on chiral stationary phase. [d] No catalyst added in this experiment. [e] n.d.: not determined. [f] Reactions were performed with 0.05 mmol of enesultam, halogenating agent (0.065 mmol), catalyst* ***CAT-6.1*** *(10 mol%) in the selected solvent (0.5 M).*

6.2.1.2 Results and discussion

It is widely known that 9-membered carbocycles exhibit various conformations with similar energies that can be readily interconverted through pseudorotation. [34] However, the presence of a fused aromatic ring, an endocyclic double bond, and the sulfonamide group introduce additional strains, preventing a systematic conformational analysis of the 16 symmetrical configurations of the carbocycle. [35]

*Instead, an MD study was conducted, which revealed the presence of two distinct conformers: a predominant conformer, **RE-A-6.1**, and smaller amounts of a second conformer, **RE-D-6.1**.*

Figure 6.5 illustrates the MD results based on the two more flexible dihedral angles α and β, and depicts the geometries of both conformers, **RE-A-6.1** and **RE-D-6.1**.

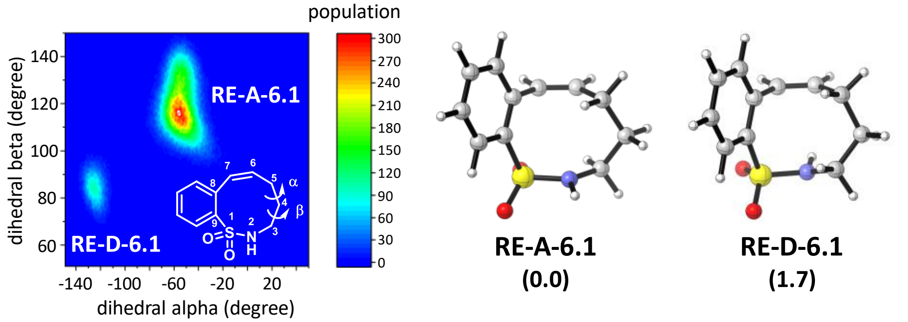

***Figure 6.5:** **(Left)** Conformational analysis of the starting enesultam by using MD simulations. Population analysis was carried out with 250.000 snapshots. The representation was made based on the more flexible dihedral angles α and β. **(Right)** Optimized structures at wb97xd/def2svp/SMD=toluene level of theory for the isomers **RE-A-6.1** and **RE-D-6.1** of the starting enesultam along with the relative energy in kcal/mol at wb97xd/def2tzvp/SMD=toluene//wb97xd/def2svp/SMD=toluene.*

Interestingly, despite being the most abundant conformers, both structures exhibit a perpendicular arrangement between the aromatic ring and the endocyclic double bond, which hinders electronic conjugation between these groups. The primary structural differences between **RE-A-6.1** and **RE-D-6.1** lie in the disposition of the endocyclic atoms 1-3. Since there is no direct TS connecting both conformers, a conformational search was necessary using Macromodel software to construct a conformational pathway to find the RDS (rate-determining stage) in the transformation between **RE-A-6.1** and **RE-D-6.1**.

Moreover, both conformers expose the same face of the endocyclic alkene to the exterior of the ring. However, since the reaction is enantioselective, the other face of the alkene must also be accessible for the reaction. Hence, structures with the opposite alkene face were also explored in the study.

Among all the obtained conformers for the starting enesultam, a conformational pathway with the lowest energy barriers was established, obtaining 6 distinct geometries and their corresponding enantiomers (**Figure 6.6, left**). It was determined that **RE-A-6.1** and **RE-D-6.1** are separated by 3 TSs and 2 energy minima corresponding to **RE-B-6.1** and **RE-C-6.1**. The TS associated with the lowest barrier for alkene face change was originated from the **RE-D-6.1** geometry, and exhibited a barrier of 17.1 kcal/mol. The IRC of this TS led to the formation of structure **RE-E-6.1**, which could further progress through two additional TSs to yield the enantiomer of structure **RE-A-6.1** (**RE-entA-6.1**), thereby restarting the cycle.

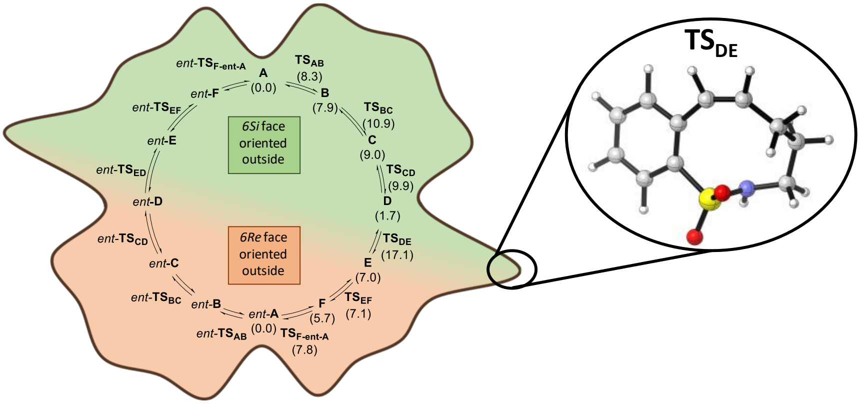
ent-TS$_{F\text{-}ent\text{-}A}$
A
(0.0)
TS$_{AB}$
(8.3)
B
(7.9)
ent-F
ent-TS$_{EF}$
TS$_{BC}$
(10.9)
C
(9.0)
6Si face oriented outside
ent-E
ent-TS$_{ED}$
TS$_{CD}$
(9.9)
D
(1.7)
ent-D
6Re face oriented outside
ent-TS$_{CD}$
TS$_{DE}$
(17.1)
E
(7.0)
ent-C
ent-TS$_{BC}$
ent-B
TS$_{EF}$
(7.1)
F
(5.7)
ent-A
(0.0)
ent-TS$_{AB}$
TS$_{F\text{-}ent\text{-}A}$
(7.8)
TS$_{DE}$

Figure 6.6: (Left) *Pseudorotational itinerary of lower energy for the starting enesultam along with a representation of the energetic profile (brown line), and the relative energy in Kcal/mol. The enantiomeric series relative energies, along with the prefix RE- and the suffix -6.1 in each structure are omitted for clarity.* ***(Right)*** *Optimized structure of the RDS TS for the pseudorotational itinerary at wb97xd/def2svp/SMD=toluene level of theory along with the relative energy in kcal/mol at wb97xd/def2tzvp/SMD=toluene//wb97xd/def2svp/SMD=toluene.*

The only structure in which the fused aromatic ring and the endocyclic double bond adopt a planar arrangement is observed in the face change TS, **TS_{DE}-6.1**, which represents the highest conformational transition state. This finding suggests that the strain within the cycle prevents electronic conjugation between these groups (**Figure 6.6, right**). The calculated kinetic constant for this barrier is 0.12 s^{-1} with a corresponding half-life ($t_{1/2}$) of 6 s at 0 °C, indicating a relatively slow conformational racemization, which is in agreement with the experimental observations.

In the cyclization reaction, the nitrogen atom will attack the 6*Re* face of the alkene in conformers **RE-A-6.1** and **RE-D-6.1**, while it will attack the opposite 6*Si* face in conformers **RE-entA-6.1** and **RE-entD-6.1**. Since there exists a conformational equilibrium connecting both enantiomeric series, the entire process can be regarded as a dynamic kinetic resolution (DKR). According to the Curtin-Hammett principle, [36] this scenario would require one of the enantiomers to undergo a faster reaction compared to the other, as well as a significantly faster equilibration between both conformers.

For the study of the cyclization reaction with the catalyst, the proposed catalytic cycle from **Scheme 6.8** was examined. The initial step of the catalytic cycle involves the formation of the catalytically active species **C1-6.1**, which is formed by the interaction between the phosphate acid **PA-6.1** and the bromine source, as reported by Denmark and Burk. [33] The coordination between the bromine source and the enesultam **RE-6.1** leads to the formation of the encounter pair **EP-6.1**. At this point, two different mechanisms can occur. The first mechanism corresponds to a stepwise process, where the first transition state (**TS1-6.1**) defines the insertion of the bromine atom into the double bond, resulting in the formation of the bromiranium intermediate **IN-6.1**. Subsequently, the nitrogen atom undergoes an intramolecular attack, breaking the bromiranium ring through **TS2-6.1** and giving rise to the formation of **PR-H-6.1**. The deprotonation of **PR-H-6.1** leads to the formation of the final product **PR-6.1**, which completes the catalytic cycle and regenerates the catalytically active species **C1-6.1**.

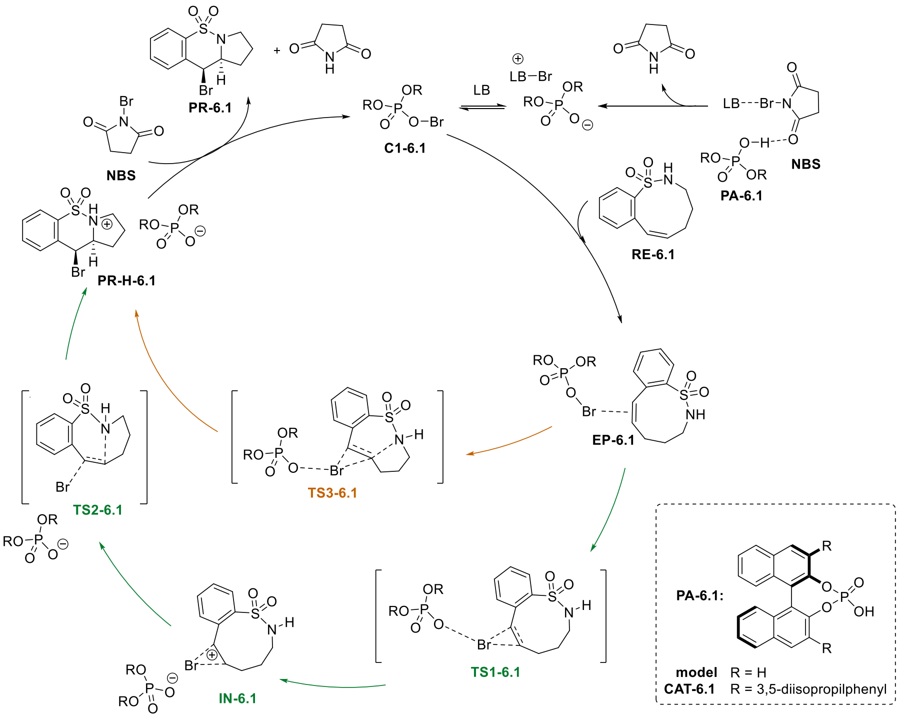

Scheme 6.8: Catalytic cycle for the enantioselective transannular reaction of ***RE-6.1****.*

The second plausible mechanism corresponds to a concerted process in which **EP-6.1** is directly transformed into **PR-H-6.1** via a single transition state (**TS3-6.1**). This mechanism is supported by the short distance between the double bond and the nitrogen atom, which is facilitated by their mutual presence in the carbocycle.

For this study, the focus will be on the transformation of **EP-6.1** to **PR-H-6.1**. Any alternative interaction between the catalytic species **C1-6.1** and the starting enesultam can be disregarded since the anti-disposition of the bromiranium cycle and the nitrogen atom is necessary for the nucleophilic attack to occur.

Considering that other conformers of the starting enesultam had high energy values, only the geometries of **RE-A-6.1**, **RE-D-6.1**, **RE-entA-6.1**, and **RE-entD-6.1** will be used to construct the starting encounter pairs, namely **EP-A-6.1** and **EP-D-6.1** for the 6*Si* face attack, and **EP-entA-6.1** and **EP-entD-6.1** for the 6*Re* face attack. To reduce computational costs, a simplified chiral structure, (*R*)-BINOL-phosphoric acid, will be used as a model for the actual catalyst **CAT-6.1**.

After an exhaustive exploration of the PES, the lowest transition states (**TS1-A-6.1** and **TS1.entA-6.1**) for the insertion of the bromine atom into the alkene were identified. IRC calculations from these points confirmed the stepwise mechanism and allowed the determination of their respective intermediates, **IN-A-6.1** and **IN-entA-6.1**, which were found to be only 1.1 and 2.1 kcal/mol below their respective transition states. This indicates a relatively low stabilization of these intermediates.

Previous studies have reported that brominations of alkenes conjugated with aromatic rings exhibit inverse regioselectivity and form benzylic carbocationic intermediates instead of bromiranium rings, thanks to the strong ability of the aromatic ring to stabilize the resulting positive charge.[37] However, as mentioned earlier, the cyclic structure of the enesultam enforces an anti-planar arrangement of the double bond with respect to the aromatic ring, preventing electronic conjugation and thereby impeding the stabilization of the hypothesized benzylic cation intermediate.

Figure 6.7 illustrates the optimized geometries of **TS1-A-6.1**, **TS1-entA-6.1**, and their respective intermediates. Upon examining the TSs, it can be observed that both structures exhibit nearly equal distances, with a shorter C-Br distance at the benzylic position, indicating the development of an initial positive charge at the homobenzylic position. NCI calculations revealed a stabilizing interaction between this homobenzylic position and the endocyclic nitrogen atom, which is also maintained in their corresponding intermediates, **IN-A/entA-6.1**. This interaction, combined with the lack of electronic conjugation between the alkene and the aromatic ring, serves as the primary factors contributing to the *a priori* reverse regioselectivity observed in brominations of aromatic-conjugated alkenes.

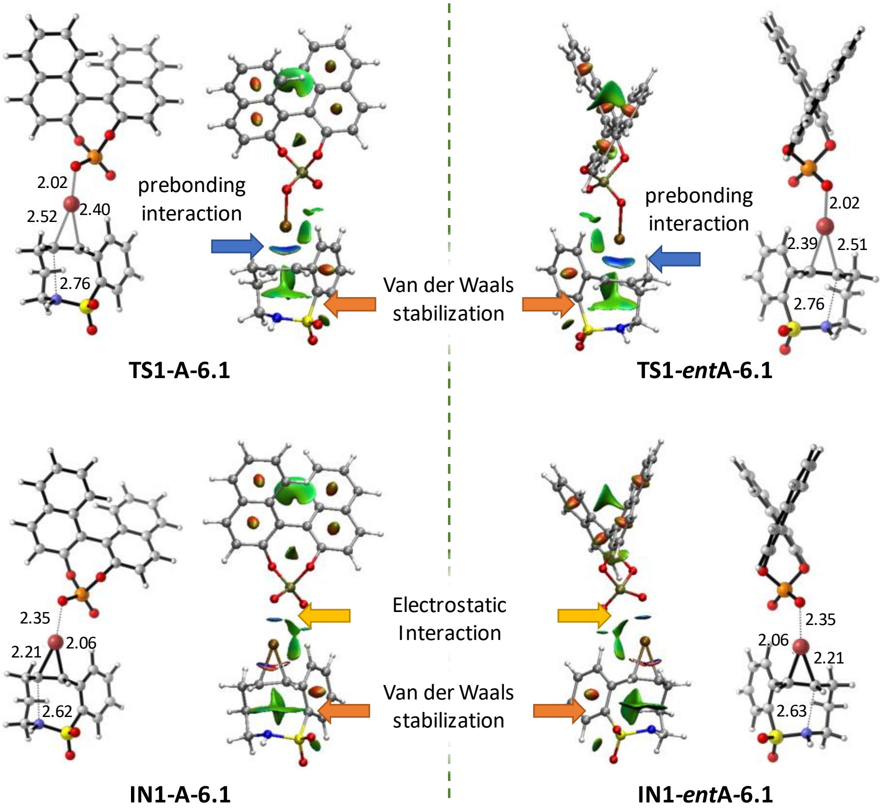
2.02
2.52
2.40
2.76
prebonding interaction
Van der Waals stabilization
prebonding interaction
2.02
2.39
2.51
2.76
TS1-A-6.1
TS1-*ent*A-6.1
2.35
2.21
2.06
2.62
Electrostatic Interaction
Van der Waals stabilization
2.35
2.06
2.21
2.63
IN1-A-6.1
IN1-*ent*A-6.1

Figure 6.7: *Optimized geometries (wb97xd/def2svp/SMD=toluene) of* ***TS1-A-6.1****,* ***TS1_entA-6.1*** *and their respective intermediates along with their NCI calculations.*

It can be observed that the extensive blue prebonding interactions in **TS1_A/entA-6.1** transform into smaller lenticular interactions in the intermediates, which are more characteristic of electrostatic interactions. Additionally, the O-Br distances increase from 2.02 Å at the TS to 2.35 Å in **IN1_A/entA-6.1**. These two observations appear to support the ionic pair nature of the intermediates. ELF analysis (**Figure 6.8**) further confirmed the ionic pair character of the intermediates by revealing the absence of electronic density between the phosphate and bromine atoms. Despite the dissimilar C-Br distances observed in the intermediates, ELF studies also verified the presence of electronic density surrounding the bromiranium intermediate, thereby confirming the formation of the three-membered ring.

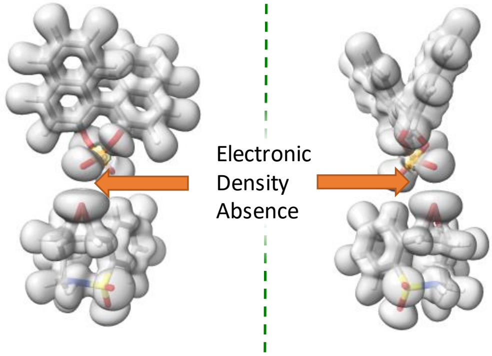

IN1-A-6.1 ***IN1-entA-6.1***

Figure 6.8: *ELF representation for IN1_A/entA-6.1.*

These intermediates must overcome a second TS, **TS2-A/entA-6.1**, during which the endocyclic nitrogen will attack the homobenzylic position, completing the transannular cyclization. The distances observed for the second TSs were nearly identical to those of the intermediates, except for the C6-N bonds, which were reduced to 2.48 Å, and the C6-Br bond, which increased to 2.33 Å due to the formation of the new C6-N bond.

The relative energies for the entire process are depicted in **Figure 6.9** . The calculation of the energy difference between the conformational equilibrium of the enesultam (black) and both reaction paths (green and orange) took into account the formation of the active catalytic species **C1-6.1** as indicated in the initial steps before the catalytic cycle from **Scheme 6.8**. Therefore, the free energy terms of the phosphate acid **PA-6.1** and **NB**S were added to the free energy of the starting enesultam, while only succinimide free energy was added to the EP energies. The thermodynamic difference between both structures indicates that this reaction requires at least 23.5 kcal/mol, which is consistent with the observed DKR-type process, featuring a barrier of 17.1 kcal/mol for the interconversion of both enantiomers. Furthermore, a nearly flat energy surface is observed along the preferred route, starting from **RE-entA-6.1**.

The energy barriers obtained for the RDS of these processes are higher than it should be expected, but still lower than the reaction in absence of catalyst. Introducing the real catalyst may introduce additional interactions that lowers the obtained energy barriers for the whole process. Notice that this new barrier should be higher than the energy needed for the interconversion of both enantiomers of the starting material or no kinetic resolution should be observed.

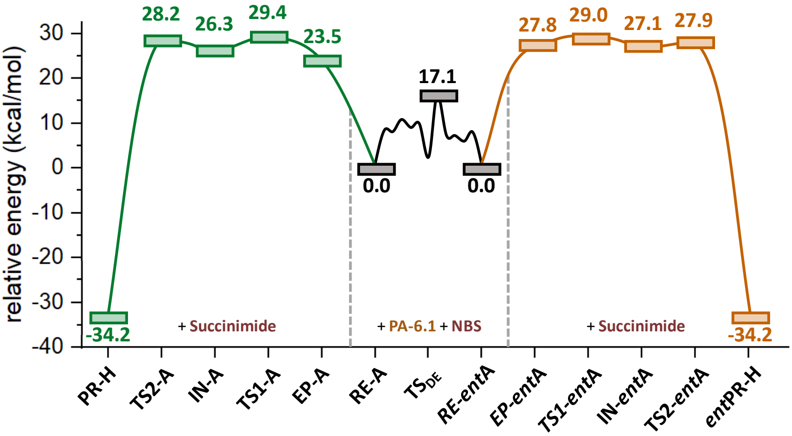

Figure 6.9: *Energy profiles (wb97xd/def2tzvp/SMD=toluene//wb97xd/def2svp/SMD=toluene) for the transformation of the enesultam* ***RE-6.1*** *to* ***PR-H-6.1*** *catalyzed by BINOL phosphoric acid* ***PA-6.1****. The energetic corrections for the summatory of other reactants is depicted below. The suffix -6.1 in each structure is omitted for clarity.*

Once the mechanism has been revealed, the model was expanded by substituting the model catalyst with the real catalyst **CAT-6.1**. After an exhaustive evaluation of conformational variability, **TS1R-A-6.1** and **TS1R-entA-6.1** were obtained as the minimum energy transition states for the first step of the reaction, with relative energy barriers of 23.4 and 24.0 kcal/mol, respectively, with only a difference of 0.6 kcal/mol between both structures.

It can be observed that lower energy barriers were obtained with the real catalyst **CAT-6.1**. NCI calculations depicted in **Figure 6.10** revealed new van der Waals interactions between the enesultam and the 3- and 3'-catalyst substituents, which justifies this energy reduction. The small difference between these barriers correctly predicts the modest enantiomeric ratio observed experimentally in several cases. The energy differences in the real model also justify a DKR-type scenario. These results are in full agreement with the experimental findings, indicating a reaction that is not highly enantioselective and may require hours to complete at room temperature.

However, all attempts to perform IRC calculations from the transition states of the real catalyst were unsuccessful due to the flatness of the PES. Additionally, any other attempts to locate the bromiranium intermediate or the second transition state also proved to be unsuccessful. In order to address this issue, relaxed scans were conducted from the **TS1R-A/*ent*A-6.1** structures in both directions. Downhill pathways were obtained in all cases, suggesting that after the insertion of the bromine atom, the subsequent attack of the endocyclic nitrogen is nearly barrierless.

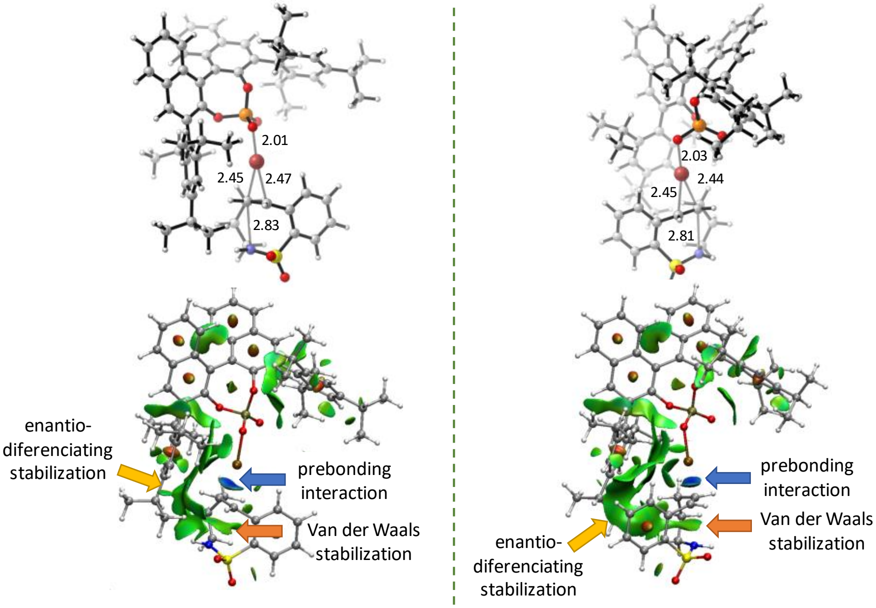
2.01
2.45
2.47
2.83
2.03
2.44
2.45
2.81
enantio-diferenciating stabilization
prebonding interaction
Van der Waals stabilization
prebonding interaction
Van der Waals stabilization
enantio-diferenciating stabilization

TS1R-A-6.1
(24.0)

TS1R-*ent*A-6.1
(23.4)

Figure 6.10: *Optimized geometries (wb97xd/def2svp/SMD=toluene) of the most favored transition structures **TS1R-A-6.1** and **TSR-entA-6.1** with the real catalyst **CAT-6.1**. Relative energies, calculated at wb97xd/def2tzvp/SMD=toluene//wb97xd/def2svp/SMD=toluene level, are given in brackets in kcal/mol.*

A comparison between the transition states of the model catalyst and the real catalyst reveals a more symmetrical insertion of the bromine atom in the real scenario, which appears to be influenced by the bulkiness of the catalyst.

As a result of this more symmetrical approach, the C6 atom of the carbocycle exhibits a lower electron deficiency, requiring less stabilization from the nitrogen atom and consequently increasing the distance between them.

The distinct van der Waals interactions between the 3- and 3'-catalyst substituents and the two enantiomers are primarily responsible for the enantio-differentiation. In **TS1R-A-6.1**, the catalyst establishes non-covalent interactions with the hydrocarbon chain, while in **TS1R-entA-6.1**, these interactions occur with the aromatic ring. This observation suggests that different aromatic substitutions could impact these interactions, altering the relative energy between the two transition states and influencing the observed enantioselectivity, as seen in experimental results.

6.2.1.3 Conclusions

The reaction is significantly influenced by the ring strain, which disrupts the electronic conjugation between the double bond and the aromatic ring.

The lack of conjugation allows for the nearly symmetrical insertion of the bromine atom into the double bond and, in combination with the electronic interactions from the endocyclic nitrogen atom, results in the slight stabilization of the bromiranium intermediate.

The subsequent transformation to the final product was found to occur with minimal barrier, making the first transition state the crucial step for enantio-differentiation.

The enantioselectivity is primarily attributed to the van der Waals interactions between the catalyst substituents and the substrate.

6.2.2 Studying the concertedness of the BINOL-derived Mg(II)/phosphate-catalyzed desymmetrizative ring expansion of 1-vinylcyclobutanols

6.2.2.1 Introduction

Continuing with the halofunctionalization of alkenes, this section focuses on a specific case of enantioselective halofunctionalization of vinyl-alcohols. In the studied cases, following halogen insertion, a semipinacol rearrangement typically occurs, leading to the formation of a carbonyl group and a new quaternary stereocenter (**Scheme 6.9**). [38] The stereoselective formation of these four C-bonded quaternary carbon atoms remains a current challenge, making these reactions valuable tools for the synthesis of quaternary-carbon-atom-containing substrates. While the stereoselective formation of a single C-C bond has been the traditional approach, the desymmetrization of achiral compounds offers several advantages, including easier access to the starting material compared to enantioselective synthesis of a quaternary carbon.

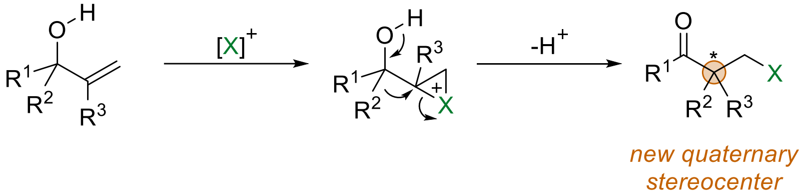

Scheme 6.9: *Semipinacol rearrangement.*

Therefore, this section concerns on semipinacol rearrangements, specifically using alkenyl cyclobutanols as substrates. These derivatives have been previously employed in this type of reaction, [38a, 39] and several enantioselective versions have been explored. [40]

The use of 3,3-disubstituted-1-alkenylcyclobutanes as starting materials for this reaction has only been attempted twice. [41] These substrates lead to the formation of cyclopentane scaffolds containing quaternary carbon stereocenters, [42] which are of great interest due to their presence in many natural products and pharmaceutical ingredients. [43]

Following these examples, the possibility of an enantioselective semipinacol rearrangement of 3,3-disubstituted-1-alkenylcyclobutanes initiated by electrophilic bromination of the alkene moiety was explored (**Scheme 6.10**). This reaction aims to provide 2,2,4,4-tetrasubstituted cyclopentanones with two newly formed stereocenters resulting from the desymmetrization of the starting material.

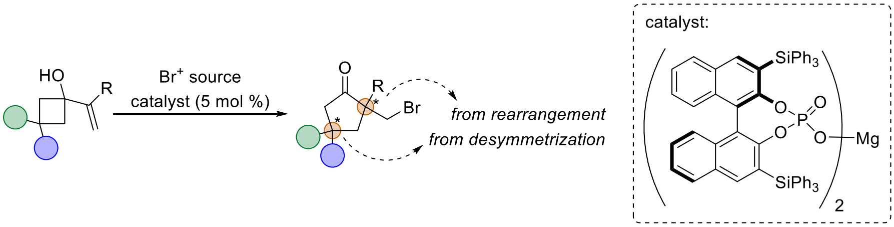

Scheme 6.10: *Catalytic asymmetric desymmetrizative semipinacol rearrangegments of vinyl-cyclobutanols.*

The mechanism of similar semipinacol rearrangements of alkenyl butanols promoted by halogenation of the alkene moiety has been previously studied by Alexakis and co-workers. [40d] They suggested the formation of the bromiranium intermediate based on kinetic measurements, although a highly asynchronous concerted mechanism could not be completely ruled out (**Scheme 6.11a**). Other related mechanistic studies include the sulfenylation-promoted enantioselective rearrangement of alkenyl cyclobutanols, where thiiranium intermediates were identified (**Scheme 6.11b**), [44] and computational studies on the Lewis base-catalyzed semipinacol rearrangement of hydroxycyclobutyl enones, which suggested the absence of intermediates in the rearrangement step (**Scheme 6.11c**). [45]

The bibliography search suggests a stepwise process with a haliranium intermediate. The formation of this intermediate has been previously studied [46] and it has been demonstrated to be a reversible process. [47]

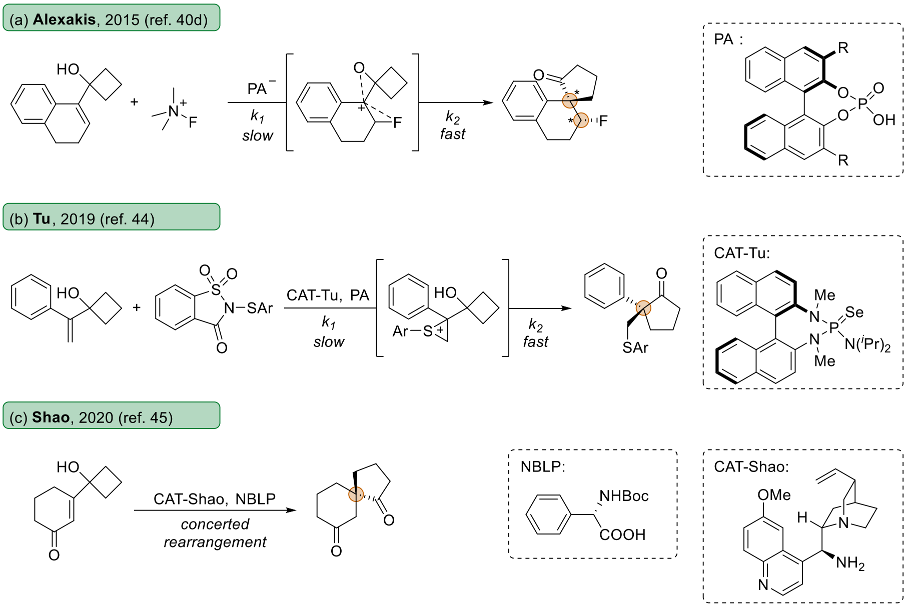
(a) **Alexakis**, 2015 (ref. 40d)
HO
+
PA⁻
k1
slow
k2
fast
PA :
R
O
P
O
OH
R
F
(b) **Tu**, 2019 (ref. 44)
HO
+
S
N−SAr
CAT-Tu, PA
k1
slow
Ar−S+
k2
fast
SAr
CAT-Tu:
Me
N
Se
P
N(iPr)2
N
Me
(c) **Shao**, 2020 (ref. 45)
HO
CAT-Shao, NBLP
concerted
rearrangement
O
NBLP:
NHBoc
COOH
CAT-Shao:
OMe
H
N
NH2
N

Scheme 6.11: *Catalytic asymmetric desymmetrizative semipinacol rearrangements from cyclobutanols.*

With all this data in mind, our collaborators from Bilbao started the process of optimizing the reaction conditions. The selection of the catalyst proved to be a crucial factor in the development of the reaction. BINOL-based phosphoric acids, which have been used previously to promote similar transformations, [40d, 44] did not yield satisfactory results. These catalysts typically resulted in 6:1 mixtures of the products **PR2d-6.2** and **PR2c-6.2** (**Scheme 6.12**), with low yield (22%), moderate diastereoselectivity (7:1), and low enantioselectivity (58:42). However, replacing these BINOL-based phosphoric acids with their corresponding alkaline metal phosphates significantly improved the performance of the reaction, with magnesium phosphate **CAT-6.2** providing the best results in terms of both the yield of isolated **PR2d-6.2** and stereoselectivity. The optimal reaction conditions using this catalyst are displayed in **Scheme 6.12**.

The formation of the side product **PR2c-6.2** is attributed to the intramolecular attack of the alcohol, and since its formation is always possible, mechanistic studies were conducted to determine the factors influencing the selectivity towards both products. Additionally, given the ambiguity in the mechanism of this reaction, the possibility of a concerted pathway will also be explored.

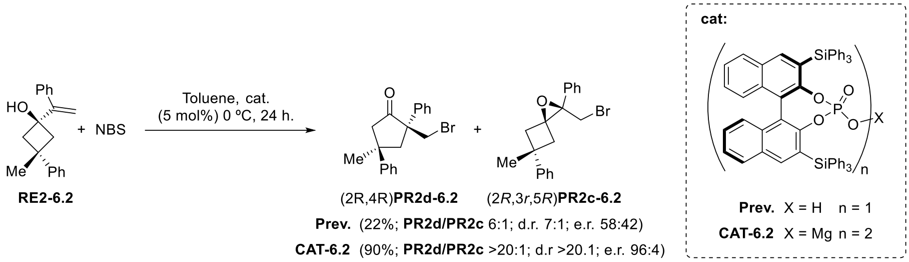
Toluene, cat.
(5 mol%) 0 °C, 24 h.
+ NBS
RE2-6.2
(2R,4R)PR2d-6.2
(2R,3r,5R)PR2c-6.2
Prev. (22%; PR2d/PR2c 6:1; d.r. 7:1; e.r. 58:42)
CAT-6.2 (90%; PR2d/PR2c >20:1; d.r >20.1; e.r. 96:4)
cat:
SiPh3
Prev. X = H n = 1
CAT-6.2 X = Mg n = 2

Scheme 6.12: *Enantioselective desymmetrization of alkenylcyclobutanol* ***RE2-6.2****.*

Two action modes can be proposed for the reaction. The first mechanism involves an H-bond between the alcohol and one of the phosphate moieties, while the metal atom is coordinated to the NBS and another phosphate group (**Figure 6.11**, **A**), as proposed by Masson and co-workers. [48] In the second mechanism, one of the phosphates of the catalyst promotes the deprotonation of the alcohol group, and the alkoxide is then coordinated to the metal atom, which is now coordinated to just one phosphate, the alkoxide, and the NBS (**Figure 6.11**, **B**). It is worth noting that the activation mode mentioned in the previous section has not been considered this time since the presence of a strong Lewis acid, in this case, the magnesium ion, prevents the formation of the P-O-Br adduct **C1-6.**1. In consequence, it should be admitted that the whole process must be better considered as a typical asymmetric catalysis with a chiral Lewis acid rather than a pure organocatalytic reaction.

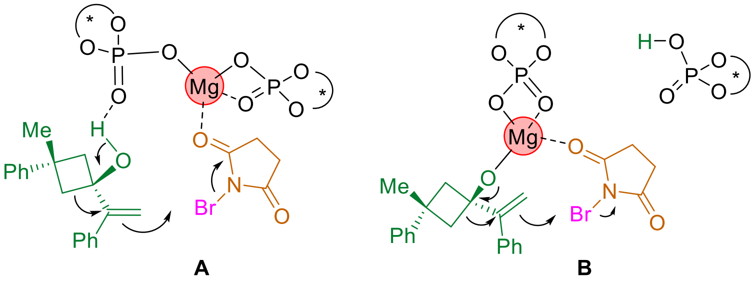

Figure 6.11: *Bromine addition models to the vinyl cyclobutanol* ***RE2-6.2****.*

Since a different number of phosphate units are present in each mechanism, nonlinear effect experiments were conducted to determine the molecularity of the RDS. The study was carried out with a 2.5 mol % catalyst loading, formed in situ from the magnesium salt and different enantiomeric ratios of the chiral phosphoric acid. The obtained results (**Figure 6.12**, **left**) demonstrated a clear linear relationship between the enantiopurity of the catalyst and the enantioselectivity of the reaction, indicating the presence of only one phosphate unit in the RDS (model **B**).

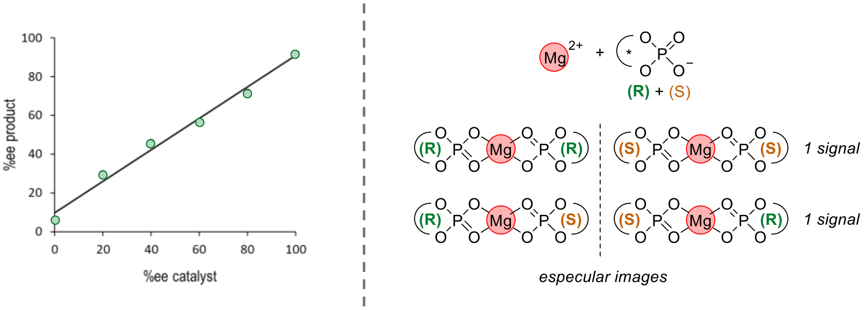

Figure 6.12: (Left) *Linear effect collected from the reaction of* ***RE-6.2*** *with NBS in the presence of preformed catalyst* ***CAT-6.2****.* ***(Right)*** *Explanation of the 2 signals obtained in ^{31}P-NMR with enantiomeric mixtures of chiral phosphoric acids.*

Furthermore, ^{31}P-NMR experiments conducted on the magnesium complex using different enantiomeric ratios of the chiral phosphate revealed the presence of two signals in equilibrium, with relative integrations similar to the enantiomeric ratio of the phosphoric acid (**Figure 6.12**, **right**), This observation supports the formation of a labile bis-phosphate ion pair.

6.2.2.2 Results and discussion

Once the molecularity of the RDS has been confirmed, the catalytic cycle was proposed. Initially, a simplified model was studied, using an achiral catalyst and replacing the phenyl groups from **RE2-6.1** with methyl groups (**Scheme 6.13**, series **1**). The entire transformation from **EC(1-4)-6.2** to both products was investigated. However, all attempts to locate the intermediate **IN(1-4)-6.2** failed, and the structures converged either to the encounter complex or to the final products.

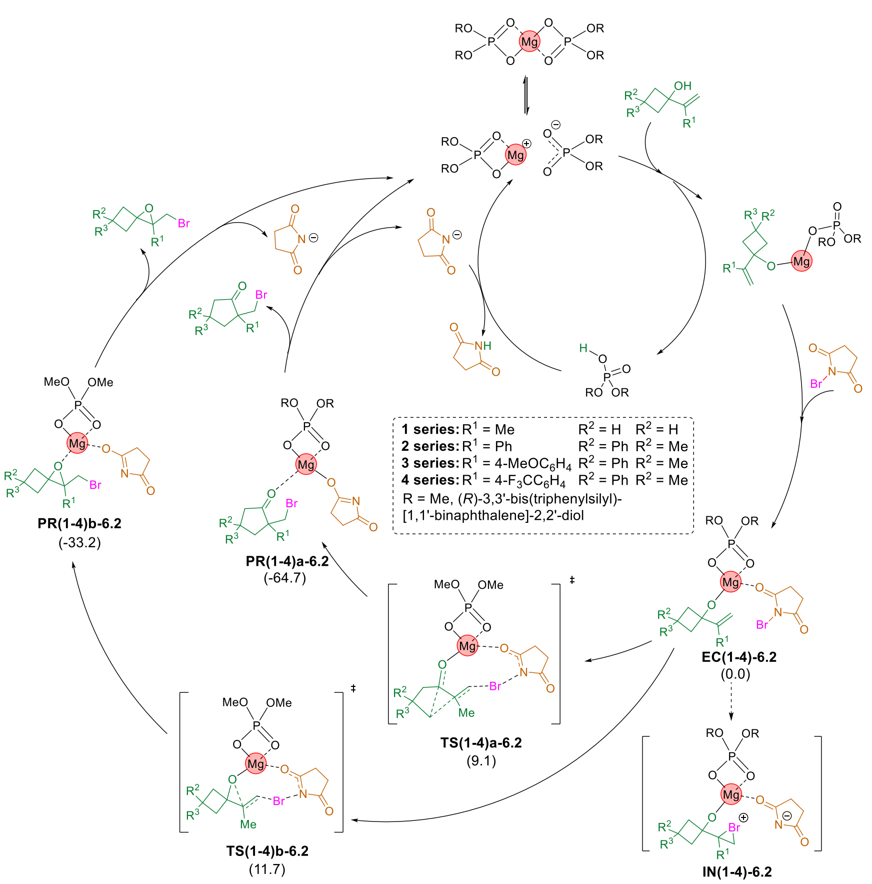
PR(1-4)b-6.2
(-33.2)
PR(1-4)a-6.2
(-64.7)
TS(1-4)a-6.2
(9.1)
TS(1-4)b-6.2
(11.7)
EC(1-4)-6.2
(0.0)
IN(1-4)-6.2
1 series: R1 = Me R2 = H R2 = H
2 series: R1 = Ph R2 = Ph R2 = Me
3 series: R1 = 4-MeOC6H4 R2 = Ph R2 = Me
4 series: R1 = 4-F3CC6H4 R2 = Ph R2 = Me
R = Me, (R)-3,3'-bis(triphenylsilyl)-[1,1'-binaphthalene]-2,2'-diol

Scheme 6.13*: Catalytic cycle proposed for the reaction of* ***RE-6.2*** *with NBS to give both cyclopentanones* ***PR(1-4)a-6.2*** *and epoxides* ***PR(1-4)b-6.2****. Intermediates* ***IN(1-4)-6.2*** *could not be located at any level of theory. The relative free energies of the series* ***1*** *calculated at the wb97xd/def2tzpv/pcm=toluene//wb97xd/def2svp level of theory are represented in brackets.*

After an extensive exploration of the potential energy surface, **TS1a-6.2** and **TS1b-6.2** were identified as the TSs with the minimum energy barriers for the transformation of **EC1-6.2** to both the cyclopentanone and the epoxide, respectively. Both IRCs depicted in **Figure 6.13** correspond to the direct transformation of the reactants to the products without the formation of any intermediate. A comparison between the two IRCs revealed a flatter PES around **TS1a-6.2**, suggesting a longer half-time for a possible transient carbocationic intermediate.

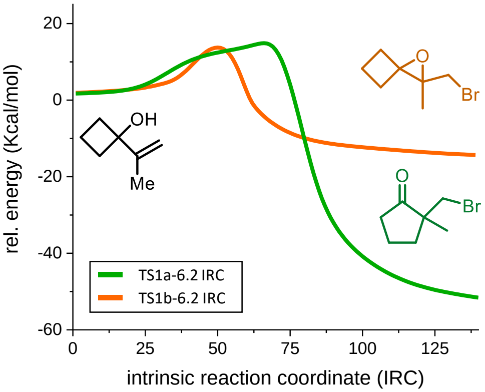

Figure 6.13: *IRCs for the reaction of* ***RE-6.2*** *with NBS to give both cyclopentanones* ***PR(1-4)a-6.2*** *and epoxides* ***PR(1-4)b-6.2****.*

Quasi-classical direct dynamic calculations were performed using PROGDYN software [49] on **TS1a-6.2** to estimate the duration of the sp^2 state for C6 after the formation of the C7-Br bond (so, when C7 is tetrahedral) which represents the half-life time of a transient carbocation. After 130 trajectories, a minimum half-life time of 70 fs was estimated for the transient carbocation (**Figure 6.14**).

Since the actual substrate features an aromatic ring instead of a methyl group at the C6 position, a longer duration of the carbocationic state is expected for the real system. Additionally, the absence of substitution at the C4 position prevents desymmetrization, and no diastereoselectivity can be studied. Therefore, the model was extended to include the real system while retaining the achiral catalyst (**Scheme 6.13**, series **2**).

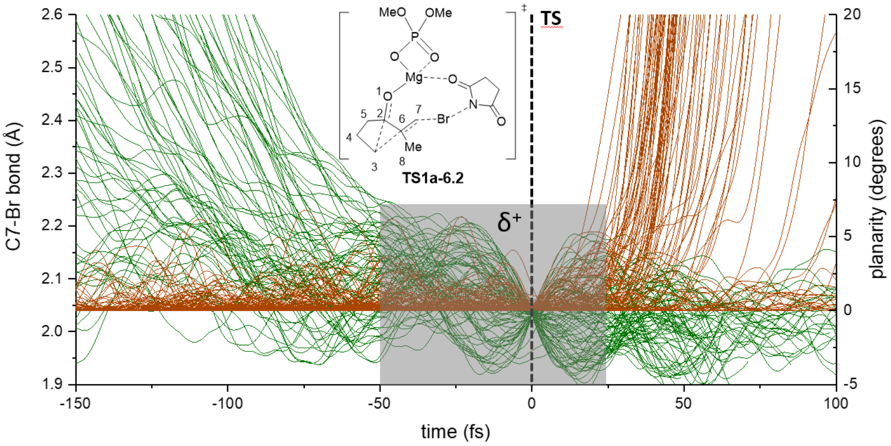

*Figure 6.14: Representation of the C7-Br distance (green lines) and planarity of C6 {orange lines; defines in degrees as 360 – [<(2,6,7) + <(7,6,8) + <(8,6,2)] for 130 trajectories starting from **TS1a-6.2**. The grey area indicates, approximately, the minimum time in which only C6 remains as sp^2 carbon, thus corresponding to a carbocation.*

Due to the absence of chirality in the catalyst, only one face of the alkene needs to be studied. From the rotation of the C7-C6-C2-C3 dihedral angle, six different approaches can be proposed to form the initial encounter pair EC2-6.2. However, only four of them maintain the interactions described in **Figure 6.11**, model **B**. In the other two approaches, the interaction between the alkoxide and the magnesium ion would be disrupted, resulting in a significant increase in their relative energy. The remaining four approaches are illustrated in **Scheme 6.14**, and similar to the previous case, the corresponding intermediates could not be located. The relative energies were found to be very close for most of them, with a range of less than one kcal/mol, which aligns with the experimental observation of both the formation of cyclopentanone and the epoxide depending on the reaction conditions.

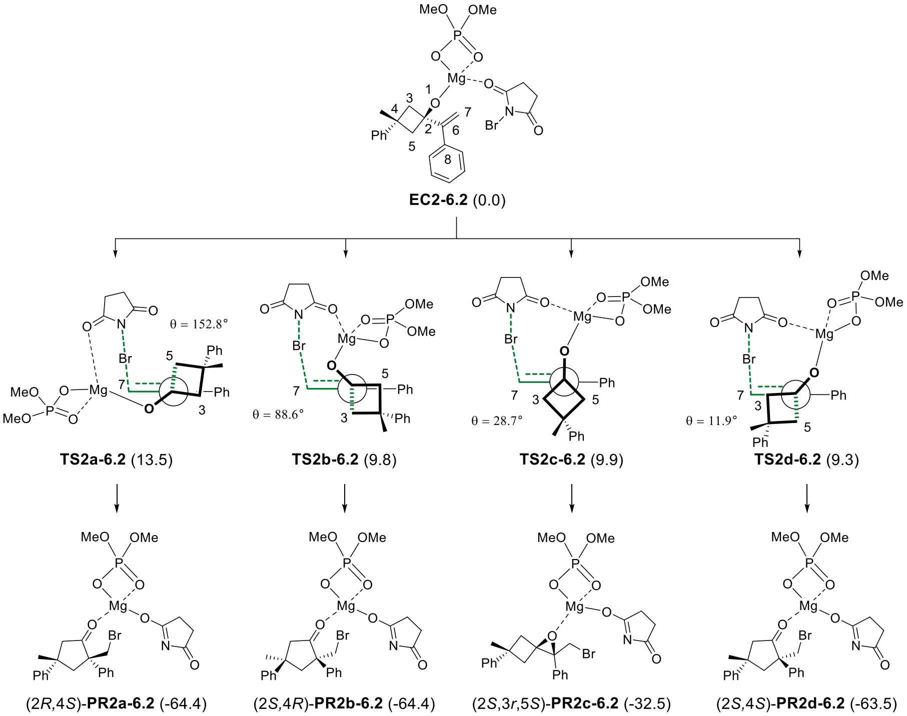

Scheme 6.14: *Viable approaches for the reaction of* ***EC2-6.2*** *leading to both epoxide and cyclopentanone isomers. Newmann projections for* ***TS2(a-d)-6.2*** *are given along the C2-C6 bond. Breaking and forming bonds are colored in green. θ refers to the C7-C6-C2-C3 dihedral angle. Relative free energy values calculated at wb97xd/def2tzpv/pcm=toluene/ /wb97xd/def2svp level, are depicted in brackets and given in Kcal/mol.*

Remarkably, in the structures **TS2b-6.2** and **TS2d-6.2**, eclipsed conformations are observed, which are initially considered less stable than staggered conformations like in **TS2c-6.2**. However, in these structures, the rearranging bond forms an angle of approximately 90° with respect to the breaking double bond. This arrangement maximizes the orbital overlap between the involved bonds, facilitating a hyperconjugative effect (**Figure 6.15**). This phenomenon significantly contributes to the concerted nature of the reaction. On the other hand, in the case of **TS2a-6.2**, steric factors prevent the TS from adopting these conformations, resulting in a notable increase in the energy barrier. For the staggered TS leading to the formation of the epoxide (**TS2c-6.2**), although it exhibits a more stable geometry, the mutual coordination of the catalyst to both the alkoxide and the NBS forces the lone pair electrons of the alkoxide to point in the opposite direction of the forming bond. As a result, a pyramidal inversion of the alkoxide is needed to form the new C-O bond. This fact increases the energy barrier enough to be competitive with the other TSs.

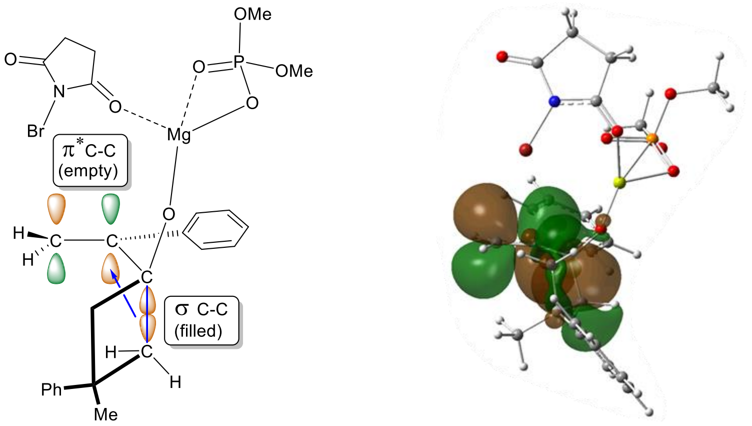

Figure 6.15: *Hyperconjugative effect ($\sigma_{C\text{-}C} \rightarrow \pi^*_{C=C}$) for the eclipsed conformation leading to **TS2d-6.2**.*

Focusing on the experimentally obtained compound **PR2d-6.2** (which is actually its enantiomer, but since no chiral catalyst is present, the results and discussion will be the same), ELF studies can be conducted over its IRC to unequivocally confirm the presence of the transient carbocation. This can be inferred from the presence of a shoulder before the transition structure in the ELF analysis.

The ELF analysis for the reaction of **EC2-6.2** through **TS2d-6.2** is shown in **Figure 6.16** (top). The reaction initiates with the N-Br bond breaking (pink trace), accompanied by an increase in the population of the nitrogen lone pair (green dotted trace). Almost instantaneously, the C7-Br bond is formed at point 51 (dark green trace). These processes coincide with the IRC shoulder, and from this point onwards, the energy continues to increase until reaching the transition state involving the breaking of the C2-C5 bond (grey trace) and the onset of the semipinacolinic rearrangement. This migration concludes at point 90 with the formation of the C5-C6 bond (dark blue trace). Consequently, the transient carbocation exists between points 51 and 90 along the IRC. By examining the C6-C8 bond (cyan trace) during this interval, a slight increase in its population can be observed, corresponding to the resonance stabilization of the transient carbocation by the aromatic ring. On the other hand, the C6-C7 bond (purple trace) does not exhibit significant variations in electron density but gradually loses population throughout the entire IRC.

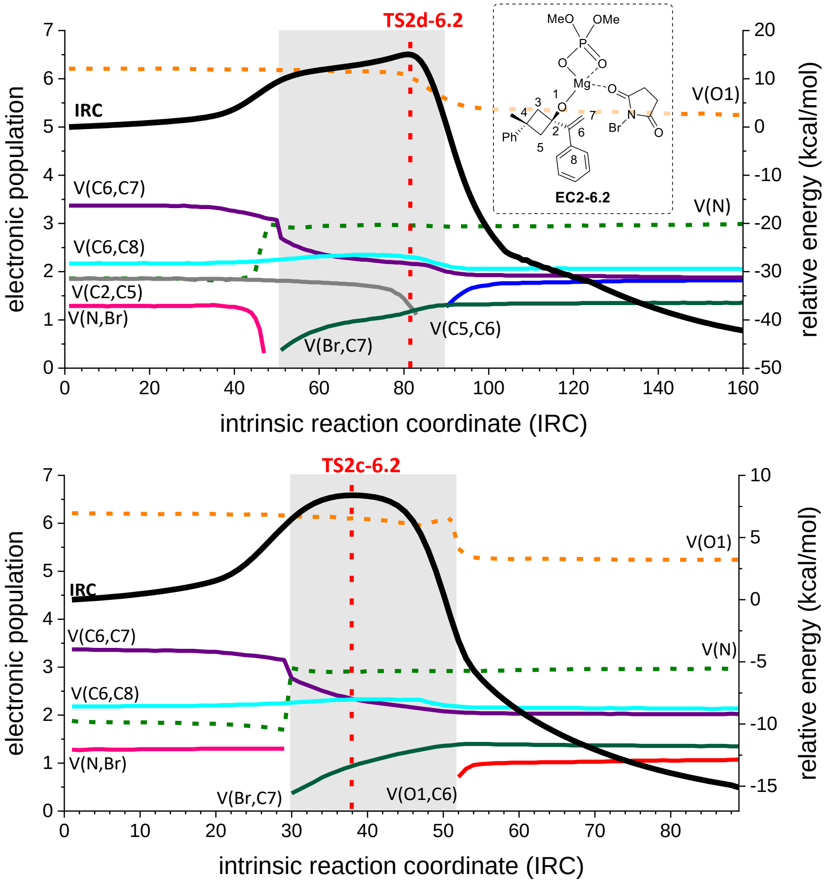

*Figure 6.16: ELF analyses for the reaction of **EC2-6.2** (R=Ph) through **TS2d-6.2** (top) and **TS2c-6.2** (bottom) to give cyclopentanone **PR2d-6.2** and epoxide **PR2c-6.2**, respectively. The numbering refers to that given in **Scheme 6.14**. Black traces correspond to IRC. Colored dotted traces refer to lone pairs (monosynaptic basins), and colored plain traces to bonds (dysinaptic basins). The vertical red line indicates the TS, while the grey area represents the carbocationic area. Only those representative atoms and bonds are shown.*

The same analysis can be done for the epoxidation through **TS2c-6.2**. However, in this case, once the C7-Br bond is formed (dark green trace) at point 30, O1 attacks the carbocation, forming the O1-C6 bond (red trace) at point 52. Consequently, the carbocation exists during 22 points of the IRC. Interestingly, the TS from this IRC does not match the breakage or formation of any bond. Instead, it corresponds to the inversion of the O1 atom. As mentioned before, its lone pairs do not point in the C6 direction. If a less coordinative catalyst is used, such as the previous phosphoric acids without magnesium, the empty orbitals from the alkoxide may be in a better position. This would decrease the TS energy and increase the obtained proportion of epoxide **PR2c-6.2**.

To evaluate the extension of the hidden carbocation and the possibility of stabilizing the intermediate, the study was expanded to include substrates with 4-methoxy and 4-trifluoromethyl substitutions at the aromatic ring linked to C6 (series **3** and **4** in **Scheme 6.13**). An increased stability of the carbocation is expected for **EC3-6.2** (R = 4-MeOC$_6$H$_4$) due to the presence of an electron-donating group on the aromatic ring. As depicted in **Figure 6.17**, an increased stabilization is observed over **TS3c/d-6.2** compared to **TS2c/d-6.2.** However, this stabilization affects **TS3c-6.2** more, leading to the epoxide, than **TS3d-6.2**, which predicts a possible inversion of regioselectivity.

On the contrary, opposite effects are expected for **EC4-6.2** (R = 4-F$_3$CC$_6$H$_4$), where the electron-withdrawing group should decrease the stability of the intermediate and increase the energy barrier. As observed for **EC3-6.2**, **TS4c-6.2** is more affected by this substitution, now increasing its relative energy 1.7 Kcal/mol compared to **TS4d-6.2**. This predicts better regioselectivities for cyclopentanone derivatives.

As summarized in **Figure 6.17**, electron-donating substituents over the aromatic ring increase the stability of the TS and the carbocation through resonance. This is evident from the increased population of the C6-C8 bond (green dotted trace) compared to the same basin population in **TS2d-6.2** (black dotted trace). Conversely, electron-withdrawing substituents induce a destabilizing effect on both the TS and the intermediate. Lower resonance effects are observed compared to an unsubstituted aromatic ring (orange dotted trace). TSs leading to the epoxide are more affected by these changes, allowing for an inversion of the product ratio with electron-donating substituents. Despite achieving higher stabilizations of the carbocation, the intermediate has not been observed in any of these scenarios.

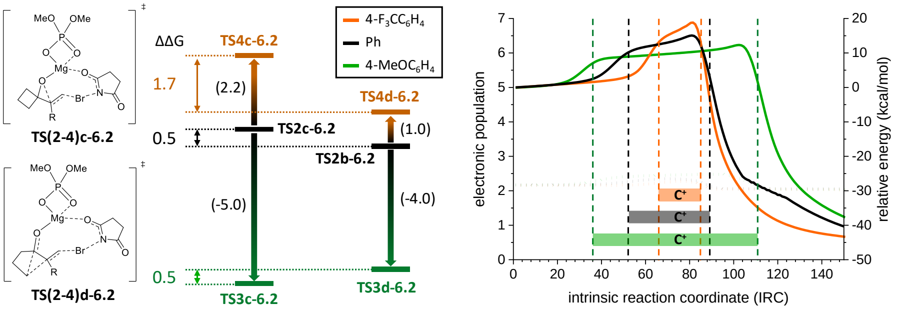

__Figure 6.17: (Left)__ (De)stabilization of __TS2c-6.2__ and __TS2d-6.2__(black traces) upon introduction of 4-MeO (__TS3c-6.2__ and __TS3d-6.2__; green traces) and 4-CF3 (__TS4c-6.2__ and __TS4d-6.2__; orange traces) in the aromatic ring linked to the double bond. Numbers in brackets indicate the gap in kcal/mol between those structures. Colored numbers indicate the relative energy difference between __c__ and __d__ series leading to epoxide and cyclopentanone, respectively. __(Right)__ IRCs from __TS2d-6.2__ (black trace), __TS3d-6.2__ (green trace) and __TS4d-6.2__ (orange trace) along with their respective population evolution from C6-C8 bond (black, green, and orange dotted traces, respectively). The three first vertical dashed lines indicate the formation of the C7-Br bond, and the three last ones the formation of the C5-C6 bond, corresponding to the end of the rearrangement, both according to ELF. The corresponding intervals, represented as horizontal bands, indicate the extension of the transient carbocation.

According to the IRC, quasi-classical direct dynamic calculations on **TS3d-6.2** afforded a wider carbocationic window compared to **TS1a-6.2**. A minimum carbocationic survivability of 200 fs was obtained, although some trajectories exhibited carbocationic windows exceeding 600 fs. **Figure 6.18** illustrates the rearrangement trajectories, represented by the hybridization to sp^3 of C6, which are concentrated within a narrow time window. On the other hand, the formation of the C7-Br bond is spread over a broader time range, reflecting the planarity of the PES prior to the TS.

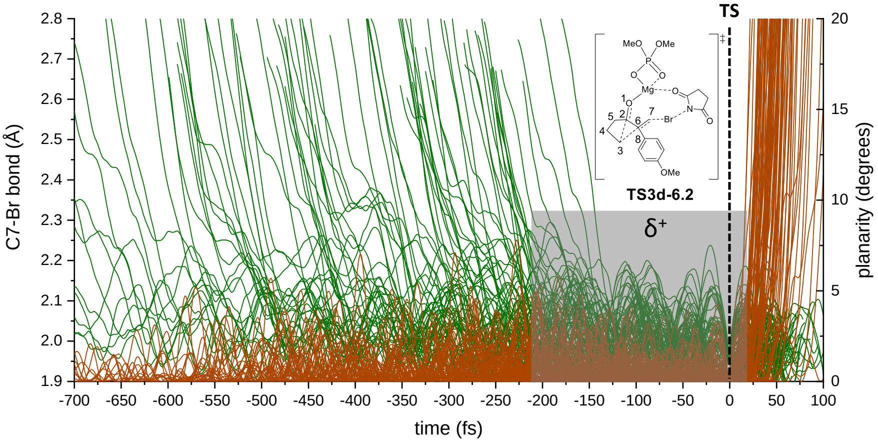

Figure 6.18: *Representation of the C7-Br distance (green traces) and C6 planarity {orange lines; defines in degrees as 360 – [<(2,6,7) + <(7,6,8) + <(8,6,2)] for 102 trajectories starting from* ***TS3d-6.2****. The grey area indicates, approximately, the minimum time in which only C6 remains as sp^2 carbon, thus corresponding to a carbocation.*

A real intermediate could only be identified through the substitution of the aromatic ring with a dimethylamino group. This group maximizes the stability of the carbocation by forming an iminium ion intermediate, **IN5-6.2**. From this species, the formation of the epoxide, **PR5c-6.2**, proceeds in an endothermic manner, with almost no barrier for returning to the intermediate (**Figure 6.19**). Therefore, the only possible pathway is the evolution towards the cyclopentanone product, **PR5d-6.2**. This last step serves as the RDS, similar to previous cases where the TS was also the second stage of the reaction.

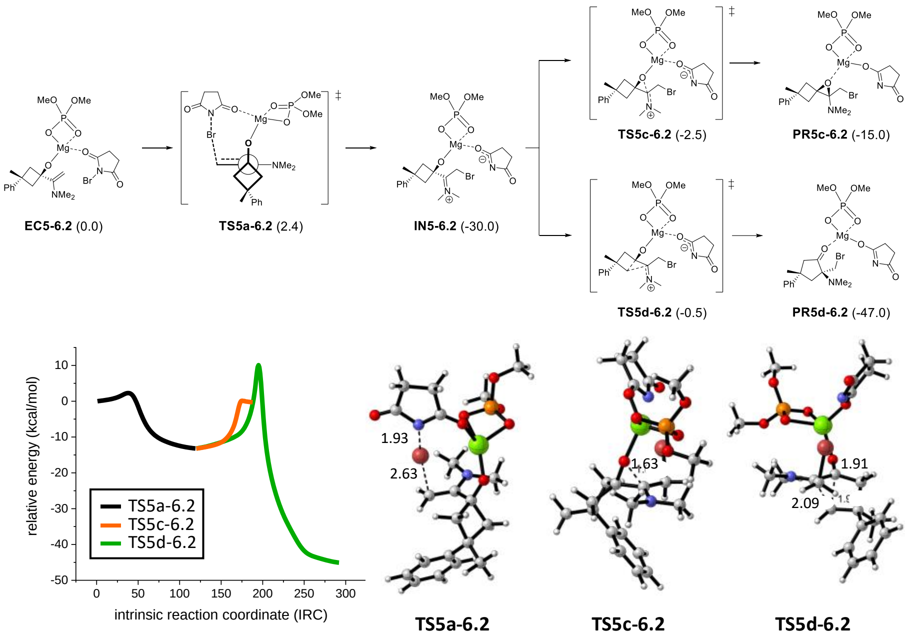
EC5-6.2 (0.0)
TS5a-6.2 (2.4)
IN5-6.2 (-30.0)
TS5c-6.2 (-2.5)
PR5c-6.2 (-15.0)
TS5d-6.2 (-0.5)
PR5d-6.2 (-47.0)
relative energy (kcal/mol)
intrinsic reaction coordinate (IRC)
TS5a-6.2
TS5c-6.2
TS5d-6.2
1.93
2.63
1.63
1.91
2.09
TS5a-6.2
TS5c-6.2
TS5d-6.2

***Figure 6.19: (Top)** Stabilization of intermediate as iminium ion. Only the attack by one face of the iminium ion has been calculated. Energies calculated at wb97xd/def2tzpv/ pcm=toluene//wb97xd/def2svp level are displayed in brackets. (Bottom-left) Merged IRCs calculated at wb97xd/def2svp corresponding to transition structures **TS5a-6.2** (black trace), **TS5c-6.2** (orange trace) and **TS5d-6.2** (green trace). (Bottom-right) Optimized geometries of transition structures.*

Finally, once the concerted nature of the reaction had been determined, the achiral model catalyst was replaced with the actual chiral catalyst. This substitution resulted in the duplication of the number of structures depicted in **Scheme 6.14**. Eight TS were located, with **TS2R-*entc*-6.2** and **TS2R-*entd*-6.2** being the two most stable ones. These TSs correspond to the reactions of **EC2R-6.2** leading to the formation of both products, namely (*2R,3r,5R*)-epoxide and (*2R,4R*)-cyclopentanone, respectively. **TS2R-*entd*-6.2** was found to be 2.3 kcal/mol more stable than **TS2R-*entc*-6.2**, indicating a higher abundance of cyclopentanone, which is in good agreement with the experimental results.

A comparison between **TS2R-*entc*-6.2** and its achiral counterpart revealed a more advanced TS characterized by greater N-Br distances and lower C7-Br and C6-O distances. On the other hand, **TS2R-*entd*-6.2** exhibited the same atom disposition as its achiral counterpart, **TS2d-6.2**, but with mirror inversion. This suggests that the bis(triphenylsilyl)BINOL moiety in this case primarily plays a steric role (**Figure 6.20**).

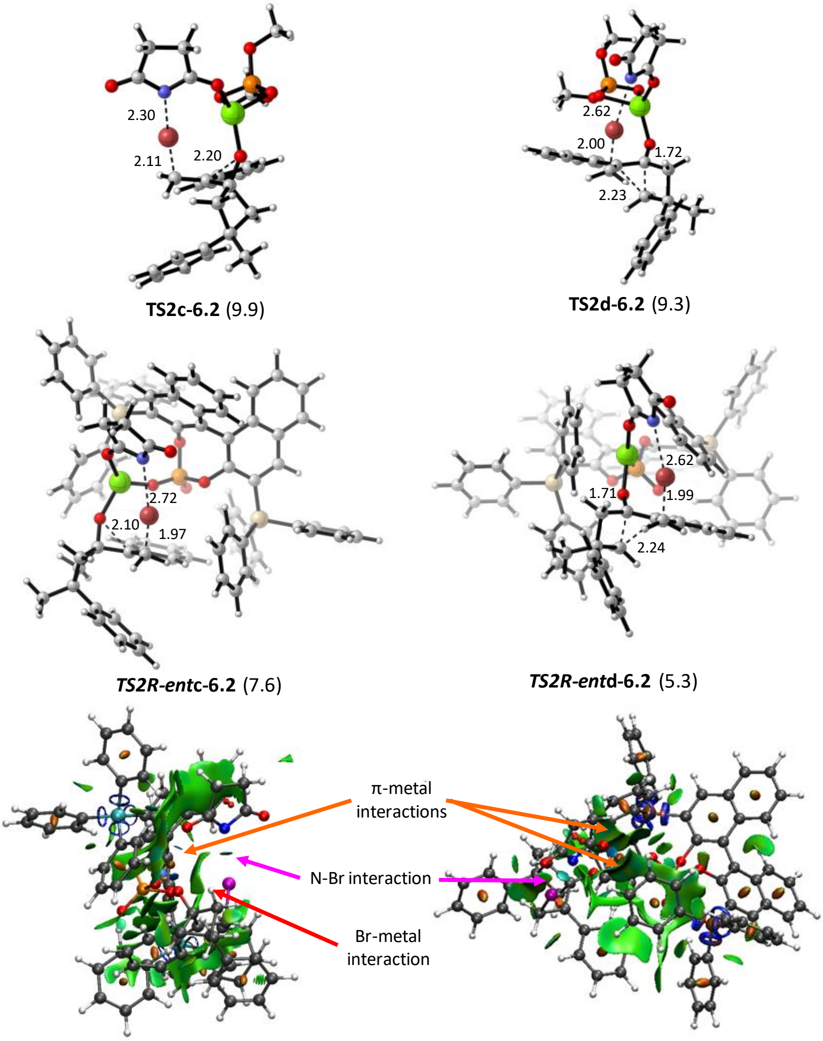

TS2c-6.2 (9.9)

TS2d-6.2 (9.3)

***TS2R-entc*-6.2** (7.6)

***TS2R-entd*-6.2** (5.3)

2.30
2.11
2.20
2.62
2.00
1.72
2.23
2.72
2.10
1.97
2.62
1.71
1.99
2.24
π-metal interactions
N-Br interaction
Br-metal interaction

Figure 6.20: *Comparison between achiral (wb97xd/def2svp) and real catalyst (wb97xd/def2svp:pm6) best TSs optimized structures for the reaction of* ***RE2-6.2*** *to both epoxide and cyclopentane. Energy barriers are displayed in brackets at wb97xd/def2tzvp level for the achiral system and at wb97xd/def2tzvp:pm6 NCI calculations of structures* ***TS2R-entc-6.2*** *and* ***TS2R-entd-6.2*** *are displayed below along with the determining interactions.*

NCI calculations revelated that despite the C7-Br bond can be considered fully formed, the remaining N-Br interactions indicate that the addition process has not yet concluded. In fact, **TS2R-*ent*c-6.2** shows a clear interaction between the bromine and the metal ion, which could explain the more advanced nature of the transition state observed with the real catalyst compared to the model catalyst. On the other hand, **TS2R-*ent*d-6.2** lacks this interaction, but instead, it is substituted by a stronger π-metal interaction. This interaction could be one of the reasons for the higher stability of **TS2R-*ent*d-6.2**.

6.2.2.3 Conclusions

This study demonstrates that the catalyzed desymmetrization and ring expansion of alkenylcyclobutanols, promoted by halofunctionalization of the alkene moiety with NBS using a magnesium phosphate catalyst, occurs in one kinetic step but two stages.

The stages involve the formation of a hidden carbocationic intermediate with a duration of ≤200 fs.

Electro-donor substituents on the alkene-bonded aromatic ring increase the stability of this intermediate but also result in a higher proportion of the epoxide byproduct.

Linearity studies support the presence of only one phosphate unit in the RDS, causing the oxygen lone-pair electrons to point in the opposite direction to the forming bond. This increases the energy required for epoxide formation.

6.2.3 Unraveling the mechanism of a switchable acid catalyzed cyclooctatetraene oxide contraction towards the enantioselective synthesis of homoallylic alcohols

6.2.3.1 Introduction

In this section, it will be explored the mechanism of the synthesis of homoallylic alcohols through the contraction of cyclooctatetraene oxide (COT oxide), catalyzed by phosphoric acids and resulting in the formation of cycloheptatriene scaffolds.

The synthesis of 7-membered rings poses a challenge due to the limited number of reactions available for their formation. [50] The conventional approach involves the use of the Buchner reaction, which is a metal-catalyzed cyclopropanation of arene derivatives, resulting in the formation of norcaradiene (NCD) derivatives in equilibrium with cycloheptatriene (**Scheme 6.15**). [51] These two isomers are connected through a 6π electrocyclic ring-opening reaction under thermal conditions. [52] The ratio between NCD and cycloheptatriene depends on the substituents present, although cycloheptatriene tends to be the major isomer. [53]

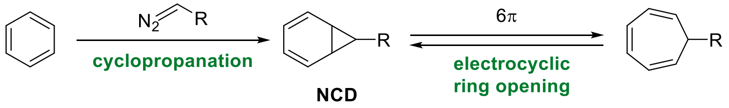

Scheme 6.15: *Buchner reaction scheme for the synthesis of cycloheptatrienes.*

Other early alternatives include the ring contraction of COT oxide with Grignard reagents [54] or the pyrolysis of COT oxide at 260 °C. [55] However, increasing the temperature above 400 °C leads to the transformation of this cycloheptatriene into phenylacetaldehyde, which is one of the major side products of the ring opening mediated by Grignard reagents (**Scheme 6.16**). Both approaches suffer from experimental issues such as low yields and limited scope, rendering them of limited utility in modern times.

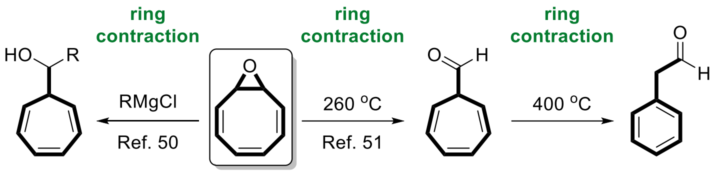
ring contraction
ring contraction
ring contraction
HO
R
RMgCl
Ref. 50
O
260 °C
Ref. 51
O
H
400 °C
O
H

Scheme 6.16: *Previous ring contraction of COT oxide.*

It has also been demonstrated that Brønsted acids can promote the ring contraction of COT oxide to phenylacetaldehyde. [56] Based on these findings, the ring contraction of COT oxide in the presence of various chiral Brønsted acids was conducted by our collaborators from Bilbao. Since these Brønsted acids are also known to catalyze the addition of allylboronates to aldehydes, [57] the possibility of coupling the ring contraction with an allylation process was also investigated. Furthermore, subsequent Cu-catalyzed borylation of the resulting homoallylic alcohols could lead to the formation of enantioenriched oxaborinanes (**Scheme 6.17**).

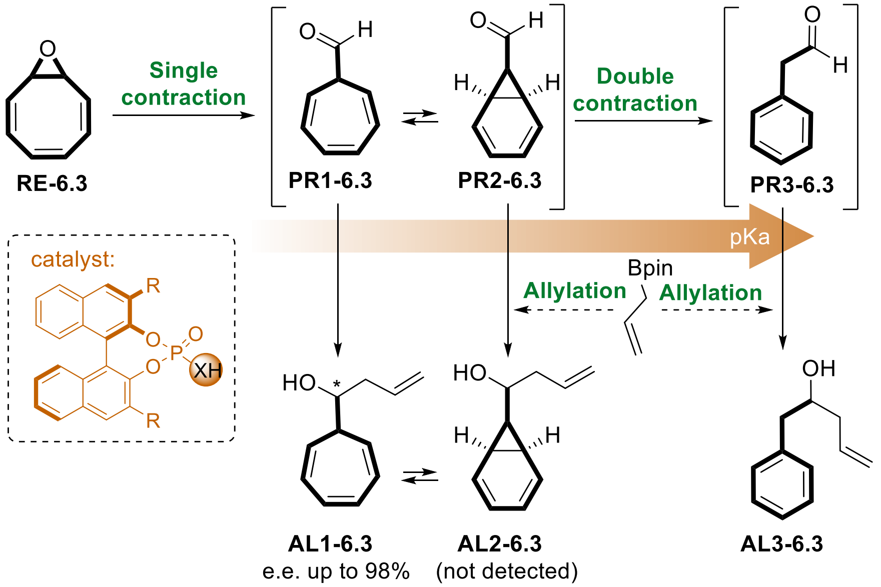
O
RE-6.3
Single contraction
O
H
PR1-6.3
O
H
H
H
PR2-6.3
Double contraction
O
H
PR3-6.3
pKa
catalyst:
R
O
P
O
O
XH
R
Bpin
Allylation
Allylation
HO
*
AL1-6.3
e.e. up to 98%
HO
H
H
AL2-6.3
(not detected)
OH
AL3-6.3

Scheme 6.17: *Switchable acid catalyzed COT oxide ring contraction/allylation towards enantioselective homoallylic alcohols and oxaborinanes.*

For the preliminary studies in Bilbao, two different achiral catalyst, **CATa1-6.3** and **CATb1-6.3**, were employed in chloroform at room temperature.

Interestingly, the cycloheptatrienyl derivative **AL1-6.3** was exclusively generated in the presence of **CATa1-6.3**, while with **CATb1-6.3**, which is a more acidic catalyst, [58] only **AL3-6.3** was detected in a faster reaction. However, when the reaction with **CATb1-6.3** was performed at lower temperatures, mixtures of both products were obtained (**Scheme 6.18**).

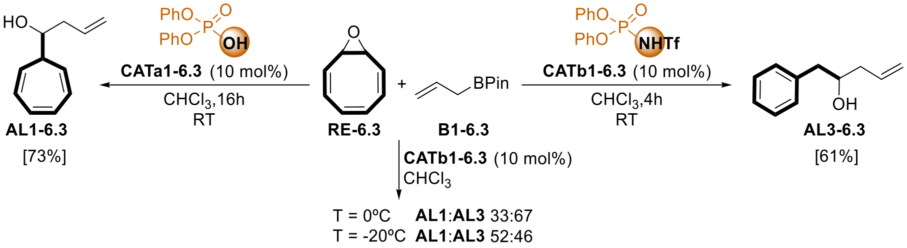

Scheme 6.18: *Preliminary reaction conditions and catalyst screening. pKa's are assigned according to ref. 54. Reactions at 0 °C and -20 °C were conducted until total consumption of the starting material.*

When pure **AL1-6.3** or mixtures of **AL1-6.3/AL3-6.3** were stirred in the presence of 10% mol of **CATb1-6.3** for 16 hours, it was observed that the reactants remained unaltered. This led to the conclusion that the reaction is not reversible, and the observed selectivity cannot be explained by thermodynamic control alone. In fact, the product ratio observed at 0 °C and -20 °C suggested that aldehyde **PR1-6.3** may serve as an intermediate in the formation of **PR3-6.3**, undergoing an irreversible allylation process. On the other hand, mixtures of **RE-6.3** and **B1-6.3** without any Brønsted acid did not show any evolution of the starting material, ruling out the possibility of the boronate participating as a Lewis acid in promoting the ring contraction of COT oxide. In this context, the mechanism of the reaction was studied using both NMR and DFT methods.

6.2.3.2 Results and discussion

The preliminary ^{1}H-NMR studies were performed at Zaragoza, and involved monitoring the reaction between COT oxide (**RE-6.3**) and a 10 mol% of each catalyst, in the absence of the boronate (**B1-6.3**), to investigate the transformation of the starting material into each aldehyde. Catalyst **CATa1-6.3** facilitated the ring contraction of COT oxide, resulting in the formation of aldehyde **PR1-6.3**. This aldehyde exists in equilibrium with its NCD tautomer, resulting in the observation of an average spectrum (**Figure 6.21**).

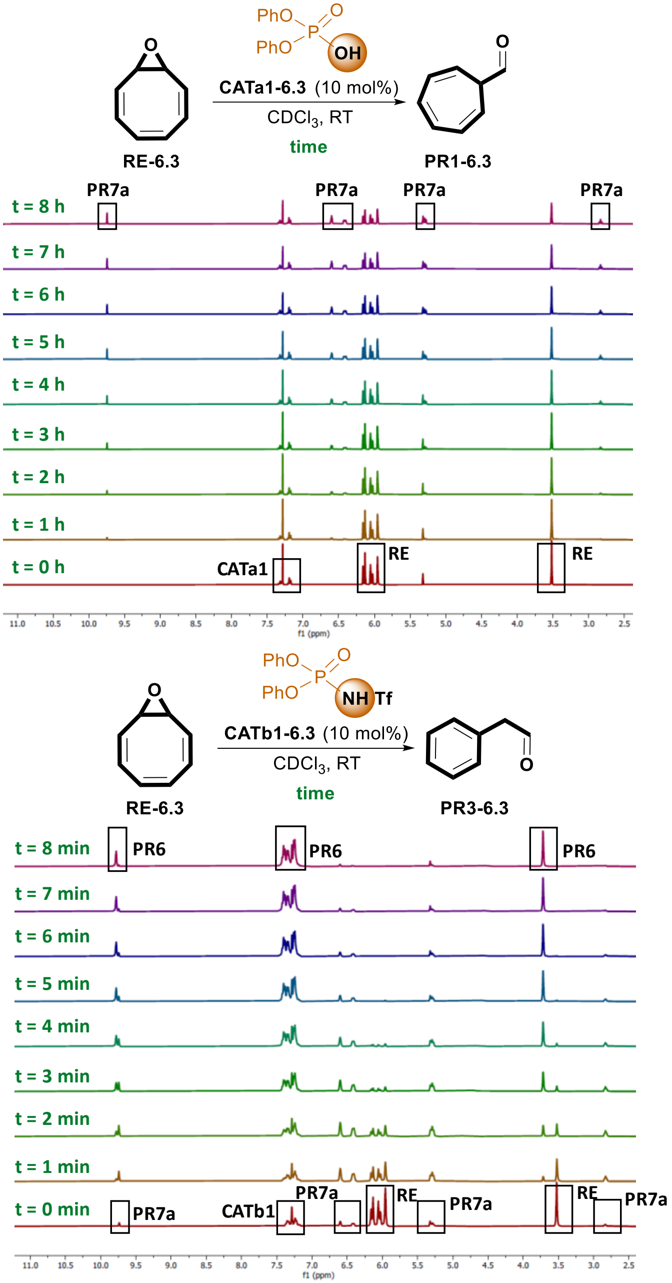

Figure 6.21: *^{1}H-NMR spectra of the crude reaction mixture of COT oxide **RE-6.3** with 10 mol% of catalyst **CATa1-6.3** (**top**) and **CATb1-6.3** (**bottom**).*

On the other hand, when the same experiment was performed with **CATb1-6.3**, a nearly instantaneous reaction occurred, leading to the clean formation of aldehyde **PR3-6.3** within 10 minutes. During this time, the appearance and disappearance of aldehyde **PR1-6.3** can be observed, suggesting its potential role as an intermediate between **RE-6.3** and **PR3-6.3**.

To further investigate the role of **PR1-6.3**, an additional experiment was conducted. COT oxide (**RE-6.3**) was stirred with 10 mol% of **CATa1-6.3** for 5 hours, resulting in a 60% conversion towards cycloheptatriene aldehyde **PR1-6.3** (which exists in equilibrium with its valence isomer **PR2-6.3**). Subsequently, 10 mol% of catalyst **CATb1-6.3** was added to the mixture, leading to the clean formation of **PR3-6.3**. This experiment confirms that aldehyde **PR1-6.3**, as depicted in **Scheme 6.17**, serves as an intermediate in the formation of **PR3-6.3** (**Scheme 6.19**).

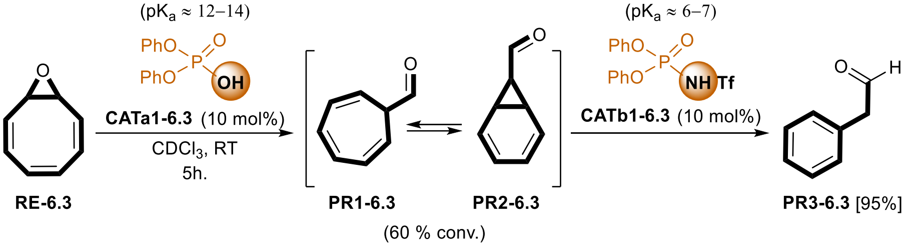

Scheme 6.19: *Catalyst switch experiment for successive single and double ring contraction.*

DFT studies were conducted to investigate the factors involved in the formation of each product. The proposed thermal rearrangement suggested by Buchi and Burguess [55c] was taken as a starting point and examined. They proposed the formation of **PR3-6.3** through the pathway indicated by the gray arrows in **Scheme 6.20**. In their publication, the formation of **PR2-*exo*-6.3** was reported through its capture in a Diels-Alder reaction. This product originates from the same NCD-cycloheptatriene equilibrium as described earlier but with the *exo* conformational isomer of **PR1-*endo*-6.3**, which allows for the proper orientation of the bicyclic structure. This pathway begins with the thermal rearrangement of **RE-*endo*-6.3**, which was found to have an energy barrier of 39.1 kcal/mol. This high energy barrier suggests that this neutral mechanism does not contribute significantly to the acid-catalyzed system.

Introducing catalyst **CATa1-6.3**, all rearrangements starting from both **REa1-*endo*-6.3** and **REa1-*exo*-6** resulted in the formation of the **PR1a1-*endo*-6.3** structure. The lowest energy barrier for this transformation was found to be 22.6 kcal/mol, corresponding to the transition state **TS1a1-6.3**. The IRC analysis of this transition state exhibited a characteristic shoulder indicative of the presence of a hidden intermediate, similar to what was observed in the previous section. [59]

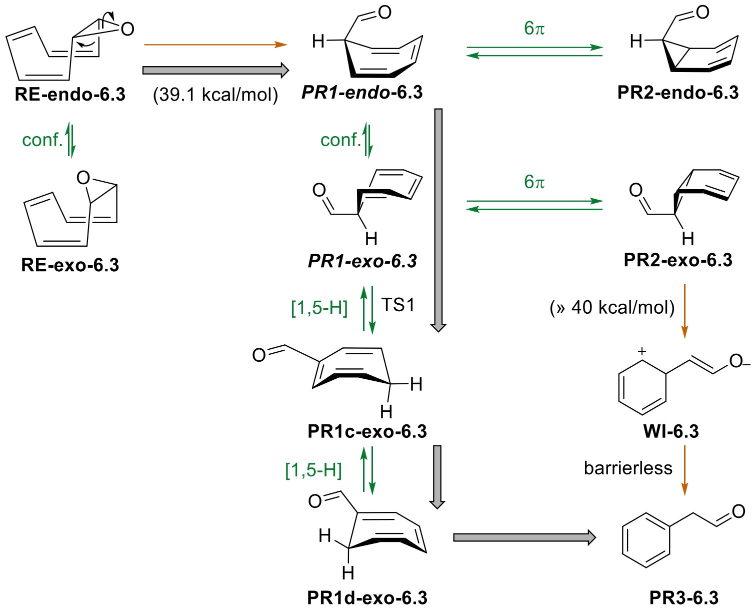
RE-endo-6.3
(39.1 kcal/mol)
PR1-endo-6.3
6π
PR2-endo-6.3
conf.
conf.
RE-exo-6.3
6π
PR1-exo-6.3
PR2-exo-6.3
[1,5-H]
TS1
(» 40 kcal/mol)
PR1c-exo-6.3
WI-6.3
[1,5-H]
barrierless
PR1d-exo-6.3
PR3-6.3

Scheme 6.20: *Proposed pathway for the conversion of **RE-6.3** into **PR3-6.3**. Gray route proposed in ref. [51c]. Orange processes are favored, and green processes are disfavored in acidic media.*

Therefore, a more detailed investigation of this step was carried out. ELF and NCI studies were conducted on **TS1a1-6.3** to accurately determine the factors driving the reaction and analyze the nature of the transient species involved. The results, along with the relevant species at each stage, are depicted in **Figure 6.22**. ELF analysis revealed the presence of two distinct transient carbocations during the formation of **PR1a1-6.3**, identified as **Aa1** and **Ba1**.

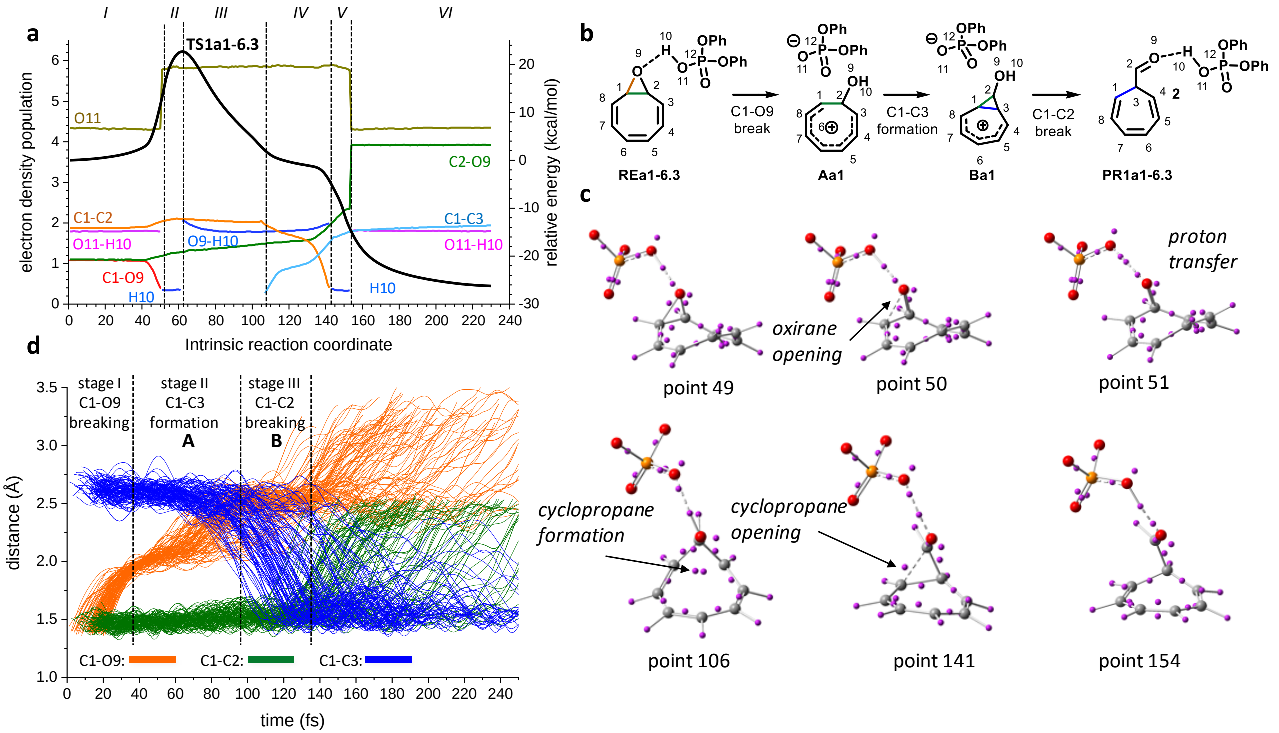

Figure 6.22:** Analysis of the reaction coordinate corresponding to the transformation of **REa1-endo-6.3** into **PR1a1-endo-6.3**. (**a**) ELF analysis. Black trace represents the IRC. (**b**) Representation of hidden carbocationic intermediates (transient species) **Aa1** and **Ba1** during the transformation of **REa1-endo-6.3** into **PR1a1-endo-6.3** corresponding to cleavage and formation of key bonds. (**c**) Representative points with descriptors (purple balls indicating maxima of electron population) of the IRC. Phenyl rings have been omitted for clarity. (**d**) Quasi-classical direct dynamic simulations. Representations of C1- O9 (orange), C1-C2 (green), and C1-C3 (blue) bonds for 180 trajectories from **TS1a1-6.3.

The initial step involves the protonation of the oxirane moiety, leading to the cleavage of the C1-O9 bond in the epoxide. This results in the formation of carbocation **Aa1**, which persists until the formation of the C1-C3 bond, generating the bicyclic carbocation **Ba1**. This rearrangement is reminiscent of the cycloheptatriene-NCD equilibrium discussed earlier. Finally, the cleavage of the C1-C2 bond and the subsequent reprotonation of the catalyst lead to the formation of **PRa1-*endo*-6.3**. This process of protonation and deprotonation underscores the crucial role of the catalyst's pKa in driving the reaction.

To estimate the duration of the hidden intermediates, directed molecular dynamic calculations were conducted using the PROGDYN software. [49] Based on the bond distances obtained from ELF analysis for the forming and breaking bonds, half-life times of 60 fs and 30 fs were assigned to **Aa1** and **Ba1**, respectively. These calculations provide insights into the transient nature of these intermediates and their relatively short lifetimes during the reaction process.

On the other hand, in the presence of **CATb1-6.3**, the barrier for the epoxide-opening TS (**TS1b1-6.3**) decreased to 21.9 kcal/mol, which is not a significant difference considering the difference in pKa values between the two acids (12-14 for **CATa1-6.3** and 6-7 for **CATb1-6.**3). [58] The optimized geometries of **TS1a1-6.3** and **TS1b1-6.3** are depicted in **Figure 6.23**, where a larger N-H distance can be observed with **CATb1-6.3** compared to the O-H distance OF **CATa1-6.3**, confirming the higher acidic character of **CATb1-6.3**. This difference is also evident from the NCI analysis, where a complete H-transfer is present in **TS1b1-6.3**, while only a partial transfer is observed in **TS1a1-6.3**. In addition, ELF studies were performed on **TS1b1-6.3**, showing a faster proton transfer due to its higher acidity.

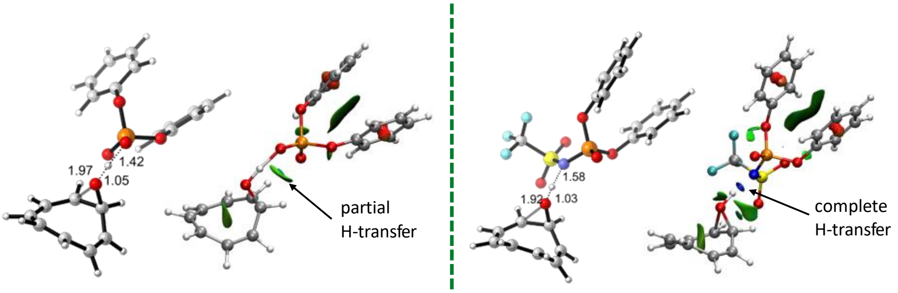

TS1a1-6.3 **TS1b1-6.3**

***Figure 6.23**: Optimized geometries of **TS1a1-6.3 (left)** and **TS1b1-6.3 (right)** at wb97xd/def2svp/ /SMD=chloroform level of theory. NCI analysis is depicted next to each structure.*

The second part of the reaction consist of the evolution of the cycloheptatriene **PR1-6.3** towards the formation of **PR3-6.3** (**Scheme 6.21**). The neutral mechanism of this reaction in neutral conditions resulted to have a barrier of more than 40 kcal/mol and need more than 250 °C to occur, so the catalyst should play a major role in this part of the reaction. For the formation of **PR2-6.3**, the NCD isomer of **PR1-6.3** must be formed trough **TS2a1-6.3** and **TS2b1-6.3** with **CATa1-6.3** and **CATb1-6.3** respectively. Only the major *-exo* conformation of **PR1-6.3** has been considered (depicted without catalyst on **Scheme 6.20**), since TSs starting from the endo conformer presented higher barriers for all the resting process.

The optimized geometries depicted in **Figure 6.24** of these transition states demonstrate that this process is not actually catalyzed by Brønsted acids, as both aldehydes are in their respective deprotonated forms. This observation is further supported by comparing their relative energy barriers to the neutral case (7.9 and 8.4 kcal/mol for **TS2a1-6.3** and **TS2b1-6.3**, respectively, compared to 8.5 kcal/mol for the uncatalyzed model).

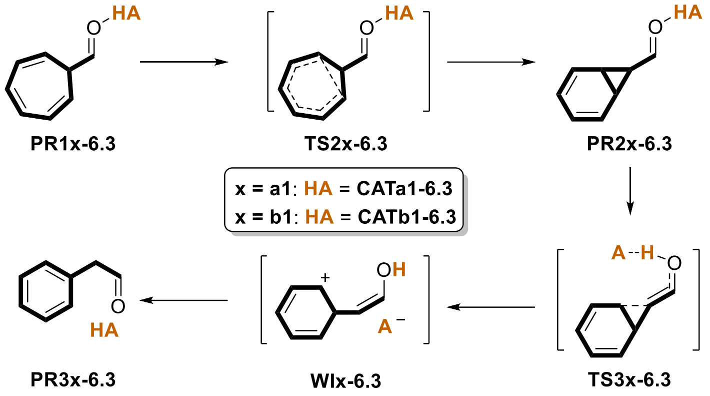

Scheme 6.21: *Mechanistic proposal for the transformation of PR1-6.3 to PR3-6.3.*

According to experimental results, the cyclopropane ring-opening step requires the protonation of the aldehyde to activate the system, as depicted in the structures shown in **Figure 6.24**, where the aldehyde is in its protonated form. The barriers for this step were determined to be 23.6 and 16.3 kcal/mol for **TS3a1-6.3** and **TS3b1-6.3**, respectively. Since this process is acid-catalyzed, a lower barrier was expected with the catalyst **CATb1-6.3**. Finally, the resulting Wheeland intermediates **WIa1-6.3** and **WIb1-6.3** undergo a barrierless process to transform into their respective enols, and through their tautomeric equilibrium, **PR3-6.3** is obtained.

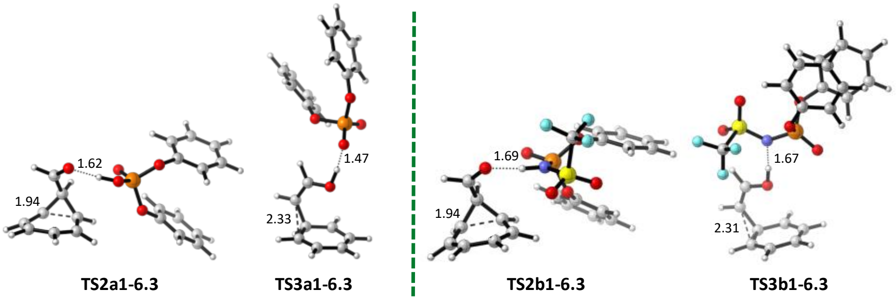

TS2a1-6.3 **TS3a1-6.3** **TS2b1-6.3** **TS3b1-6.3**

Figure 6.24: *Optimized geometries of **TS2a1-6.3** and **TS3a1-6.3** (left) along with **TS2b1-6.3** and **TS3b1-6.3** (right) at wb97xd/def2svp/SMD=chloroform level of theory.*

The depicted energy profile in **Figure 6.25** reveals that although both processes seem to proceed in an analogous way, the RDS with each catalyst is not the same. With **CATa1-6.3**, the RDS consists of the evolution of **PR2a1-**

6.3 to the Wheeland intermediate through **TS3a1-6.3**, with a barrier of 23.6 kcal/mol. On the other hand, with **CATb1-6.3**, the first step, i.e., the ring opening of the COT oxide, becomes the RDS, with a lower barrier of 21.9 kcal/mol.

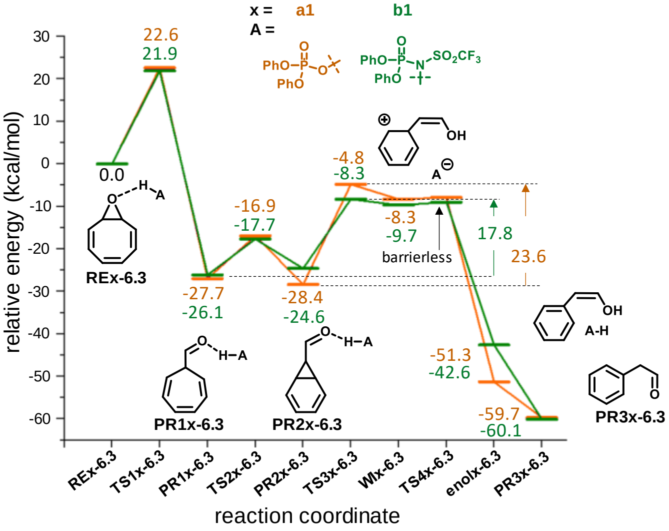

*Figure 6.25: Energy profile for the transformation of **RE-6.3** into **PR3-6.3** using **CATa1-6.3** (orange) and **CATb1-6.3** (green) at wb97xd/def2tzvp/SMD=chloroform//wb97xd/def2svp/ /SMD=chloroform level of theory.*

This difference is sufficient to justify the varying rates of both reactions. The reaction with **CATa1-6.3** is the slowest, with an estimated half-time of approximately 6 hours at 25 °C, whereas **CATb1-6.3** exhibits a much faster reaction with a half-time of around 21 minutes. Furthermore, the different product ratios obtained with each catalyst can also be explained. With **CATa1-6.3**, species **PR1-6.3** and **PR2-6.3** are expected to accumulate at room temperature, leading to the allylation reaction predominantly occurring on these structures.

On the other hand, with the other catalyst, as the RDS is the first one, the only species expected to accumulate is **PR3-6.3**. Consequently, the allylation reaction will predominantly proceed through this aldehyde. To accurately predict the product mixtures at lower temperatures, the TSs for allylation must exhibit similar energy barriers to **TS3b1-6.3**.

Kinetic experiments were conducted in the absence of allylboronate to support the previously proposed mechanism and verify if the RDS aligns with the computational calculations. To achieve this, the reaction between **RE-6.3** and 10 mol% of both catalysts, **CATa1-6.3** and **CATb1-6.3**, was monitored by ^{1}H-NMR at room temperature. The results are presented in **Figure 6.26**. These findings corroborate a two-step sequential process, wherein **RE-6.3** transforms into **PR1-6.3**, which exists in equilibrium with its tautomer, **PR2-6.3**. Due to the relatively low energy barrier between these tautomers (8 - 11 kcal/mol), an averaged spectrum is observed, with **PR1-6.3** being the predominant species in solution, as previously reported. [53b, 60]

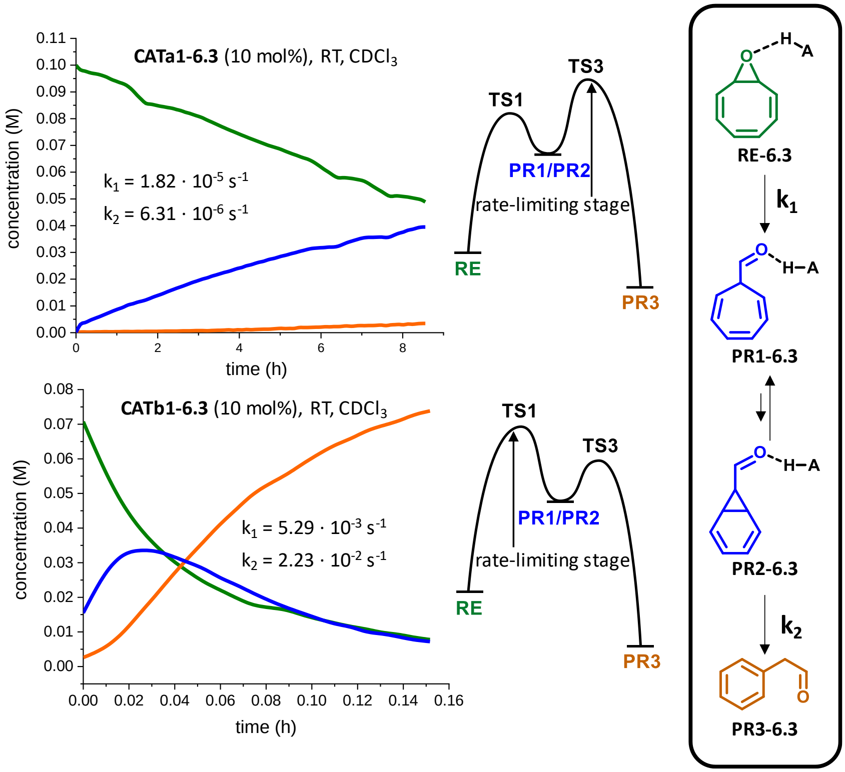

***Figure 6.26**: Isomerization of **RE-6.3** in the presence of 10 mol% of **CATa1-6.3** (**top**) and **CATb1-6.3** (**bottom**) in deuterated chloroform, at room temperature.*

Similar to the previous experiments, a significant difference in reaction rates is observed with each catalyst. This difference is reflected in the kinetic constants for the process, which fall within the range of 10^{-5}-10^{-6} s^{-1} for

CATa1-6.3 and aproximately 10^{-2}-10^{-3} s^{-1} for **CATb1-6.3**. By applying Eyring's equation, these constants can be converted into energy barriers that can be compared to the barriers obtained through computational calculations.

When **CATa1-6.3** is employed, the second step becomes the RDS, resulting in the accumulation of **PR1-6.3**. The experimental energy barriers, determined using Eyring's equation, are found to be 23.9 kcal/mol for the first step and 24.5 kcal/mol for the second step. These values exhibit excellent agreement with the corresponding theoretical barriers of 22.6 and 23.6 kcal/mol, respectively.

On the other hand, when **CATb1-6.3** is utilized, a significantly faster reaction is observed, resulting in higher kinetic constants. The initial accumulation of **PR1-6.3** is rapidly replaced by an increasing concentration of **PR3-6.3**, which ultimately becomes the predominant product at the end of the reaction. Transforming the kinetic constants into energy barriers, we obtain values of 20.6 kcal/mol for the first step and 19.7 kcal/mol for the second step. When compared to the computational barriers of 21.9 and 17.8 kcal/mol, respectively, these results fall within the acceptable error range for DFT calculations, typically around 1-2 kcal/mol. [61]

Additionally, the reactions were carried out at different temperatures to investigate if the same behavior was observed. The results are presented in **Figure 6.27**. The reaction with **CATa1-6.3** was replicated at 50 °C, and although the reaction rate increased, there was no significant increase in the concentration of **PR3-6.3**. Conversely, due to the rapid reaction rate at room temperature, the reaction with **CATb1-6.3** was repeated at 0 °C, where a similar behavior was once again observed. Besides the reduction in reaction rate, the only notable difference was a slight increase in the maximum concentration of **PR1-6.3**. This suggests that k_2 is less affected by temperature compared to k_1, which could be one of the reasons for the different product mixtures obtained when using this catalyst at lower temperatures.

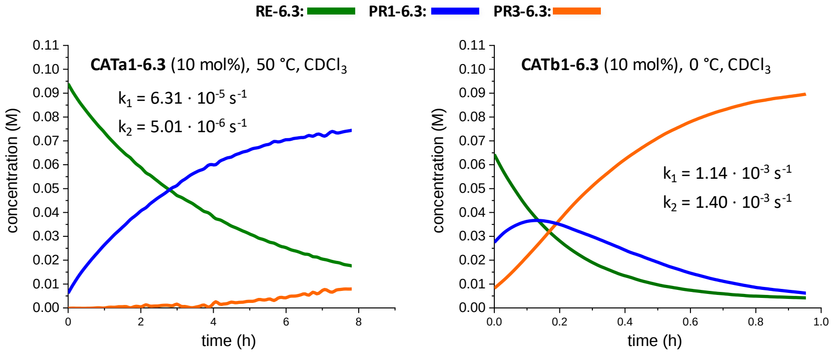

Figure 6.27: *Isomerization of* ***RE-6.3*** *in the presence of 10 mol% of* ***CATa1-6.3*** *at 50 °C (**left**) and* ***CATb1-6.3*** *at 0 °C (**right**) in deuterated chloroform.*

Once the computational model has been validated, and the kinetic barriers for ring-contraction have been determined, the next step involves examining the energy profile of allylboronation for the aldehydes **PR1-6.3**, **PR2-6.3**, and **PR3-6.3**. This reaction, including enantio-control, has previously been investigated by Goodman and colleagues, who established that the reaction proceeds through a chair-like TS characterized by interactions between the allylboronate and the aldehyde. [62] However, in this model, it is observed that the catalyst forms a hydrogen bond with the oxygen atoms from the boronate, rather than with the aldehyde as in the previous reaction.

The model structure, along with the theoretical barriers for allylation, is depicted in **Scheme 6.22**, while the corresponding TS with **CATa1-6.3** are illustrated in **Figure 6.28**. The TSs with **CATb1-6.3** exhibit a similar arrangement and distances. Comparing the energy barriers using both catalysts reveals the limited influence of the catalyst's acidity on the barriers. However, this observation does not imply that the acidity of the catalyst has no impact on the reaction's progression.

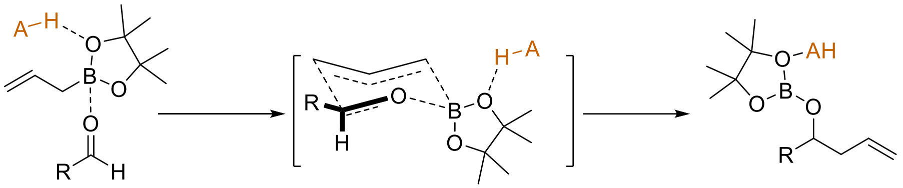

EC1a1,b1
EC2a1,b1
EC3a1,b1

TS4a1 (7.3) **TS4b1** (7.3)
TS5a1 (10.8) **TS5b1** (9.8)
TS6a1 (7.5) **TS6b1** (7.2)

AL1a1,b1
AL2a1,b1
AL3a1,b1

1 series and **TS4a1,b1** from aldehyde **PR1a1,b1**
2 series and **TS5a1,b1** from aldehyde **PR2a1,b1**
3 series and **TS6a1,b1** from aldehyde **PR3a1,b1**

a1 series using **CATa1-6.3** as a catalyst
b1 series using **CATb1-6.3** as a catalyst

Scheme 6.22: *Calculation of the allylation reaction from the corresponding encounter complexes* ***EC*** *to the final complexes* ***AL****. Section extensions -6.3 has been removed for clarity. Relative barriers of the corresponding TS are given in kcal/mol and has been calculated at wb97xd/def2tzvp/SMD=chloroform//wb97xd/def2svp/SMD=chloroform.*

The barriers obtained for allylation are always lower than the ring-contraction of **PR2-6.3**, leading to **PR3-6.3**. This means that the allylation of this product should not be observed. However, this reaction needs a deprotonated aldehyde as a starting point. With **CATa1-6.3**, its low acidity allows a higher proportion of deprotonated aldehyde compared to **CATb1-6.3**, where almost 100% of the aldehyde is in its protonated form. This fact, together with the new kinetic dependence of the allylboronate concentration, can slow down the allylation step enough to be competitive with the ring contraction of **RE2-6.3**.

Both computational and experimental results demonstrate the crucial role of the catalyst's acidity in the reaction. Thus, other acids were used as catalysts to establish a correlation between the selectivity for each aldehyde and the acid pK_a. As depicted in **Figure 6.29**, a clear trend is observed. Firstly, there is a minimum pK_a necessary to induce the ring-opening of the COT oxide **RE-6.3**. Acids such as benzoic acid (pK_a = 21.5) or perfluorophenol (pK_a = 20.5) [63] were not strong enough to catalyze the reaction, resulting in no product obtained.

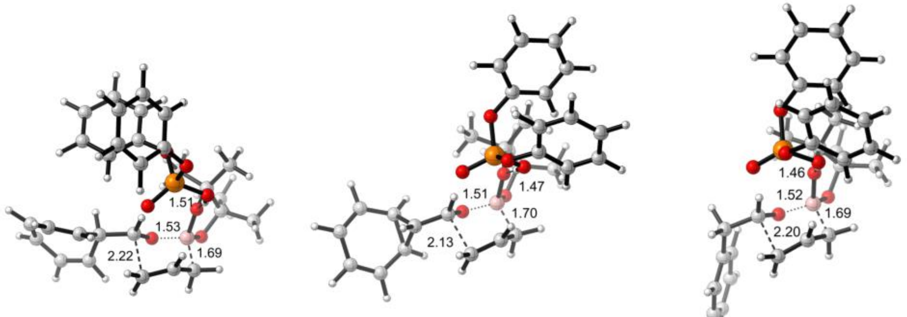

TS4a1-6.3 **TS5a1-6.3** **TS6a-6.3**

Figure 6.28: *Optimized geometries of the TS corresponding to the allylboronation at wb97xd/def2svp/SMD=chloroform using* ***CATa1-6.3****. Optimized structures using* ***CATb1-6.3*** *present almost the same disposition, with bond differences lower than 0.2 Å around the reacting points compared to the illustrated.*

With a stronger acid such as 4-$CF_3C_6F_4OH$ (pK_a=16.6), low conversions to **PR1-6.3** were observed after a prolonged reaction time. Moving to **CATa1-6.3** (pk_a= 13.6), a complete disappearance of **RE-6.3** was observed after 12 h. Increasing acidities led to an increasing proportion of **PR3-6.3**, once again demonstrating the crucial role of the catalyst's pK_a in the product ratio of the ring-contraction of COT oxide. [58, 64]

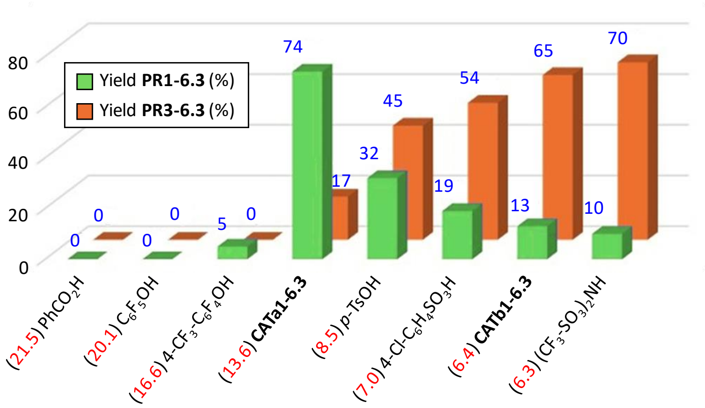

Figure 6.29: *Correlation of catalyst acidity versus selectivity in the acid-catalyzed ring contraction of* ***RE-6.3****. Blue numbers represent selectivity in % and red numbers represent* pK_a.

Once the mechanism and the influence of the catalyst have been clarified, the next step is to develop an enantioselective version of this reaction. In this version, COT oxide **RE-6.3** undergoes a single ring contraction in the presence of allylboronate **B1-6.3** and a chiral Brønsted acid, resulting in the formation of the enantioenriched homoallylic alcohol **AL1-6.3**. The double ring contraction to **PR3-6.3** has not been studied, as this reaction can be performed using commercially available phenylacetaldehyde. [65]

To induce chirality, a list of BINOL-derived phosphoric acids was tested. The reaction conditions were optimized, including solvent, temperature, and concentrations. The optimized conditions are shown in **Scheme 6.23**, with **CATa2-6.3** being the catalyst that provided higher yields and enantioselectivity. Interestingly, the use of a derivative of the previous diphenylphosphoramide catalyst, **CATb2-6.3**, resulted in an **AL1-6.3**/**AL3-6.3** mixture in which **AL1-6.3** was obtained with a 76% enantiomeric excess, while **AL3-6.3** resulted in a racemic mixture.

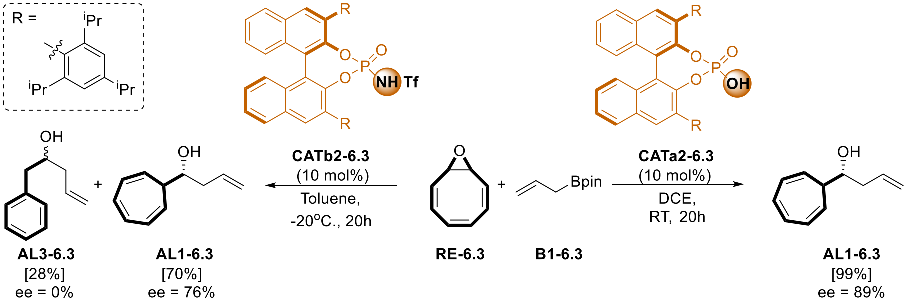

Scheme 6.23: *Optimized reaction conditions of the enantioselective acid-catalyzed ring contraction/allylation along with the results using* ***CATb2-6.3****.*

Computational calculations were performed using the chiral catalyst **CATa2-6.3**, applying the Goodman model as in the previous cases. The reaction using **CATb2-6.3** was also studied for comparison. For this purpose, the catalyzed reactions between allylboronate **B1-6.3** and aldehydes **PR1-6.3** (**TS4a2/b2-6.3**), **PR2-6.3** (**TS5a2/b2-6.3**), and **PR3-6.3** (**TS6a2/b2-6.3**) were used as a model. Both the *Re* and *Si* faces of the aldehyde, along with the conformational variability of the TS, were studied, resulting in a total of 36 TSs. The lowest energy barrier TS are depicted in **Figure 6.30**.

Starting with the reaction using **CATa2-6.3**, the calculations predict the predominant formation of the *Re* enantiomer, with a difference of 3.0 kcal/mol compared to the attack from the other face. This is in excellent agreement with the experimentally observed 89% ee.

On the other hand, calculations with **CATb2-6.3** also predicted high enantioselectivity towards the *Re* isomer when starting from **PR1-6.3**, with a slightly smaller difference compared to the attack from the opposite face (2.5 kcal/mol). Additionally, calculations indicated a practically racemic mixture when starting from **PR3-6.3**, with a slight preference (0.5 kcal/mol) for the *Si* face attack. These results are in excellent agreement with the experimental findings.

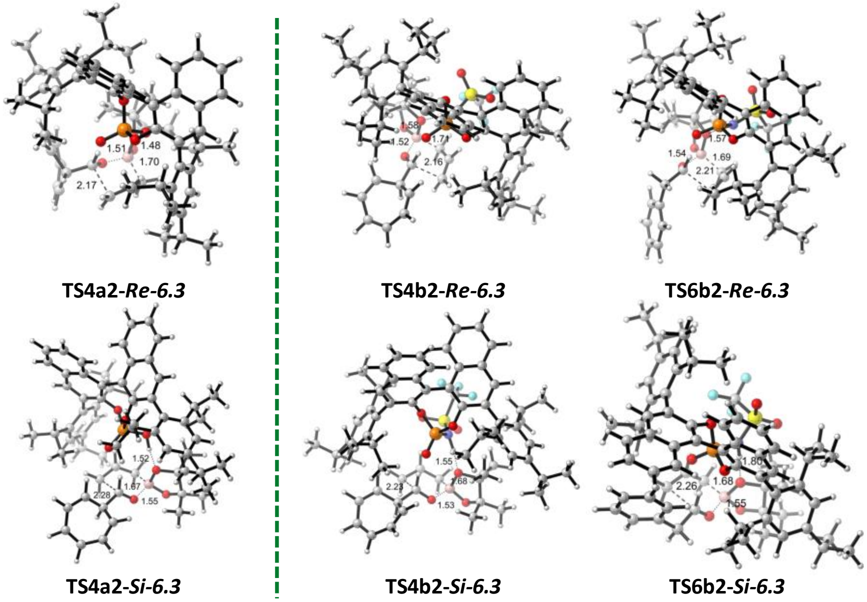

TS4a2-*Re-6.3* **TS4b2-*Re-6.3*** **TS6b2-*Re-6.3***

TS4a2-*Si-6.3* **TS4b2-*Si-6.3*** **TS6b2-*Si-6.3***

Figure 6.30: *Optimized geometries at wb97xd/def2svp:pm6 level of theory for the lower TSs corresponding to the enantioselective allylboronation.*

6.2.3.3 Conclusions

COT oxide **RE-6.3** can undergo both single and double ring contractions depending on the acidity of the catalyst.

While some acidity is required to initiate the ring-opening of the epoxide, higher catalyst acidities increase the proportion of the double ring contraction product **PR3-6.3** over the single ring-contracted **PR1-6.3**, which has a more interesting structure.

The process occurs in a concerted manner, where the starting material **RE-6.3** is transformed into the cycloheptatrienyl-aldehyde **PR1-6.3** through the formation of two different transient carbocations.

The RDS of this process depends on the catalyst acidity, with the evolution from **PR1-6.3** to **PR3-6.3** becoming the RDS when a low acidity catalyst is used. When a stronger acid is employed, the first step becomes the RDS, leading directly to the formation of **PR3-6.3**. This mechanism has been confirmed through kinetic experiments.

The ring contraction can be coupled *in situ* with an allylation reaction process, providing a straightforward method for synthesizing enantioenriched cycloheptatrienyl-substituted homoallylic alcohols.

Computational evaluation using the chiral catalyst also reproduced the observed experimental results.

6.2.4 Mechanistic study over an organocatalytic enantioselective vinylcyclopropane-cyclopentene rearrangement

6.2.4.1 Introduction

In this section, the reaction studied involved the ring expansion of vinylcyclopropanes to provide cyclopentenes. It had been previously reported in 1959, [66] although the utility of this reaction was very limited due to the extreme reaction conditions that involved temperatures around 500 °C (**Scheme 6.24a**). Over time, this reaction has been tuned to operate under milder conditions, incorporating specific substitution patterns over the vinylcyclopropane scaffold or using transition metal or photochemical activations. [67]

Focusing on the possibility of performing this rearrangement to provide enantio-enriched cyclopente solutions, all attempts have been limited to enantiospecific reactions, using enantiomerically enriched vinylcyclopropanes as starting materials. [68] Recently, Christmann and co-workers reported an enantiospecific divinylcyclopropane-cycloheptene rearrangement using enamine organocatalysis to activate the cyclopropane moiety (**Scheme 6.24b**). [69] However, it was demonstrated that the absolute configuration of the product was only dependent on the starting material's, making it impossible to control the absolute configuration of the product with the catalyst.

In particular, a catalyst-controlled enantioselective vinylcyclopropane-cyclopentene rearrangement has been studied (**Scheme 6.24c**). The activation of the starting material is achieved through enamine organocatalysis, which utilizes the donor-acceptor structure around the cyclopropane moiety to facilitate the ring-opening of the enamine **EN-6.4** by stabilizing the intermediate **IN-6.4**, which has lost all the chiral information from the starting material. Subsequently, the intermediate undergoes ring-closure to form a cyclopentene scaffold **FC-6.4** in which the stereochemical outcome is controlled by the catalyst. The final product is obtained after the hydrolysis of the iminium moiety. Overall, this process can be categorized as a type-II DYKAT. [70] Further explanation on this matter will be provided in the subsequent pages.

As in the previous examples, the reaction was first performed experimentally by or collaborators from Bilbao, to study the influence of the catalyst, solvent and temperature over the yield, diastereo- and enantioselectivity. **REa-6.4** was selected for screening the best reaction conditions, and it was found that the reaction with **CAT-6.4** in dichloromethane at 0 °C provided the highest yields and selectivities. Only 5 min. were necessary to achieve full conversion of **REa-6.4** to **PR1a-6.4**, resulting in high yields but only moderate diastereoselectivity. The subsequent isomerization of **PR1a-6.4** led to the clean formation of **PR2a-6.4** with excellent enantioselectivity. The best reaction conditions, are depicted in **Scheme 6.25**.

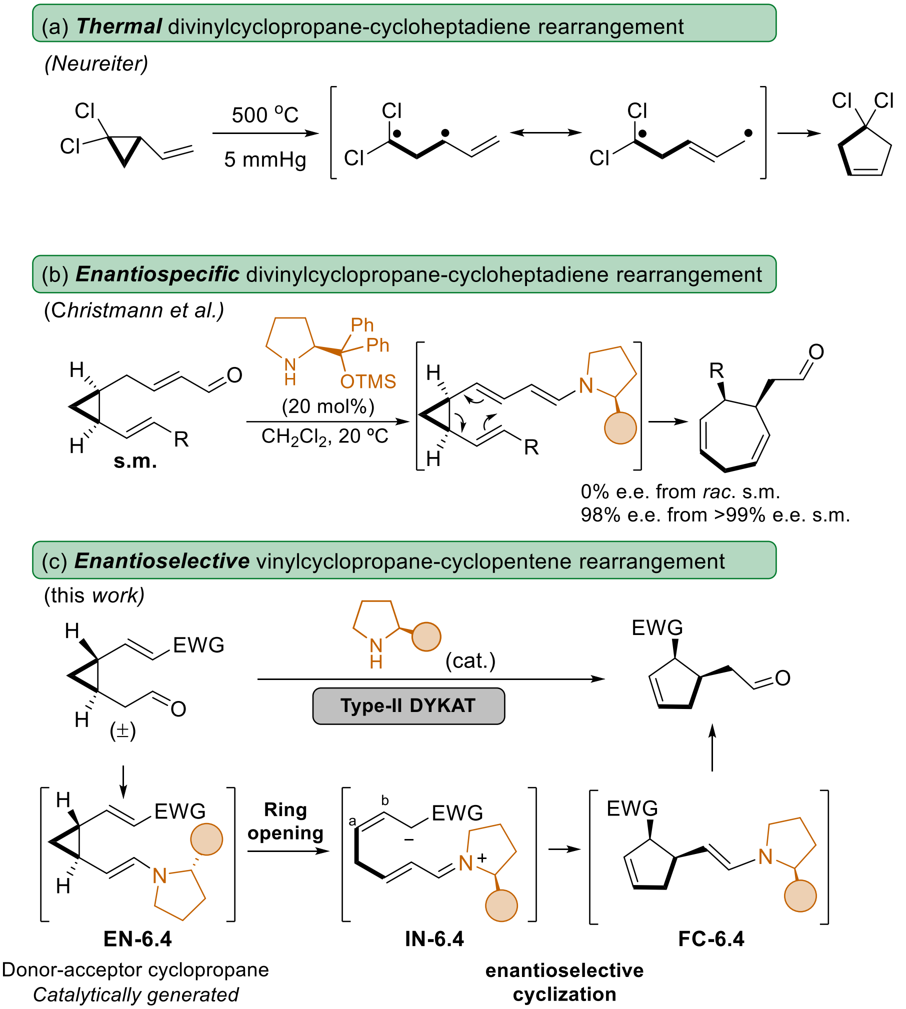
(a) **Thermal** divinylcyclopropane-cycloheptadiene rearrangement
(Neureiter)
500 °C
5 mmHg
Cl
(b) **Enantiospecific** divinylcyclopropane-cycloheptadiene rearrangement
(Christmann et al.)
Ph
OTMS
(20 mol%)
CH2Cl2, 20 °C
s.m.
R
0% e.e. from rac. s.m.
98% e.e. from >99% e.e. s.m.
(c) **Enantioselective** vinylcyclopropane-cyclopentene rearrangement
(this work)
EWG
(cat.)
Type-II DYKAT
(±)
Ring opening
EN-6.4
Donor-acceptor cyclopropane
Catalytically generated
IN-6.4
enantioselective cyclization
FC-6.4

Scheme 6.24: *Vinylcyclopropane rearrangements through (a) thermal conditions, (b) dienamine, and (c) enamine activation manifolds.*

All other substrates, including electron-donating and electron-withdrawing substituted vinylcyclopropanes, as well as alkyl-substituted ones afforded high yields and enantiocontrols demonstrating the robustness of the reaction. The moderate diastereoselectivity in the formation of **PR1a-6.4** is irrelevant since both isomers can be easily converted into the same product **PR2a-6.4**.

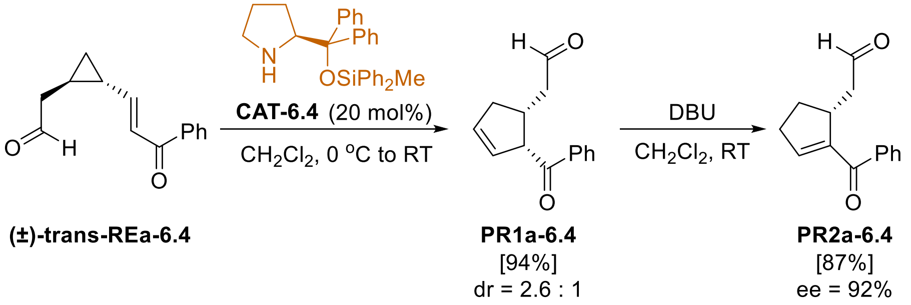
CAT-6.4 (20 mol%)
CH_2Cl_2, 0 °C to RT
DBU
CH_2Cl_2, RT
(±)-trans-REa-6.4
PR1a-6.4
[94%]
dr = 2.6 : 1
PR2a-6.4
[87%]
ee = 92%

***Scheme 6.25:** Optimized reaction conditions for the ring expansion and isomerization of vinylcyclopropanes. Reaction carried out in a 0.1 mmol scale of a racemic mixture of vinylcyclopropane **trans-REa-6.4**, using 20 mol % of catalyst **CAT-6.4** in dichloromethane.*

The same reaction conditions were applied to the *cis*-configured cyclopropane **(±)-*cis*-REa-6.4**. As shown in **Scheme 6.26**, the results in terms of yield and enantioselectivity are quite similar to those obtained for the *trans*-cyclopropane **REa-6.4**. Similarly, the diastereoselectivity observed in the formation of **PR1a-6.4** from the cis-vinylcyclopropane follows a similar trend, with the cis-configured diastereomer being more abundant.

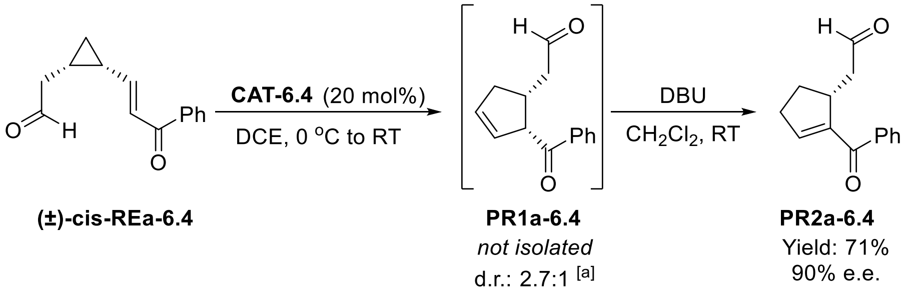
CAT-6.4 (20 mol%)
DCE, 0 °C to RT
DBU
CH_2Cl_2, RT
(±)-cis-REa-6.4
PR1a-6.4
not isolated
d.r.: 2.7:1 [a]
PR2a-6.4
Yield: 71%
90% e.e.

***Scheme 6.26:** Vinylcyclopropane-cyclopentene rearrangement under optimized reaction conditions using a cis-configured cyclopropane substrate. [a] Determined by NMR analysis of the crude reaction mixture.*

This fact demonstrated that regardless the initial configuration of the starting cyclopropane, the same enantiomer is mostly obtained. The reason for this lies in the formation of the intermediate **INa-6.4**, where all the initial configurational information from the vinylcyclopropane has been lost, allowing for a interconversion between different isomers. This situation, depicted in

Scheme 6.27, is classic in kinetic resolutions. To determine its specific type and understand the chemical processes involved in the isomerization, the mechanism of the reaction was studied using computational tools. In particular, **REa-6.4** was used for the reaction modeling, with a focus on the evolution of the enamine **ENa-6.4** to the iminium ion intermediate **FCa-6.4**.

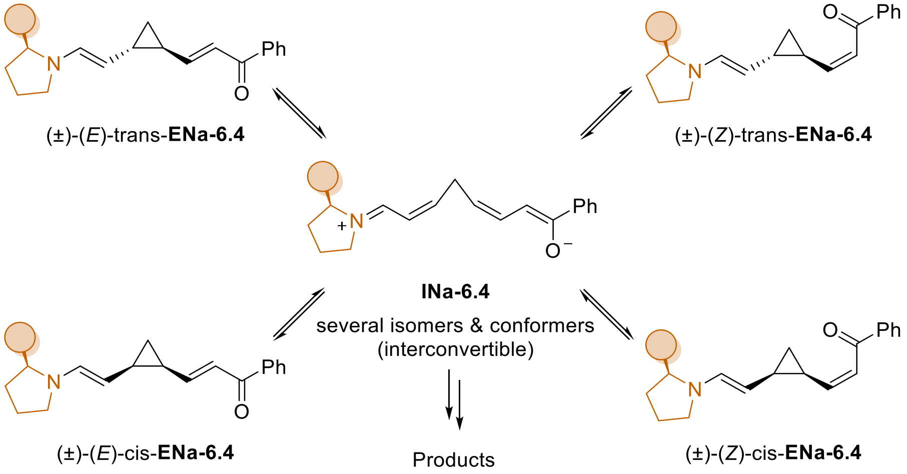
(±)-(*E*)-trans-**ENa-6.4**
(±)-(*Z*)-trans-**ENa-6.4**
INa-6.4
several isomers & conformers
(interconvertible)
(±)-(*E*)-cis-**ENa-6.4**
Products
(±)-(*Z*)-cis-**ENa-6.4**
Ph
O
N
O⁻
+N

Scheme 6.27: *Transformation of configurational information into conformational information and vice versa. All isomers are connected with the same intermediate* ***Ina-6.4*** *in which all the stereochemical information coming from the cyclopropane starting material had been removed.*

6.2.4.2 Results and discussion

For the initial exploration of the PES, the chiral catalyst **CAT-6.4** was substituted with a simpler and achiral pyrrolidine. Since conformational information is transformed in configurational information during the reaction, the first step involved evaluating the conformations of the initial enamine **ENa1-6.4**. It was found that conformer **ENa1-B-6.4** exhibited the lowest energy structure for **ENa1-6.4**. However, this conformation would result in the formation of a *trans* C6-C7 double bond once the cyclopropane ring is broken. This disposition if the double bond would lead to the formation of a highly strained *trans* cyclopentene, resulting in a dead-end. Therefore, this structure must undergo a conformational TS to become conformer **ENa1-A-6.4**, from which *cis*-cyclopentenes are formed (**Figure 6.31**).

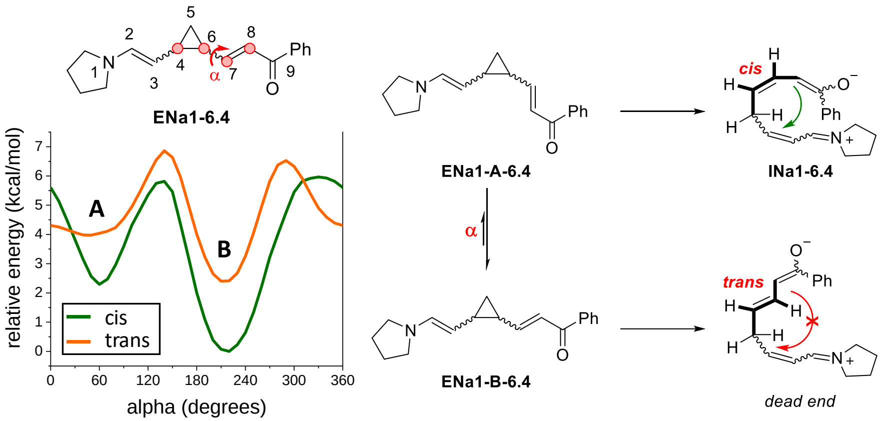

Figure 6.31: *Conformational analysis of the cis- (green line) and trans- isomers (orange line) of the starting intermediate ENa-6.4. α angle is defined as the C4-C6-C7-C8 dihedral angle.*

However, as conformation and configuration information are inverted after the breakage of the cyclopropane ring from conformer **ENa1-A-6.4**, a total of 32 different conformers of **INa1-6.4** can be formed. Attending to crystallographic data from Seebach and co-workers, only *s-trans* C2-C3 iminium ions can be observed in the solid state, [71] and so the 32 initial structures can be reduced to 16, considering only the variables displayed in **Table 6.2**.

Table 6.2: *Variables considered for defining TS.*

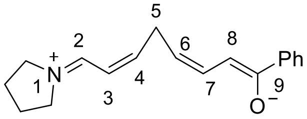

INa1-6.4

Bond	Variables	Isomers Derived
C2-C3	fixed as *s-trans*	1
C3=C4	*E* / *Z*	2
C4-C5 **C5-C6**	*Re*(im)-*Si*(enol) *Re*(im)-*Re*(enol)	2
C6=C7	only Z productive	1
C7-C8	*s-cis* / *s-trans*	2
C8=C9	*E* / *Z*	2
		TOTAL: 16

Out of these 16 geometries, attempts to locate the TS for the cyclopropane ring-opening were unsuccessful, suggesting a flat PES around this species. Instead, TSs close to the formation of **FCa1-6.4** were found, resulting in a total of 10 TSs derived from the initially proposed 16 structures. Among these structures, *cis*-**TSa1-6.4** and *trans*-**TSa1-6.4,** were identified as the minimum energy pathways for the formation of the two possible product isomers, *cis*-**FCa1-6.4** and *trans*-**FCa1-6.4**, respectively**.** IRC calculations from these TSs confirmed the flatness of the PES and revealed a typical shoulder shape indicative of hidden intermediates (**Figure 6.32, left**). [59, 72]

After the ring-opening of the cyclopropane, a highly polar structure is formed, and its stability relies on the interactions between the opposite charged fragments. These interactions also play a crucial role in determining the stability of the corresponding TSs, as indicated by the analysis of the NCI (**Figure 6.32, right**). [73] It can be observed that *cis*-**TSa1-6.4** exhibits a continuous surface that is larger than the interrupted surface of *trans*-**TSa1-6.4**, indicating its lower stability. The energy difference between the two TS accurately predicts a moderate diastereoselectivity, which is consistent with the experimental results.

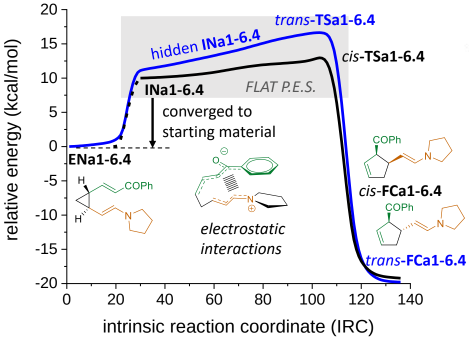

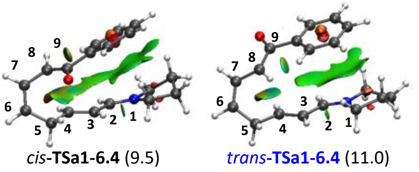

Bond	*cis*-TSa1-6.4	*trans*-TSa1-6.4
C2-C3 🔒	*s-trans*	*s-trans*
C3=C4	*E*	*E*
C4-C5 **C5-C6**	*Re*(im)-*Si*(enol)	*Re*(im)-*Re*(enol)
C6=C7 🔒	*Z*	*Z*
C7-C8	*s-cis*	*s-trans*
C8=C9	*Z*	*Z*

***Figure 6.32: (Left)** IRC of the most stable TS corresponding to the attack by the two different diastereotopic faces, leading to cis-**FCa1-6.4** and trans-**FCa1-6.4**. Dashed line indicates a complementary relaxed scan from the starting point of the IRC from cis-**TSa1-6.4**. **(Right)** Optimized geometries (wb97xd/def2svp/SMD=CH_2Cl_2) of cis-**TSa1-6.4** and trans-**TSa1-6.4** showing a NCI analysis representing the electrostatic interactions between the two parts of the intermediate, along with a table summarizing the conformational differences between both TS. Respective free energy barriers are depicted in brackets (wb97xd/def2tzvp/SMD=CH_2Cl_2//wb97xd/def2svp /SMD=CH_2Cl_2).*

The concerted pathway discovered contrasts with the previously proposed explanation of a common achiral intermediate. Since the reaction follows a concerted mechanism, theoretically, each starting geometry should lead to a unique pathway, and thus no kinetic resolution should be observed. However, when all the intrinsic reaction coordinate (IRC) pathways from the 10 previously identified transition states (only 8 displayed) are superimposed, as depicted in

Figure 6.33, it becomes apparent that the planar surfaces corresponding to all the hidden intermediates are very close in energy. This proximity allows for intercrossing between the IRC pathways. In other words, once a hidden intermediate is formed, it can either continue along the predetermined IRC pathway or bypass lower conformational transition states to transition from one IRC pathway to another. This merging occurs in the more stable conformations of the hidden intermediates, ultimately driving the reaction through the lowest transition states for cyclopentene ring closure.

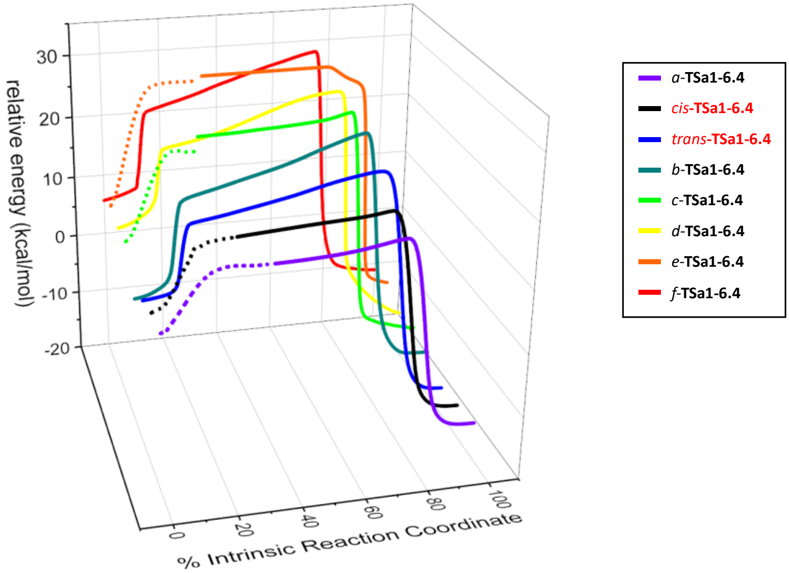

Figure 6.33: *IRC superposition from the 10 TSs geometries found for the ring-opening reaction of **ENa1-6.4**, only 8 out of 10 IRCs afforded normal termination, and these last are the only ones that could be displayed. Dashed lines indicate complementary relaxed scans from the starting point of each IRC. Cis-**TSa1-6.4** and trans-**TSa1-6.4** are written in red for clarity.*

Next, the real system was investigated by introducing the C-2 substituent of the pyrrolidine in the achiral system. Previous studies on the catalyst **CAT-6.4**, conducted by Hayashi and co-workers, [74] demonstrated that this catalyst leads to highly energetically favored *s-trans-(E,E)*-eniminium ions, in which the new exocyclic C-C bond adopts a *sc-exo* conformation.

This significantly reduced the number of conformers that needed to be considered for the chiral system. To explore the remaining conformational variables, the *cis*-**TSa1-6.4** and *trans*-**TSa1-6.4** models were grown, substituting the previous pyrrolidine catalyst with **CAT-6.4**, and performing Macromodel searches over these new structures. The searches only allowed exploration of the conformational variability around the new catalyst, including the C-2 substituent and the puckering of the pyrrolidine ring (**Error! Reference source not found.**).

Further optimization of these structures led to the identification of *cis*-**TSa2-(1R,2S)-6.4**, *cis*-**TSa2-(1S,2R)-6.4** as the minimum energy TSs derived from *cis*-**TSa1-6.4**. Similarly, *trans*-**TSa2-(1R,2R)-6.4** and *trans*-**TSa2-(1S,2S)-6.4** were identified as the minimum energy TSs derived from *trans*-**TSa1-6.4**. The calculated relative free energy distribution predicted a 1.3:1 ratio in favor of the *cis* isomer, which is in good agreement with the experimental results (2.6:1). Furthermore, high enantioselectivities were also predicted, once again consistent with the experimental results (90% e.e.).

As in the achiral model, NCI calculation explained the preference for one TS. Two major interactions can be defined in this system: the electrostatic interaction between both fragments of the previous cyclopropane ring, produced by the different charge of the enol and the imine moieties (as in the achiral system), and the London and π-interactions, between the catalyst C-2 substituent and the imine fragment.

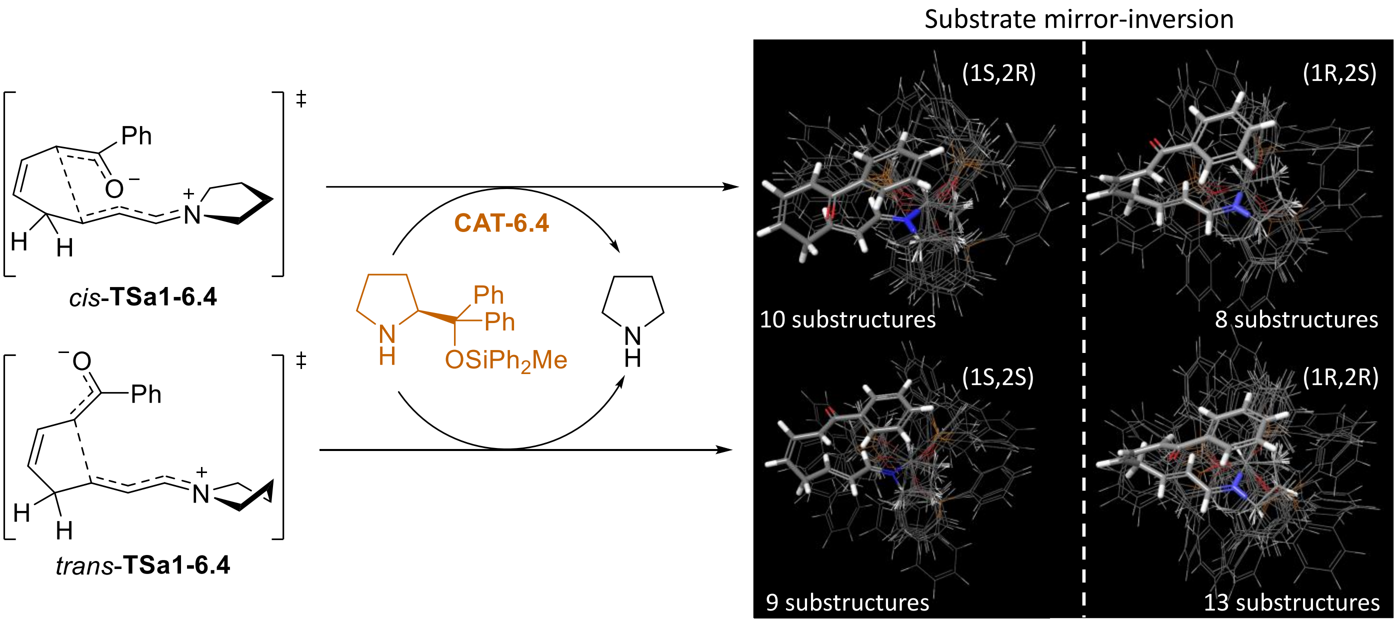
Substrate mirror-inversion
‡
Ph
O−
+
N
H
H
cis-TSa1-6.4
‡
−O
Ph
+
N
H
H
trans-TSa1-6.4
CAT-6.4
N
H
Ph
Ph
OSiPh2Me
N
H
(1S,2R)
10 substructures
(1R,2S)
8 substructures
(1S,2S)
9 substructures
(1R,2R)
13 substructures

Figure 6.34: *Procedure for the model growing from the achiral system. Pyrrolidine catalyst has been replaced by* ***CAT-6.4*** *in the normal, and mirror-inverted geometries of the achiral TSs. In the conformer structure superposition, thick bonds represent the fixed part of the molecule.*

The highest TS of these four structures (*trans*-**TSa2-(1S,2S)-6.4**) lacks from any of the strong interactions previously described. The second and third highest TSs present only one strong interaction with the imine moiety, having *cis*-**TSa2-(1S,2R)-6.4** a strong electrostatic interaction between both cyclopropane fragments, and *trans*-**TSa2-(1R,2R)-6.4** a strong interaction with the catalyst. Finally, the lowest TS, *cis*-**TSa2-(1R,2S)-6.4** presents a stronger interaction with both parts of the molecule, promoting the highest stability of this latter (**Figure 6.35**).

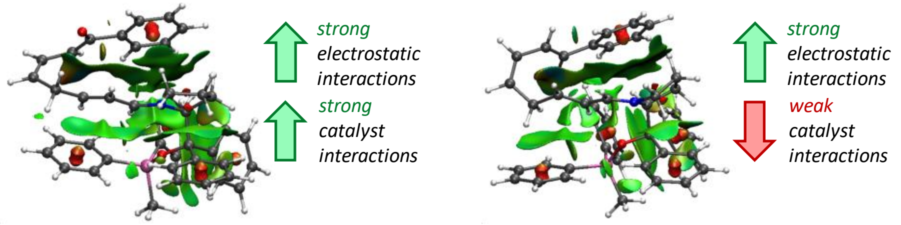
strong electrostatic interactions
strong catalyst interactions
strong electrostatic interactions
weak catalyst interactions

cis-**TSa2-(1R,2S)-6.4**
(8.2)

cis-**TSa2-(1S,2R)-6.4**
(12,9)

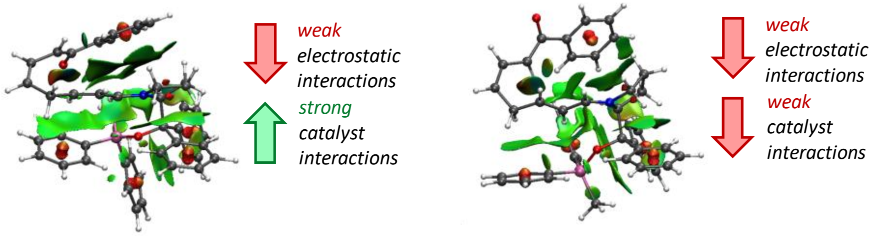
weak electrostatic interactions
strong catalyst interactions
weak electrostatic interactions
weak catalyst interactions

trans-**TSa2-(1R,2R)-6.4**
(9.7)

trans-**TSa2-(1S,2S)-6.4**
(18.6)

Figure 6.35: *Comparison between NCI interactions in the optimized geometries of the TSs corresponding to the chiral real model at wb97xd/def2svp/SMD=CH_2Cl_2.*

6.2.4.3 Conclusions

The different selectivities of the reaction are influenced by both steric and electronic factors, with the critical variables being the electrostatic interactions between the cyclopropane fragments and the interactions with the catalyst.

The loss of configurational information and the planar surface connecting the different hidden intermediate conformations enable a type II DYKAT process.

Regardless of the configuration of the starting material, one, unique, major enantiomer is obtained as the product.

6.3 Conclusions

In this chapter various organocatalytic processes has been explored. Computational techniques along with the experimental data has allowed for the accurate determination of the mechanism of multiple types of reactions. The enantioselectivity induced by the chiral catalysts has also been explored, obtaining similar results compared to the experimental. Other types of calculations, such as ELF, NCI and MD had demonstrated its utility as valuable tools for studying not only singular molecular species, but the whole reaction pathway.

It is evident that the future of DFT calculations holds great promise for significant improvements. Through ongoing advancements in computational power, algorithmic developments, and the integration of machine learning techniques, the accuracy and efficiency of DFT calculations are poised to reach new heights. The incorporation of more accurate exchange-correlation functionals and the exploration of novel theoretical approaches will enhance the predictive capabilities of DFT, enabling the study of larger and more complex systems with higher precision.

Additionally, the continued collaboration between experimentalists and theorists will facilitate the validation and refinement of DFT methods, further bolstering their reliability. As computational resources become more accessible and specialized, DFT calculations will become more routine, empowering researchers across various scientific domains to explore and uncover the intricacies of matter and phenomena with unprecedented detail. Ultimately, the future of DFT calculations appears promising, paving the way for groundbreaking discoveries and applications in materials science, chemistry, and beyond.

6.4 References

[1] F.D.A., https://www.fda.gov/regulatory-information/search-fda-guidance-documents/development-new-stereoisomeric-drugs, (visited May 29th, 2023).

[2] D. Seebach, E. Hungerbühler, in *Modern Synthetic Methods* (Ed.: R. Scheffold), Salle + Sauerländer, Frankfurt, Germany, **1980**.

[3] E. Reyes, L. Prieto, A. Milelli, *Molecules* **2023**, *28*, 271.

[4] M. C. Holland, R. Gilmour, *Angew. Chem. Int. Ed.* **2015**, *54*, 3862-3871.

[5] a) J. Izquierdo, G. E. Hutson, D. T. Cohen, K. A. Scheidt, *Angew. Chem., Int. Ed. Engl.* **2012**, *51*, 11686-11698; b) E. Reyes, U. Uria, L. Carrillo, J. L. Vicario, *Synth.* **2017**, *49*, 451-471; c) P. Bellotti, M. Koy, M. N. Hopkinson, F. Glorius, *Nat. Rev. Chem.* **2021**, *5*, 711-725.

[6] a) S. Khong, T. Venkatesh, O. Kwon, *Asian J. Org. Chem.* **2021**, *10*, 2699-2708; b) H. Guo, Y. C. Fan, Z. Sun, Y. Wu, O. Kwon, *Chem. Rev.* **2018**, *118*, 10049-10293.

[7] a) J. Chen, X. Gong, J. Li, Y. Li, J. Ma, C. Hou, G. Zhao, W. Yuan, B. Zhao, *Science* **2018**, *360*, 1438-1442; b) C. Hou, B. Peng, S. Ye, Z. Yin, J. Cao, X. Xiao, B. Zhao, *Nat. Catal.* **2022**, *5*, 1061-1068.

[8] A. Parra, *Chem. Rev.* **2019**, *119*, 12033-12088.

[9] R. S. J. Proctor, A. C. Colgan, R. J. Phipps, *Nat. Chem.* **2020**, *12*, 990-1004.

[10] a) A. G. Doyle, E. N. Jacobsen, *Chem. Rev.* **2007**, *107*, 5713-5743; b) M. Žabka, R. Šebesta, *Molecules* **2015**, *20*, 15500-15524; c) J. Merad, C. Lalli, G. Bernadat, J. Maury, G. Masson, *Chem. Eur. J.* **2018**, *24*, 3925-3943; d) C. Min, D. Seidel, *Chem. Soc. Rev.* **2017**, *46*, 5889-5902.

[11] a) S. Shirakawa, K. Maruoka, *Angew. Chem. Int. Ed.* **2013**, *52*, 4312-4348; b) T. E. Schirmer, B. König, *J. Am. Chem. Soc.* **2022**, *144*, 19207-19218.

[12] W. Notz, F. Tanaka, C. F. Barbas, *Acc. Chem. Res.* **2004**, *37*, 580-591.

[13] a) S. Bahmanyar, K. N. Houk, *J. Am. Chem. Soc.* **2001**, *123*, 12911-12912; b) E. J. Mattioli, M. Calvaresi, A. Bottoni, T. D. Marforio, *Mol. Catal.* **2022**, *522*, 112245.

[14] K. E. Ozboya, T. Rovis, *Chem. Sci.* **2011**, *2*, 1835-1838.

[15] a) S. Mukherjee, B. Biswas, *ChemistrySelect* **2020**, *5*, 10704-10726; b) S. Hanessian, A. K. Chattopadhyay, *Org. Lett.* **2014**, *16*, 232-235; c) C. Grondal, M. Jeanty, D. Enders, *Nat. Chem.* **2010**, *2*, 167-178.

[16] H. B. Hepburn, L. Dell'Amico, P. Melchiorre, *Chem. Rec.* **2016**, *16*, 1787-1806.

[17] a) S. Duce, I. Alonso, A. M. Lamsabhi, E. Rodrigo, S. Morales, J. L. García Ruano, A. Poveda, P. Mauleón, M. B. Cid, *ACS Catal.* **2018**, *8*, 22-34; b) G.-L. Zhao, I. Ibrahem, H. Sundén, A. Córdova, *Adv. Synth. Catal.* **2007**, *349*, 1210-1224.

[18] a) J. F. Austin, D. W. C. MacMillan, *J. Am. Chem. Soc.* **2002**, *124*, 1172-1173; b) N. A. Paras, D. W. C. MacMillan, *J. Am. Chem. Soc.* **2002**, *124*, 7894-7895; c) L. Hojabri, A. Hartikka, F. M. Moghaddam, P. I. Arvidsson, *Adv. Synth. Catal.* **2007**, *349*, 740-748; d) S.-K. Xiang, B. Zhang, L.-H. Zhang, Y. Cui, N. Jiao, *ChemComm.* **2011**, *47*, 5007-5009.

[19] a) B. List, R. A. Lerner, C. F. Barbas, *J. Am. Chem. Soc.* **2000**, *122*, 2395-2396; b) A. B. Northrup, D. W. C. MacMillan, *J. Am. Chem. Soc.* **2002**, *124*, 2458-2460.

[20] W. S. Jen, J. J. M. Wiener, D. W. C. MacMillan, *J. Am. Chem. Soc.* **2000**, *122*, 9874-9875.

[21] M. Harmata, S. K. Ghosh, X. Hong, S. Wacharasindhu, P. Kirchhoefer, *J. Am. Chem. Soc.* **2003**, *125*, 2058-2059.

[22] S. E. Denmark, G. L. Beutner, *Angew. Chem. Int. Ed.* **2008**, *47*, 1560-1638.

[23] a) L. Ratjen, M. van Gemmeren, F. Pesciaioli, B. List, *Angew. Chem. Int. Ed.* **2014**, *53*, 8765-8769; b) M. Lupi, O. Salmi, C. Viglianisi, S. Menichetti, *Adv. Synth. Catal.* **2023**, *365*, 1705-1712; c) L. C. Morrill, A. D. Smith, *Chem. Soc. Rev.* **2014**, *43*, 6214-6226.

[24] a) S. G. Nelson, T. J. Peelen, Z. Wan, *Tetrahedron Lett.* **1999**, *40*, 6541-6543; b) S. G. Nelson, Z. Wan, T. J. Peelen, K. L. Spencer, *Tetrahedron Lett.* **1999**, *40*, 6535-6539; c) T. Nakagawa, H. Fujisawa, Y. Nagata, T. Mukaiyama, *Bull. Chem. Soc. Jpn.* **2005**, *78*, 236-246.

[25] a) S. Saulnier, N. Mehiaoui, S. Leleu, L. Jean, *ChemistrySelect* **2023**, *8*, e202301218; b) H. Santos, L. A. Zeoly, M. T. Rodrigues, Jr., F. S. Fernandes, R. C. Gomes, W. P. Almeida, F. Coelho, *ACS Catal.* **2023**, *13*, 3864-3895; c) R. F. André, A. Palazzolo, C. Poucin, F. Ribot, S. Carenco, *ChemPlusChem* **2023**, *88*, e202300038; d) S. M. Fischer, P. Kaschnitz, C. Slugovc, *Catal. Sci. Technol.* **2022**, *12*, 6204-6212; e) K. Muthuvel, T. Gandhi, *ChemCatChem* **2022**, *14*.

[26] a) K. Maruoka, *Org. Process Res. Dev.* **2008**, *12*, 679-697; b) T. Ooi, K. Maruoka, *Angew. Chem., Int. Ed. Engl.* **2007**, *46*, 4222-4266.

[27] P. Vachal, E. N. Jacobsen, *J. Am. Chem. Soc.* **2002**, *124*, 10012-10014.

[28] a) T. Akiyama, J. Itoh, K. Fuchibe, *Adv. Synth. Catal.* **2006**, *348*, 999-1010; b) M. S. Taylor, E. N. Jacobsen, *Angew. Chem. Int. Ed.* **2006**, *45*, 1520-1543; c) S. J. Connon, *ChemComm.* **2008**, 2499-2510.

[29] a) E. Marsault, A. Toró, P. Nowak, P. Deslongchamps, *Tetrahedron* **2001**, *57*, 4243-4260; b) S. Handa, G. Pattenden, *Contemp. Org. Synth.* **1997**, *4*, 196-215; c) E. Capel, J. Luis-Barrera, A. Sorazu, U. Uria, L. Prieto, E. Reyes, L. Carrillo, J. L. Vicario, *J. Org. Chem.* **2022**, *87*, 10062-10072; d) A. Rizzo, S. R. Harutyunyan, *Org. Biomol. Chem.* **2014**, *12*, 6570-6579.

[30] a) K. I. Takao, H. Kai, A. Yamada, Y. Fukushima, D. Komatsu, A. Ogura, K. Yoshida, *Angew. Chem., Int. Ed. Engl.* **2019**, *58*, 9851-9855; b) X. Liu, J. Liu, J. Wu, G. Huang, R. Liang, L. W. Chung, C.-C. Li, *J. Am. Chem. Soc.* **2019**, *141*, 2872-2877; c) T. Kang, K. L. White, T. J. Mann, A. H. Hoveyda, M. Movassaghi, *Angew. Chem., Int. Ed. Engl.* **2017**, *56*, 13857-13860; d) M. Ohtawa, M. J. Krambis, R. Cerne, J. M. Schkeryantz, J. M. Witkin, R. A. Shenvi, *J. Am. Chem. Soc.* **2017**, *139*, 9637-9644; e) A. Minassi, F. Pollastro, G. Chianese, D. Caprioglio, O. Taglialatela-Scafati, G. Appendino, *Angew. Chem. Int. Ed.* **2017**, *56*, 7935-7938.

[31] a) O. Knopff, J. Kuhne, C. Fehr, *Angew. Chem. Int. Ed.* **2007**, *46*, 1307-1310; b) E. P. Balskus, E. N. Jacobsen, *Science* **2007**, *317*, 1736-1740; c) N. S. Rajapaksa, E. N. Jacobsen, *Org. Lett.* **2013**, *15*, 4238-4241; d) R. Mato, E. Reyes, L. Carrillo, U. Uria, L. Prieto, R. Manzano, J. L. Vicario, *ChemComm.* **2020**, *56*, 13149-13152; e) J. Sendra, R. Manzano, E. Reyes, J. L. Vicario, E. Fernández, *Angew. Chem. Int. Ed.* **2020**, *59*, 2100-2104.

[32] a) M. Cakmak, P. Mayer, D. Trauner, *Nat. Chem.* **2011**, *3*, 543-545; b) M. K. Boukanoun, X. Hou, L. Nikolajev, S. Ratni, D. Olson, A. Claing, S. A. Laporte, S. Chemtob, W. D. Lubell, *Org. Biomol. Chem.* **2015**, *13*, 7750-7761; c) N. D. P. Atmuri, W. D. Lubell, *J. Org. Chem.* **2020**, *85*, 1340-1351.

[33] S. E. Denmark, M. T. Burk, *Org. Lett.* **2012**, *14*, 256-259.

[34] a) M. Saunders, *J. Comput. Chem.* **1991**, *12*, 645-663; b) K. B. Wiberg, *J. Org. Chem.* **2003**, *68*, 9322-9329.

[35] M. Randić, *Int. J. Quantum Chem.* **1995**, *56*, 61-73.

[36] J. I. Seeman, *Chem. Rev.* **1983**, *83*, 83-134.

[37] W. Kumaki, H. Kinoshita, K. Miura, *Tetrahedron* **2022**, *110*, 132687.

[38] a) S.-H. Wang, B.-S. Li, Y.-Q. Tu, *ChemComm.* **2014**, *50*, 2393-2408; b) T.-L. Zheng, Y. Zhang, A. L. Gou, F. Cheng, S.-Z. Liu, L. Yu, M.-Y. Cui, X.-T. Xu, K. Zhang, S.-H. Wang, *Org. Lett.* **2020**, *22*, 7073-7077; c) J. Yang, X.-M. Zhang, F.-M. Zhang, S.-H. Wang, Y.-Q. Tu, Z. Li, X.-C. Wang, H. Wang, *Angew. Chem. Int. Ed.* **2020**, *59*, 8471-8475.

[39] a) X.-M. Zhang, Y.-Q. Tu, F.-M. Zhang, Z.-H. Chen, S.-H. Wang, *Chem. Soc. Rev.* **2017**, *46*, 2272-2305; b) Z. L. Song, C. A. Fan, Y. Q. Tu, *Chem. Rev.* **2011**, *111*, 7523-7556.

[40] a) D. H. Lukamto, M. J. Gaunt, *J. Am. Chem. Soc.* **2017**, *139*, 9160-9163; b) H. Wu, Q. Wang, J. Zhu, *Chem. Eur. J.* **2017**, *23*, 13037-13041; c) Q.-W. Zhang, C.-A. Fan, H.-J. Zhang, Y.-Q. Tu, Y.-M. Zhao, P. Gu, Z.-M. Chen, *Angew. Chem. Int. Ed.* **2009**, *48*, 8572-8574; d) F. Romanov-Michailidis, M. Romanova-Michaelides, M. Pupier, A. Alexakis, *Chem. Eur. J.* **2015**, *21*, 5561-5583; e) Z. Chai, T. J. Rainey, *J. Am. Chem. Soc.* **2012**, *134*, 3615-3618.

[41] a) T. Seiser, N. Cramer, *Angew. Chem. Int. Ed.* **2008**, *47*, 9294-9297; b) E. Zhang, C.-A. Fan, Y.-Q. Tu, F.-M. Zhang, Y.-L. Song, *J. Am. Chem. Soc.* **2009**, *131*, 14626-14627.

[42] a) D. J. Mack, J. T. Njardarson, *ACS Catal.* **2013**, *3*, 272-286; b) E. Leemans, M. D’hooghe, N. De Kimpe, *Chem. Rev.* **2011**, *111*, 3268-3333.

[43] B. Heasley, *Eur. J. Org. Chem.* **2009**, *2009*, 1477-1489.

[44] Y.-Y. Xie, Z.-M. Chen, H.-Y. Luo, H. Shao, Y.-Q. Tu, X. Bao, R.-F. Cao, S.-Y. Zhang, J.-M. Tian, *Angew. Chem. Int. Ed.* **2019**, *58*, 12491-12496.

[45] C.-X. Yan, F.-L. Yang, K. Lu, X. Yang, P.-P. Zhou, X. Shao, *Org. Chem. Front.* **2020**, *7*, 1845-1861.

[46] S. M. Islam, R. A. Poirier, *J. Phys. Chem. A* **2007**, *111*, 13218-13232.

[47] R. S. Brown, *Acc. Chem. Res.* **1997**, *30*, 131-137.

[48] A. Alix, C. Lalli, P. Retailleau, G. Masson, *J. Am. Chem. Soc.* **2012**, *134*, 10389-10392.

[49] B. R. Ussing, C. Hang, D. A. Singleton, *J. Am. Chem. Soc.* **2006**, *128*, 7594-7607.

[50] a) S. A. Blaszczyk, D. A. Glazier, W. Tang, *Acc. Chem. Res.* **2020**, *53*, 231-243; b) A. G. Lohse, R. P. Hsung, *Chem. Eur. J.* **2011**, *17*, 3812-3822; c) H. Butenschön, *Angew. Chem. Int. Ed.* **2008**, *47*, 5287-5290; d) M. A. Battiste, P. M. Pelphrey, D. L. Wright, *Chem. Eur. J.* **2006**, *12*, 3438-3447.

[51] a) S. E. Reisman, R. R. Nani, S. Levin, *Synlett.* **2011**, *2011*, 2437-2442; b) E. Buchner, *Ber. Dtsch. Chem. Ges.* **1896**, *29*, 106-109; c) E. Buchner, T. Curtius, *Ber. Dtsch. Chem. Ges.* **1885**, *18*, 2377-2379.

[52] Z. Chen, H. Jiao, J. I. Wu, R. Herges, S. B. Zhang, P. v. R. Schleyer, *J. Phys. Chem. A* **2008**, *112*, 10586-10594.

[53] a) L. M. Bateman, O. A. McNamara, N. R. Buckley, P. O'Leary, F. Harrington, N. Kelly, S. O'Keeffe, A. Stack, S. O'Neill, D. G. McCarthy,

A. R. Maguire, *Org. Biomol. Chem.* **2015**, *13*, 11026-11038; b) G. Boche, R. Eiben, *Tetrahedron Lett.* **1985**, *26*, 1289-1292.

[54] a) M. Tsutomu, S. Masahiko, *Bull. Chem. Soc. Jpn.* **1967**, *40*, 174-177; b) M. Ogawa, M. Sugishita, M. Takagi, T. Matsuda, *Tetrahedron* **1975**, *31*, 299-304.

[55] a) A. C. Cope, B. D. Tiffany, *J. Am. Chem. Soc.* **1951**, *73*, 4158-4161; b) A. C. Cope, N. A. Nelson, D. S. Smith, *J. Am. Chem. Soc.* **1954**, *76*, 1100-1104; c) G. Büchi, E. M. Burgess, *J. Am. Chem. Soc.* **1962**, *84*, 3104–3109.

[56] C. R. Ganellin, R. Pettit, *J. Chem. Soc. (Resumed)* **1958**, 576-581.

[57] a) P. Jain, J. C. Antilla, *J. Am. Chem. Soc.* **2010**, *132*, 11884-11886; b) L. Clot-Almenara, C. Rodríguez-Escrich, L. Osorio-Planes, M. A. Pericàs, *ACS Catal.* **2016**, *6*, 7647-7651; c) S. Gao, M. Duan, J. Liu, P. Yu, K. N. Houk, M. Chen, *Angew. Chem. Int. Ed.* **2021**, *60*, 24096-24106.

[58] K. Kaupmees, N. Tolstoluzhsky, S. Raja, M. Rueping, I. Leito, *Angew. Chem. Int. Ed.* **2013**, *52*, 11569-11572.

[59] E. Kraka, D. Cremer, *Acc. Chem. Res.* **2010**, *43*, 591-601.

[60] M. Balci, H. Fischer, H. Günther, *Angew. Chem., Int. Ed. Engl.* **1980**, *19*, 301-302.

[61] A. N. Bootsma, S. Wheeler, *ChemRxiv. Cambridge: Cambridge Open Engage* **2019**.

[62] M. N. Grayson, S. C. Pellegrinet, J. M. Goodman, *J. Am. Chem. Soc.* **2012**, *134*, 2716-2722.

[63] A. Kütt, S. Tshepelevitsh, J. Saame, M. Lõkov, I. Kaljurand, S. Selberg, I. Leito, *Eur. J. Org. Chem.* **2021**, *2021*, 1407-1419.

[64] P. Christ, A. G. Lindsay, S. S. Vormittag, J.-M. Neudörfl, A. Berkessel, A. C. O'Donoghue, *Chem. Eur. J.* **2011**, *17*, 8524-8528.

[65] a) J. Yuan, P. Jain, J. C. Antilla, *J. Org. Chem.* **2020**, *85*, 12988-13003; b) J. Yuan, P. Jain, J. C. Antilla, *J. Org. Chem.* **2022**, *87*, 8256-8266.

[66] N. Neureiter, *J. Org. Chem.* **1959**, *24*, 2044-2046.

[67] T. Hudlicky, J. W. Reed, *Angew. Chem. Int. Ed.* **2010**, *49*, 4864-4876.

[68] a) S. Clergue, O. Rousseau, T. Delaunay, G. Dequirez, T.-V. Tran, S. El Aakchioui, G. Barozzino-Consiglio, R. Robiette, *Chem. Eur. J.* **2018**, *24*, 11417-11425; b) J. Wu, J. Becerril, Y. Lian, H. M. L. Davies, J. A. Porco Jr., J. S. Panek, *Angew. Chem. Int. Ed.* **2011**, *50*, 5938-5942; c) C. Doubleday, M. Nendel, K. N. Houk, D. Thweatt, M. Page, *J. Am. Chem. Soc.* **1999**, *121*, 4720-4721; d) T. Hudlicky, A. Fleming, L. Radesca, *J. Am. Chem. Soc.* **1989**, *111*, 6691-6707.

[69] C. Apel, S. S. Hartmann, D. Lentz, M. Christmann, *Angew. Chem. Int. Ed.* **2019**, *58*, 5075-5079.

[70] a) J. Steinreiber, K. Faber, H. Griengl, *Chem. Eur. J.* **2008**, *14*, 8060-8072; b) K. Faber, *Chem. Eur. J.* **2001**, *7*, 5004-5010.

[71] a) D. Seebach, R. Gilmour, U. Grošelj, G. Deniau, C. Sparr, M.-O. Ebert, A. K. Beck, L. B. McCusker, D. Šišak, T. Uchimaru, *Helv. Chim. Acta* **2010**, *93*, 603-634; b) U. Grošelj, D. Seebach, D. M. Badine, W. B. Schweizer, A. K. Beck, I. Krossing, P. Klose, Y. Hayashi, T. Uchimaru, *Helv. Chim. Acta* **2009**, *92*, 1225-1259; c) D. Seebach, U. Grošelj, D. M. Badine, W. B. Schweizer, A. K. Beck, *Helv. Chim. Acta* **2008**, *91*, 1999-2034.

[72] S. Alvi, D. A. Singleton, *Org. Lett.* **2021**, *23*, 2174-2177.

[73] a) E. R. Johnson, S. Keinan, P. Mori-Sánchez, J. Contreras-García, A. J. Cohen, W. Yang, *J. Am. Chem. Soc.* **2010**, *132*, 6498-6506; b) J. Contreras-García, E. R. Johnson, S. Keinan, R. Chaudret, J.-P. Piquemal, D. N. Beratan, W. Yang, *J. Chem. Theory Comput.* **2011**, *7*, 625-632.

[74] Y. Hayashi, D. Okamura, T. Yamazaki, Y. Ameda, H. Gotoh, S. Tsuzuki, T. Uchimaru, D. Seebach, *Chem. Eur. J.* **2014**, *20*, 17077-17088.

CHAPTER VII

GENERAL CONCLUSIONS

7.1 General conclusions

During this research project, a multitude of systems have been studied, and the most innovative computational techniques have been applied to determine the mechanism and justify the experimentally observed selectivities.

Techniques like ELF or NCI have been crucial for the analysis of intermediates and transition states, providing clear and concise explanations for the various interactions that have guided the reaction along the observed path. Alternatives such as molecular dynamics or Macromodel have allowed for more in-depth and efficient conformational analyses than the classical approach, thus reducing potential errors in energy barrier calculations.

Nevertheless, on many occasions, experimental data have been key to distinguishing between possible mechanisms and/or corroborating computational results, offering precise and direct information about the kinetics and selectivity of the studied reactions. This fact once again demonstrates the synergistic nature of computational and experimental chemistry. The use of both methodologies is crucial for designing new synthetic routes and developing more efficient catalysis.

Computational techniques have proven to be valuable tools for studying and identifying reaction mechanisms, particularly in cases where intermediate stability is low or involves transient intermediates.

Finally, with the new technological advancements in computational capacity, algorithms, functionals, and bases, and adding the equation the new machine learning techniques, significant progress is anticipated in the development of these computational methods, enhancing their efficiency and precision.

ANNEX

CONCLUSIONES GENERALES

Durante este proyecto de investigación se han estudiado multitud de sistemas, y aplicado las más novedosas técnicas computacionales para la determinación del mecanismo y la justificación de las selectividades observadas experimentalmente.

Técnicas como ELF o NCI han sido fundamentales para el análisis de intermedios y estados de transición, y han permitido justificar de manera clara y concisa las diferentes interacciones que han dirigido a la reacción por el camino observado. Alternativas como la dinámica molecular o Macromodel han permitido realizar análisis conformacionales con mayor profundidad y eficiencia que la vía clásica, reduciendo así posibles errores en el cálculo de barreras de energía.

Sin embargo, en muchas ocasiones los datos experimentales han sido la clave para poder discernir entre posibles mecanismos y/o corroborar los resultados computacionales, proporcionando información precisa y directa sobre la cinética y la selectividad de las reacciones estudiadas, demostrando una vez más el carácter sinérgico de la química computacional y la experimental. La utilización de ambas metodologías es crucial para el diseño de nuevas rutas sintéticas y el desarrollo de una catálisis más eficiente.

Las técnicas computacionales han demostrado ser una buena herramienta para el estudio e identificación de mecanismos de reacción, sobre todo en aquellos casos en los que la estabilidad del intermedio es reducida o se trata de intermedios transientes.

Finalmente, con los nuevos avances tecnológicos tanto en la capacidad cálculo, como en los algoritmos, funcionales y bases utilizadas, y añadiendo a esta ecuación las nuevas técnicas de *machine learning*, se prevé un gran avance en el desarrollo de estos métodos computacionales aumentando su eficiencia y precisión.

SCIENTIFIC MEETINGS

1. **IX National Conference BIFI 2019**, 30th January to 1st February 2019, Zaragoza. *Poster communication.* Title: Computational study of organic reactions synchronicity through a study case.
2. **XXXVII Reunión Bienal de la Real Sociedad Española de Química (RSEQ)**, 26th-30th May 2019, Donostia-San Sebastián. *Poster communication.* Title: (4+3) Cycloaddition's Synchronicity between Nitrones and 1,2-Diaza-1,3-dienes.
3. **RSEQ symposium 2021**, 27th-30th September 2021, on-line. *Poster communication.* Title: Oxidation of Hydroxylamines with Ruthenium Tetroxide: A Computational Journey through Oxidation Mechanism.
4. **I Symposium in Molecular Chemistry and Catalysis**, 3rd June 2022, Zaragoza. *Oral presentation.* Title: Insights on the oxidation of 5-member cyclic hydroxlyalmines with RutheniumTetraoxide (2nd price).
5. **XXXVIII Reunión Bienal de la Real Sociedad Española de Química (RSEQ)**, 27th-30th June 2022, Granada. *Oral flash presentation.* Title: Mechanistics insights in the pseudopericyclic oxidation of 5-member cyclichydroxylamine with ruthenium tetroxide.
6. **XXVIII Reunión Bienal del Grupo Especializado de Química Orgánica (GEQOR)**, 1st July 2022, Granada. *Poster communication.* Title: 3' Substituent effects on the Oxidation of 5-Memberer Cyclic Hydroxylamines with Ruthenium Tetroxide.
7. **10ª Jornada de Jóvenes Investigadores (Química y Física) de Aragón**, 14th December 2022. *Oral communication.* Title: Estudio Teórico sobre la Aminohalogenación Transanular Enantioselectiva de Enesultamas.

PUBLICATIONS BASED ON THE CONCEPT OF THE THESIS

1. M. Pedrón, L. Legnani, M. A. Chiaccio, P. Caramella, T. Tejero, P. Merino, Transient and Intermediate Carbocations in Ruthenium Tetroxide Oxidation of Saturated Rings, *Beilstein J. Org. Chem*., **2019**, 15, 1552 – 1562.
2. E. Capel, M. Rodríguez-Rodríguez, U. Uria, M. Pedrón, T. Tejero, J. L. Vicario, P. Merino, Absence of Intermediates in the BINOL-Derived Mg(II)/Phosphate Catalyzed Desymmetrizative Ring Expansion of 1-Vinylcyclobutanols, *J. Org. Chem*., **2022**, 87, 693 – 707.
3. R. Lassfolk, M. Pedrón, T. Tejero, P. Merino, J. Wärnå, R. Leino, Acyl Group Migration in Pyranosides as Studied by Experimental and Computational Methods, *Chem. Eur. J.*, **2022**, 28, e2022004.
4. J. Luis-Barrera, S. Rodriguez, U. Uria, E. Reyes, L. Prieto, L. Carrillo, M. Pedrón, T. Tejero, P. Merino, J.L. Vicario, Brønsted Acid versus Phase-Transfer Catalysis in the Enantioselective Transannular Aminohalogenation of Enesultams, *Chem. Eur. J.*, **2022**, 28, e202202267.
5. R. Lassfolk, M. Pedrón, T. Tejero, P. Merino, J. Wärna, R. Leino, Acetyl Group Migration in Xylan and Glucan Model Compounds as Studied by Experimental and Computational Methods, *J. Org. Chem*., **2022**, 87, 14544−14554.
6. J. Sendra, O. Salvado, M. Pedrón, E. Reyes, T. Tejero, E. Fernández, P. Merino, J. L. Vicario, Switchable Brønsted Acid-Catalyzed Ring Contraction of Cyclooctatetraene Oxide Towards the Enantioselective Synthesis of Cycloheptatrienyl-Substituted Homoallylic Alcohols and Oxaborinanes, *Adv. Synth. Catal*., **2023**, 365, 1058–1071.
7. G. Garay, J. Hurtado, M. Pedrón, L. García, E. Reyes, E. Sánchez-Díez, T. Tejero, L. Carrillo, P. Merino, J. L. Vicario, Organocatalytic Enantioselective Vinylcyclopropane-Cyclopentene (VCP-CP) Rearrangement, *Angew. Chem. Int. Ed.,* **2023**, 62, e202302416.